



Capacity Estimation and Trajectory Prediction of Lithium-ion Batteries Based on Time-Frequency Analysis and Machine Learning Algorithms

El-Dalahmeh, Ma'd

Director of Studies: Dr Maher Al-Greer

Supervisors: Professor Michael Short, Dr Musbahu Muhammad

School of Computing, Engineering and Digital Technologies

A thesis submitted in partial fulfilment of the requirements of Teesside University for the
degree of Doctor of Philosophy

May - 2023

Abstract

Lithium-ion batteries have become increasingly popular, particularly in electromobility, due to their advantages, such as low costs, high energy/power densities, and low-self discharge rate. Nonetheless, like most electrochemical systems, lithium-ion batteries experience performance degradation over time during both usage and storage, highlighting the importance of assessing the battery's longevity and reliability under operation. Therefore, proper monitoring of lithium-ion battery capacity and precise prediction of battery degradation contributes to maintenance, safety, and asset optimisation and lays the foundation for the technical and economic analysis of potential second-life applications. However, accurately estimating and predicting the capacity of lithium-ion batteries is far from a simple task, as battery ageing is a complex nonlinear process involving various internal mechanisms that are extremely difficult to measure and model with precision. To address this need, this thesis concentrates on developing a framework that accurately estimates and predicts battery capacity by integrating advanced signal processing techniques with data-driven algorithms.

This thesis introduces a multi-domain feature time-frequency analysis and machine learning approach for lithium-ion battery capacity estimate and prediction. Time-frequency analysis is used to reveal hidden characteristics in the recorded nonlinear and nonstationary voltage signal. Specifically, Continuous wavelet transform (CWT) is used to obtain diagnostic features on lithium-ion battery deterioration by converting 1D terminal voltage signals into 2D pictures (wavelet energy concentration). The 2D deep learning convolutional neural network approach extracts battery voltage characteristics from produced images. Extracting characteristics predicts lithium-ion battery capacity. Due to its ability to extract electrochemical characteristics from the non-stationary and non-linear battery signal in both time and frequency domains, time-frequency analysis vividly visualised the battery deterioration process. The suggested technique achieves 95.60% prediction accuracy, showing strong potential for battery management system design.

To prevent battery failure, a general framework that estimates lithium-ion battery capacity regardless of operating parameters, such as cycle current profile and working temperature, must be developed. Thus, a unique generalised lithium-ion battery capacity estimation method based on the adaptive empirical wavelet transform (EWT) and long-short-term memory neural

network (LSTM) has been developed. In the time-frequency domain, the adaptive EWT can analyse the charging-discharging terminal voltage signal with non-stationary and transient lithium-ion battery phenomena. 13 statistical characteristics are retrieved to see if capacity decline is correlated with them. After that, the LSTM model estimates LIB capacity. The suggested technique accurately calculates LIB capacity with an average root mean square error of 1.26% and a maximum of 2.74%.

Finally, to ensure safe, dependable, and low-cost operation, lithium-ion battery capacity deterioration must be predicted. Predicting lithium-ion battery capacity deterioration is difficult. Regeneration also affects capacity degradation trajectory prediction accuracy. This thesis presents three time-frequency analysis methods and the nonlinear autoregressive neural network algorithm to increase lithium-ion battery capacity deterioration trajectory forecast accuracy. The time-frequency analysis approach and nonlinear autoregressive neural network predicted with a 2.385% root mean square error and a maximum error of 1.6%.

Dedication

This thesis is dedicated to my parents, Prof Suleiman and Sabah El-Dalahmeh, for their endless love, support, and encouragement.

Your son

Ma'd El-Dalahmeh

Acknowledgements

First and foremost, I would like to express my profound gratitude to Allah the Almighty, the Most Gracious and the Most Merciful, for granting me the patience to complete this work. All praise be to God.

I would also like to convey my heartfelt appreciation to my supervisors, Dr Maher Al-Greer, Dr Imran Bashir, Dr Musbahu Muhammad, and Prof. Michael Short, for their invaluable guidance, advice, and help. Their knowledge in their respective fields and dedication to academic excellence has been vital in helping me refine my ideas and accomplish my research objectives. I am particularly grateful to Dr Maher Al-Greer for his exceptional mentorship, expertise, and encouragement throughout the entire research process. His insightful feedback, constructive criticism, and timely support have been crucial in shaping the direction and quality of my work.

I also wish to thank my friend since day one on the earth, my twin brother Mo'ath, who offered helpful comments, suggestions, motivation, and collaboration in battery research during this study. His insights, feedback, and support have been invaluable in assisting me in refining my arguments and enhancing the clarity and coherence of my work.

I sincerely thank my fellow researchers and colleagues at the M7.06 office for the engaging discussions, shared experiences, and camaraderie. I particularly want to express my gratitude to Dr Ahmed Gailani, Princewill Ikpeka, and Vishak Dudhee for their friendship, encouragement, and indispensable help during challenging times.

I especially appreciate the unwavering support and friendship of Hazim Al-Dghameen, Bassem Al-Ahmad, Loay Al-Ahmad, Obada Al-Sabaybah, Anas Al-Hindawi, Shaden Momani, Mahasen Qahwaji, and Danya Al-Hendawi. Your encouragement, assistance, and laughter have made this demanding journey a pleasant and unforgettable experience. I am truly fortunate to have you all as friends.

Lastly, my deepest gratitude goes to my father and mother, whose constant love, support, and encouragement have been the bedrock of strength and inspiration throughout my life. Their sacrifices, guidance, and prayers have been instrumental in shaping my personal and academic

journey, and I attribute my success to their unswerving faith in me. I warmly thank all my sisters, Safaa, Ghader, and Bushra, and my brothers Moawiah, Mo'ath, Adi, Ghaith, and Qais, for their ongoing love, support, and encouragement. Your support has been invaluable in helping me surmount the challenges and obstacles I faced during this journey.

Contents

List of Figures.....	x
List of Tables	xiv
Nomenclature.....	xv
Chapter 1 Introduction and Scope of The Thesis	19
1.1 The Motivation for The Proposed Research.....	20
1.1.1 Why Do We Need Lithium-ion Batteries?.....	20
1.1.2 The Challenges Facing the Lithium-ion Batteries.....	23
1.2 Aim, Research Questions, and Objectives.....	27
1.3 Key Contribution of the Research	28
1.4 List of Publications	30
1.5 Thesis Organisation	31
Chapter 2 Advanced Techniques for The Capacity Estimation of Lithium-ion Batteries 34	
2.1 Brief Introduction	35
2.2 Principle Operation of Lithium-ion Batteries.....	35
2.3 Degradation in Lithium-ion Batteries.....	38
2.4 Measurement of Degradation	41
2.4.1 Capacity loss and power loss	41
2.4.2 BOL, EOL, SOH, RUL	41
2.5 Experimental Techniques	43
2.5.1 Coulomb Counting	43
2.5.2 Open Circuit Voltage	44
2.5.3 Electrochemical Impedance Spectroscopy.....	46
2.5.4 Incremental Capacity Analysis and Differential Voltage Analysis-based Techniques	50
2.6 Model-based Techniques	55
2.6.1 Equivalent Circuit Models (ECM)	56
2.6.2 Electrochemical Models (EM)	67
2.7 Data-Driven Techniques.....	73
2.7.1 Feature Extraction based on Charging Curve.	75
2.7.2 Feature Extraction based on Differential Curve.....	83
2.7.3 Feature Extraction based on the EIS curve	89

2.8	Summary	94
Chapter 3 Time-Frequency Image Analysis and Transfer Learning CNN for Capacity Prediction of Lithium-ion Batteries97		
3.1	Brief Introduction	98
3.2	The Proposed Capacity Imaging Analysis Scheme	99
3.2.1	Randomised Battery Dataset	100
3.2.2	Time-Frequency Image (TFI) Analysis.....	104
3.2.3	Time-Frequency Image Analysis and Classification Using Deep Learning Algorithm 111	
3.3	Results and Discussions.....	114
3.3.1	Time-Frequency Image Results	114
3.3.2	Deep Learning Classification CNN Results.....	120
3.3.3	Deep Learning Regression CNN Results	131
3.4	Summary.....	135
Chapter 4 Capacity Estimation of Lithium-ion Batteries Based on Adaptive Empirical Wavelet Transform and Long Short-term Memory Neural Network.....137		
4.1	Brief Introduction	138
4.2	The Proposed Framework for Capacity Estimation	139
4.2.1	Experimental Datasets.....	140
4.2.2	Empirical Wavelet Transform (EWT).....	150
4.2.3	Fundamental Mode Filtering.....	152
4.2.4	Feature Extraction and Selection.....	153
4.2.5	Long Short-Term Memory Neural Network (LSTM).....	155
4.2.6	Evaluation Criteria	158
4.3	Results and Discussion	160
4.3.1	EWT Results	160
4.3.2	Features Extraction Results.....	165
4.3.3	Capacity Estimation Results.....	169
4.3.4	Comparative Analysis with The State-Of-The-Art Methods	178
4.3.5	Computational Complexity	180
4.4	Summary.....	181
Chapter 5 Lithium-ion Batteries Capacity Degradation Trajectory Prediction Based on Decomposition Techniques and NARX Algorithm183		
5.1	Brief introduction	184
5.2	The Proposed Framework for Capacity Degradation Trajectory Prediction.....	184
5.2.1	Lithium-ion Batteries Datasets.....	185
5.2.2	Discrete Wavelet Transform (DWT).....	188
5.2.3	Empirical Mode Decomposition (EMD).....	193

5.2.4	Variational Mode Decomposition (VMD)	195
5.2.5	Nonlinear Autoregressive with Exogenous Input (NARX) Data-Driven Algorithm 197	
5.3	Results and Discussion	198
5.3.1	DWT, EMD, and VMD Results	198
5.3.2	NARX Prediction Results	205
5.4	Summary.....	216
Chapter 6	Conclusion and Future Work	217
6.1	Conclusions	218
6.1.1	Time-Frequency Image technique and Deep Learning CNNs for Capacity estimation of LIBs	218
6.1.2	The general framework for Capacity Estimation Based on Adaptive Empirical Wavelet Transform and LSTM.	218
6.1.3	Capacity Degradation Trajectory Prediction of LIBs	219
6.2	Future work.....	220
References		223
Appendix A TFI Code.....		245
Appendix B EWT-LSTM Code		248

List of Figures

Figure 1.1 Visual representation showing the gravimetric energy and power densities of different battery technologies at the cell levels.....	21
Figure 1.2 The global electric cars stock, 2010-2021. BEV: battery electric vehicle; PHEV: plug-ion hybrid electric vehicle [10].	22
Figure 1.3 Energy density of LIBs packs, 2008-2020.....	22
Figure 1.4 Example of failed LIBs in (a) Tesla EV and (b) Boeing 787 Dreamliner.	24
Figure 1.5 BMS architecture.	26
Figure 1.6 An overview of the aim of this thesis.	27
Figure 1.7 Thesis organisation.	33
Figure 2.1 Main parts of the LIB.....	36
Figure 2.2 The movement of lithium-ion during discharge and charge processes.	37
Figure 2.3 Degradation mechanisms in lithium-ion batteries [25, 41].....	40
Figure 2.4 Degradation modes and their effect in lithium-ion batteries [25].....	40
Figure 2.5 Capacity investigation methods.	42
Figure 2.6 (a) low-rate discharge current (b) OCV measurement.....	45
Figure 2.7 The evolution of the OCV measurements throughout the battery lifetime.....	46
Figure 2.8 Measurement principle of EIS (galvanostatic mode).	47
Figure 2.9 The obtained processes by EIS of the lithium-ion battery.....	48
Figure 2.10 The evolution of the impedance of LIB over time.....	49
Figure 2.11 Equivalent circuit model.	50
Figure 2.12 The IC curve of LIB [86].	52
Figure 2.13 Original and smoothed IC curve.....	53
Figure 2.14 The evolution of the IC curves of the LIB over the battery lifetime.	53
Figure 2.15 The evolution of DVA over battery lifetime [82].....	54
Figure 2.16 LIBs modelling methods.....	56
Figure 2.17 LIB equivalent circuit modelling approaches.....	57
Figure 2.18 Voltage response to the pulse discharge current signal.	58
Figure 2.19 Thevenin equivalent circuit models: (a) <i>Rint</i> model, (b) 1-RC model, and (c) 2-RC model.....	59
Figure 2.20 Schematic diagram of Thevenin model parameters identification.	62
Figure 2.21 The LIB equivalent circuit model using EIS measurement.	63
Figure 2.22 The P2D model of LIB.	68
Figure 2.23 The schematic of the SPM.	70

Figure 2.24 The general framework for the capacity estimation of LIB using model-based methods.	71
Figure 2.25 The general flowchart for the capacity estimation of LIBs based on data-driven techniques.	75
Figure 2.26 Feature extraction methods.	75
Figure 2.27 (a) CC-CV voltage and (b) CC-CV current curves.	76
Figure 2.28 CC-CV voltage curves at different SOH (capacity values).	77
Figure 2.29 Health feature extraction from three different voltage ranges [187].	79
Figure 2.30 Discretised partial voltage, current, and charge capacity [189].	79
Figure 2.31 The proposed multi-model fusion algorithm for the capacity of LIBs [190]. .	81
Figure 2.32 CC-CV voltage and current showing the relaxation period [192].	81
Figure 2.33 IC curves of a LIB over its lifetime.	84
Figure 2.34 The extracted health features are based on the IC curve in [218].	85
Figure 2.35 The extracted health features based on the IC curve in [86].	86
Figure 2.36 The calculated IC curves of a) LFP, b) NMC, and c) LTO LIBs [215].	88
Figure 2.37 Three types of feature extraction methods based on EIS data.	91
Figure 3.1 Graphical abstract of the proposed TFI method.	99
Figure 3.2 General flow chart of the proposed method for TFI capacity estimation.	100
Figure 3.3 The cycle processes.	101
Figure 3.4 Voltage, current, and temperature of the first 100 steps measured for battery RW9.	102
Figure 3.5 Voltage, current, and temperature of the last 100 steps measured for battery RW9.	102
Figure 3.6 Capacities of the measured cells for four batteries, RW9, RW10, RW11, and RW12.	104
Figure 3.7 Window functions of (a) STFT and (b) CWT.	107
Figure 3.8 (a) Example of STFT and CWT in analysing signal in time-frequency domain. (a) The analysed signal, (b) the CWT spectrogram, and (c) the STFT spectrogram.	109
Figure 3.9 Measured LIB voltage and transformed TFI energy concentration spectrum information of the measured voltage at three different capacity values.	111
Figure 3.10 Deep learning convolutional neural network architecture.	113
Figure 3.11 Max pooling layer. The maximum number in each region is selected.	114
Figure 3.12 Time-domain measured voltage and plot of TFI energy concentration spectrum of battery cell (RW9): (a) measured voltage signal (beginning of life), (b) wavelet energy concentration spectrum (beginning of life), (c) measured voltage signal (end of life), and (d) wavelet energy concentration spectrum (end of life).	117
Figure 3.13 TFI energy concentration spectrum results of the battery RW9 measured voltage at different capacities: (a) 2.1 Ah, (b) 1.8 Ah, (c) 1.6 Ah, (d) 1.4 Ah, (f) 1.2 Ah, (e) 0.8 Ah.	118
Figure 3.14 AlexNet model structure.	121

Figure 3.15 VGG-16 model structure.	123
Figure 3.16 Example of the input TFIs images at BOL and EOL of RW9 LIB fed into the AlexNet DL-CNN.	125
Figure 3.17 Overall flowchart of the given example.	125
Figure 3.18 The activation functions of the norm1 layer for TFI in the BOL state.	126
Figure 3.19 The activation functions of the norm1 layer for TFI in the EOL state.	126
Figure 3.20 The activation functions of the deeper layer (conv5) in the AlexNet DL-CNN at the BOL of the LIB.	127
Figure 3.21 The activation functions of the deeper layer (conv5) in the AlexNet DL-CNN at the EOL of the LIB.	128
Figure 3.22 The obtained results of the Grad-CAM visualisation technique for deeper and shallow layers for TFI in the BOL of LIB.	128
Figure 3.23 The obtained results of the Grad-CAM visualisation technique for deeper and shallow layers for TFI in the EOL of LIB.	129
Figure 3.24 The obtained results of the occlusion sensitivity visualisation method with lower and high-resolution sensitivity of LIB at its BOL.	130
Figure 3.25 The obtained results of the occlusion sensitivity visualisation method with lower and high-resolution sensitivity of LIB at its EOL.	130
Figure 3.26 AlexNet structure transfer learning from image classification into image regression—all the parameters from conv1 to conv3-3 layers transferred without any modification.	132
Figure 3.27 Capacity estimation results of AlexNet and VGG-16 DL-CNNs.	134
Figure 3.28 The RMSE for capacity estimation of four LIBs using AlexNet and VGG-16 DL-CNNs.	135
Figure 4.1 Graphical abstract of the proposed framework for the capacity estimation of LIBs.	139
Figure 4.2 The proposed method for capacity estimation of LIBs based on EWT.	140
Figure 4.3 The cycle process for the NASA Randomised dataset.	142
Figure 4.4 Voltage and current signals of the cell RW9 at (a) the beginning of life (BOL) and (b) the end of life (EOL).	145
Figure 4.5 The measured voltage and current signals for three different LIBs.	146
Figure 4.6 The capacity fade for all the LIBs of each group.	148
Figure 4.7 UDDS current profile and the measured voltage signals.	149
Figure 4.8 The discharge capacity of the Stanford dataset.	150
Figure 4.9 LSTM structure.	156
Figure 4.10 The structure of the designed LSTM model.	158
Figure 4.11 Cross-validation approach for training, validating, and testing the LSTM model. In each cross-validation iteration, one LIB was selected as the test set.	160
Figure 4.12 EWT decomposition modes of the measured voltage for battery RW9 at its (a) first cycle and (b) last cycle.	162

Figure 4.13 Central frequencies and bandwidth of EWT decomposition for battery RW9 at its (a) first cycle and (b) last cycle.	164
Figure 4.14 Example of the correlation between the IMFs and measured voltage. (a) and (c) the IMFs at the BOL, (b) and (d) the IMFs at the EOL of the LIBs.	165
Figure 4.15 Example visualisation of the 13 extracted features for LIB RW1 in group 1 from the NASA dataset.	166
Figure 4.16 Example visualisation of the 13 extracted features for LIB W8 in Stanford University's dataset.	167
Figure 4.17 The correlation matrix of the extracted features for all the selected LIBs from the NASA and Capacity Estimation Results.	169
Figure 4.18 Validation results of the first scenario.	174
Figure 4.19 Capacity estimation results of the second scenario.	178
Figure 5.1 The proposed framework for capacity trajectory prediction of LIBs.	185
Figure 5.2 Capacity degradation of NASA dataset.	186
Figure 5.3 Capacity degradation of CALCE dataset.	188
Figure 5.4 Translation and scaling functions of the DWT [303].	189
Figure 5.5 Haar mother wavelet function.	191
Figure 5.6 Daubechies (db4) mother wavelet function.	191
Figure 5.7 Daubechies (db8) mother wavelet function.	192
Figure 5.8 Symlets (sym4) mother wavelet function.	192
Figure 5.9 Coiflets (coif4) mother wavelet function.	193
Figure 5.10 Schematic diagram of the implementation of the EMD.	195
Figure 5.11 The architecture of the NARX model.	198
Figure 5.12 The extracted IMFs and RES of (a) DWT, (b) EMD, and (c) VMD.	201
Figure 5.13 Pearson correlation results of (a) DWT, (b) EMD, and (c) VMD.	204
Figure 5.14 The denoised capacity results of (a) B005 and (b) CS2-35 LIBs.	205
Figure 5.15 Capacity trajectory prediction results of NASA and CALCE datasets.	209
Figure 5.16 (a) RMSE and (b) MAE results for DWT, EMD, and VMD decomposition techniques.	210
Figure 5.17 Capacity trajectory prediction results of NASA and CALCE datasets at the early-life case.	214
Figure 5.18 (a) RMSE and (b) MAE results for DWT, EMD, and VMD decomposition techniques.	215
Figure 6.1 Flowchart of the cloud-based approach for online capacity estimation of LIB.	221
Figure 6.2 Flowchart of the proposed future work for sorting the retired LIB.	222

List of Tables

Table 2.1 List different equivalent elements in equivalent circuit models [61].	64
Table 2.2 List of ECMs based on the impedance spectroscopy measurement.	65
Table 2.3 Advantages and disadvantages of ECMs modelling methods.	66
Table 2.4 Overview of the most applied filters/observers' algorithms for state estimation of LIB.	72
Table 2.5 Recent proposed methods for the capacity estimation of LIBs based on charging curves.	82
Table 3.1 The general characteristics of the tested cells.	101
Table 3.2 TFI energy for different LIBs at different capacity values.	119
Table 3.3 Hyperparameter settings for the trained AlexNet model.	121
Table 3.4 AlexNet architecture.	122
Table 3.5 Capacity prediction accuracy for each battery cell using AlexNet.	122
Table 3.6 VGG-16 architecture.	123
Table 3.7 Capacity prediction accuracy for each battery cell using VGG-16.	124
Table 3.8 RMSE and AE of AlexNet DL-CNN.	134
Table 3.9 RMSE and AE of VGG-16 DL-CNN.	134
Table 4.1 The properties of the LIBs.	142
Table 4.2 Summary of the seven cycling protocols applied to NASA LIBs.	143
Table 4.4 The technical specifications of INR21700-M50T NMC LIB.	149
Table 4.5 Extracted characteristics features.	153
Table 4.6 RMSEs and AEs of the capacity estimation results in a noise-free scenario.	171
Table 4.7 RMSEs and AEs of the capacity estimation results in a noisy scenario.	175
Table 4.8 Comparison of the RMSEs of NASA randomised data set for capacity estimation of LIBs.	179
Table 4.9 The PC specifications for implementing the proposed framework.	180
Table 4.10 The results of the computational time for training and testing datasets.	180
Table 5.1 The properties of the LIBs for the NASA dataset.	186
Table 5.2 The properties of the LIBs for CALCE dataset.	187
Table 5.3 Implementation steps of VMD algorithm.	196

Nomenclature

LIB	Lithium-ion Batteries
NMC	Lithium Nickel Manganese Cobalt Oxide
LFP	Lithium Iron Phosphate
LTO	Lithium Titanate
BMS	Battery Management System
EV	Electric Vehicles
GHG	Greenhouse Gas
ICE	Internal Combustion Engine
BOL	Beginning Of Life
EOL	End Of Life
SOC	State Of Charge
SOH	State Of Health
SOP	State Of Power
SOE	State Of Energy
TFA	Time-Frequency Analysis
TFI	Time-Frequency Image
DL-CNN	Deep Learning Convolutional Neural Network
ML	Machine Learning
STFT	Short-Time Fourier Transform
WVD	the Wigner-Ville Distribution
CWT	Continuous Wavelet Transform
DWT	Discrete Wavelet Transform
EWT	Empirical Wavelet Transform
EMD	Empirical Mode Decomposition
VMD	Variational Mode Decomposition
SEI	Solid Electrolyte Interphase
LLI	Loss of Lithium Inventory

LAMNE	Loss of Active Material of the Negative Electrode
LAMPE	Loss of Active Material of the Positive Electrode
OCV	Open Circuit Voltage
CC-CV	Constant Current- Constant Voltage
EIS	Electrochemical Impedance Spectroscopy
ECM	Equivalent Circuit Model
EM	Electrochemical Model
ICA	Incremental Capacity Analysis
DVA	Differential Voltage Analysis
LS	Least Square Algorithm
PSO	Particle Swarm Optimisation
CPE	Constant-Phase Element
P2D	Pseudo-2D Porous Electrode model
SPM	Single Particle Model
PDE	Partial Differential Equation
KF	Kalman filter
EKF	Extended Kalman Filter
DEKF	Dual Extended Kalman Filter
UKF	Unscented Kalman Filter
SPKF	Sigma-Point Kalman Filter
FOMIUKF	Fractional-Order Multi-Innovations Unscented Kalman Filter
ASREKF	Dual Adaptive Square Root Extended Kalman Filter
SMO	Sliding Mode Observer
PF	Particle Filter
PDE	Partial Differential Equation
SVR	Support Vector Regression
RF	Random Forest Regression
GPR	Gauss Progress Regression
NCA	Neighbourhood Component Analysis
RNN	Recurrent Neural Network
LSTM	Long Short-Term Memory

NARX	Nonlinear Autoregressive with Exogenous Input
MLR	Multiple Regression
ANN	Artificial Neural Networks
GRU	Gated Recurrent Neural Network
FFT	Fast Fourier transform
MRA	Multiresolution Analysis
SGDM	Stochastic Gradient Descent with Momentum
ADAM	Adaptive Mata Momentum
CMMW	Complex Morlet Mother Wavelet Transform
IMF	Intrinsic Mode Functions
RPT	Reference Performance Test
UDDS	Urban Dynamometer Driving Schedule
PCA	Principal Component Analysis
AE	Absolute Error
RMSE	Root Mean Square Error

Chapter 1 **Introduction and Scope of The Thesis**

1.1 The Motivation for The Proposed Research

1.1.1 Why Do We Need Lithium-ion Batteries?

Electrifying transportation is a crucial step towards decarbonising the transportation sector and addressing the challenges of air pollution, oil dependency, and climate change [1, 2]. By transitioning from fossil-fuelled vehicles to Electric Vehicles (EVs), we can significantly reduce the transportation sector's carbon footprint. EVs powered by clean, renewable energy sources produce substantially fewer greenhouse gas (GHG) emissions than traditional internal combustion engine (ICE) vehicles, helping to mitigate the impacts of climate change [3]. Additionally, electrification can reduce our dependence on finite, non-renewable resources like oil, promoting a more sustainable energy mix [4]. Lithium-Ion Batteries (LIBs) have been considered a promising solution to decarbonise the transportation sector and achieve a net-zero carbon economy [5, 6]. LIBs have been growing rapidly in recent years due to their high energy density, high power density, low-self discharge rate, and long cycle life [7, 8]. LIBs are now widely used in various applications, including portable electronics, EVs, and renewable energy storage systems. Numerous kinds of electrochemical cells exist, yet LIBs presently dominate the market for sustainable energy storage in commercial use. This predominance is due to their advanced state of technology, the already considerable scale of the industry, an optimal balance of energy density and power density, and a cost that fits the budget for a wide range of applications.

High gravimetric power and energy densities are essential for acceleration and range in EV applications. A high volumetric energy density is required in applications with limited space, such as mobile electronics. As shown in Figure 1.1, the gravimetric energy and power densities of various electrochemical cells are depicted. It is essential to remember that solid-state, Li-S, and Li-O₂ batteries are still in their developmental stage, making LIBs the best option for commercial use at present [9].

The global EV sales have rapidly increased in recent years, driven by a combination of factors, including government incentives, improvements in battery technology, and growing consumer awareness about the environmental impact of gasoline-powered vehicles. According

to a recent report published by International Energy Agency (IEA) [10], EV sales doubled in 2021 from the previous year to a new record of 6.6 million.

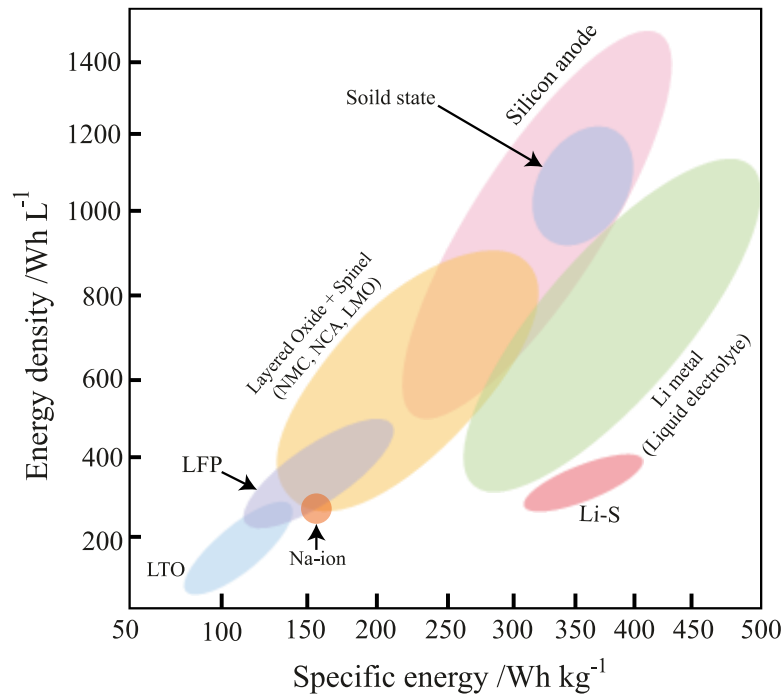


Figure 1.1 Visual representation showing the gravimetric energy and power densities of different battery technologies at the cell levels.

Back in 2012, just 120,000 EVs were sold worldwide. In 2021, more than 350,000 EVs are sold each week. Nearly 10% of global car sales were electric in 2021, four times the market share in 2019. This brought the total number of EVs on the world's roads to about 16.5 million, triple the amount in 2018, as shown in Figure 1.2. Global sales of EVs have kept rising strongly in 2022, with 2 million sold in the first quarter, up 75% from the same period in 2021. Multiple factors are driving the success of EVs. Improvement in LIBs technology is the main pillar. According to an industrial-wide trend, the energy density of LIBs used in EVs has risen from 60 Wh/L in 2008 to 450 Wh/L in 2020, as shown in Figure 1.3 [11]. Moreover, a recent report by McKinsey & Company [12] states that battery pack prices are now under \$230/kWh, representing a decrease of almost 80% from the 2010 cost of \$1000/kWh.

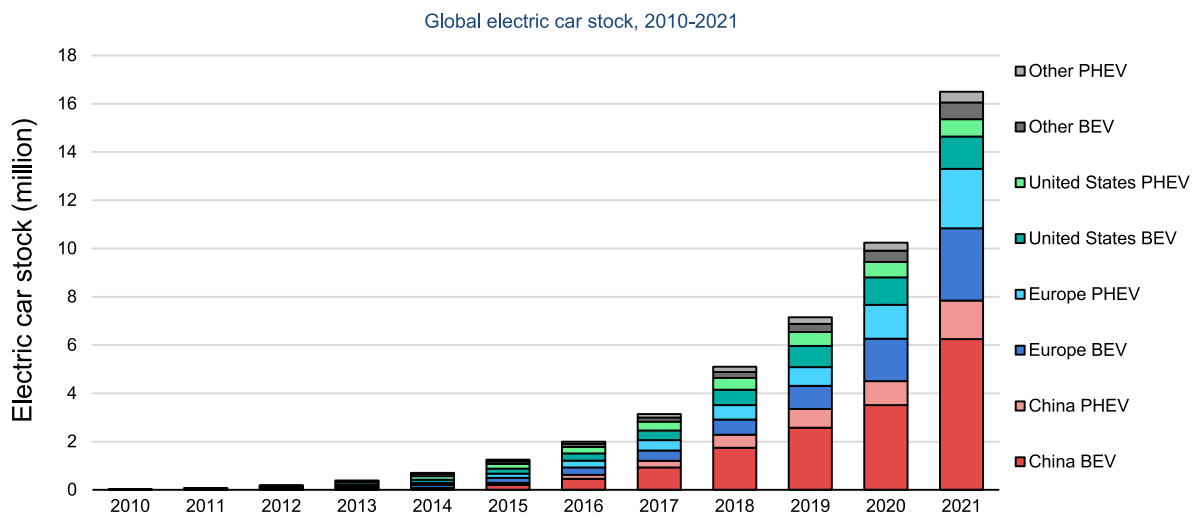


Figure 1.2 The global electric cars stock, 2010-2021. BEV: battery electric vehicle; PHEV: plug-ion hybrid electric vehicle [10].

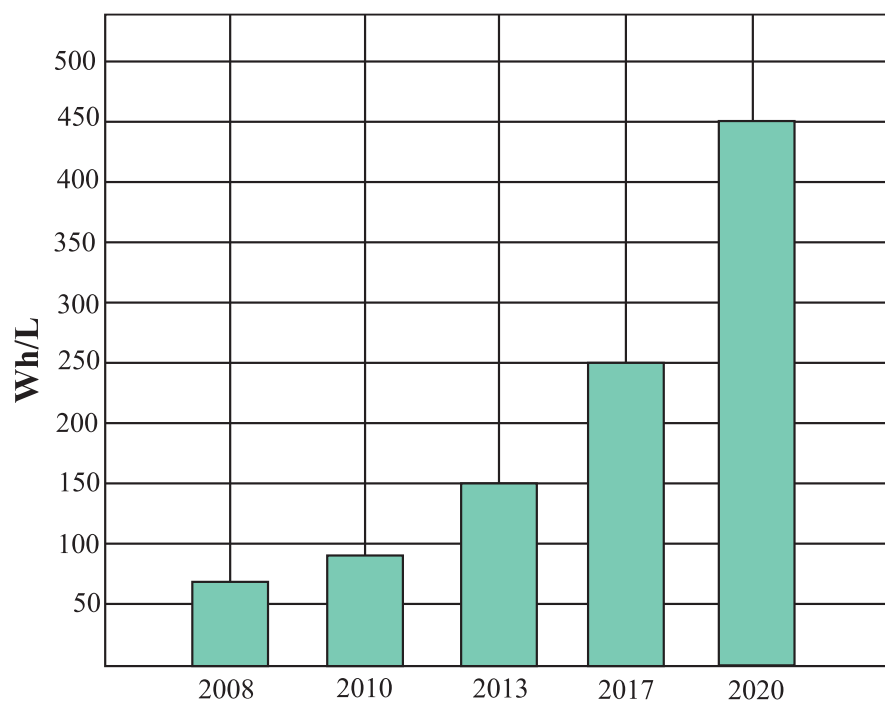


Figure 1.3 Energy density of LIBs packs, 2008-2020.

Public spending on EV subsidies and incentives nearly doubled in 2021 to almost USD 30 billion [10]. Numerous countries have committed to ending internal combustion engines or

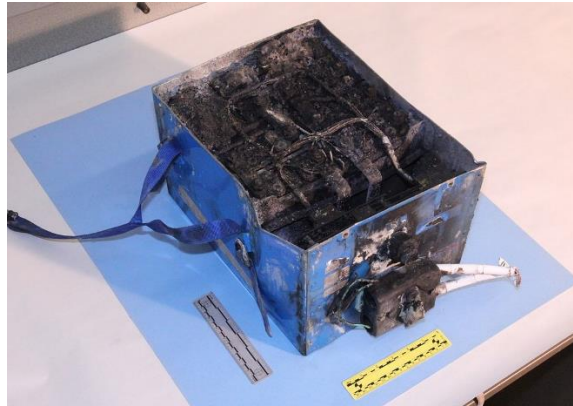
have set ambitious goals for vehicle electrification in the forthcoming years. In parallel, various automobile manufacturers have plans for fleet electrification that exceed governmental goals. Notably, the number of new EV models launched in 2021 was five times greater than in 2015, enhancing their appeal to consumers. Presently, the market offers approximately 450 different EV models.

1.1.2 The Challenges Facing the Lithium-ion Batteries.

A necessity to all these mentioned applications of LIBs is a management system, which, in simple terms, serves as the brain of the battery, monitoring/controlling every aspect of the operation. The battery management system (BMS) plays a significant role in ensuring a safe operating envelope whilst maximising the battery's energy and/or power delivery capabilities and improving its overall service lifetime [13, 14]. Figure 1.4 (a) and (b) illustrate fire-damaged LIBs packed out of Tesla Model 3 and Boeing 787 Dreamliner, respectively [15, 16]. The root cause of the failure in both cases is strongly linked to a defective BMS, which led to a thermal runaway event in some constituent cells. Moreover, A sharp or unexpected decline in capacity could indicate a catastrophic failure, such as a short circuit, battery overheat, or other internal malfunctions. By utilising robust capacity estimation method, the BMS can pre-emptively detect such failures before they escalate into serious incidents. Thus, this estimation acts as a crucial warning system that triggers preventative measures, enabling timely intervention and potentially averting catastrophic outcomes.



(a) Tesla EV.



(b) Boeing 787 Dreamliner.

Figure 1.4 Example of failed LIBs in (a) Tesla EV and (b) Boeing 787 Dreamliner.

From Figure 1.4, a reliable BMS is of utmost importance for safety-critical LIB applications, especially in transportation applications, where a battery failure can risk passengers' lives.

The BMS is responsible for several hardware and software operations that always keep the LIB under safe working conditions. Figure 1.5 shows the general architecture of the BMS. Several sub-systems lie in the BMS, such as the charging controller, thermal management, battery balancing, and state estimation systems. The detail description of each sub-system as follows:

- 1- Battery Monitoring (State estimation) system: This sub-system keeps track of the individual cell voltages within the battery pack, along with the pack's overall voltage, current, and temperature. It allows the BMS to determine the battery's state of charge (SoC) and state of health (SoH), which are critical for ensuring optimal performance and longevity.
- 2- Battery Balancing system: Over time, the cells in a battery pack may start to charge and discharge at slightly different rates, causing an imbalance that can reduce the pack's performance and lifespan. The battery balancing system works to equalize the state of charge among the cells, ensuring they all charge and discharge uniformly.
- 3- Safety management system: This sub-system safeguards the battery pack against potential damaging conditions like overcharge, over-discharge, over-temperature, short-circuit, and over-current. By continually monitoring these parameters, the protection

circuit can cut off the battery's connection if any of these thresholds are exceeded, preventing potential damage or hazards.

- 4- Thermal Management system: Keeping an optimal temperature range is crucial for the battery's health and performance. The thermal management system uses various techniques, such as active cooling (fans, chillers) or passive cooling (heat spreaders, phase change materials), to keep the battery pack within the ideal temperature range.
- 5- Data Collection and Communication (Sensor interface) system: This part of the BMS collects data from all other subsystems and communicates it to the EV's central control unit. It could use various protocols like CAN (Controller Area Network), LIN (Local Interconnect Network), or others for this purpose. The information collected is used for diagnostics, performance optimization, and predictive maintenance.
- 6- Charge/Discharge Control system: This sub-system controls the charging and discharging process of the battery. It ensures the battery is charged in a controlled and safe manner, managing the flow of current into the battery during charging and out of the battery during discharging.

Amongst these sub-systems, the state estimation system plays a significant role in providing accurate monitoring of the actual states of the LIBs during their operation and over their lifetime. The states estimation system performs various tasks in parallel such as:

- 1- State of Charge estimation (SOC).
- 2- State of Health estimation (SOH).
- 3- State of Power estimation (SOP).
- 4- State of Energy estimation (SOE).
- 5- Capacity degradation trajectory prediction.

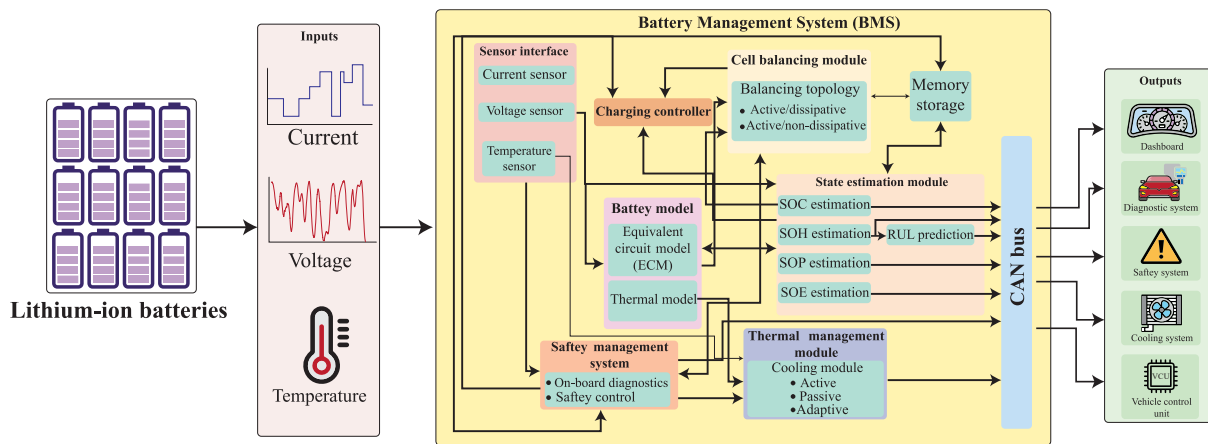


Figure 1.5 BMS architecture.

In recent years, countless approaches have been developed to estimate the quantities mentioned above accurately, significantly develop advanced algorithms for the estimation of SOH and capacity degradation trajectory prediction of LIBs in real-time have gained the most attention from both the academia and industry due to their importance in the BMS to ensure reliable performance of the LIB [17, 18]. In addition, to meet the technical necessities for the realisation of modern BMS architectures, there is also a societal need to earn the consumer's trust in the safety aspect of LIBs to increase the future uptake of such energy storage devices in a broader range of safety-critical applications, e.g., in EV/HEVs and commercial aircraft. However, the difficulty is that the capacity/SOH cannot be measured directly; because it is a composite of multiple factors, many of which are difficult to quantify precisely. Specifically, the SOH of a battery is influenced by various elements such as the total capacity of the battery, internal resistance, energy efficiency, and physical aging, which includes cycle life, calendar life, and the influence of various operational conditions (temperature, charge-discharge rates, etc.). therefore, the SOH must be estimated by the BMS. Nevertheless, monitoring the SOH by the BMS is crucial due to the complex and nonlinear degradation mechanisms of LIBs [19, 20]. Therefore, this thesis aims to expand upon the current state of the art of capacity estimation and trajectory prediction of LIBs by developing novel techniques for the capacity estimation and trajectory prediction based on Time-Frequency Analysis (TFA) and Machine Learning (ML) algorithms.

1.2 Aim, Research Questions, and Objectives

This thesis aims to develop novel capacity estimation and capacity trajectory prediction algorithms based on TFA and ML techniques. Figure 1.6 illustrates an overview of the aim and the critical research questions developed throughout the duration of the PhD. The detailed research questions are:

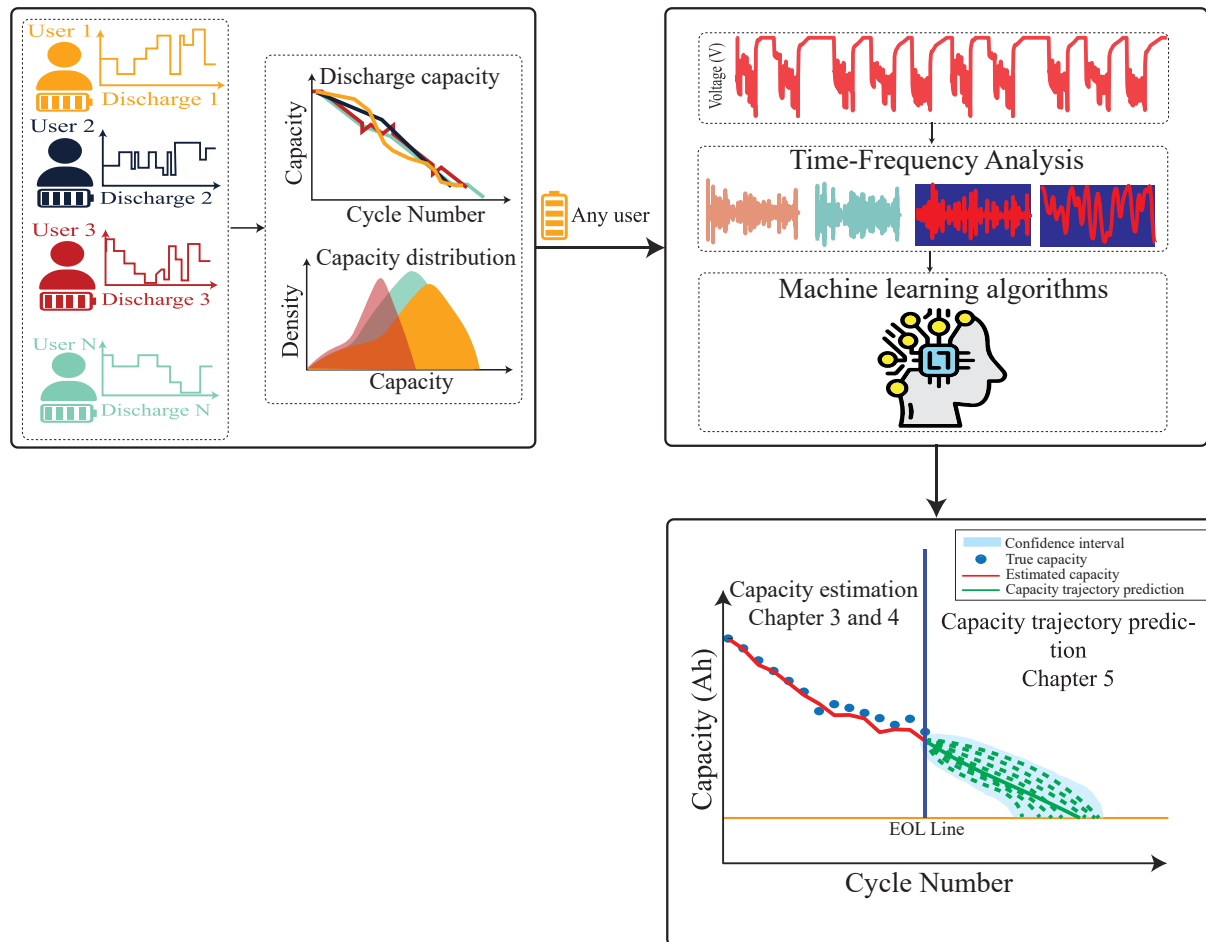


Figure 1.6 An overview of the aim of this thesis.

- 1- Can only the measured voltage signals give enough information about the degradation phenomena inside the LIB during its operation?
- 2- How will TFA be an excellent method to extract a promising health indicator related to the degradation inside the LIBs?

- 3- Can TFA be helpful if the LIBs are cycled under real-world operating conditions (i.e., different current profiles and temperatures)?
- 4- Can the proposed technique be used as a general model that copes with various user-driving behaviours?
- 5- What is the robustness of TFA in capturing the nonlinearity and nonstationary degradation behaviour of the LIBs?
- 6- What is the robustness of TFA and ML methods in a noisy environment?
- 7- Is the proposed technique capable of predicting the LIB's future capacity degradation?

It should be noted that these questions are the main questions, and several sub-research questions have been addressed throughout the thesis. Moreover, the following objectives are addressed to meet the thesis's aim and answer the research questions:

- 1- Identify the gap in the literature and propose a new and novel capacity estimation framework; therefore, a systematic literature review was conducted for the latest state-of-the-art capacity estimation of LIBs. (Addressed in Chapter 2)
- 2- Investigate and develop a time-frequency image (TFI) technique combined with deep learning convolutional neural networks (DL-CNN) to convert the measured voltage signal from time-domain (1-D) to time-frequency image spectrum (2-D) and classify the developed images to different capacity classes (Addressed in Chapter 3).
- 3- Develop a general framework to estimate the capacity of LIB cycled under many operating conditions using the adaptive TFA method and long-short-term memory neural network (LSTM). (Addressed in Chapter 4).
- 4- Investigate the validity of TFA and non-linear autoregressive neural network (NARX) to predict the future capacity degradation trajectory of LIBs. (Addressed in Chapter 5).

1.3 Key Contribution of the Research

This thesis aims to develop a new approach for the capacity estimation and capacity degradation trajectory prediction of LIBs based on the TFA and ML techniques under real-world operating conditions. Below is a summary of the contributions developed in this thesis:

-
- **Time-Frequency image analysis for capacity estimation of LIBs:** To improve the capacity estimation accuracy of the LIBs, the first part of this thesis introduces a new paradigm based on a multi-domain features TFI analysis and Transfer Deep Learning algorithm to extract diagnostic characteristics on the capacity loss inside the LIB. CWT is used to transfer the one-dimensional (1D) terminal voltage signals of the LIB into two-dimensional (2D) TFIs (i.e., wavelet energy concentration). The generated TFIs are fed into the 2D deep learning algorithms to extract the features from the LIB voltage images. The extracted features are then used to predict the capacity of the LIB.
 - **Generalised framework for capacity estimation of LIBs using adaptive TFA:** a novel generalised approach for estimating the capacity of LIBs is developed based on the adaptive EWT. The EWT is a potent tool for analysing the charging-discharging terminal voltage signal with non-stationary and transient phenomena in LIBs. EWT-based multi-resolution analysis (MRA) is used to extract information about the degradation trend in the time-frequency domain. Using the EWT in conjunction with wavelet decomposition, the ageing features of LIBs can be retrieved from the charging/discharging voltage signal over a frequency band range. 13 statistical features are extracted to investigate the correlation between the capacity degradation and the extracted features. Afterwards, a LSTM model is developed to estimate the capacity of the LIBs. The proposed approach has been compared with CWT.
 - **Future capacity degradation trajectory prediction based on TFA:** Monitoring the future capacity degradation trajectory of the LIB is extensively critical to prevent the failure or explosion of the LIB during its operation. Accurate, early prediction of the battery's capacity help assists in maintenance, safety, and getting the most out of the assets. Also, the early and accurate forecast of the capacity is a starting point for the economic analysis of possible second-life applications. Therefore, this work aims to monitor the future capacity degradation trajectory of LIBs using three TFA methods; Discrete wavelet transform (DWT), Empirical mode decomposition (EMD), and Variational mode decomposition (VMD) in denoising the regeneration capacity of the LIBs cycled under different conditions. In addition, a nonlinear autoregressive with exogenous input (NARX) algorithm is developed to predict the future capacity of the

LIBs. The advantage of the NARX algorithm is its high capability to learn the nonlinear relationship between the input and output of the LIBs.

1.4 List of Publications

The following articles have been published during the period of this PhD study:

Journal articles:

1. **El-Dalahmeh, M.D.**, Al-Greer, M., El-Dalahmeh, M.A. and Short, M., 2020. "Time-frequency image analysis and transfer learning for capacity prediction of lithium-ion batteries". *Energies*, 13(20), p.5447.
2. **El-Dalahmeh, M.D.**, Al-Greer, M., El-Dalahmeh, M.A. and Imran, B., 2022. "Capacity Estimation of Lithium-ion Batteries based on Adaptive Empirical Wavelet Transform and Long Short-Term Memory Neural Network". *Journal of Energy Storage* 2023.
3. **El-Dalahmeh, M.D.**, Al-Greer, M., El-Dalahmeh, M.A., Imran, B., Aykut, D., and Ozan, K. 2022. "Autonomous Faults Detection of Electrical Machines Using Combined Variational Mode Decomposition Pulse Hilbert-Huang Transform and Convolution Neural Network". *Journal of Computers and Electrical engineering* 2023.
4. El-Dalahmeh, M.A., Al-Greer, M., **El-Dalahmeh, M.D.** and Short, M., 2021. Smooth particle filter-based likelihood approximations for remaining useful life prediction of Lithium-ion batteries. *IET Smart Grid*, 4(2), pp.151-161.
5. M., El-Dalahmeh, Al-Greer, M., **El-Dalahmeh, M.D** and Bashir, I., 2023. Physics-based model informed smooth particle filter for remaining useful life prediction of lithium-ion battery. *Measurement*, 214, p.112838.

Conference articles:

1. **El-Dalahmeh, M.D** I. Bashir, M. Al-Greer and M. El-Dalahmeh, "Lithium-ion Batteries Capacity Degradation Trajectory Prediction Based on Decomposition Techniques and NARX Algorithm," 2022 57th International Universities Power

- Engineering Conference (UPEC), Istanbul, Turkey, 2022, pp. 1-6, doi: 10.1109/UPEC55022.2022.9917597.
2. **El-Dalahmeh, M.D.** J. Lillystone, M. Al-Greer and M. El-Dalahmeh, "State of Health Estimation of Lithium-ion Batteries Based on Data-Driven Techniques," 2021 56th International Universities Power Engineering Conference (UPEC), Middlesbrough, United Kingdom, 2021, pp. 1-6, doi: 10.1109/UPEC50034.2021.9548209.
 3. **El-Dalahmeh, M.D.** P. Thummarapally, M. Al-Greer and M. El-Dalahmeh, "Time and Frequency Domain Health Indicators for Capacity Prediction of Lithium-ion Battery," 2021 56th International Universities Power Engineering Conference (UPEC), Middlesbrough, United Kingdom, 2021, pp. 1-6, doi: 10.1109/UPEC50034.2021.9548150.
 4. **M. El-Dalahmeh**, M. Al-Greer, A. Demirel and O. Keysan, "Active fault detection using time and frequency diagnostic features for electrical machine," 11th International Conference on Power Electronics, Machines and Drives (PEMD 2022), Hybrid Conference, Newcastle, UK, 2022, pp. 405-410, doi: 10.1049/icp.2022.1084.
 5. M. El-Dalahmeh, M. Al-Greer, **M. El-Dalahmeh** and I. Bashir, "Online Hybrid Prognostic Health Management Prediction Using a Neural Network and Smooth Particle Filter for Lithium-ion Batteries," 2022 57th International Universities Power Engineering Conference (UPEC), Istanbul, Turkey, 2022, pp. 1-6, doi: 10.1109/UPEC55022.2022.9917930.
 6. A. Gailani, R. Mokidm, M. El-Dalahmeh, **M. El-Dalahmeh** and M. Al-Greer, "Analysis of Lithium-ion Battery Cells Degradation Based on Different Manufacturers," 2020 55th International Universities Power Engineering Conference (UPEC), Turin, Italy, 2020, pp. 1-6, doi: 10.1109/UPEC49904.2020.9209759.

1.5 Thesis Organisation

Figure 1.7 illustrates the organisation of the thesis comprising six chapters. A summary of each chapter is expressed below.

Chapter 1 has introduced the motivation and the contribution of this thesis. The aim, research questions, objectives, and publications have been presented.

Chapter 2 begins by explaining the LIBs and presents the main degradation mechanisms occurring inside the LIBs. Then, the chapter presents a critical review of the state-of-the-art for the capacity estimation and prediction of LIBs, including experimental, model-based, and data-driven techniques. Lastly, the chapter presents a summary of the knowledge gap.

Chapter 3 presents the implementation of the time-frequency image analysis method combined with deep learning convolutional neural network to predict the capacity of the LIB. The chapter starts by expressing why the time-frequency technique is vital to extract useful information about the degradation inside the LIBs. Then, from section 3.2 onwards, the obtained results are discussed.

Chapter 4 improves the capacity estimation process of the LIBs performed in Chapter 3 by adopting an adaptive empirical wavelet transform to develop a general capacity estimation framework for LIBs. The Chapter starts by showing the power of the adaptive empirical wavelet transform in feature extraction of the measured voltage signal of the LIB, even if the LIB is cycled at different current profiles and temperatures. A long short-term memory neural network (LSTM) data-driven algorithm is developed to estimate the capacity based on the extracted features from the empirical wavelet transform. The developed general framework has been tested and validated using two datasets.

Chapter 5 provides a framework to predict the capacity degradation trajectory using three time-frequency techniques: variational mode decomposition, discrete wavelet transforms, empirical mode decomposition, and a non-linear autoregressive neural network (NARX) machine learning algorithm.

Chapter 6 provides the key conclusions based on this work. It also discusses the limitation of this work and suggests areas for future work.

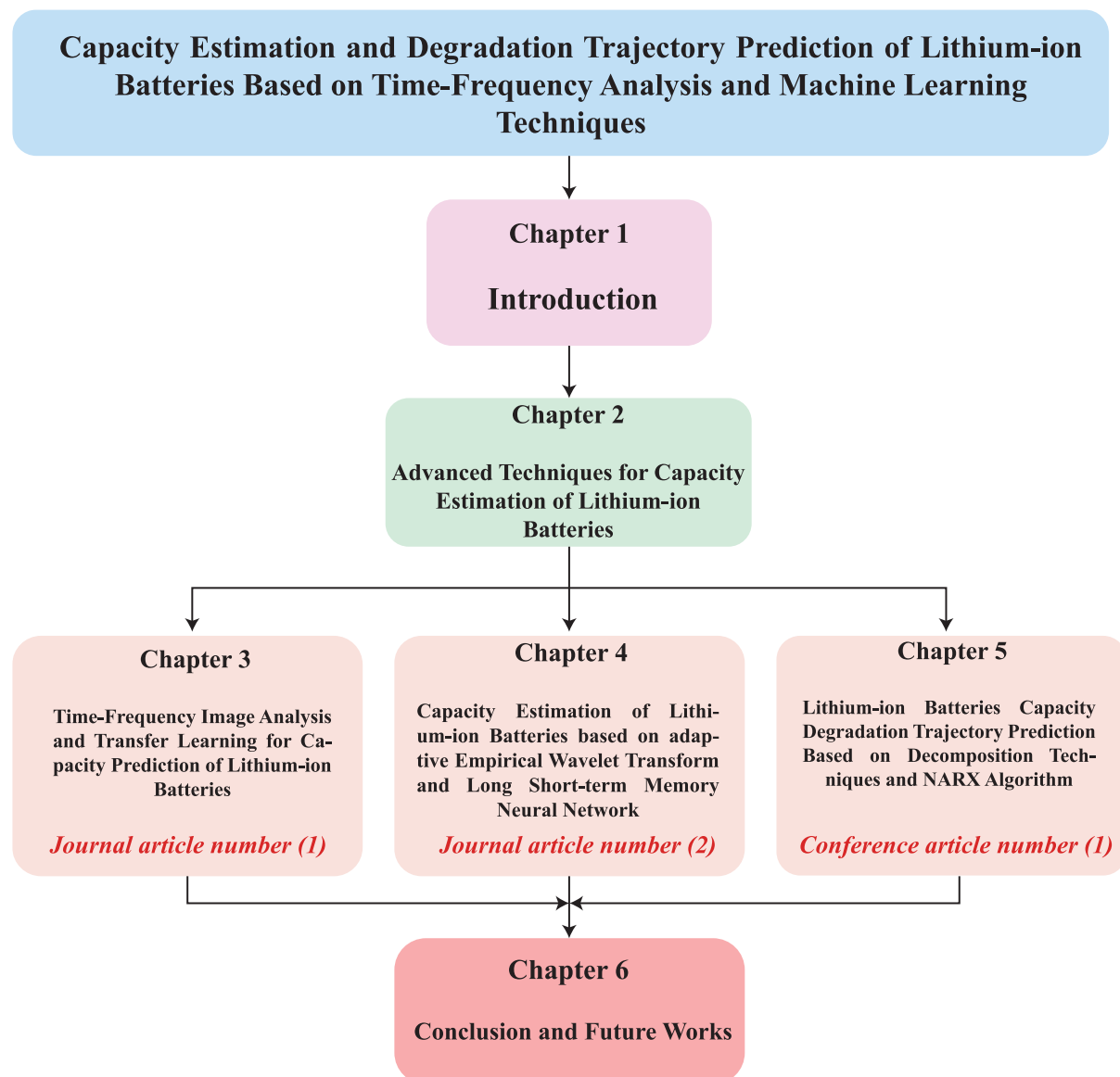


Figure 1.7 Thesis organisation.

Chapter 2 Advanced Techniques for The Capacity Estimation of Lithium-ion Batteries

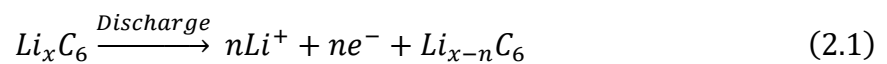
2.1 Brief Introduction

This Chapter focuses on the capacity estimation and prediction techniques in LIBs and how ageing affects the battery's performance in terms of capacity and power throughout its lifespan. The current methods for assessing the capacity of the LIBs are reviewed, emphasising commonly used approaches such as experimental, model-based, and data-driven techniques. This chapter highlights the research contributions presented in this thesis by identifying gaps in the existing literature.

2.2 Principle Operation of Lithium-ion Batteries

LIBs consist of five primary parts. The cathode and anode, also called the positive and negative electrodes, are separated by an insulating separator and immersed in an ion-conducting electrolyte [21]. The outer surfaces of the electrodes are attached to current collectors. The cathode and anode are porous materials, even though they switch roles between the cathode and anode during charging and discharging [22]. Figure 2.1 shows the five main components of LIB.

Once the LIB is completely charged, all of the usable lithium is stored in the porous anode, which is typically composed of graphitic carbon. The potential difference between the anode and cathode, caused by their differing thermodynamic potential, is measured across the two terminals. When a load is connected to the terminals, reactions take place at the interface between the electrode and electrolyte, resulting in the separation of lithium into lithium ions and electrons at one electrode and the opposite process occurring at the other electrode [23]. The electrochemical reaction for a conventional graphitic carbon anode is as follows:



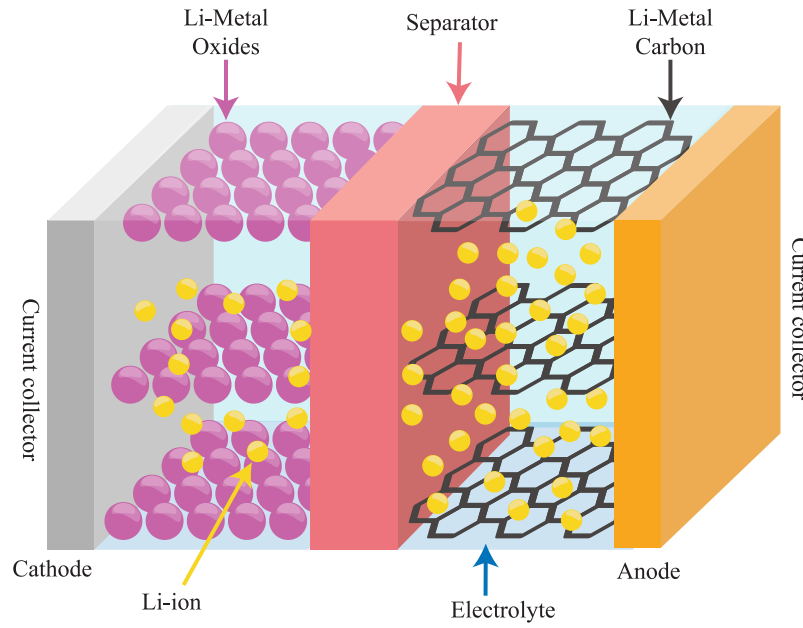
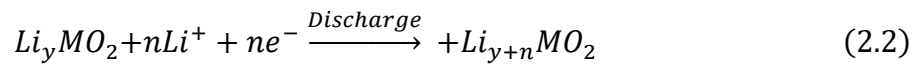


Figure 2.1 Main parts of the LIB.

Due to the concentration gradient of lithium, it is energetically favourable for lithium ions to move through the electrolyte and separator to the cathode. The movement of lithium ions leads to the flow of electrons through the external circuit, resulting in the generation of electrical work. As electrons cannot pass through the electrically insulating separator, this process occurs through the current collectors. At the cathode, lithium ions combine with electrons and the cathode material, resulting in the formation of a cathode material that is rich in lithium. The electrochemical reaction of a metal oxide cathode is expressed as follows:



When the LIB is being charged, the entire process is reversed. Lithium is removed from the cathode at the interface with the electrolyte, and the lithium ions diffuse to the surface of the anode, where they are reinserted. Overall, the LIB works by shuttling lithium ions between the anode and the cathode through an electrolyte solution, which allows for the storage and release of electrical energy, as shown in Figure 2.2.

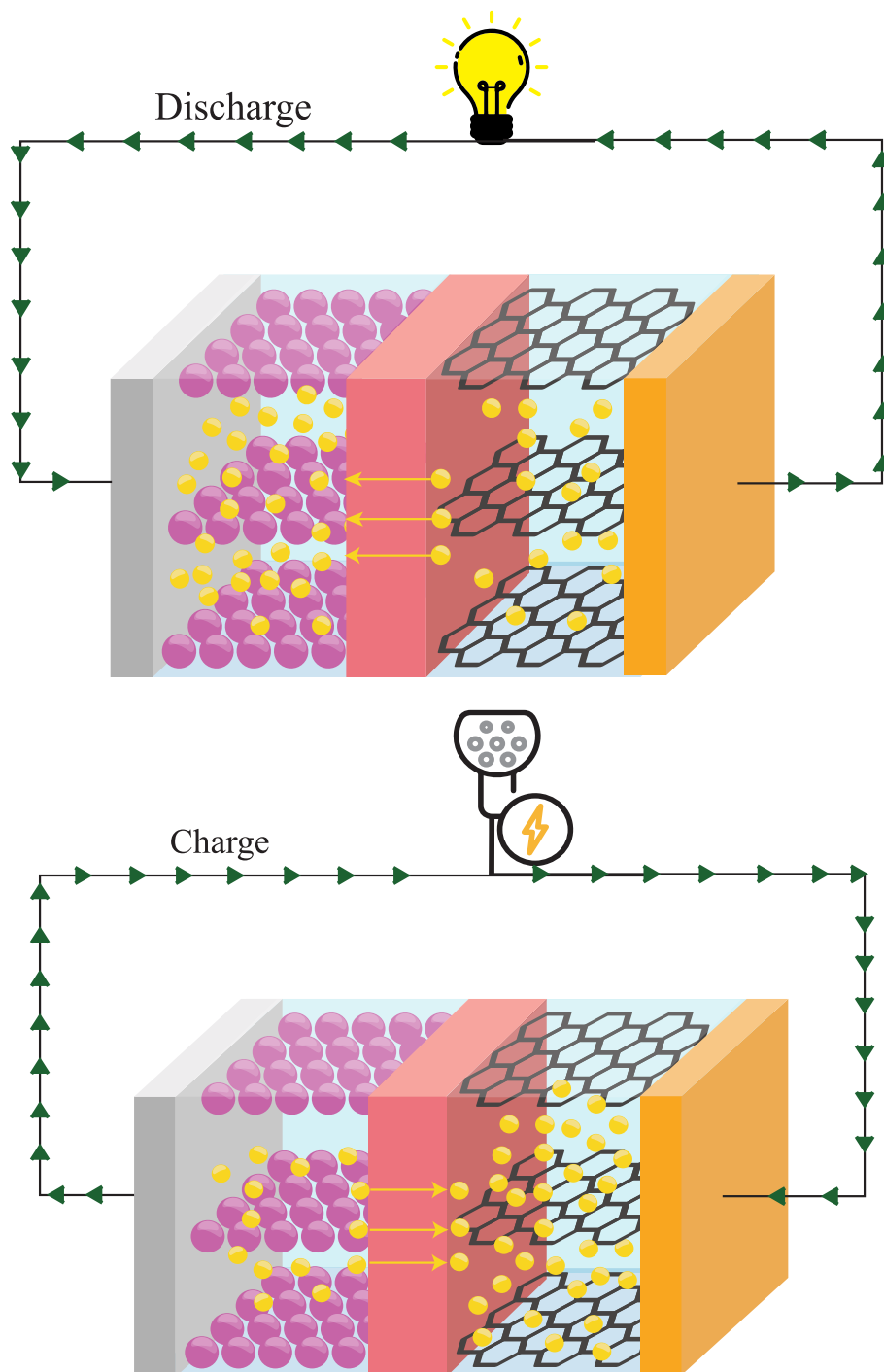


Figure 2.2 The movement of lithium-ion during discharge and charge processes.

2.3 Degradation in Lithium-ion Batteries

The degradation of LIBs refers to the gradual loss of capacity and increase in internal resistance that occurs over time and with use. Various factors, such as overcharging, over-discharging, high temperatures, and mechanical stress, can cause this. As the battery degrades, it will be able to hold less charge and not deliver as much power. Eventually, it may need to be replaced [24].

Several degradation mechanisms can occur in the LIBs, each with its own specific causes, effects, and degradation signatures [25].

- 1- Electrode degradation: This is caused by the accumulation of lithium ions and solid electrolyte interphase (SEI) layer formation on the electrodes, leading to decreased capacity and increased internal resistance. Effects include capacity fade and power fade. Degradation signatures involve impedance spectra and voltage profile changes during charge/discharge cycles [26].
- 2- Electrolyte degradation: This is caused by oxidation and reduction reactions in the electrolyte leading to a decrease in conductivity and an increase in viscosity. Effects include capacity fade and power fade. Degradation signatures include impedance spectra changes and voltage profiles during charge/discharge cycles [27, 28].
- 3- Separator degradation: This is caused by the formation of micro-shorts between the electrodes and the breakdown of the separator material leading to an increase in internal resistance. Effects include power fade and thermal runaway. Degradation signatures include impedance spectra changes and voltage profiles during charge/discharge cycles [29, 30].
- 4- Mechanical degradation: This is caused by mechanical stress such as bending, twisting, or puncture, leading to a decrease in capacity and an increase in internal resistance. Effects include capacity fade and power fade. Degradation signatures involve impedance spectra changes, voltage profile changes during charge/discharge cycles, and physical damage to the battery [31-33].
- 5- Thermal degradation: This is caused by exposure to high temperatures leading to a decrease in capacity and an increase in internal resistance. Effects include capacity fade

and power fade. Degradation signatures involve changes in the impedance spectra, changes in the voltage profile during charge/discharge cycles, as well as changes in the thermal behaviour of the battery [34-36].

It is important to note that these degradation mechanisms can be interrelated and can occur simultaneously, leading to a complex degradation behaviour of the battery [37]. Figure 2.3 shows the degradation mechanisms of the LIB. Generally, all the presented degradation mechanisms and their impact can be classified into three major degradation modes. These degradation modes are:

- 1- Loss of lithium inventory (LLI): LLI is a phenomenon that occurs in LIBs, where a portion of the lithium in the electrodes is permanently lost and cannot be recharged. This can happen for various reasons, such as overcharging, high temperatures, or mechanical stress. LLI can significantly reduce a lithium-ion battery's overall capacity and performance over time. LIBs are usually designed with safety features to prevent LLI and operate within specific temperature and voltage limits [38].
- 2- Loss of active material of the negative electrode (LAMNE): LAMNE is a phenomenon that occurs in LIBs, where the active material in the negative electrode gradually degrades or becomes inactive over time. This degradation can lead to a decrease in battery capacity and overall performance[38, 39].
- 3- Loss of active material of the positive electrode (LAMPE): LAMPE is similar to LAMNE, but this phenomenon occurs in the positive electrode of the LIBs [38, 40].

Figure 2.4 illustrates the degradation mechanisms, their cause, effect, and their links to the degradation modes.

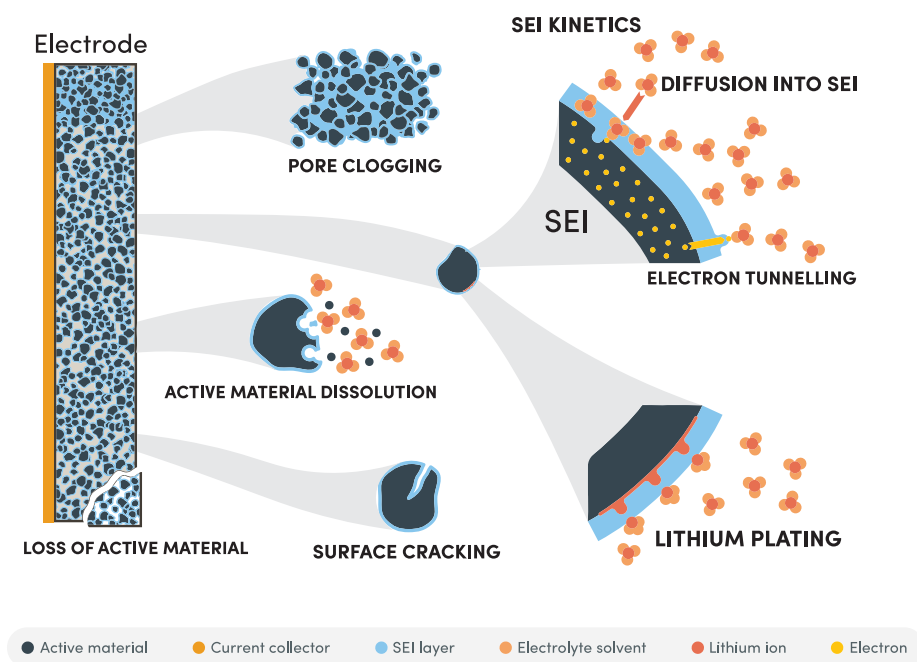


Figure 2.3 Degradation mechanisms in lithium-ion batteries [25, 41].

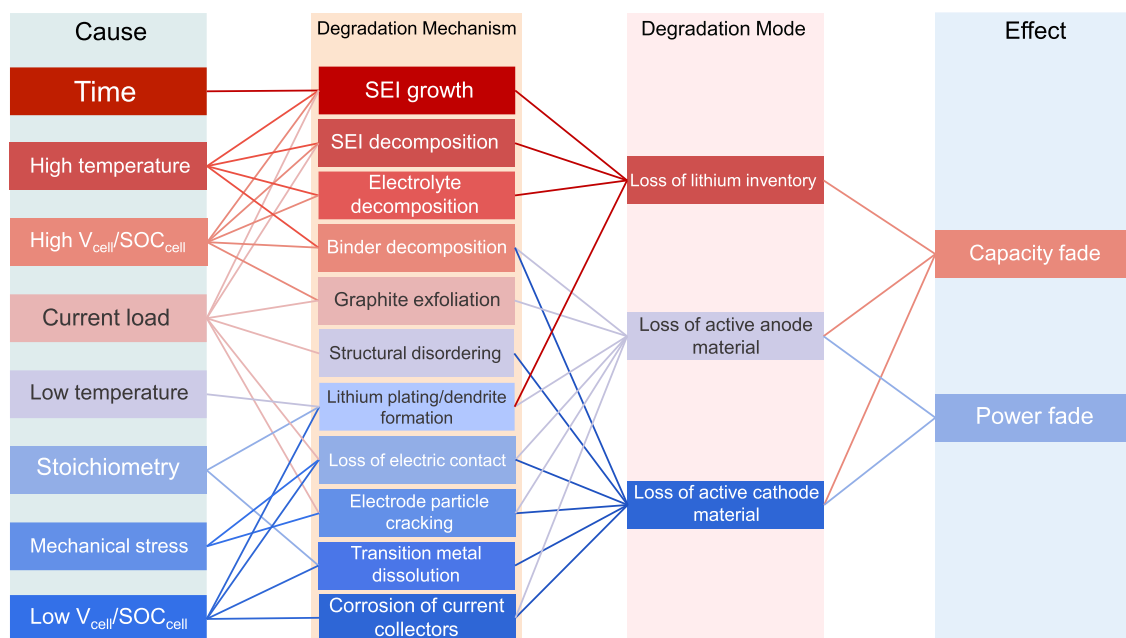


Figure 2.4 Degradation modes and their effect in lithium-ion batteries [25].

2.4 Measurement of Degradation

It is crucial to have a proper method for measuring battery degradation in order to avoid battery failure and maintain a long/safe functioning. Standardised metrics used in the industry today and cutting-edge concepts are outlined in subsequent sections.

2.4.1 Capacity loss and power loss

The two most significant characteristics are a battery's capacity and power. The most straightforward method for finding how much a battery has been degraded is to look at its capacity and power levels over time. These measurements are also known as capacity fade and power fade. These metrics indicate the loss of the LIB capacity in ampere-hours (Ah) or power in watt-hours (Wh) relative to the initial values at the beginning of its service life. Specifically, the capacity loss in a LIB refers to the decrease in the battery's ability to hold a charge over time. Power loss refers to reducing the battery's ability to deliver power over time.

2.4.2 BOL, EOL, SOH, RUL

SOH is the quantitative measurement (usually represented in percentages) of how much the cell has degraded with respect to its fresh state. There is no fixed definition for the SOH; however, the current industry standard would simply be the capacity loss. Again, there is no standardised measurement procedure for capacity. The most common method seems to be a constant current 1C discharge at room temperature from the upper voltage limit of the cell to its lower voltage limit. The unit “C” represents the cell's C-rate, which describes the current with respect to the cell's capacity. For example, a 1C discharge of a 5 Ah cell would be 5 A, and a 2 C discharge of the same cell should be about 10 A. Due to the lack of standardised measurement, every mention of capacity should include precisely how the parameter was measured each time.

State-of-function (SOF) and remaining-useful-life (RUL) are less common yet still employed degradation measurements. SOF determines the battery's ability to deliver a certain

amount of energy or power under given operating conditions. RUL defines the amount of overall operational lifetime left of the cell.

Beginning-of-life (BOL) is the cell's fresh state, i.e., 100% SOH. End-of-life (EOL) marks the end of a battery operation after significant ageing. EOL is often defined as 20% capacity loss or 80% SOH.

Among these quantitative measurements, SOH is one of the most important quantitative has been investigated in recent years because it is vital to determine the remaining capacity/power of the LIB. However, the difficulty is that the SOH cannot be measured directly and must be estimated by the BMS. Nevertheless, monitoring the SOH by the BMS is crucial due to the complex and nonlinear degradation mechanisms of LIBs. Therefore, several approaches for SOH estimation have been proposed in recent years. Generally, these approaches can be categorised into three groups: controlled experimental methods, model-based methods, and data-driven methods, as shown in Figure 2.5 [42, 43]. Moreover, **Error! Reference source not found.** shows the co-occurrence network of high-frequency words used to review the state of the art for SOH of LIBs.

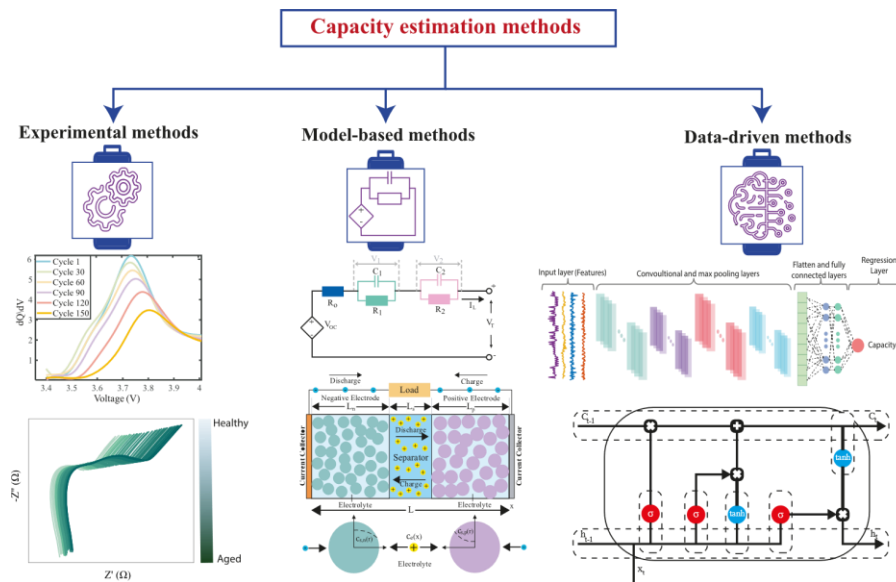


Figure 2.5 Capacity investigation methods.

2.5 Experimental Techniques

2.5.1 Coulomb Counting

As a straightforward and trustworthy procedure, Coulomb counting (Ah counting) is utilised for the majority of practical testing, defining the capacity as explained previously. Its primary function is calculating the amount of energy entering or leaving the battery by integrating the current measurement over time. By monitoring the quantity of Ah transferred between the battery and load, the battery's remaining capacity is estimated and utilised to evaluate the state of health. The mathematical expression of the coulomb counting is given in [44] as

$$Q_{act} = SOC_0 + \frac{1}{Q_n} \int_0^t I_d(t) dt \quad (2.3)$$

Where I_d is the total discharge current of the battery cell. Once the battery capacity is calculated, the SOH of the battery can be calculated, as shown in (2.2).

$$SOH = \frac{Q_{act}}{Q_{nom}} \cdot 100\% \quad (2.4)$$

Where Q_{act} is the actual measured capacity of the battery after several cycles, as shown in (2.3) and Q_{nom} is the nominal measured capacity of the battery at the beginning of its life (BOL). The coulomb counting method has been applied in several studies for state of charge (SOC) and SOH estimation [45-48] due to its simplicity and highly accurate state estimation capability. However, the integration in (2.3) leads to difficulties when the battery is not tested in a laboratory environment. Moreover, this method struggles to preserve its accuracy as the battery degrades and the capacity. Q_{nom} decreases; thus, a calibration step for the capacity is required frequently to maintain the accuracy of the coulomb counting method. In addition, a highly accurate current sensor and a precise initial SOC_0 are fundamentally required to ensure accurate SOC and SOH estimation results [49].

2.5.2 Open Circuit Voltage

The open circuit voltage (OCV) of LIBs plays a crucial role in battery state estimation due to the amount of information that can be utilised to identify the battery's SoC and the available useful capacity of the electrodes [50]. The OCV of a lithium-ion battery is the potential difference between the positive and negative electrodes when the electrode potentials are in equilibrium, and no current is flowing. The OCV is measured by charging and discharging the LIB using a very low (e.g., C/10) constant current-voltage (CC-CV) protocol. Specifically, the LIB is first charged to its fully upper cut-off limit voltage; then, the battery is discharged at a constant low current rate until fully discharged (to the lower cut-off limit voltage). Afterwards, the battery is rested for some period (around 2 h); then, the battery will be fully charged at the same current rate. The voltage at this low current rate represents the OCV of the battery at an equilibrium state [51]. Figure 2.6 (a) and (b) show an example of the low-rate discharge current and the corresponding measured voltage with the OCV period, respectively. Several studies have been presented in the literature for capacity estimation of LIBs based on the OCV measurement due to the direct correlation between the OCV and the capacity and power fade of the LIBs [50, 52-56]. Figure 2.7 shows the evolution of the OCV measurements throughout the LIB lifetime. As illustrated in Figure 2.7, the correlation between the measured OCV and the capacity of the LIB can be clearly observed; as the LIB degrades, the discharging time becomes faster (the LIB reaches its upper and lower voltage limits with a minimum amount of time). This change in the OCV characteristics is related to the degradation process that occurred inside the LIB [57, 58]. However, it is important to note that direct and online measurement of OCV is not typically feasible in practical applications. This is primarily due to the requirement of the battery to be in a relaxed state, i.e., a state of neither charging nor discharging, for a significant amount of time to achieve an accurate OCV reading, which is not often possible in continuous operation scenarios. Therefore, we rely on model-based estimation techniques for obtaining an approximation of the OCV. These methods use complex mathematical models and algorithms to estimate the OCV based on the available battery data. Although this method may not give a direct and absolute measurement of the OCV, it provides a reasonably accurate estimation, making it viable for real-time applications.

On another note, capturing accurate onboard OCV curves can aid in understanding battery behaviour, but it doesn't necessarily provide a complete solution to the SoH estimation problem. There are several underlying root causes that contribute to the degradation of battery SoH, which can be tricky to quantify directly through OCV measurements alone.

For example, the growth of the Solid Electrolyte Interphase (SEI) layer is a well-known phenomenon in LIBs that leads to a decrease in capacity and efficiency over time. Furthermore, parasitic reactions between the electrodes and the electrolyte can also contribute to battery degradation. Lastly, lithium plating, a process where lithium deposits on the anode surface during charging, can severely affect the capacity. All these factors complicate the relationship between OCV and SoH, making it a challenging problem to solve using OCV curves alone [59].

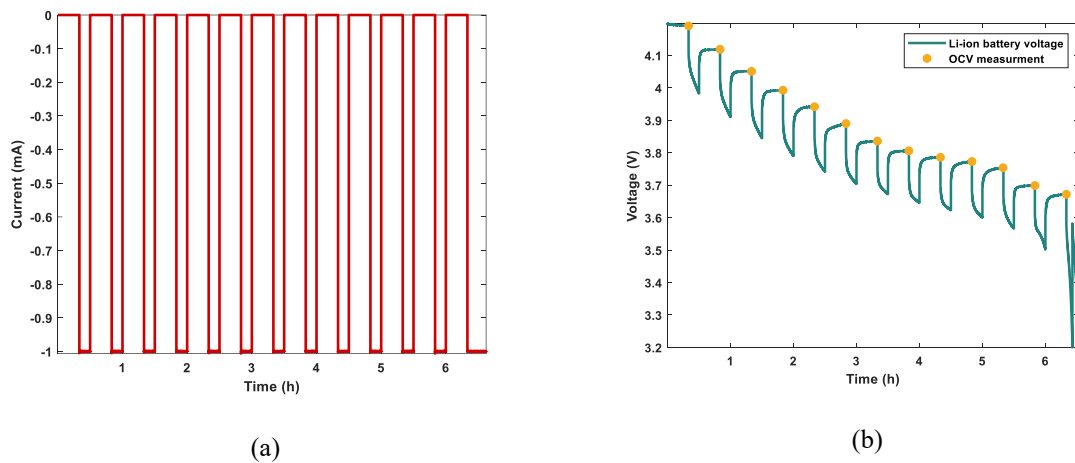


Figure 2.6 (a) low-rate discharge current (b) OCV measurement.

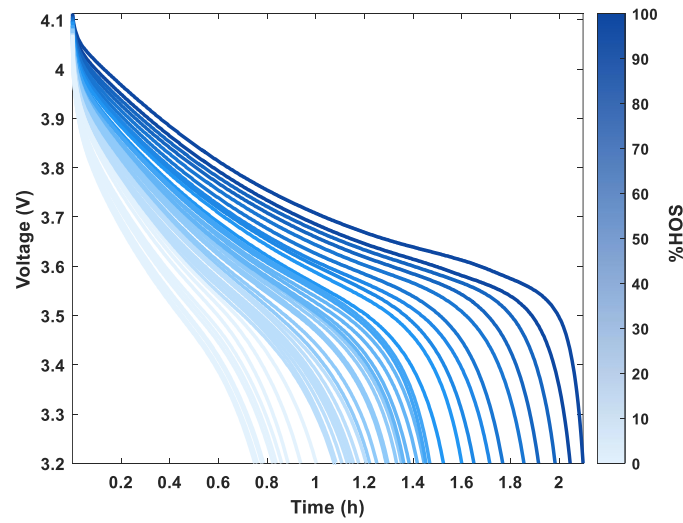


Figure 2.7 The evolution of the OCV measurements throughout the battery lifetime.

2.5.3 Electrochemical Impedance Spectroscopy

Electrochemical impedance spectroscopy (EIS) is a powerful method for characterising the electrochemical systems. The main factor that makes the EIS method extremely attractive for the state estimation of LIB is that the EIS data may be associated with several critical physical parameters, such as diffusion and reaction rates and microstructural characteristics [60]. The impedance of the LIB is measured by applying a small sinusoidal current signal after the LIB is relaxed for a sufficient time [61, 62]. The measured voltage response should be less than 10 mV to satisfy the measurement conditions [62]. The EIS of a LIB can be measured in potentiostatic (controlled potential is applied as an input to the battery) or galvanostatic (controlled current is applied as an input to the battery) mode. The mathematical expression of the potentiostatic and galvanostatic modes is presented in (2.5) and (2.6), respectively.

$$u = U \sin(\omega t + \phi_u) \quad (2.5)$$

$$i = I \sin(\omega t + \phi_i) \quad (2.6)$$

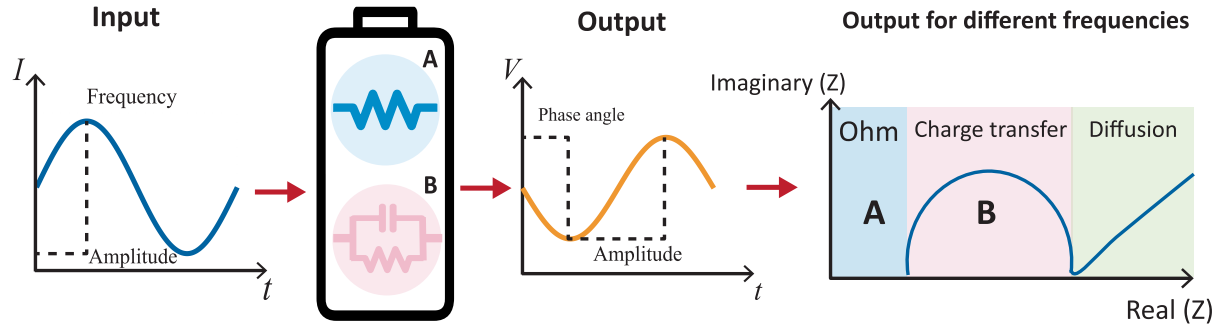


Figure 2.8 Measurement principle of EIS (galvanostatic mode).

Typically, the galvanostatic mode is more selected than the potentiostatic mode because the LIB impedance is so low a potentiostatic mode can easily result in overcurrent [63, 64]. Figure 2.8 shows the measurement principle of the impedance of the LIB. Precisely, the impedance of the LIB can be measured by dividing the voltage response by the input current signal, and the impedance in the frequency domain can be expressed in (2.7).

$$z = \frac{u}{i} = \frac{U \sin(\omega t + \phi_u)}{I \sin(\omega t + \phi_i)} \quad (2.7)$$

Moreover, the impedance amplitude and its phase angle can be expressed as presented in (2.8) and (2.9), respectively [64].

$$|z| = \frac{U}{I} \quad (2.8)$$

$$\phi = \phi_u - \phi_i \quad (2.9)$$

The obtained impedance of the LIB can be presented as a complex number with real and imaginary parts, as shown in (2.10).

$$z = Z' + Z''j \quad (2.10)$$

Taking the real and imaginary parts of the measured impedance, the Nyquist plot can illustrate the battery impedance at several frequencies [65].

Figure 2.9 illustrates the standard EIS of a LIB. It is shown that the impedance in various frequency bands exhibits distinct characteristics. For example, the impedance is roughly a

straight line in the low-frequency region. The impedance spectrum resembles arcs in the mid and high-frequency ranges; however, in the ultra-high frequency range, it is a smooth curve below the real axis [66].

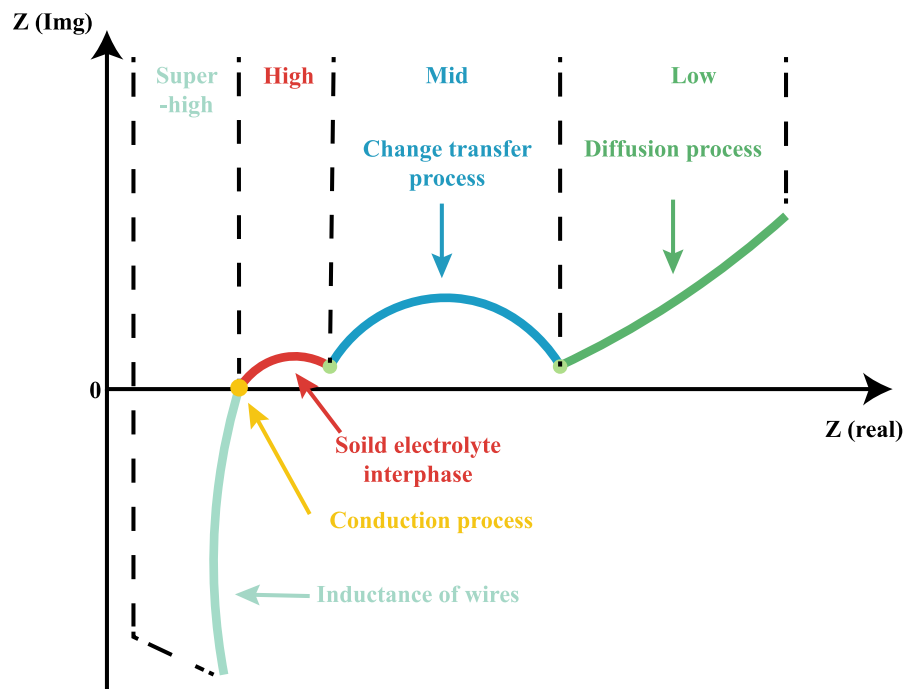


Figure 2.9 The obtained processes by EIS of the lithium-ion battery.

Specifically, the spectrum in Figure 2.9 presents the characteristic behaviour of the LIB, represented by five regions shown in Figure 2.9. These regions have been correlated to specific kinetic processes as follows [67]:

- 1- Super-high region (inductive elements): The spectrum exhibits inductive behaviour at super-high frequencies because of the reactance of metallic materials in the battery and wires.
- 2- Ohmic resistance (Conduction process): The intersection of the spectrum with the real axis represents the ohmic resistance of the battery, which is the sum of the resistances of the current collectors, active material, electrolyte, and separator.
- 3- High-frequency region: In most cases, the high-frequency semicircle is correlated to the solid electrolyte interface (SEI), and it is created during cycling on the surface of the anode.

- 4- Mid-frequency region: The semicircle shows the electrodes' double-layer capacity and charge transfer resistance.
- 5- Low-frequency region: Diffusion processes in the active material of the electrodes are represented by the very low-frequency response, which appears as a straight line in the impedance plot.

Note that not all impedance spectra of LIBs display the same features as Figure 2.9; this is something that should be kept in mind due to the basic principles of the various types of batteries; they might be very different from one another [68, 69]. Employing the EIS data of LIB for capacity estimation has been investigated extensively in the literature review due to the significant amount of information that describes the internal state of the battery [70-75].

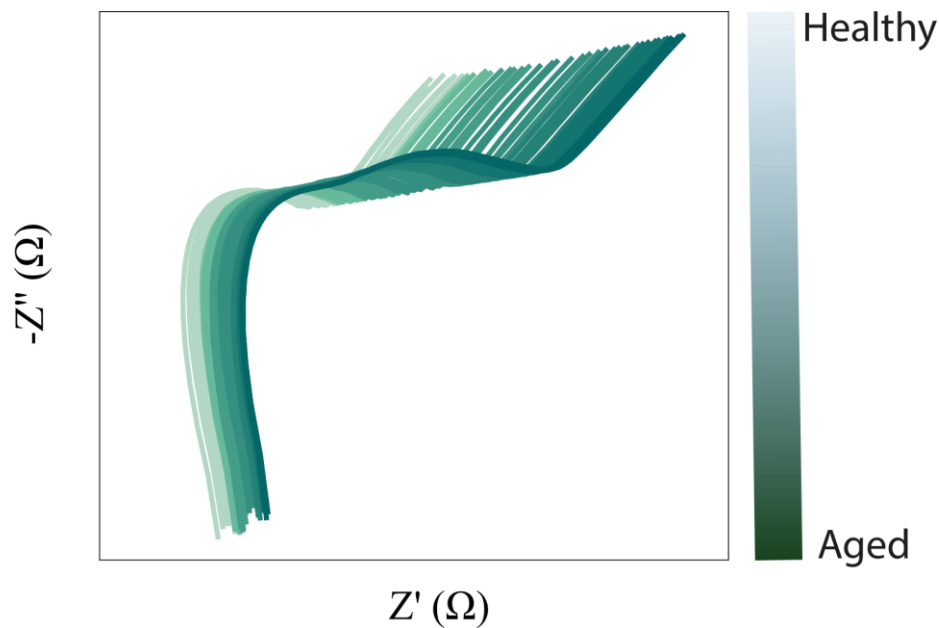


Figure 2.10 The evolution of the impedance of LIB over time.

For example, Figure 2.10 illustrates the impedance evolution of the LIB over time—the battery's impedance increases over time due to the degradation mechanisms inside the battery [76]. The literature utilises this observation in the measured EIS spectrum to fit it to an electrical model known as ECM to facilitate dynamic modelling of the electrochemical behaviour of the battery [77, 78]. Figure 2.11 shows the EIS spectrum of the LIB with the

corresponding ECM. Each parameter in the equivalent circuit model represents a particular process of the EIS spectrum. More details on the ECM are presented in section 2.2.1. However, using the EIS-based method for online capacity estimation of LIBs is challenging since this approach requires extra components installation to the BMS.

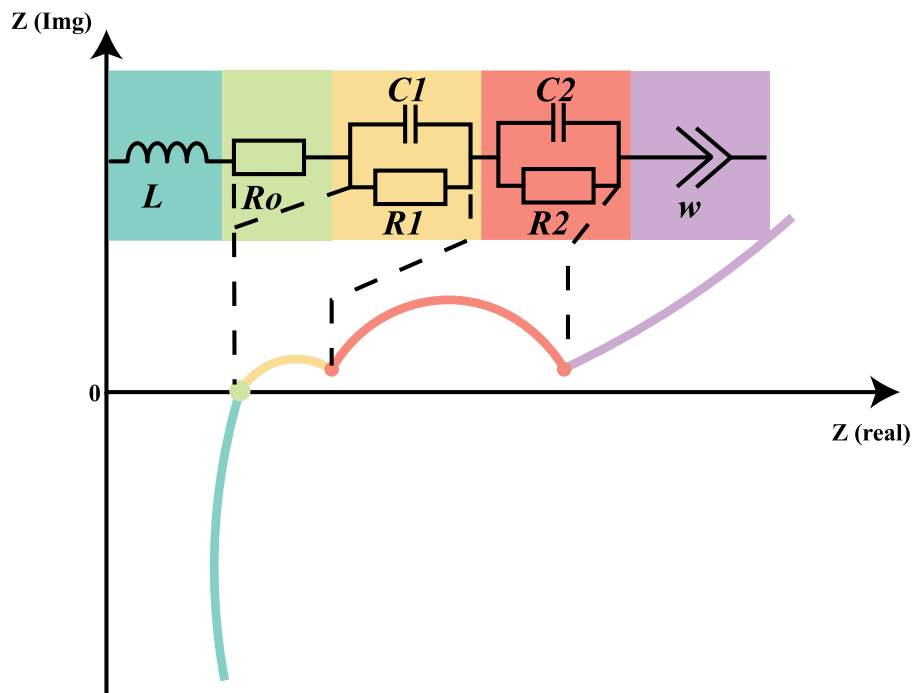


Figure 2.11 Equivalent circuit model.

2.5.4 Incremental Capacity Analysis and Differential Voltage Analysis-based Techniques

Incremental Capacity Analysis (ICA) and Differential Voltage Analysis (DVA) based techniques have been applied to investigate the degradation mechanisms and perform capacity estimation and prediction of LIBs [79-84]. This section will discuss the ICA and DVA techniques simultaneously since both methods have a similar procedure.

2.5.4.1 ICA Method

The ICA method is generally recognised as an effective tool for analysing batteries' capacity deterioration. The incremental capacity (IC) curve is obtained from the charging process under

a constant-current protocol using differential equations [85]. Specifically, the IC curve can be defined as the incremental capacity over each succeeding voltage step. Therefore, the battery charging capacity, as well as the voltage, must be determined prior to the calculation of IC curve values [85]. The capacity and the voltage values can be defined as expressed in (2.11) and (2.12), respectively.

$$Q_{ch} = I \cdot t \quad (2.11)$$

$$V = f(Q_{ch}) \rightarrow Q_{ch} = f^{-1}(V) \quad (2.12)$$

Where I represents the constant charging current and t is the charging time. After obtaining the charge capacity and voltage, the IC curve can be calculated as illustrated in (2.11) [80].

$$(f^{-1})' = \frac{dQ}{dV} = \frac{I \cdot dt}{dV} = I \cdot \frac{dt}{dV} \quad (2.13)$$

Figure 2.12 shows an example of the calculated IC curve of a LIB. As shown in Figure 2.12, the calculated IC curve suffers from noise due to the derivation step in (2.11); the peaks in the IC curve are extremely sensitive to noise [86]. However, monitoring the capacity of the LIB using the noisy calculated IC curves is a very tricky challenge due to the sensitivity of the IC curves to the noise [87]. Therefore, the calculated IC curve must be smoothed using smoothing or filtering techniques such as moving average filter (MA) [88, 89], Gaussian filter [89, 90], and Butterworth filter [91]. For instance, the authors in [89] applied a Gaussian filter to the IC curves prior to employing the IC curves for feature extraction and capacity estimation of LIBs. However, the filtering process needs to be carried out with extreme precision since the smoothness of the IC curve is highly dependent on both the sample interval and the filter's window size.

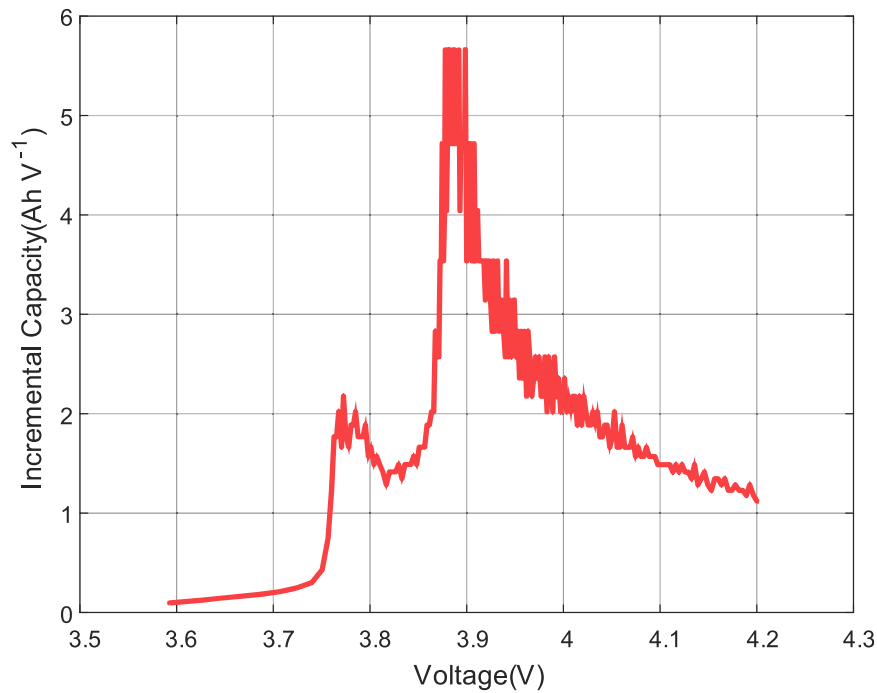


Figure 2.12 The IC curve of LIB [86].

Figure 2.13 compares the original noisy IC curve and the smoothed (filtered) IC curve using a moving average window (window length = 50). As shown in Figure 2.13, the smoothed IC curve clearly shows the IC curve's peaks. Furthermore, the calculated IC curve changes as the LIB degrades, as shown in Figure 2.14. The evolution of the IC curves over the battery lifetime obviously can be associated with the capacity loss of the LIB. In addition, monitoring the IC curves in Figure 2.14 shows that the overall IC curves tend to shift to the lower right as the battery ages.

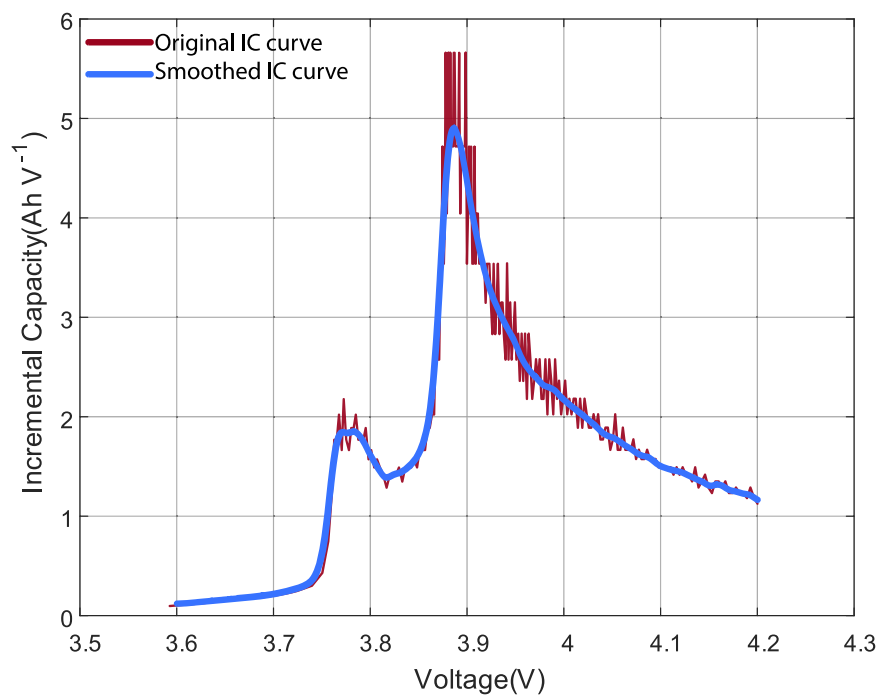


Figure 2.13 Original and smoothed IC curve.

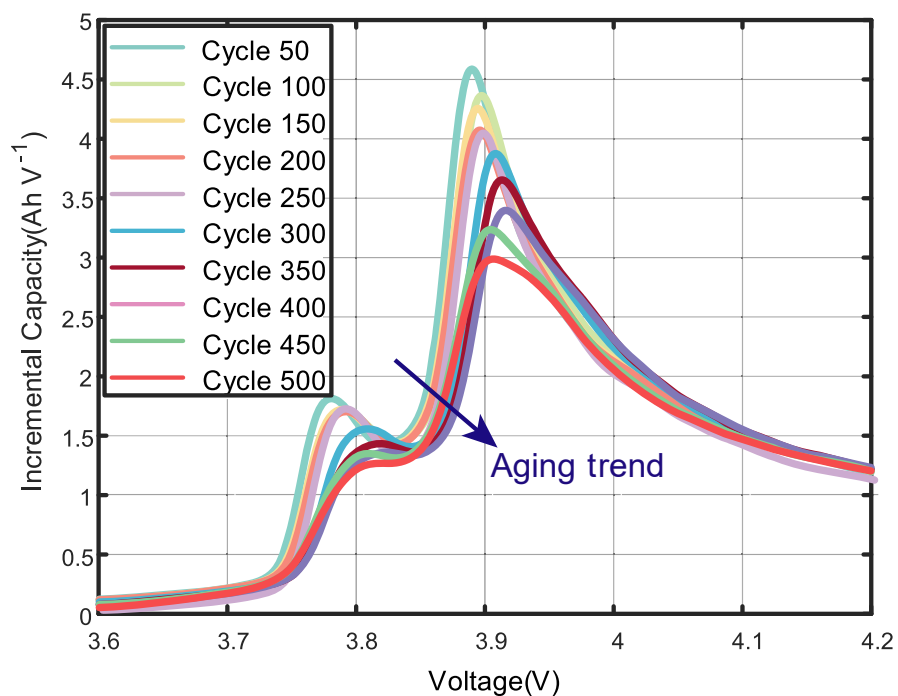


Figure 2.14 The evolution of the IC curves of the LIB over the battery lifetime.

2.5.4.2 DVA Method

Like the ICA method, the DVA method has also been extensively applied to the capacity estimation of lithium-ion batteries.

$$dV/dQ = \frac{(V(t+T) - V(t))}{(I(t+T) - I(t))} \quad (2.14)$$

Where t is the current time, and T is the sample period. However, this causes a significant fluctuation due to measurement noise. A median filter and moving average filter were applied to eliminate the noise. The median filter removed the intermittent impulse noise, and the moving average filter reduced continuous and low-level noise.

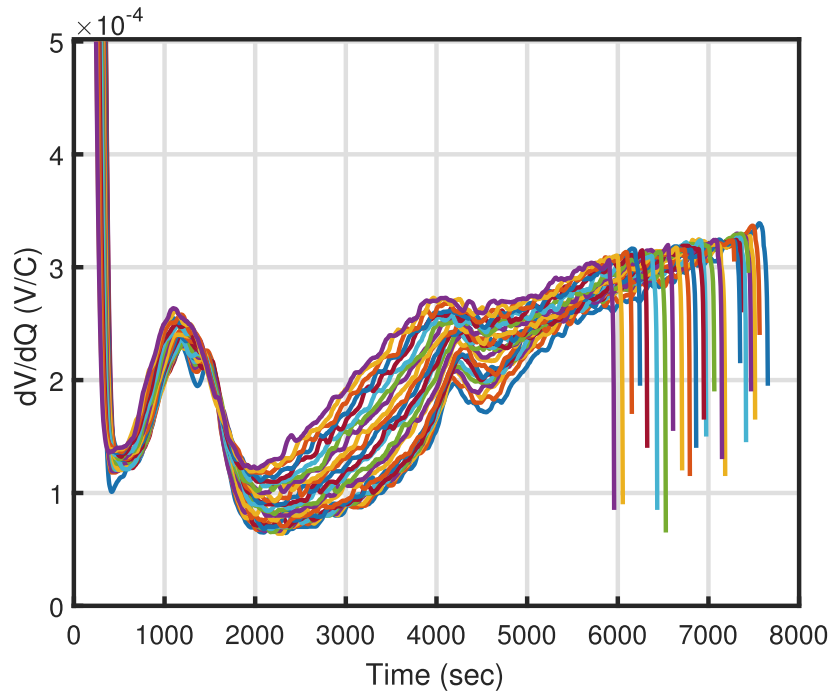


Figure 2.15 The evolution of DVA over battery lifetime [82].

The results are shown in Figure 2.15. Rises in dV/dQ during the ageing cycles for the five battery packs were observed. Figure 2.15 shows two peaks on the dV/dQ for all ageing cycles. The first and second peaks are revealed in the low and middle SOC ranges, respectively. Despite the degradation, the shape of dV/dQ near the first peak was almost unchanged, and only a small offset was added. However, the curve at the second peak changed drastically. The peaks were even difficult to distinguish in severely aged batteries [82].

2.6 Model-based Techniques

Until now, each of the direct measurement techniques for capacity estimation has encountered challenges when applied alone. While counting Coulombs is accurate for short intervals, it requires initial circumstances and drifts over time. In contrast, the OCV approach may estimate the capacity without any prior information; however, it cannot be used in a broad range of LIB discharge processes.

The model-based approach is borrowed from control engineering to combine both advantages; parallel to the actual system, a mathematical model predicts the output or the battery's terminal voltage. Estimating a system's hidden states can be enhanced by employing the difference between the predicted and actual measurements.

Model-based methods are an effective solution for accurate and robust capacity estimation, the performance of which heavily relies on the battery model. The LIB modelling methods that have been proposed in the published research primarily differ in terms of the model structure, model complexity, required processing power, and dependability of the results that have been achieved. When the electrochemical processes that take place during the operation of a battery can be recreated with a higher level of precision by the battery model being used, the results acquired can be a higher level of accuracy [92]. Generally, the battery models are classified into two categories: (1) ECMs and (2) Electrochemical Models (EMs), as shown in Figure 2.16.

This section mainly focuses on the battery modelling methods, which can potentially be used for the capacity estimation of LIBs.

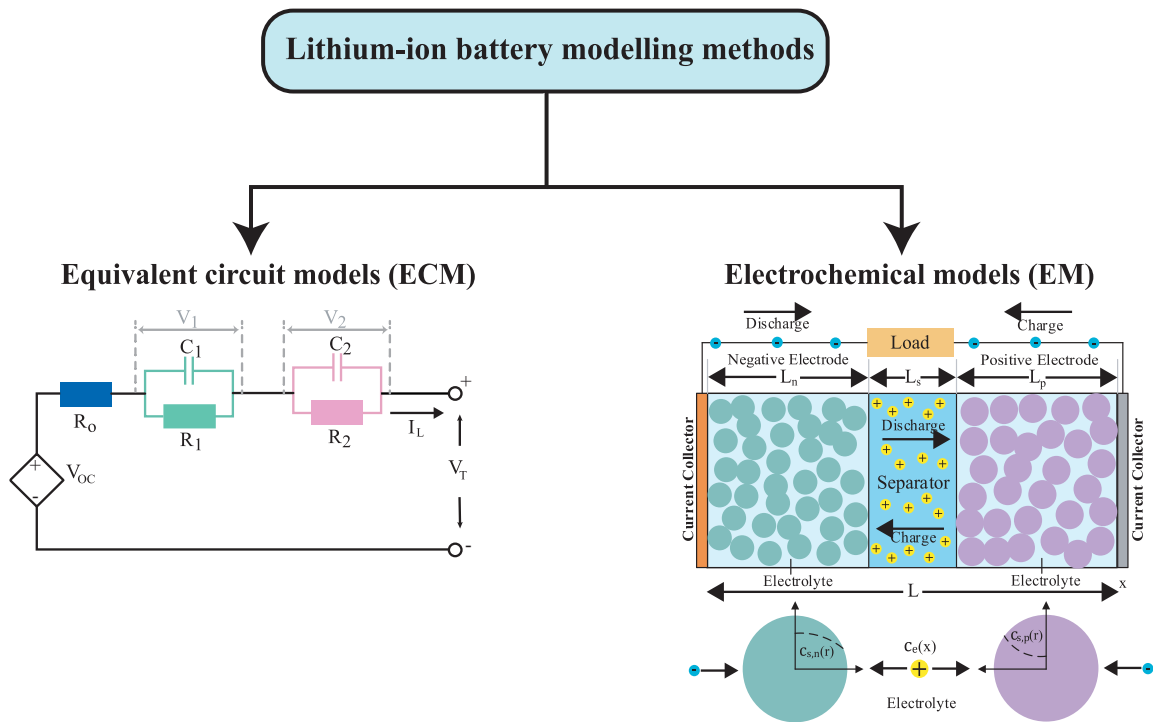


Figure 2.16 LIBs modelling methods.

2.6.1 Equivalent Circuit Models (ECM)

The ECMs are used to imitate the dynamic electrical behaviour of the LIB. Specifically, the ECMs described the battery behaviour using a combination of lumped parameters such as resistors, capacitors, and inductors [93, 94]. The ECMs have been extensively studied in the literature, especially for the SOC and capacity estimation of the LIB, due to their simplicity and the low-computational burden, which make them suitable for being implemented in the BMS [95, 96]. In addition, the ECM has been utilised for power management control of the LIB.

According to [97], the ECMs of the LIB can be divided into two main groups. The first group is known as the Thevenin models, which are created using several parallel RC circuits. The model parameters of the Thevenin models can be identified using a time-domain pulse charge/discharge technique. While the second group is known as impedance models, which usually comprise a constant-phase and Warburg elements. The model parameters of this group can be identified using EIS measurement. Figure 2.17 illustrates both modelling approaches, which will be explained in the following subsections.

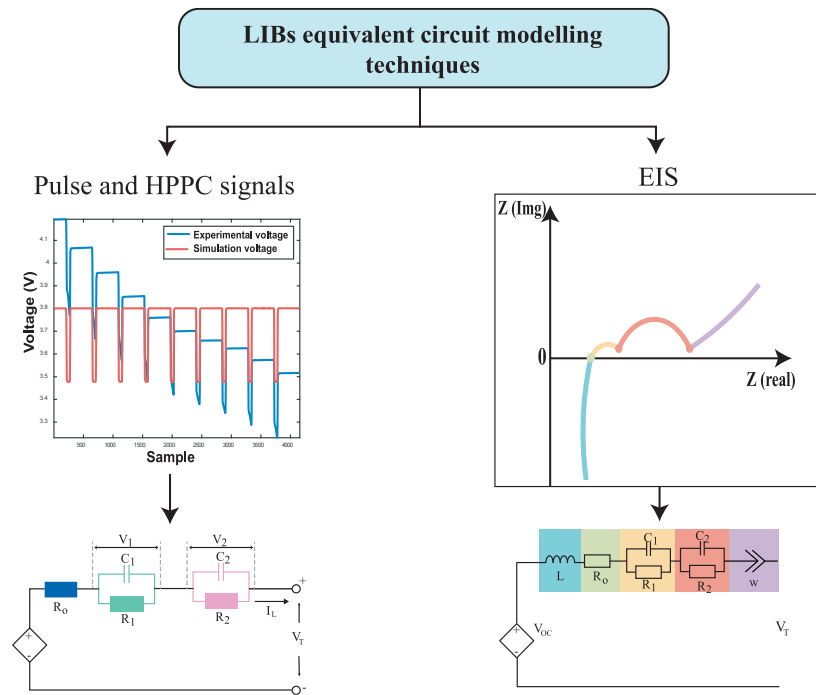


Figure 2.17 LIB equivalent circuit modelling approaches.

2.6.1.1 Thevenin models

The first modelling approach of the LIBs equivalent circuit model is the Thevenin models technique. This approach presents the input-output relationship of the LIB using a combination of parallel RC circuits. The concept behind the Thevenin modelling strategy is to apply a pulse discharge current signal to the LIB and monitor the output voltage response to represent the time-dependent effects of charge depletion and recovery, as shown in Figure 2.18. Precisely, when the pulse discharge current is applied to the battery, the voltage drops instantaneously due to the internal resistance of the battery; then, the battery's voltage decreases exponentially, which can be described as the double layer capacitance of the electrodes and mass transport processes that occur within the electrolyte inside the LIB, which can be presented using parallel RC circuit [98].

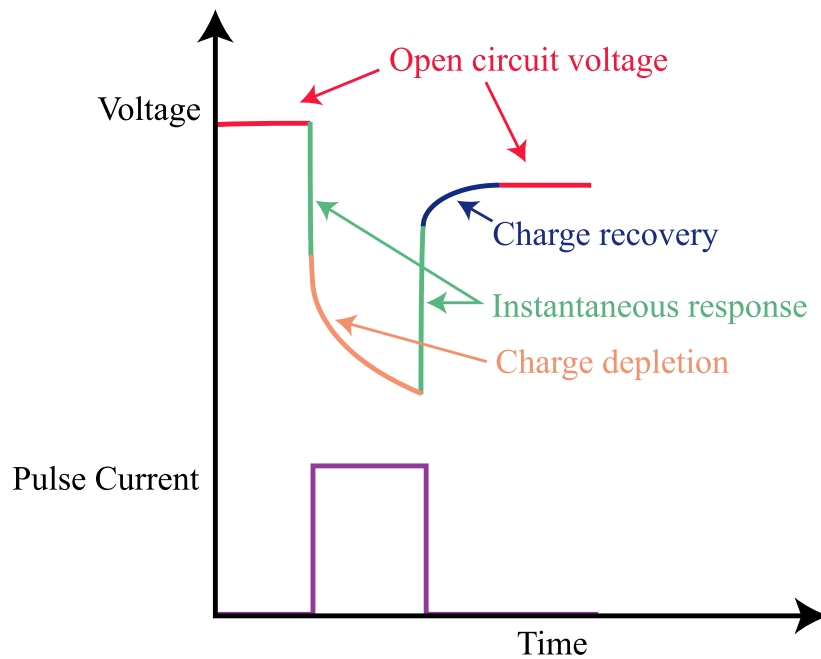


Figure 2.18 Voltage response to the pulse discharge current signal.

Moreover, once the pulse discharge current is removed, the measured voltage of the battery is instantaneously increased (it seems like the battery recharged itself) because of chemical compounds that diffuse from within the body of the battery to both the anode and the cathode. After then, the measured voltage is increased slowly in an exponential form, known as the charge recovery period. The time duration of the charge recovery period varies from one battery to another based on the chemistries of the LIB [99]. Therefore, the main question for modelling the dynamic response of the battery is what is the simplest ECM that gives the same response when the battery is discharged/charged [100]. To answer this question, literature has proposed numerous ECMs that mimic the actual battery's response. For instance, the authors in [100] and [101] have carried out a symmetrical overview of the extensively-used ECM. Figure 2.19 illustrates the three often used Thevenin equivalent circuit models: 1) R_{int} ; 2) 1-RC model; and 3) 2-RC model.

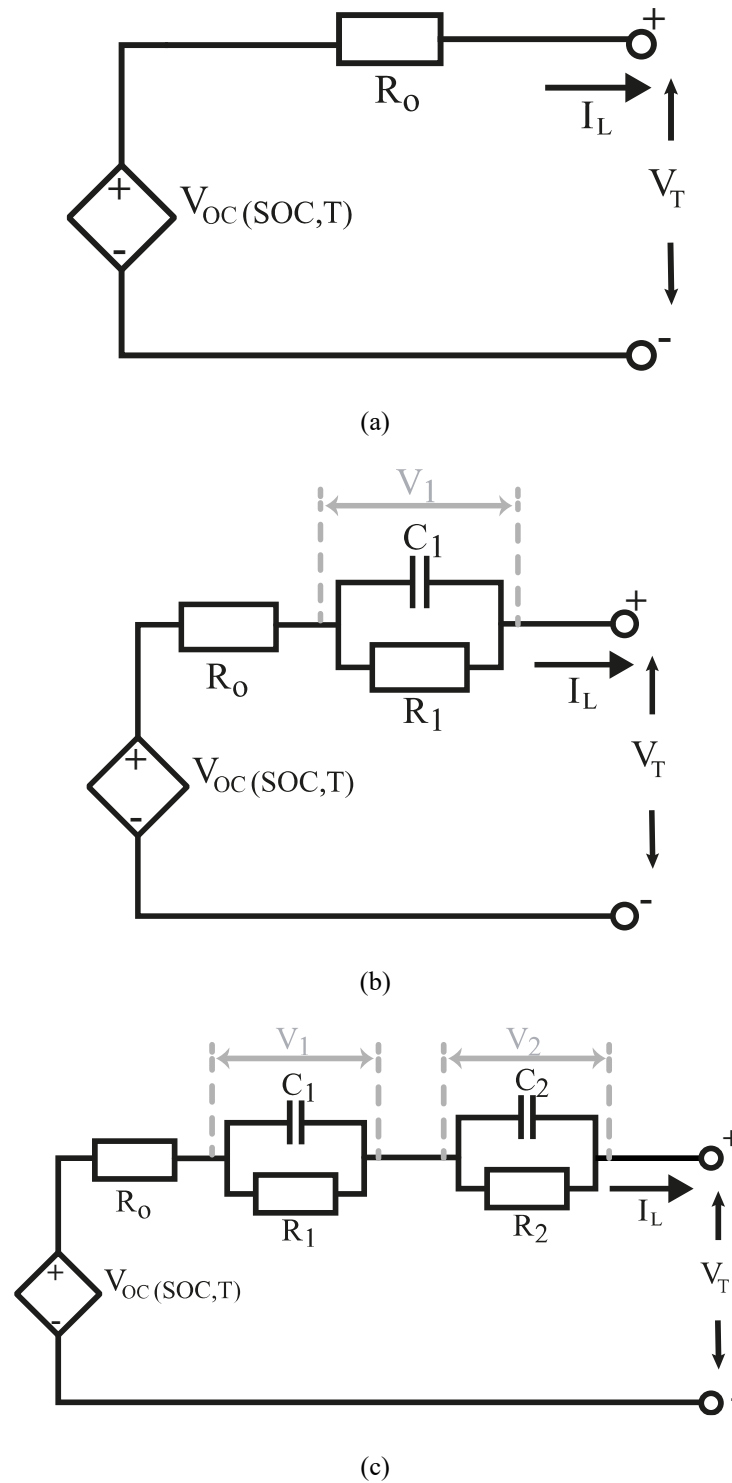


Figure 2.19 Thevenin equivalent circuit models: (a) R_{int} model, (b) 1-RC model, and (c) 2-RC model.

The Rint model, as shown in Figure 2.19 (a) and in (2.15), implements an ideal voltage source. V_{OC} to define the battery VOC. Both resistance R_O and open-circuit voltage V_{OC} are functions of SOC, SOH and temperature. I_L is load current with a positive value at discharging and a negative value at charging, V_T is the terminal voltage.

$$V_T = V_{oc} - I_L R_O \quad (2.15)$$

The 1-RC model, as shown in Figure 2.19(b), consists of one parallel resistor-capacitor (R_1, C_1) component, which characterises the exponential decay of the charge depletion and charge recovery regions shown in Figure 2.18. Moreover, the series resistor (R_O) represents the instantaneous voltage drops in Figure 2.18 corresponding to the LIB's internal resistance. The analysis of the 1-RC ECM is expressed in (2.16) and (2.17) by using Kirchhoff's law:

$$V_T = V_{oc} - I_L R_O - V_1 \quad (2.16)$$

$$\frac{dV_1(t)}{dt} = \frac{1}{R_1 C_1} V_1(t) + \frac{1}{C_1} I_L(t) \quad (2.17)$$

The 2-RC model is shown in Figure 2.19 (c); as shown in this figure, the ECM has another parallel RC circuit better to represent the battery behaviour than the 1-RC model. The capacitor C_1 , which has a small capacitance and mainly represents the surface effects of a battery, is named the surface capacitor. The capacitor C_2 , which has a large capacitance and represents the ample capability of a battery to store charge chemically, is called a bulk capacitor. The voltage across the bulk capacitor can determine SOC. Resistors R_O, R_1, R_2 is named terminal resistor, end resistor and capacitor resistor, respectively. V_1 and V_2 are the voltages across $R_1 C_1$ and $R_2 C_2$, respectively. The electrical behaviour of the circuit can be expressed by (2.18) and (2.19).

$$V_T = V_{oc} - I_L R_O - V_1 - V_2 \quad (2.18)$$

$$\frac{dV_1(t)}{dt} = \frac{1}{R_1 C_1} V_1(t) + \frac{1}{C_1} I_L(t) \quad (2.19)$$

$$\frac{dV_2(t)}{dt} = \frac{1}{R_2 C_2} V_2(t) + \frac{1}{C_2} I_L(t)$$

The ECMs mentioned above have been significantly applied for SOC estimation [102, 103] and capacity estimation [104, 105] of LIBs by monitoring the model parameters variation as

the battery degraded. For instance, the authors in [106] estimate the SOC of the LIB by fitting the n-RC model parameters to the OCV using an adaptive unscented Kalman filter (AUKF). The authors summarised that the 2-RC ECM outperformed the performance of the 1-RC ECM in terms of model accuracy. Furthermore, a combined SOC and capacity estimation of LIBs based on 1-RC ECM and extended Kalman filter has been presented in [49]. The authors precisely infer the battery's SOC by identifying the model parameters using a recursive least square algorithm alongside a second-order extended Kalman filter. At the same time, they estimated the capacity of the LIB by monitoring the variation of the model's internal resistance using a fourth-order extended Kalman filter.

Moreover, Qiu et al. [107] created a 2RC model combined with UKF to predict the future capacity degradation of the LIBs. However, the estimation accuracy of the studies mentioned above mainly depends on the model's accuracy in imitating the real operation of the LIB. Therefore, several parameter identification algorithms have been applied in the literature, such as least square algorithm (LS) [108], particle swarm optimisation (PSO) [109], and wolf optimisation algorithm [110]. A comparative study of nine optimisation algorithms for parameter identification of LIBs has been conducted in [109]. Figure 2.20 illustrates the schematic diagram of the Thevenin ECMs parameters identification.

As shown in Figure 2.20, a discharge pulse current signal is applied to the battery. The corresponding battery model and the measured voltage are compared; the difference between the measured and simulated voltage is used as input to the optimisation algorithm to update the model parameters. Once the measured and simulated voltage difference becomes zero (or almost zero), the optimisation algorithm will stop updating the model parameters.

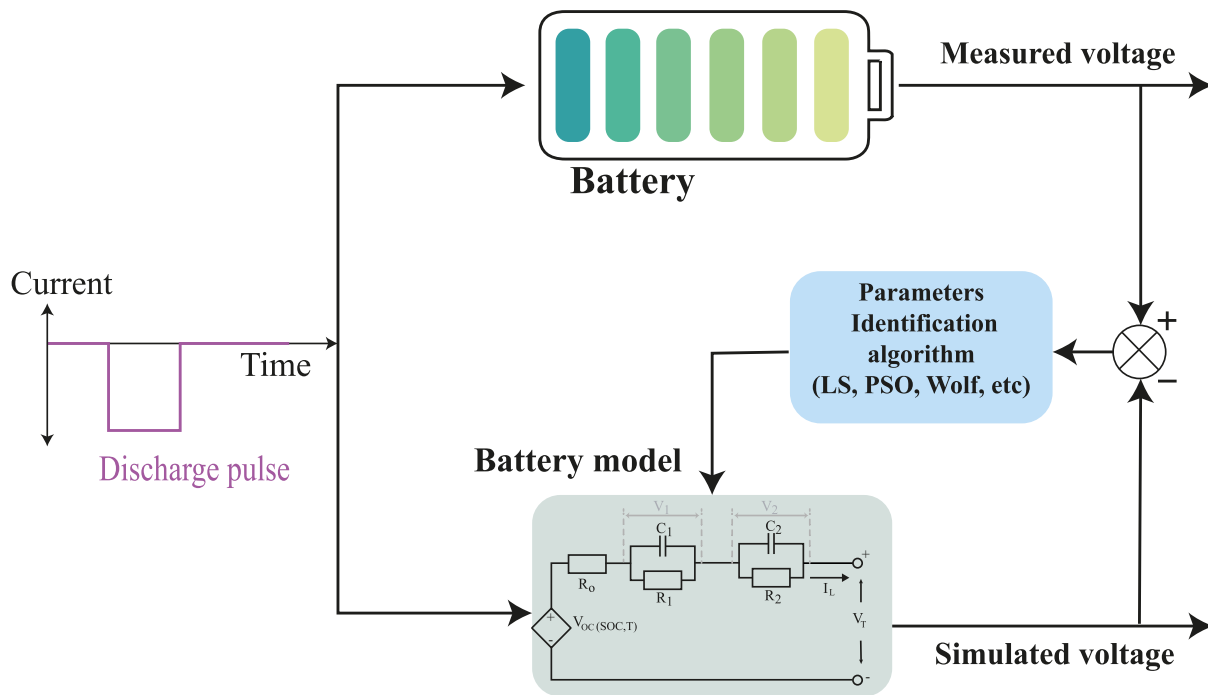


Figure 2.20 Schematic diagram of Thevenin model parameters identification.

2.6.1.2 Impedance models

The second battery modelling technique is the impedance model, which is based on the experimental approach of EIS (See section 2.3.3)—recall Figure 2.8 in Section 2.3.3 to clarify the concept of using the measured impedance in battery modelling. As shown in Figure 2.21, each frequency region in the EIS measurement can be modelled using electrical components such as a resistor, capacitor, and inductor. The difference between the impedance models and Thevenin models is the use of constant-phase element (CPE) and Warburg element, which provides more accurate modelling of the dynamic behaviour and impedance of the LIB [61, 111]. Table 2.1 illustrates different elements are usually used to model the battery impedance at different frequency regions.

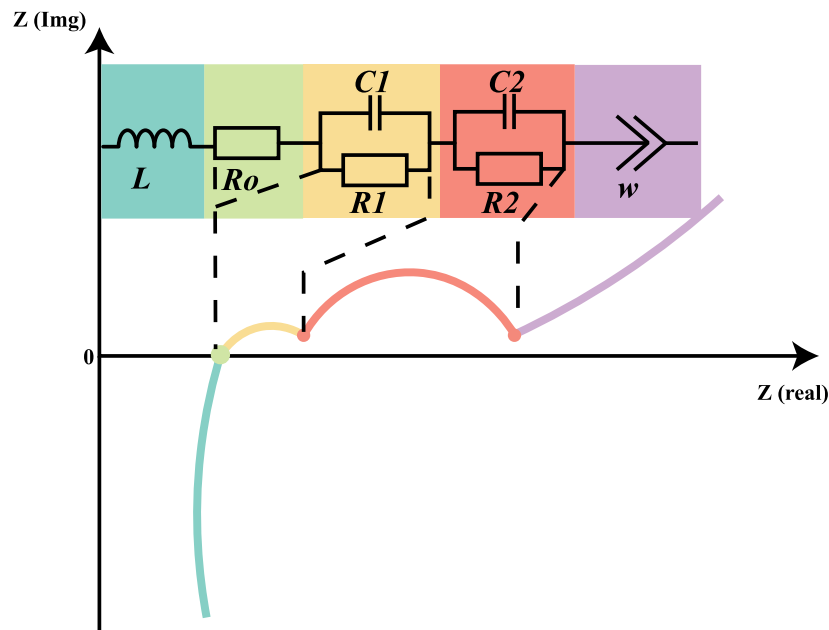


Figure 2.21 The LIB equivalent circuit model using EIS measurement.

As shown in Table 2.1, each impedance spectrum region can be modelled using a specific combination of equivalent elements. For example, the impedance spectrum of the charge-transfer process (the red semicircle in Figure 2.21) can be modelled by using parallel RC elements or R-CPE elements.

Similarly, the impedance spectrum of the low-diffusion process (the purple line in Figure 2.21) can be represented using different CPE types, as shown in Equations (2.22 – 2.24). The selection process of which equivalent element can be used to reflect the impedance spectrum of the battery based on the shape of the measured impedance spectrum from the EIS; since, as discussed in Section 2.3.3, the measured impedance of the LIB is changed based on the chemistry of the battery [112].

Therefore, several ECMs have been reported in the literature to describe the battery impedance. Table 2.2 presents the most applied ECMs to model the battery's impedance.

Table 2.1 List different equivalent elements in equivalent circuit models [61].

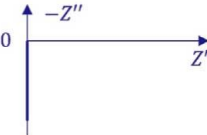

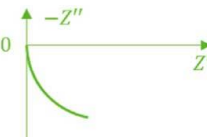

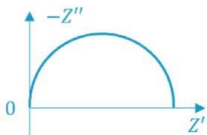

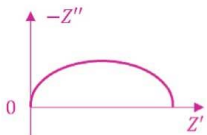

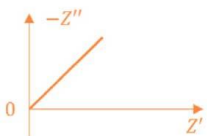

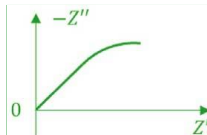



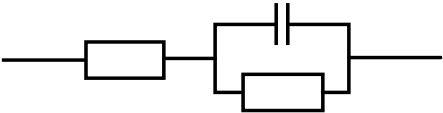
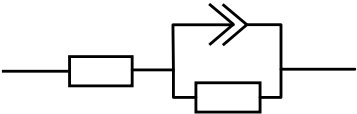
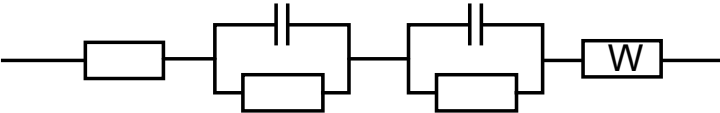
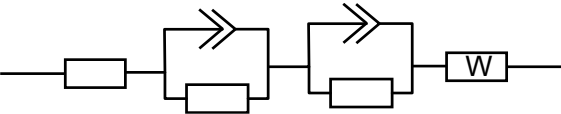
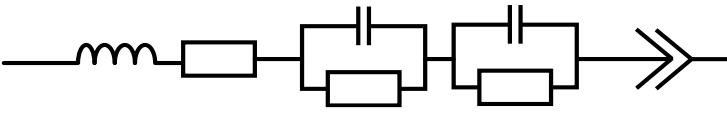
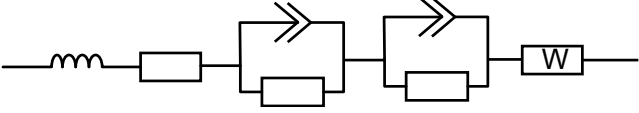
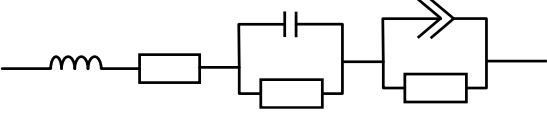
Impedance spectrum	Equivalent element	Impedance expression	
		$Z = j\omega L$	(2.20)
		$z = \frac{j\omega RL}{R + j\omega L}$	(2.21)
		$z = \frac{R}{1 + j\omega RC}$	(2.22)
		$z = \frac{R}{1 + (j\omega)^p RQ}$	(2.23)
		$z = \frac{R_W}{(j\omega)^{0.5}}$	(2.24)
		$z = R_W \frac{\tanh[(j\omega T_W)^{p_w}]}{(j\omega T_W)^{p_w}}$	(2.25)
		$z = R_W \frac{\coth[(j\omega T_W)^{p_w}]}{(j\omega T_W)^{p_w}}$	(2.26)

Table 2.2 List of ECMs based on the impedance spectroscopy measurement.

ECM	Reference
1) 	[113]
2) 	[114]
3) 	[115, 116]
4) 	[117, 118]
5) 	[119]
6) 	[120]
7) 	[121]

The developed ECMs based on EIS measurement have been employed for SOC and capacity estimation of LIBs [119, 120]. For example, the authors in [120] have estimated the capacity of the LIB by fitting the obtained impedance spectroscopy to an ECM (Figure number 6 in Table 2.2) and monitoring the growth of the charge transfer resistance over the LIB lifetime. The authors conclude that the battery reached its EOL when the charge transfer resistance enlarged to three-time compared to its initial value at the BOL of the LIB. Moreover, Xiong et al. [122] estimated the capacity of the LIB by studying the correlation between the SEI resistance and the battery's remaining capacity through the battery lifetime. In contrast, the authors in [74] predicted the remaining capacity of the retired LIB by tracking the variation of the CPE element in their developed ECM. The model parameters identification step of impedance-based models is similar to the parameter identification step of Thevenin models by using optimisation algorithms such as LS, PSO, and wolf algorithms [123].

Table 2.3 summarises the advantages and disadvantages of both ECMs modelling techniques (Thevenin and impedance-based models). Generally, both ECMs methods can emulate the electrical behaviour of the LIB. However, the major limitation of these ECMs is that they do not present any information related to the physical characteristics of the LIB. Moreover, the SOC and capacity estimation accuracy relies highly on the model accuracy, which means any uncertainties from the developed ECM will significantly affect the estimation accuracy. Furthermore, the ECMs were designed using a predefined and specific operating condition and have shown good performance for laboratory data generated under controlled conditions. However, if these models are exposed to real-world operating circumstances, it is impossible for them to maintain their accuracy assurances, which can lead to significant variations in the predictions. Lastly, identifying and fine-tuning the parameters of the ECMs to ensure that they capture all of the underlying battery degradation mechanisms is a complex and frequently expensive computational task. This task is further complicated by the requirement to simultaneously estimate the SOC, which adds another layer of complexity [124].

Table 2.3 Advantages and disadvantages of ECMs modelling methods.

Modelling method	Thevenin models	Impedance models
-----------------------------	------------------------	-------------------------

Advantages	1- Deficient error in the modified test.	1- A higher-order model is simple to modify.
	2- Obtaining the parameters using standard techniques such as least squares is simple.	2- Works on a broader frequency range.
	3- No Extra installation is needed to obtain the required data.	
Disadvantages	1- High error with pulses of various dynamics.	1- EIS measurement test is needed (Extra installation).
	2- Difficult to adjust a higher-order model.	2- Long testing time to obtain the battery impedance at different frequency ranges.
	3- It is challenging to alter a higher-order model.	3- Some parameters, such as CPE and Warburg element, cannot be simulated in the time domain.
	4- No information about the chemical behaviour of the battery.	

2.6.2 Electrochemical Models (EM)

In contrast to equivalent circuit modelling techniques, electrochemical models (EMs) physically characterise the chemical processes inside the LIB in great detail, making them the most precise, accurate battery models. The first EMs is the pseudo-2D (P2D) porous electrode model, initially established by Doyle, Fuller, and Newman [125, 126]. The P2D model forms a set of connected partial differential equations (PDEs). In contrast to the ECMs, the P2D model is founded on physics, and it not only has the ability to estimate the outward properties of the LIB, but it can also provide insight into the electrochemical states that are occurring internally in the LIB. Understanding these internal electrochemical states helps analyse deterioration mechanisms, extend the battery's life, predict power limits, and design optimal charge

strategies [127]. Figure 2.22 is a schematic of the P2D model of the LIB. As seen in Figure 2.22, there are four main components in a typical P2D model of the LIB:

- 1- The negative electrode is connected to the negative terminal of the battery.
- 2- The positive electrode is connected to the positive terminal of the battery.
- 3- The separator in the middle region between the negative and positive electrodes.
- 4- The electrolyte.

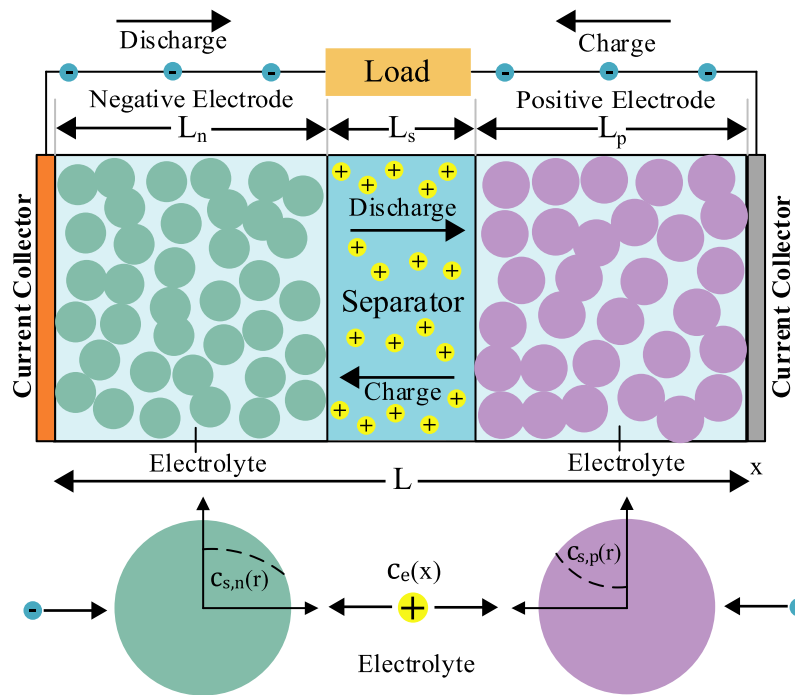


Figure 2.22 The P2D model of LIB.

The negative electrode typically comprises lithium in the form of Li_xC_6 contained in graphite lattice sites. The positive electrode can have a variety of chemical compositions, often a metal oxide or intermetallic oxide like $Li_xMn_2O_2$ or Li_yCoO_2 [127]. Throughout the discharge process, lithium ions diffuse to the surface of Li_xC_6 active material particles (solid phase, the green circles in Figure 2.22) in the negative electrode. They go through a series of electrochemical reactions and are then transferred into a liquid electrolyte solution (solution phase). The positively charged lithium ions travel through the electrolyte solution via diffusion and ionic conduction to the positive electrode, where they react and diffuse towards the inner regions of metal oxide active material particles (solid phase). This process is very similar to

charging, except that the lithium ions travel in the reverse direction, leaving the lattice sites in the positive electrode and entering the lattice sites in the negative electrode [128]. This process is called intercalation, which is why the LIB is commonly known as the rocking chair model [129]. The porous separator acts as an electric insulator. It directs the flow of electrons in a different direction than that of the ions, either through an external circuit or a load. Nevertheless, the separator permits lithium ions to travel through it during battery operation [130]. The governing partial differential equations used to formulate the P2D model can be found in [125, 126]. For instance, the authors in [131] have estimated the capacity of the LIB by developing a P2D model to monitor the evolution of the SEI layer and lithium plating for the negative electrode over the battery's lifetime.

However, despite the magnificent modelling accuracy of the P2D model, this model cannot be employed for online states estimation of LIBs in embedded microcontrollers because the nonlinear partial differential equations usually take hours to spatially discretise the system by using numerical methods such as finite element method and Finite difference method. Thus the computational complexity will be significantly increased [132]. Therefore, various reduced-order electrochemical models have been reported in the literature. For instance, the authors in [133] have proposed a reduced version of the P2D model known as the single particle model (SPM). Specifically, the SPM is designed based on two assumptions [133]:

- 1- The negative and positive electrodes are modelled as two spherical particles.
- 2- The changes in the electrolyte concentration are ignored.

Considering these two assumptions in the modelling step reduces the number of nonlinear partial differential equations to five. Moreover, the advantages of the SPM compared to the P2D model can be summarised in the following points [134]:

- 1- It is simpler than the P2D model since five equations are used to create the SPM.
- 2- Less computational burden is needed.
- 3- It can be applied for the online SOC and capacity estimation.

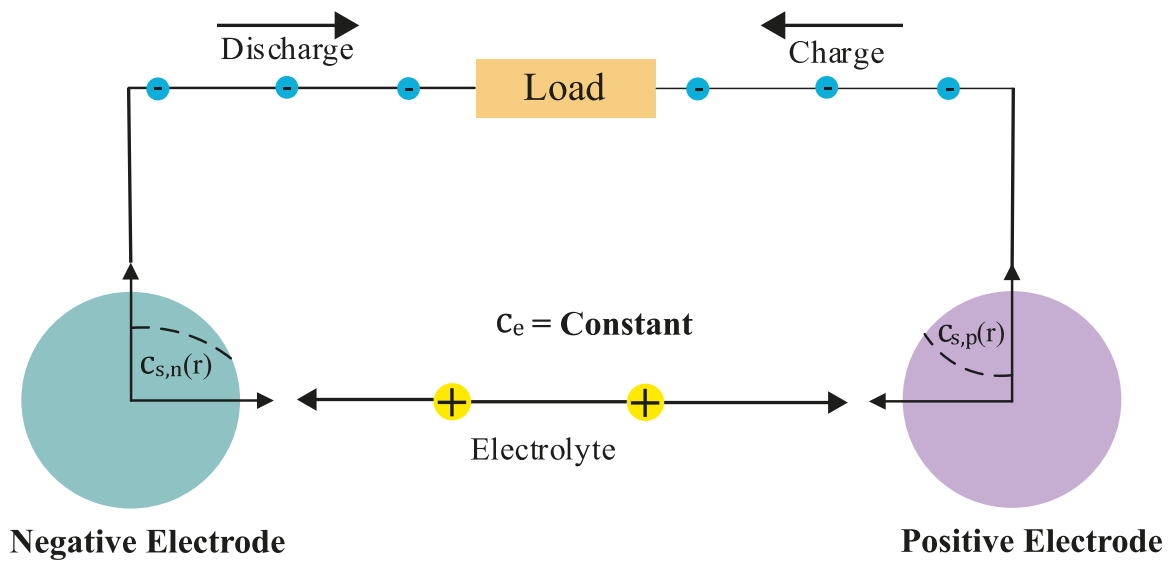


Figure 2.23 The schematic of the SPM.

Figure 2.23 shows the schematic of the SPM. The SPM has been applied for SOC estimation [135-137], capacity estimation [138-140], and RUL prediction [141, 142]. For example, Li et al. [138] developed SPM for capacity fade estimation by monitoring the formation and growth of the SEI layer at the anode as a function of cycle number over a wide range of temperatures. Similarly, Allam et al. [143] developed an SPM to estimate the lithium concentration and capacity degradation by considering the growth of the SEI layer as the primary ageing mechanism. The authors in [144] developed an SPM-based PF model to forecast the future capacity degradation of LIBs.

Usually, once the LIB's model (ECM or EM) is created, filters/observers with closed-loop control and feedback are designed to estimate the capacity of the LIB. The general operation framework for the capacity estimation of LIBs using model-based methods is shown in Figure 2.24. As shown in Figure 2.24, many filters/observers algorithms coupled with ECMs, or EMs, have been applied for the capacity estimation, such as Kalman filter family [145], H-infinity filter [146], sliding mode observer [147], partial differential equation (PDE) observer [148], and nonlinear observer [149].

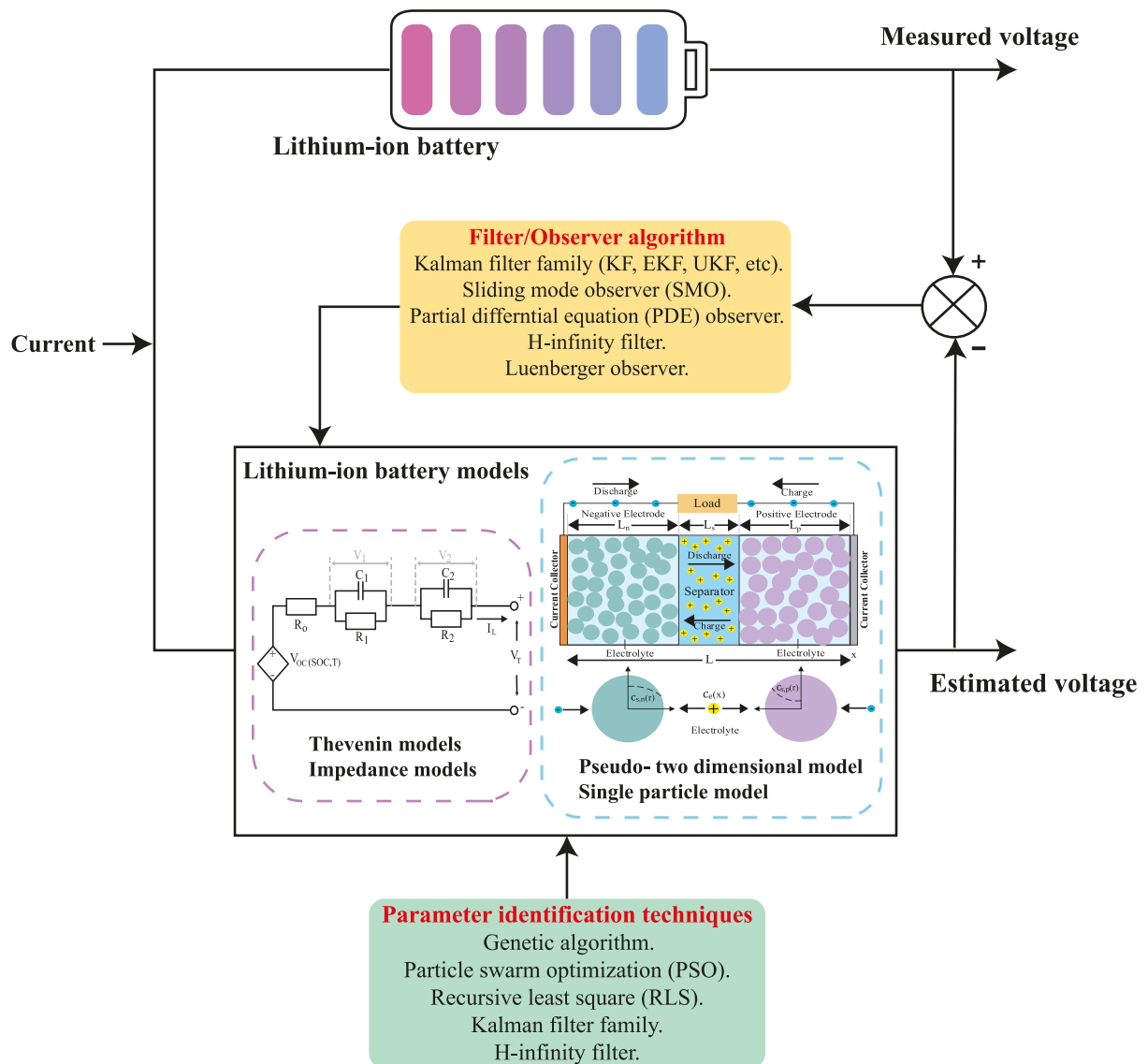


Figure 2.24 The general framework for the capacity estimation of LIB using model-based methods.

Table 2.4 presents an overview of state of the art is state estimation of LIBs using model-based methods. The Kalman filter (KF) is one of the most extensively used estimating algorithms and has gained significant interest for model parameters and state estimation. KF employs a feedback and correction system to continually approach the true value and eliminate noise. Nevertheless, KF-based algorithms presume that the statistical properties of noise are identified in advance and subject to model errors [150]. To tackle these limitations of the KF-based algorithm, several other filters/ observers have been proposed in the literature, such as the H-infinity filter [146] and particle filter [151].

Nonetheless, the model-based techniques primarily rely on the physical or electrochemical modelling performance of degradation behaviour when depicting the battery capacity decline trajectory. Typically, the model consists of algebraic and differential or empirical equations, which are better suited to certain application circumstances. Moreover, the structure and accuracy of the constructed model are crucial to its authenticity [152]. To overcome the limitations of the model-based approaches, data-driven approaches have recently received extensive attention regarding the capacity estimation of LIBs due to their superior advantages and performance accuracy. The following section will detail the data-driven methods for the capacity estimation of LIBs.

Table 2.4 Overview of the most applied filters/observers' algorithms for state estimation of LIB.

Reference	Estimated state (s)	Filter/Observer	Model
[153]	SOC	EKF	ECM (1-RC)
[154]	SOC and capacity	Dual adaptive square root extended Kalman filter (ASREKF)	ECM (1-RC)
[155]	SOC	DEKF	ECM (1-RC)
[156]	SOC and capacity	UKF	ECM (2-RC)
[157]	SOC and capacity	SPKF	ECM (2-RC)
[158]	SOC and capacity	DEKF	ECM (2-RC)
[159]	SOC and capacity	Fractional-order multi-innovations unscented Kalman filter and unscented Kalman filter (FOMIUKF)	ECM (2-RC)

[107]	SOC and capacity	Cubature Kalman filter (CKF)	ECM (2-RC)
[160]	SOC and capacity	AUKF	ECM (2-RC)
[161]	SOC	SPKF	EM (P2D)
[162]	SOC, Lithium-ion concentration, potentials	AUKF	Reduced-order EM (SPM)
[137]	SOC	Luenberger observer	Reduced-order EM (SPM)
[163]	SOC and capacity	CKF	Reduced-order EM (SPM)
[164, 165]	SOC and capacity	Partial differential equation (PDE) observer	Reduced-order EM (SPM)
[166]	SOC and capacity	Sliding mode observer (SMO)	ECM (1-RC)
[151]	SOC and capacity	Particle Filter (PF)	EM (P2D)
[131]	Capacity	Particle Filter (PF)	EM (P2D-SPM)

2.7 Data-Driven Techniques

Capacity estimation of LIBs based on data-driven techniques has attracted considerable attention as a result of the rapid expansion of computing capabilities, data storage, and communication technologies. Furthermore, data-driven algorithms are effective in estimating the capacity of LIBs because they do not need interpretation of the implicit electrochemical events occurring within LIBs [167]. Meanwhile, the capacity estimation methods by data-driven algorithms do not require developers to understand the batteries' material and electrochemical characteristics [168].

Several data-driven algorithms for the capacity estimation of LIBs have been reported in the literature, such as support vector regression (SVR) [169, 170], Random Forest Regression (RF) [171-173], Gaussian Process Regression (GPR) [174-176], and deep neural networks (DNN) [177-179].

As depicted in Figure 2.25, the standard implementation approach for employing data-driven algorithms to estimate the capacity of LIBs consists of four phases: data collection, feature extraction, model training, and model testing. Initially, offline experiments measure and record the original data, including current, voltage, temperature, and time. Next, a set of health features with M dimensions is extracted from the original measurement data with N dimensions to capture the main alterations throughout degradation; thus, $M < N$. The third phase involves training the data-driven model with inputs of health features and outputs of the capacity and optimising and tuning the model parameters. The final stage is to validate and predict the capacity using the developed model.

The main challenge of these four steps is extracting relevant features from the collected signals to explain the battery's deterioration phenomenon throughout its lifetime. Feature extraction is a crucial step in implementing data-driven algorithms and significantly impacts the estimation accuracy of the capacity. More important and valuable feature input will certainly produce more accurate estimation results [180]. At present, the feature extraction process is mainly based on the charging curve features, differential curves features, and EIS curve features, as shown in Figure 2.26. The following subsections will detail the procedure of these feature extraction methods.

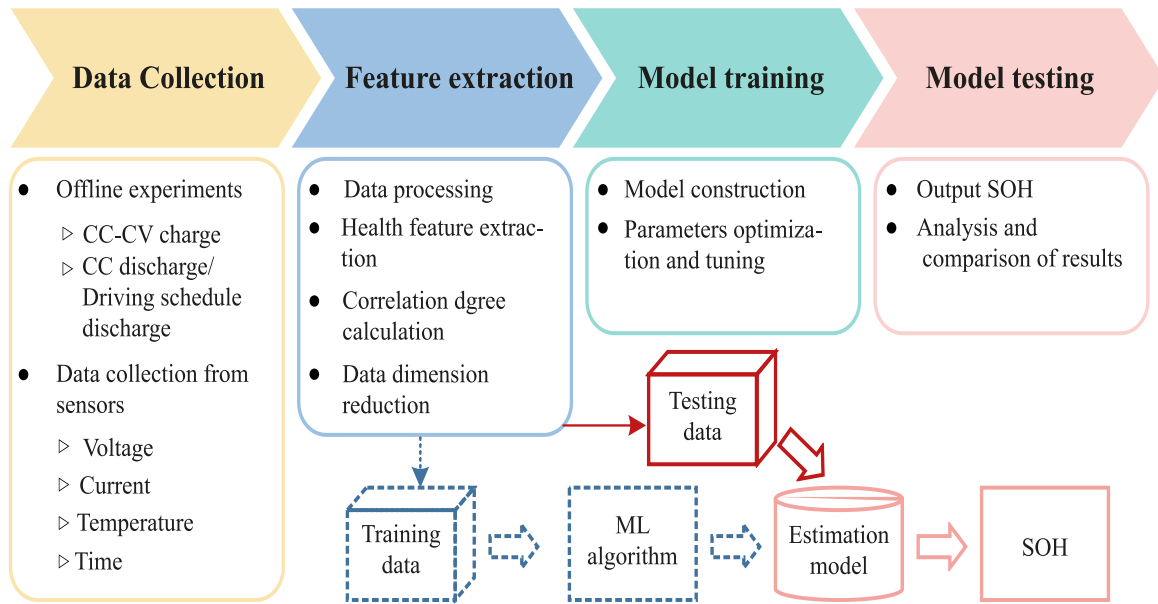


Figure 2.25 The general flowchart for the capacity estimation of LIBs based on data-driven techniques.

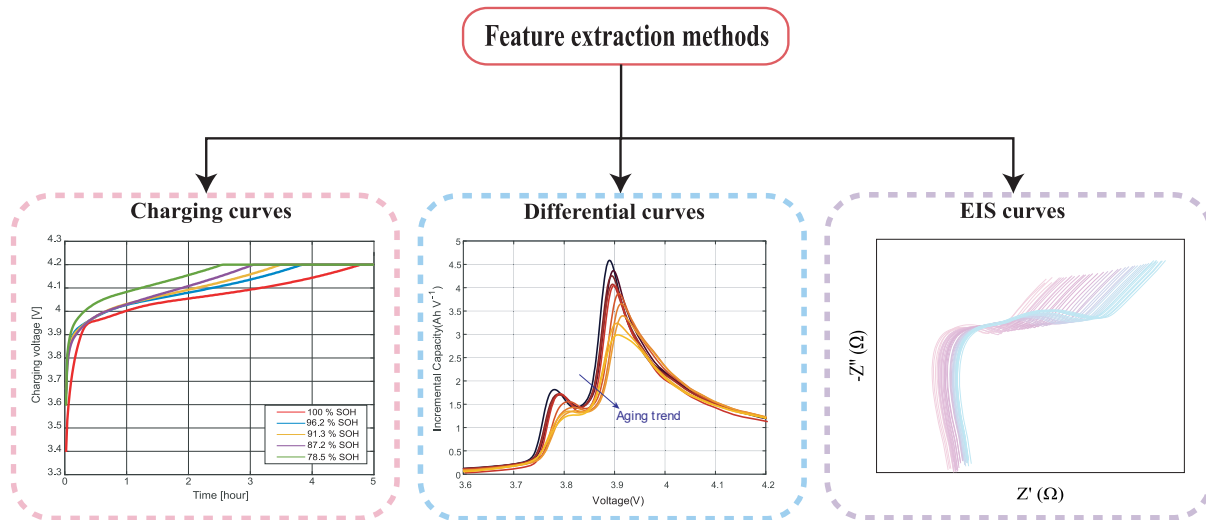
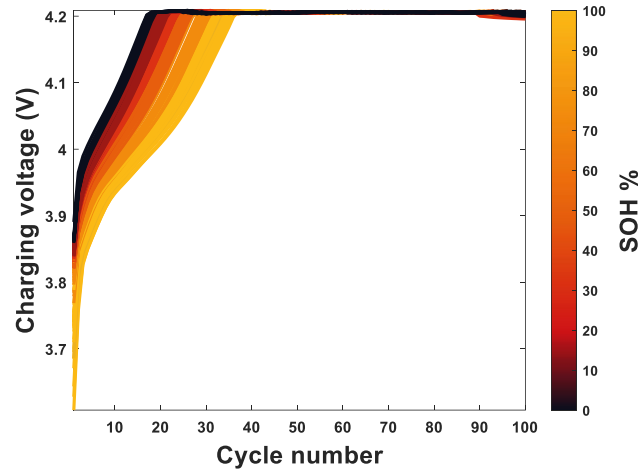


Figure 2.26 Feature extraction methods.

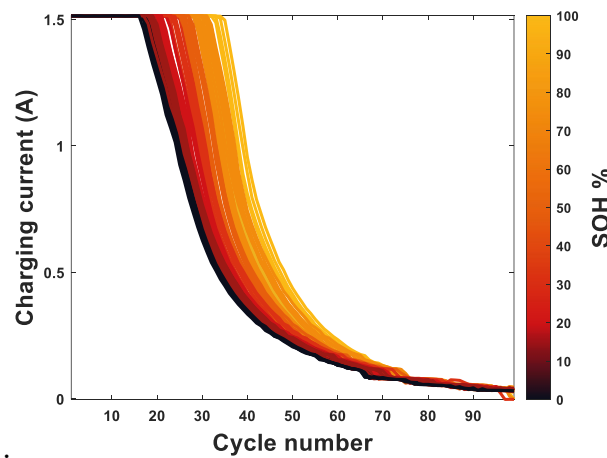
2.7.1 Feature Extraction based on Charging Curve.

Figure 2.27 shows the CC-CV charging profiles of the LIB at different capacity values, where the CC process's charging time gradually reduces. Conversely, the constant voltage (CV)

charging procedure results in a noticeable increase in charging time. As a result, the charging time throughout the corresponding CC and CV processes can be viewed as a health feature.



(a)



(b)

Figure 2.27 (a) CC-CV voltage and (b) CC-CV current curves.

The battery feature characteristics typically determined by the charging curve are the initial charging voltage, constant current charging time, charging capacity, full charging time, and the maximum slope of the current curve in the CV phase [181]. For instance, the authors in [182] utilised the time duration between two voltage points as a health feature for the capacity estimation of LIBs. This time duration can be calculated as expressed in (2.27).

$$t_{i,t} = t_{i,V_2} - t_{i,V_1} \quad (2.27)$$

Where t_t is the duration of charge from V_1 to V_2 at the i_{th} cycle, t_{i,V_2} and t_{i,V_1} represent the time to reach V_2 and V_1 at the i_{th} cycle. As shown in Figure 2.28, the charging duration of the battery when the SOH is 93.1% is much smaller than the charging duration at the beginning of the battery's life.

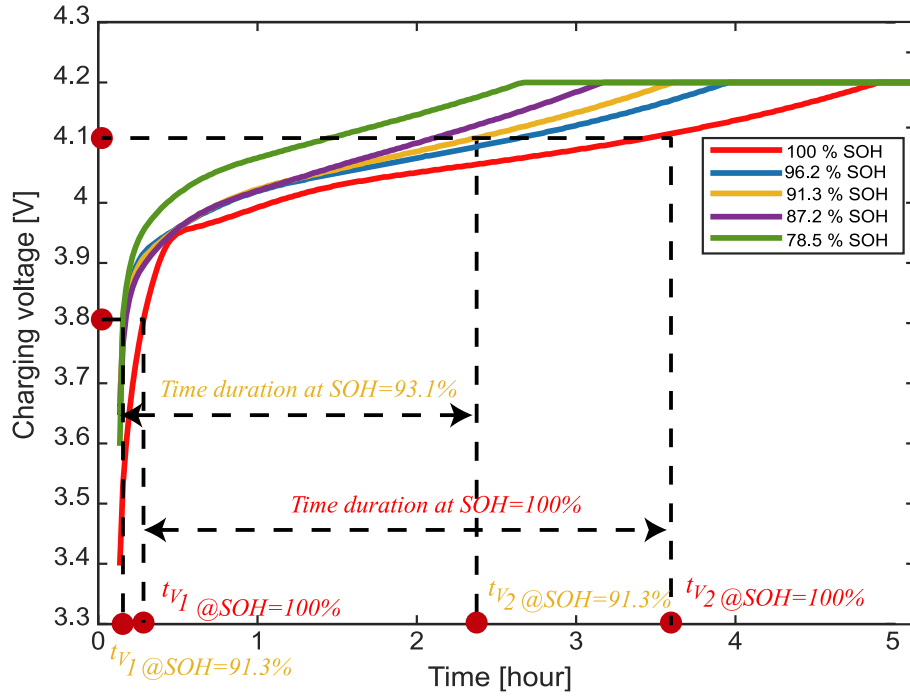


Figure 2.28 CC-CV voltage curves at different SOH (capacity) values.

Yang et al. [183] extracted four health features from the charging voltage curve. These health features are (1) the time duration of the CC period, (2) the time duration of the CV period, (3) the slope of the curve at the end of the CC charging period, and (4) the vertical slope at the corner of the CC charging curve. The extracted health features are then fed into the GPR model for capacity estimation of LIBs. Similarly, Cao et al. [184] estimated the remaining capacity of the LIB by extracting 17 health features from the charging voltage, current, capacity, and temperature curves. Specifically, the authors divided the extracted health features into five groups: (1) charge-capacity-related features, (2) charge-time related features, (3) charge-temperature-related features, (4) slope of the charge-curve related features, and (5) sample

entropy related features. After that, the extracted features are fed into a deep belief network for training and testing the developed model using the extracted features for capacity estimation.

Similarly, the authors in [185] extracted 15 health features from the charging curves of voltage, current, and temperature signals. The extracted health features are grouped into five groups based on the charging curve of the health feature extracted (e.g., voltage, current, or temperature). A Neighbourhood component analysis (NCA) reduction method is applied in order to eliminate redundant information in the extracted health features and thus reduce the computational complexity of the proposed method. In fact, LIBs are typically neither fully charged nor charged from an empty state.

Consequently, determining health characteristics from the partial charging curves conforms more closely to actual conditions. In this manner, Li et al. [186] developed an online capacity estimation model based on the charging voltage data from the partial constant current charging curve and long short-term memory network (LSTM). The authors in [187] investigated the impact of the extracted health features from the partial charging curve at three different voltage ranges on the model estimation accuracy. These three voltage ranges are shown in Figure 2.29; each region is utilised as an input for a data-driven algorithm known as the random forest algorithm. The capacity estimation results found that using the extracted health features from region 2 (setting 2 in Figure 2.29) gives more accurate estimation accuracy than the other two settings. The predetermined CC voltage for a given time is divided by Richardson et al. [188] into various segments. The amount of time it takes for the voltage to reach a consistent state throughout the charging process is considered a health feature.

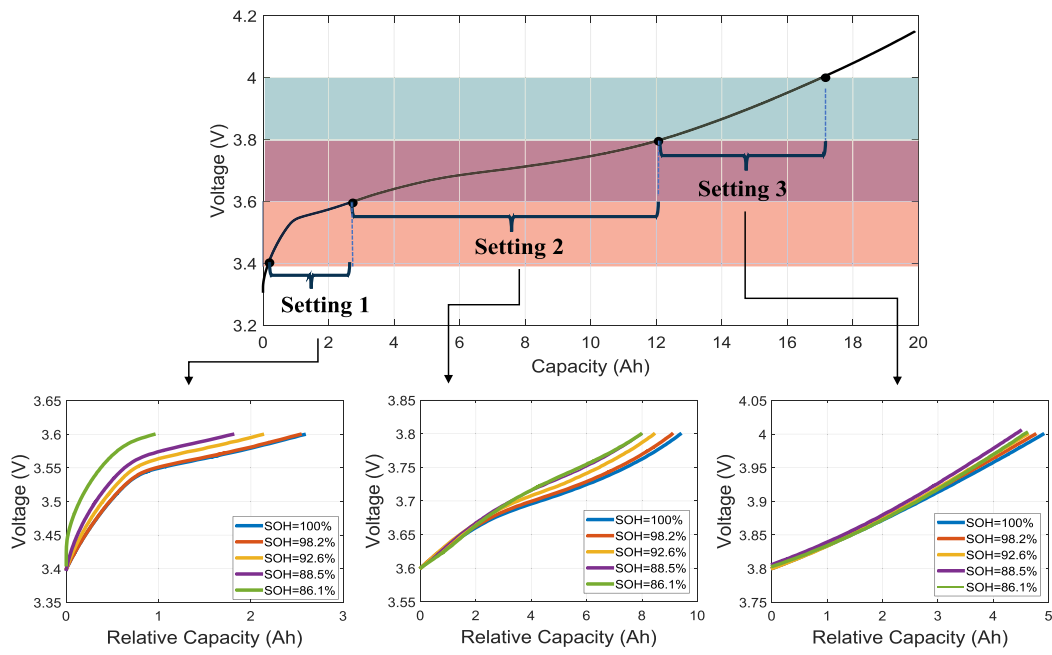


Figure 2.29 Health feature extraction from three different voltage ranges [187].

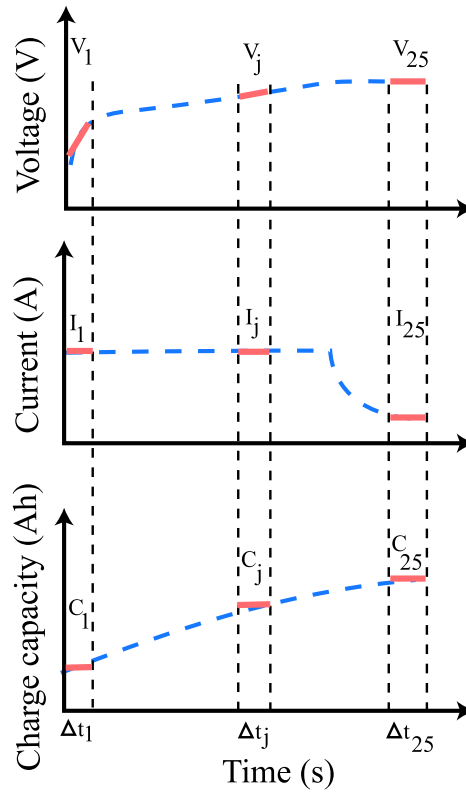


Figure 2.30 Discretised partial voltage, current, and charge capacity [189].

The voltage/time segment data are then used to train the GPR model to estimate the capacity of the LIBs. Furthermore, the authors in [189] discretised the partial voltage, current, and charge capacity into 25 segments, as shown in Figure 2.30. Then, the segmented health features are fed into a DLCNN for capacity estimation. In addition, a comparison is made between the effects of duration, the voltage, current, and charge capacity at their lowest points and the number of segments. Taking into account the fact that various voltage, current, and charge capacity ranges will have a significant effect on the precision of capacity estimation. To improve the performance of the developed data-driven model for the capacity estimation of LIBs based on the charging curves, Lin et al. [190] proposed an approach based on a multi-feature-multi-model fusion technique for the capacity estimation of LIBs. In particular, the extracted health features from the voltage, temperature, and incremental capacity analysis are used as input to a single data-driven model. Then, three data-driven algorithms, which are multiple linear regression (MLR), SVR, and GPR, are utilised to estimate the battery's capacity. The estimated capacity for each model is then used as input into an RF regression model for fusing the multi-model and estimating the final capacity value of the LIB, as shown in Figure 2.31. Similarly, the authors in [191] used a multi-stage artificial neural networks (ANN) fusion model for the capacity estimation of LIBs based on the extracted features from the partial charging current curves.

A recently published research paper [192] estimated the capacity of the LIB by extracting the health features from the relaxation period only in the charge voltage curve, as shown in Figure 2.32. Six health features were extracted from the relaxation period; these health features are (1) variance, (2) skewness, (3) maxima, (4) minima, (5) mean, and (6) excess kurtosis. The extracted health features are then fed as input into a transfer-learning data-driven model known as the XGBoost model to learn the relationship between the extracted health features and the target output (capacity of the battery). Moreover, the authors in [193] have selected the energy in the constant current (CC) charging curve, constant voltage (CV) charging curve, and the energy in an equal discharge voltage interval as health features combined with GPR for the capacity estimation of LIBs.

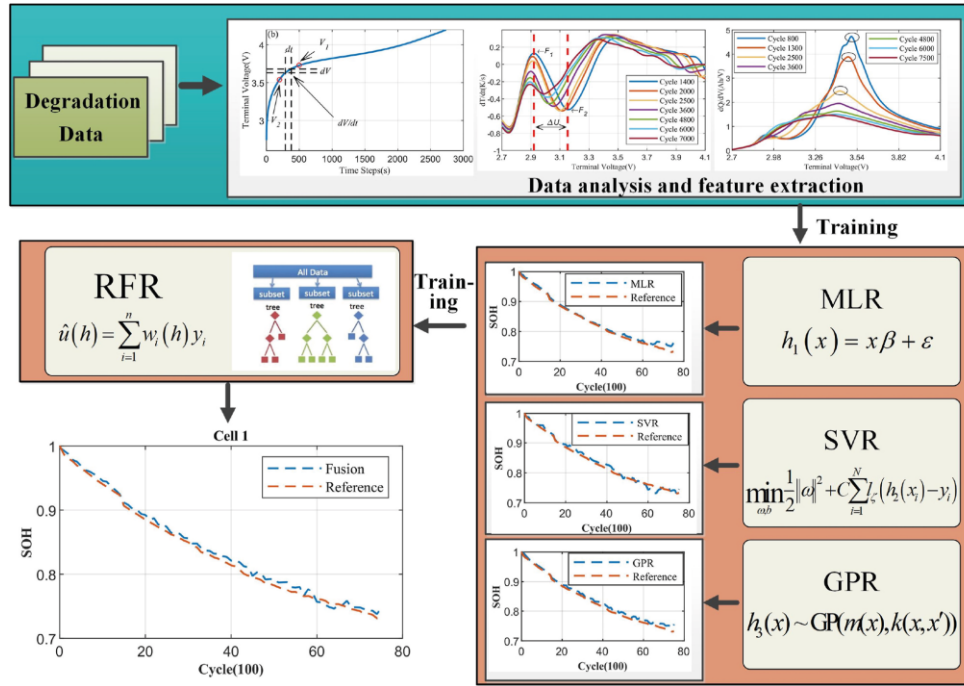


Figure 2.31 The proposed multi-model fusion algorithm for the capacity of LIBs [190].

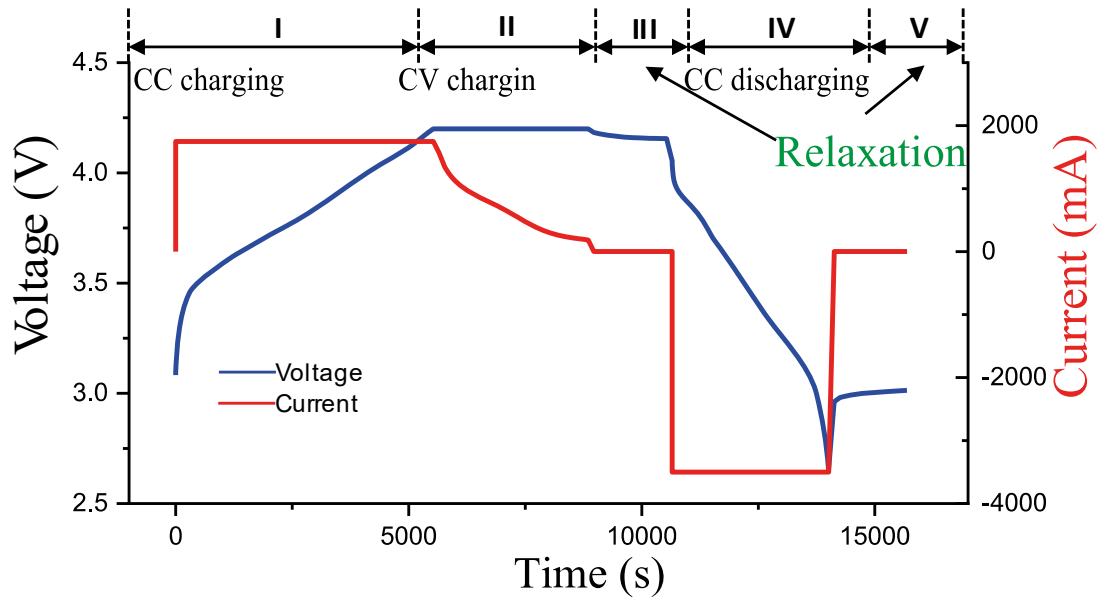


Figure 2.32 CC-CV voltage and current showing the relaxation period [192].

Similarly, Cai et al. [194] utilised the energy in the CC-CV charging curves as a health feature integrated with the GPR algorithm to estimate the capacity of LIBs. Moreover, the authors in [195] developed a many-to-one LSTM model to predict the future capacity degradation of the LIB; the charging current, voltage, temperature, and capacity were used as input to the LSTM. The authors in [196] proposed an autoencoder DL-CNN to predict the RUL of NASA's dataset. Table 2.5 presents the recent state-of-art for the capacity estimation and prediction of LIBs based on the extracted health features from the charging curves.

Table 2.5 Recent proposed methods for the capacity estimation of LIBs based on charging curves.

Ref	Charge curve	Number of health feature
[197]	CC-CV curves	30
[198]	CC-CV curves	2
[199]	CC, CV, and T curves	8
[171]	CC-CV curves	4
[200]	CV curve	1
[201]	CC-CV and T curves	6
[202]	T curve	6
[203]	CC-CV and T curves	3
[204]	CV curve	1
[205]	CC-CV and T curves	3
[206]	CC-CV and T curves	5

In conclusion, the charging curve-based methods described above demand an extremely high level of integrity and regularity from the charge curves. In the case of a short-term recharge, it is more challenging to get these health features because of the concern that owners of EVs experience regarding their vehicles' operating range (distance range). Moreover, this approach's primary challenge is that specific LIBs (primarily lithium-ion-phosphate) have an extended flat constant charge voltage region. This phenomenon causes the voltage to fluctuate slowly as the amount of electric charge increases/decreases. In the meantime, the voltage charge curves of

various aged LIBs overlap in the flat region, making it difficult to distinguish the different health conditions of LIBs over a short period of charge voltage [207]. In addition, the requirements for charging are often either constant-current charging or charging with both constant current and voltage. It is still a question that needs to be investigated whether or if the aforementioned health features can still be utilised with the step-current charging approach in real-world engineering applications.

2.7.2 Feature Extraction based on Differential Curve

Differential analysis is used in the context of LIBs and is based on differentiating curves such as electrical, thermal, or mechanical. These curves are collected by charging or discharging the LIB. The most common analyses regularly used are ICA and DVA techniques. This subsection provides an overview of using these techniques for the capacity estimation of LIBs based on the extracted health features.

ICA/DVA offers a non-destructive method of characterising LIBs and has been utilised extensively to detect ageing mechanisms [208]. As presented in section 2.3.4, calculating the IC curve involves differentiating between the change in battery capacity and the change in terminal voltage over a sufficiently short period. On the other hand, DV can be understood as the inverse of IC. The differentiation process converts voltage plateaus in charge/discharge curves into easily distinguishable peaks in the IC curves and valleys in the DV curves. Peaks show phase transitions in the DV curve plotted against electrode battery capacity. On the other hand, peaks in the IC curve represent the position of phase equilibria [209].

Each peak on the curve has distinctive characteristics, such as intensity and position, which are illustrative of a particular electrochemical process taking place within the LIB. One key distinction exists between the two techniques regarding the information they can supply about ageing. The cell voltage, which can be a direct indicator of the state of the battery, is what is referred to as an IC curve. DV curves, on the other hand, refer to the cell capacity, which is a secondary indicator that varies with the deterioration of the battery and loses its reliability as a reference as the battery ages. After the IC/DV curves have been obtained, the progression of

the health features can be associated with the capacity fade of the LIB. These health features can be peak location [90], height [210], and integrated peak area [211].

As mentioned above, the core concept behind the ICA is calculating the derivative of the charging capacity to the battery's voltage. In other words, the goal of the approach is to determine the rate of change. In the charging capacity at a given voltage and thereby converting the voltage plateaus on the V - Q curve into clearly distinguishable peaks on the ICA curve, as shown in Figure 2.33. The ICA-based method has been comprehensively studied for the capacity estimation of LIBs [212-217].

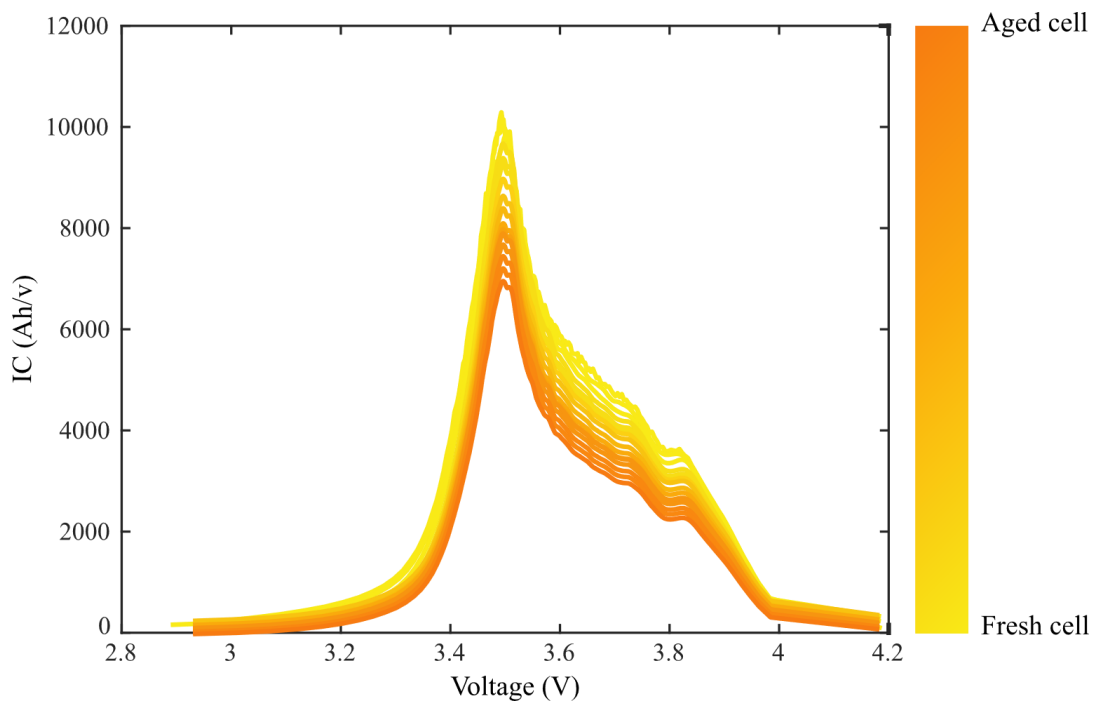


Figure 2.33 IC curves of a LIB over its lifetime.

For example, Chng et al. [218] extracted five health features from the obtained IC curves of LIBs (NMC battery type). These health features were grouped into three categories (1) peak value, (2) peak position, and (3) slope of the peak, as shown in Figure 2.34. The correlation between the extracted health features and the capacity degradation of the battery was analysed using the Pearson correlation method. The most crucial health features are used to train a NN model to estimate the capacity of the LIB. The authors in [218] found that peak number 1 (Figure 2.35) and its position strongly correlate with the battery's capacity degradation over

its lifetime. Similarly, the authors developed an ICA-based method for the capacity estimation approach linked with a Gaussian smoothing filter [219]. It was proved that the proposed method could accurately estimate battery capacity ageing using only partial constant charging data.

Pan et al. [86] extracted eight health features from the obtained IC curve of a LIB, as shown in Figure 2.35.

Moreover, the extracted eight health features are ranked based on their importance using two ranking methods: (1) Pearson and (2) Spearman techniques. Lastly, the most critical health features are fed into a GPR model to estimate the capacity of the LIBs.

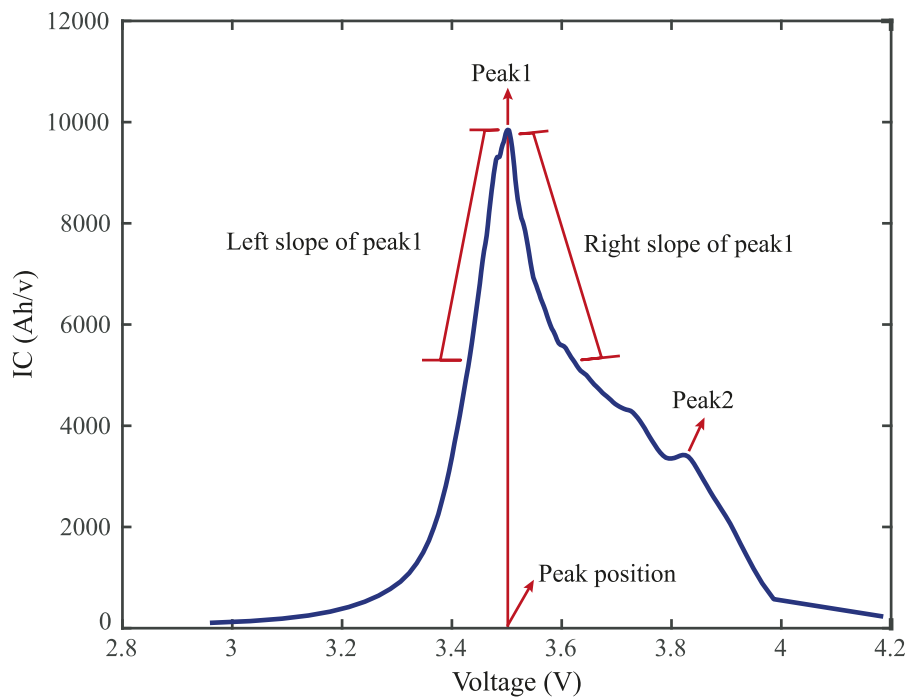


Figure 2.34 The extracted health features are based on the IC curve in [218].

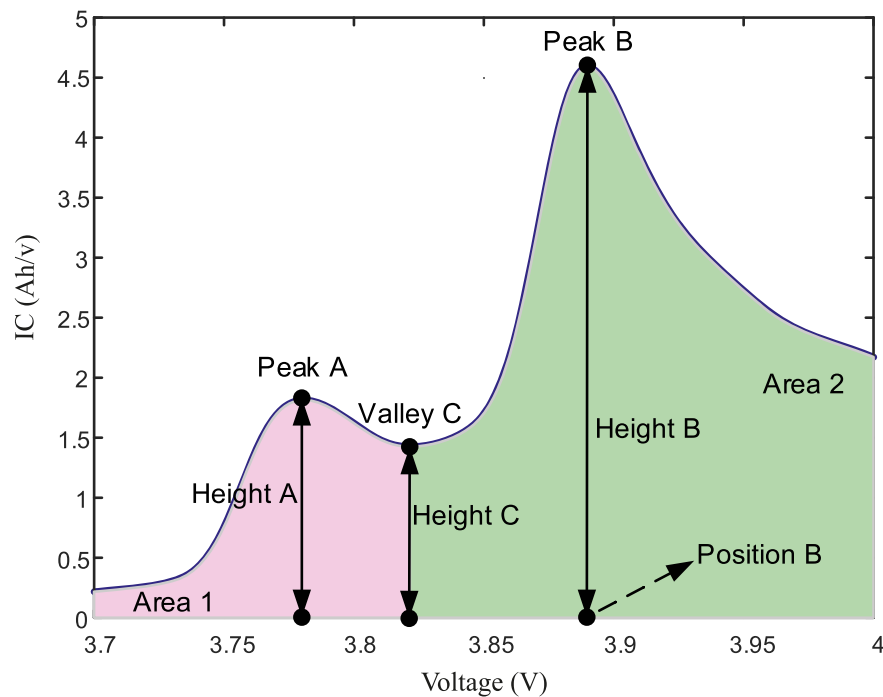
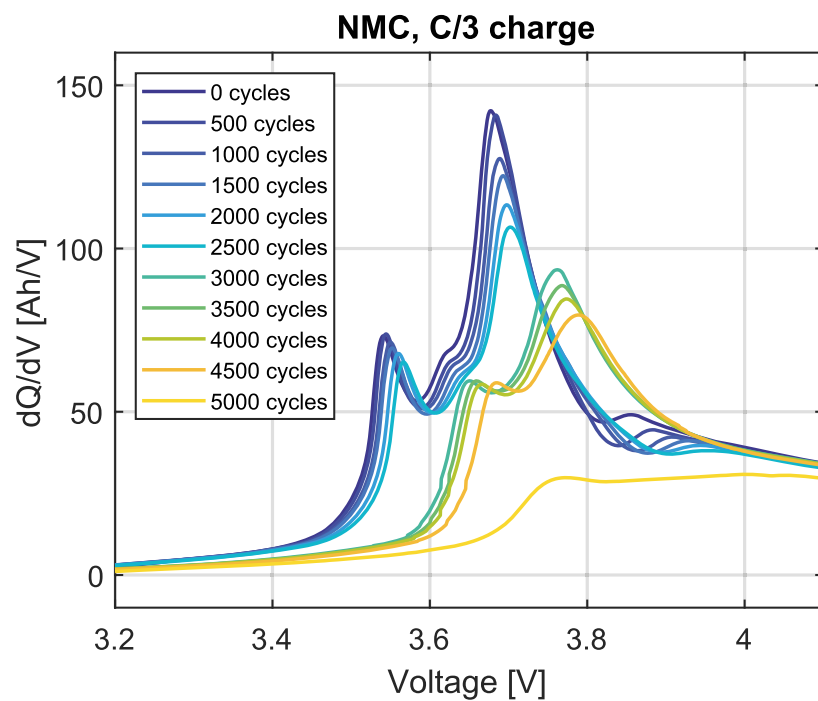
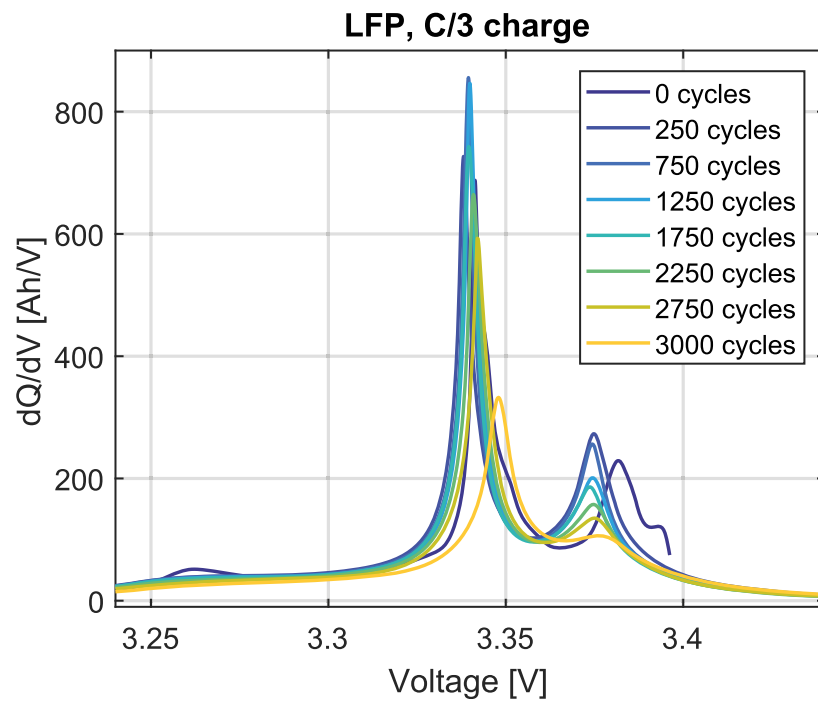
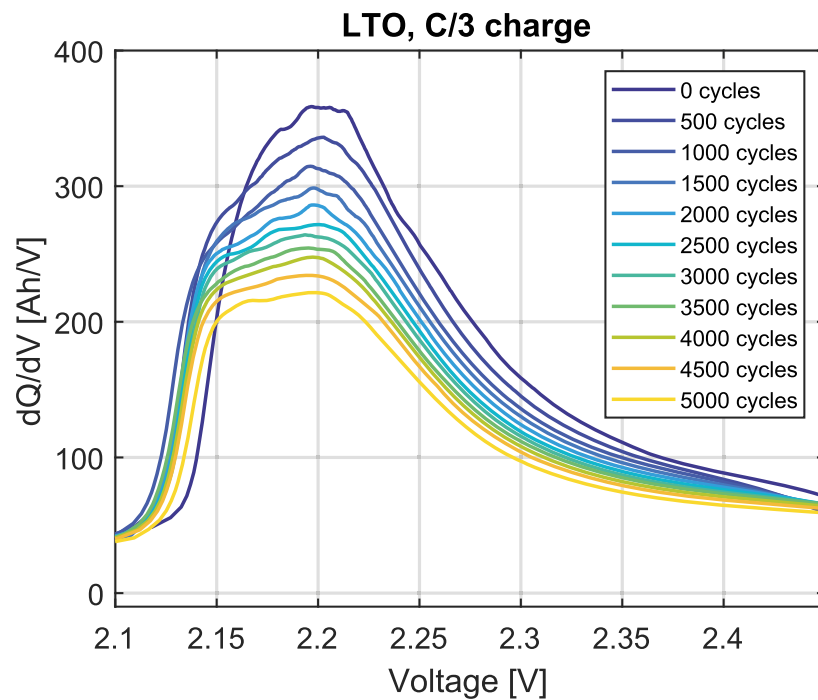


Figure 2.35 The extracted health features based on the IC curve in [86].

It is worth paying attention to the shape of the obtained IC curves of the LIB; the IC curves in Figure 2.34 and Figure 2.35 clearly show that both curves are different. This difference between the above IC curves is due to the materials used to formulate the cathode in the battery. In particular, the result in Figure 2.34 is for the NMC cathode, while the IC curve in Figure 2.35 is for the LCO cathode. Therefore, it is critically important to investigate the impact of the battery's materials on the extracted health features from the obtained IC curves. Thus, the authors in [215] have investigated the capability of the ICA for the capacity estimation of different types of LIBs. In particular, lithium nickel manganese cobalt oxide (NMC), lithium iron phosphate (LFP), and lithium titanate (LTO) batteries have been used in this study. The calculated IC curves are shown in Figure 2.36.





(c) LTO.

Figure 2.36 The calculated IC curves of a) LFP, b) NMC, and c) LTO LIBs [215].

As shown in Figure 2.36, the IC curve of the LFP LIB comprises two unique peaks; the first peak is located at about 3.34 V. The second peak is found at around 3.38 V. There have been reports in the scientific literature of up to five peaks occurring when the LFP cell is charged at a low C-rate [220, 221]. Moreover, there are two distinct peaks in the NMC battery's IC curve (Figure 2.36 (b)): the main peak at 3.7 V and a minor side peak at 3.55 V. As the battery ages; there is a distinct reduction in both peaks and a trend towards higher voltages. Lastly, there is only one wide peak in the IC curve of the LTO LIB, which can be shown in Figure 2.36 (c). This peak covers practically the full voltage range that occurs during charging. The maximum voltage of the peak is approximately 2.2 volts, which is equivalent to around 20% SOC. Even though earlier investigations on capacity assessment using the ICA approach have demonstrated its efficiency, there are still several significant problems to be faced, including the following:

- The computational complexity and efficiency are both necessary components for vehicular online state estimation, particularly for generalising the ICA approach to estimate battery capacity from a single cell to multi-dimension levels. Moreover,

some existing IC curve smoothing methods may be time-consuming and/or require a large variety of charging data to compute the IC value in a single pass. Because of the complications, using this technique to estimate the capacity of the LIB online is difficult.

- The charging state affects the IC curves significantly; however, prior ICA studies have mostly focused on standard charging (charging from 0% SOC with 0.5C current at 25 °C). Because batteries in vehicles are rarely discharged to zero (0% SOC), they are often charged from a SOC that is not zero. Since the polarisation process of charging a battery from a non-zero SOC is distinct from charging a battery from a 0% SOC, the resulting IC curves will be deformed. In addition, battery temperature might affect internal resistance during charging, potentially resulting in a different IC curve. Consequently, the flexibility of the ICA method will be tested by the non-standard charging methods.

2.7.3 Feature Extraction based on the EIS curve.

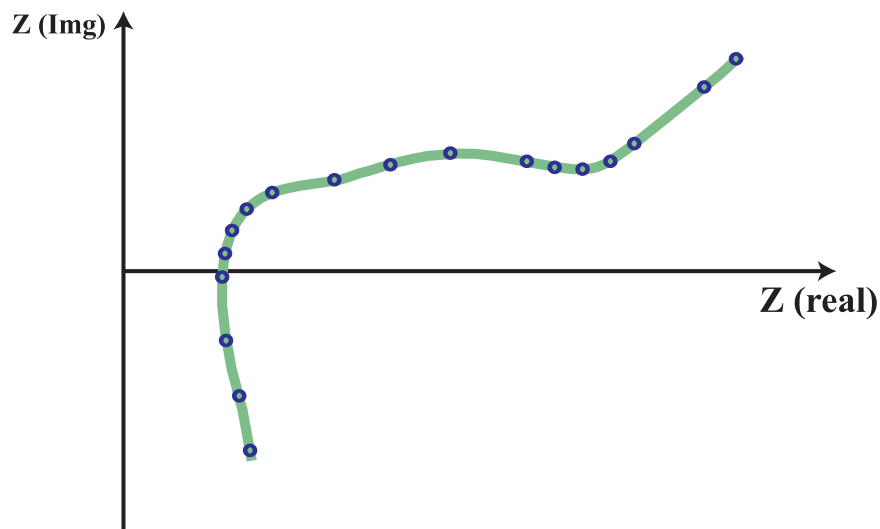
EIS is an essential tool for obtaining crucial information about LIBs, and it plays a vital role in battery management technologies [61]. Currently, impedance is commonly used for estimating battery SOC [222], temperature [223], RUL [224, 225], and degradation mode identification [226, 227]. Researchers have attempted to use EIS to estimate the health of LIBs by extracting features from the data inspired by traditional data-driven techniques that use battery charging features. Existing literature categorises three types of feature extraction methods based on EIS data, as shown in Figure 2.37:

- 1- Feature extracted from the whole band of the EIS data.
- 2- Feature extracted from the fitted ECM (this section is covered in section 2.5.1.2).
- 3- Feature extracted from a fixed frequency band of the EIS data.

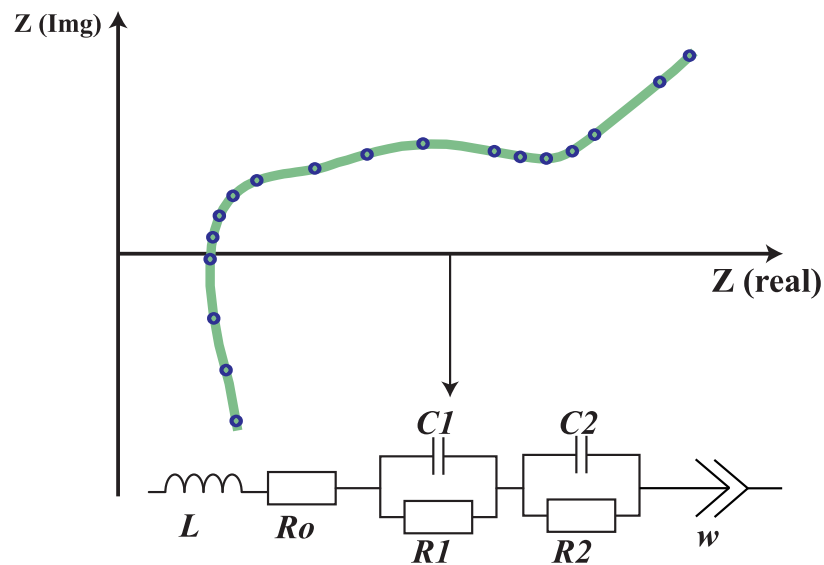
For the extracted feature from the complete EIS data, Schuster et al. [228] relied on data from a broad EIS, which included information about SEI film impedance, double-layer capacitors, and charge transfer impedance as health features. The linear regression method models the functional relationship between capacity fade and the extracted features. The

frequency range corresponding to the ohmic impedance or charge transfer impedance spans from tens to thousands of hertz, which challenges the charger's current reaction time and data sampling frequency. Similarly, Zhang et al. [229] trained their model for estimating and predicting the capacity and the RUL of the LIB with the help of a machine learning algorithm (GPR model) on complete unprocessed EIS data. According to the automatic relevance determination made by the EIS, there were two characteristic frequencies. The first thing to look at is the frequency at which the charge transfer impedance has its characteristic resonance. The other frequency is when the intermediate frequency changes to the low frequency. This frequency corresponds to the transition in the Nyquist diagram from a semicircle to a line.

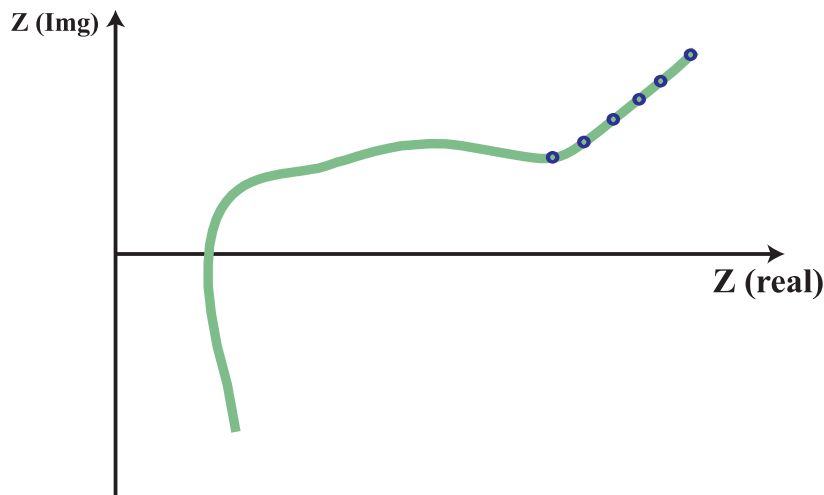
Moreover, the authors in [230] estimated the capacity of the LIBs by using seven extracted features from the full range of the EIS data. The extracted features are then fed into the GPR model to learn the correlation between the capacity loss and the evolution of the extracted features.



(a) Feature extracted from the whole band of EIS.



(b) Feature extracted from the ECM.



(c) Feature extracted from a fixed-frequency band of EIS

Figure 2.37 Three types of feature extraction methods based on EIS data.

Xu et al. [231] developed a hybrid approach combining the extracted features from EIS data and IC curves to estimate the capacity of the LIBs. However, the feature identification process from the entire band of the EIS data is consuming too much computing time. Therefore, extracting the feature from the ECM and fixed-frequency range of EIS has been proposed in the literature. For example, the authors in [232] estimated the capacity of retired LIBs based on EIS data's low and medium-frequency bands. Specifically, the authors constructed a

simplified ECM of LIB based on low and medium-frequency regions of EIS data. The parameters of the ECM are used as a feature to track the degradation inside the LIB. The obtained characteristics are then used to train a gated recurrent neural network (GRU) for the capacity estimation of LIB. Similarly, the authors in [233, 234] estimated the capacity of the LIB by developing ECM based on the low and mid frequency range of the EIS data.

Su et al. [235] utilised the low-frequency region of the EIS data combined with the GPR model to estimate the capacity of LIB. In particular, the authors extracted six features from the low-frequency part of EIS data and then fed these features into a GPR model for estimating the capacity of the LIB. On the other hand, Zhou et al. [236] developed a recurrent GPR model for the capacity estimation of LIBs based on the extracted features from the high and medium frequency range of EIS data. Jiang et al. [237] conducted a comparative study of different components extracted from EIS data for the capacity of LIBs. The finding of this research highlighted that using the extracted features from a fixed-frequency region in the EIS data outperforms the extracted features from the entire band of EIS data in the capacity estimation of LIBs.

To sum up, the EIS method is helpful for the capacity estimation of LIBs. However, the current approach to obtain the EIS is to apply a square wave or multi-sine synthesis signal to the LIB and then use a fast Fourier transform (FFT) to calculate the impedance [238, 239]. But because of the battery's nonlinear properties, square or multi-sine waveforms' amplitudes are not comparable to the respective sine waves of their separate frequencies. In addition, a designed excitation source is needed, and a high sampling frequency is essential for determining the entire EIS. Due to these technical limitations, EIS is rarely used in an online capacity estimation.

Jonghoon Kim [240] proposed an advanced signal processing method known as discrete wavelet transform (DWT) with multiresolution analysis (MRA) to analyse the non-linearity and non-stationarity behaviour of the battery terminal voltage under a dynamic load profile. This was done to improve the quality of the extracted diagnostic characteristics under a variable current profile. Additional helpful diagnostic signals were retrieved for capacity evaluation in both the time and frequency domains. Using a 3 Daubechies wavelet (DB3) as a mother wavelet

and scale five as the ideal decomposition level, the LIB's charge/discharge terminal voltage is divided into five levels. After that, the features were taken from the approximation component (A_5) and the detail component (D_5), respectively. The variation in voltage is chosen as the primary characteristic to analyse to estimate the capacity of the LIB.

Similarly, the authors in [241] proposed a fast wavelet transform (FDWT) to extract the dynamic features of voltage and current signals combined with an xD-Markov machine learning model. In specific, the battery voltage and current time series signals are utilised. The time series of the data are normalised first to produce non-stationary sequences. After that, the FDWT technique is applied to get the dynamic information from the time series that has been normalised. The authors employed discharge voltage and current signals due to the typical variation in EV operating conditions between idle and driving states. They found that driving conditions, which include acceleration and deceleration, offer the most dynamic information and significantly demonstrate the voltage response characteristics of the LIB. These measured signals were decomposed into five levels using a 3 Daubechies wavelet (DB3) as a mother wavelet. Afterwards, the xD-Markov machine model was established to capture the variation of the decomposed signals and estimate the capacity of the LIBs.

Jun et al. [242] proposed DWT for relative capacity estimation of LIB using the 4 Daubechies wavelet (DB4) as a mother wavelet. Similarly, the authors in this study utilised the discharge voltage signal for the feature extraction step by using DWT to decompose the voltage into five levels. The standard deviation value of the approximation and detail components is considered a promising feature for estimating the capacity of the LIB. The estimation accuracy of the proposed method was less than 2.5%. Hoshi et al. [243] calculated the impedance spectrum of the LIB from the measured voltage and current signals by converting the measured signals from the time domain into the time-frequency domain using DWT. Specifically, a Morlet wavelet was selected as a mother wavelet to transform the signals from the time domain to the time-frequency domain. Then, the wavelet coefficients of voltage and current in the time-frequency domain were used to calculate the impedance spectrum of the LIB. The obtained impedance spectrum result using DWT was validated by comparing it to the measured impedance spectrum using a frequency response analyser (FRA). The comparison results show that the error between the calculated impedance from DWT and the measured impedance from

FRA was less than 5%, which indicates the proposed approach's effectiveness in finding out the LIB's impedance from the measured signals.

The authors in [244] proposed a unified framework for the capacity prediction of LIB using an adaptive representation method known as empirical mode decomposition (EMD). The function of EMD is to decompose the historical capacity data into intrinsic mode functions to extract the degradation trend of the LIB. EMD decomposes the signal into the oscillatory modes by interpolating the local maxima and minima, taking the mean, extracting the low-frequency modes, subtracting from original data, repeat the process until all principal oscillatory modes (to high frequency) present in the data have been obtained. Although EMD shows promising results for non-stationary signal analysis, EMD depends on methods for finding extrema, interpolation and stopping criteria for recursive sifting and no mathematical theoretical framework. Moreover, The capacity regeneration phenomenon is caused by chemical reactions occurring within the LIBs during the resting process, resulting in a modest recovery of capacity [245]. Therefore, many signal processing techniques have been applied to analyse the regenerated capacity and help to improve the RUL prediction accuracy. For instance, the authors in [246] proposed wavelet decomposition transform (WDT) to decompose the measured capacity into multi-scale signals with high and low frequencies to extract the capacity's global and local degradation trend. After then, a neural network was developed to predict the future capacity degradation of the LIB using the extracted trend from the WDT. Moreover, the EMD method combined with the LSTM model is also proposed to improve the future capacity degradation prediction accuracy by minimising the influence of the regenerated capacity by decomposing the capacity data into a series of IMFs with different frequencies [245].

2.8 Summary

This chapter has comprehensively reviewed the state-of-the-art for the capacity estimation and prediction of LIBs. The current capacity estimation and prediction methods are mainly divided into three methods:

Experimental methods (Section 2.5): These methods estimated the capacity of the LIB by finding the quantity of charge entering and exiting the battery through the use of Coulomb counting, tracking the change in the OCV over the battery's lifespan, or measuring the LIB's impedance spectrum with the EIS technique. Although these methods offer high accuracy, their implementation for online usage is challenging due to the extensive testing time needed and the added setup required, as in the case of the EIS method.

Model-based methods (Section 2.6): These methods estimated LIB capacity by modelling its operation. These models (ECM and EM) estimate LIB capacity using filters/observers. However, estimating LIB capacity with these models is difficult. ECMs cannot provide LIB physical properties, which is a major limitation. EMs are unsuitable for online capacity estimation of LIB using embedded microcontrollers because nonlinear partial differential equations require hours for spatial discretisation using numerical methods like the finite element method and finite difference method. Computational complexity rises.

Data-driven methods (Section 2.7): These approaches assessed LIB capacity by learning the association between extracted characteristics from observed signals and capacity. The data-driven approaches fall into three categories: charge curve-based features, differential curve-based features, and EIS curve-based features. Charge curves must be consistent and uniform for charging curve-based approaches (Section 2.7.1). In (Section 2.7.2), it was revealed that the charging state considerably impacts the differential curves (particularly IC curves), while earlier research has mostly focused on standard charging (charging from 0% SOC with 0.5C current at 25°C). Thus, non-standard charging techniques will challenge differential-based method adaptability.

The EIS-based technique found that the current method for getting the EIS comprises applying a square wave or multi-sine synthesis signal to the LIB and using FFT to calculate impedance. Due to the battery's nonlinearity, square or multi-sine waveform amplitudes cannot be compared to sine waves at their separate frequencies. For EIS capture, a purpose-built excitation source and high sampling rate are needed. EIS rarely estimates real-time capacity due to technical constraints.

Considering the limitations of existing methods for capacity estimation and prediction of LIBs, this thesis aims to establish a novel approach for estimating and forecasting future capacity degradation in LIBs based on time-frequency analysis and data-driven algorithms. Time-frequency analysis is a powerful technique for examining and extracting concealed information from nonlinear, non-stationary signals in both time and frequency domains. Meanwhile, employing model-free, data-driven algorithms for estimating and predicting LIB capacity has demonstrated significant improvements in accuracy while eliminating the need for developing a model that increases the computational burden on the BMS. Therefore, this thesis leverages the benefits of time-frequency analysis to enhance the quality of extracted features from measured signals and the advantages of data-driven techniques.

Chapter 3 Time-Frequency Image Analysis and Transfer Learning CNN for Capacity Prediction of Lithium-ion Batteries

3.1 Brief Introduction

Chapter two shows that most of the present data-driven techniques for capacity estimation of LIBs rely mainly on the quality of the features extracted from measured signals under strict operating conditions. To improve flexibility and accuracy, this chapter introduces a new paradigm based on a multi-domain features Time–Frequency–Image (TFI) analysis and Transfer Deep Learning algorithm to extract diagnostic characteristics on the degradation inside the LIB. Continuous Wavelet Transform (CWT) is used to transfer the one-dimensional (1D) terminal voltage signals of the LIB into two-dimensional (2D) time-frequency images (i.e., wavelet energy concentration). The generated TFIs are fed into the 2D deep learning algorithms to extract the features from the battery voltage images. The extracted features are then used to predict the capacity of the LIB. Experimental data on LIB cells from the experimental datasets published by the Prognostics Center of Excellence (PCoE) NASA validated the proposed technique (Section 3.2.1). The results show that the TFI analysis clearly visualised the degradation process of the battery due to its capability to extract different information on electrochemical features from the non-stationary and non-linear nature of the battery signal in both the time and frequency domains. AlexNet and VGG-16 transfer deep learning neural networks combined with stochastic gradient descent with momentum (SGDM) and adaptive data momentum (ADAM) optimisation algorithms are examined to classify the obtained TFIs at different capacity values. Figure 3.1 presents the graphical abstract for the proposed capacity estimation method.

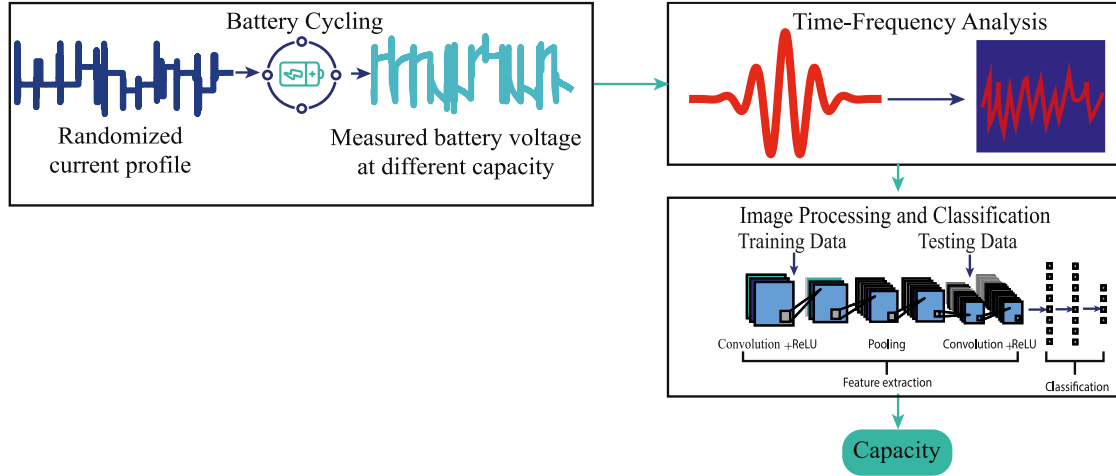


Figure 3.1 Graphical abstract of the proposed TFI method.

3.2 The Proposed Capacity Imaging Analysis Scheme

Figure 3.2 shows the block diagram of the proposed TFI paradigm. Here, the terminal voltage of the cycled battery using randomised current profile data has been utilised to predicate the battery's capacity. Initially, the terminal voltage of the battery is measured at different capacities. Then, a CWT algorithm transforms the measured voltage from 1-D raw data to a 2-D time–frequency image (TFI). The raw data of the measured voltage for the LIB at different capacities contains only the time–domain information, but the converted 2-D TFI features of the raw data clearly represent the time and frequency domain information at once. Finally, the generated TFIs for different battery capacities are fed into a deep-learning convolutional neural network for feature extraction and image classification. The following subsections explain the capacity prediction steps in detail.

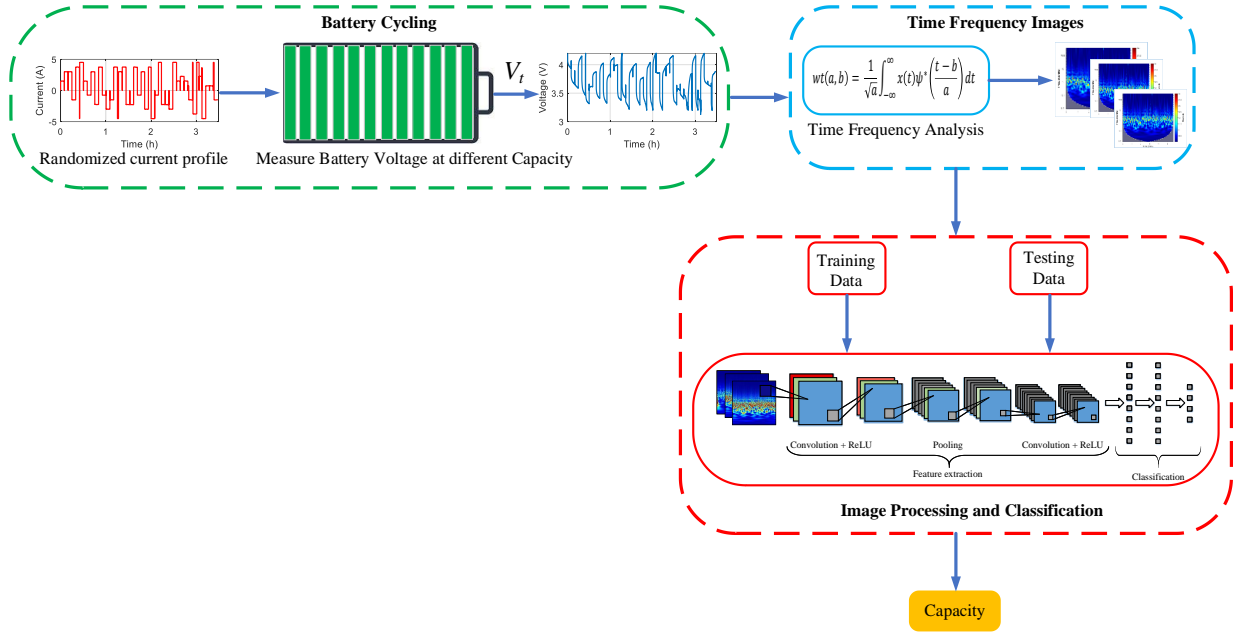


Figure 3.2 General flow chart of the proposed method for TFI capacity estimation.

3.2.1 Randomised Battery Dataset

The practical operating environment of a real-world EV battery includes a dynamic and partial driving pattern. Most of the literature utilises a battery dataset with limited assumptions; for example, the battery is cycled using only a constant current profile and specific voltage limit. Nevertheless, these assumptions do not cover the real operating situation of EV batteries. This study adopted a randomised battery usage dataset from NASA Ames Prognostics Center of Excellence [247] to ascertain the impact of actual, dynamic EV driving cycles. This dataset contains the ageing results of four LIBs named RW9, RW10, RW11, and RW12, acquired at room temperature. The general properties of the battery are summarised in Table 3.1. These four LIBs were cycled using two cycling protocols known as random walk cycling mode and reference charge and discharge cycling mode. The cycle process is shown in Figure 3.3.

Table 3.1 The general characteristics of the tested cells.

Battery properties	18650 LIBs
Manufacture	LG Chem
Chemistry	18650 lithium cobalt oxide vs graphite
Nominal capacity	2.10 Ah
Capacity range	2.10 Ah \rightarrow 0.80 Ah
Voltage range	4.2 – 3.2 V

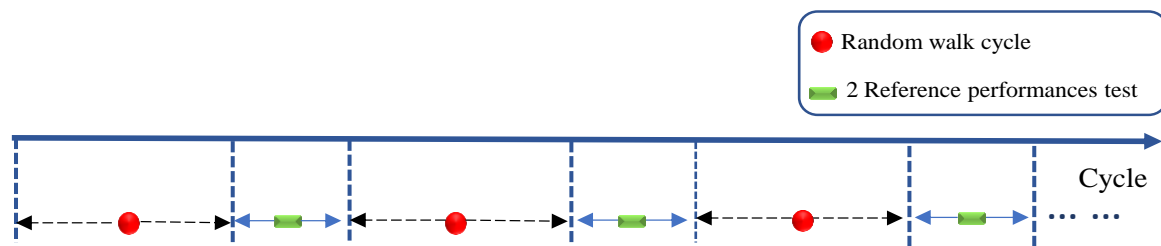


Figure 3.3 The cycle processes.

3.2.1.1 Random walk cycling mode.

A sequence of currents set varying between (-4.5 A, -3.75 A, -3 A, -2.25 A, -1.5 A, -0.75 A, 0.75 A, 1.5 A, 2.25 A, 3 A, 3.75 A, 4.5 A) is used for charging and discharging, and the four LIBs were continuously cycled. Hence, negative currents are related to the charging operation, while positive currents denote the discharge operation of the batteries. This charging and discharging protocol mode is known as Random Walk (RW) operation mode. The aforementioned current sequence is randomly applied to a LIB for five minutes, which is identified as a step in the dataset. It is essential to mention that a single RW cycle consists of 1500 RW steps and 1500 rests; each RW profile consists of many RW cycles. After every RW profile, the battery undergoes several reference charging and discharging tests to measure capacity and calculate its SOH value. Figures 3.4 and 3.5 show the measured voltage, current, and temperature of the first and last 100 RW charging and discharging steps of battery RW9.

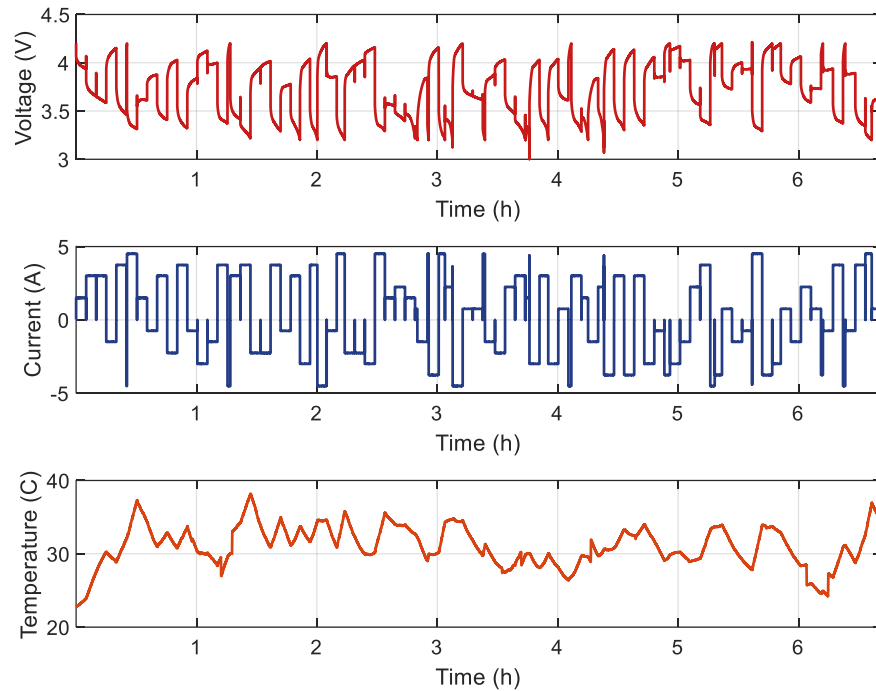


Figure 3.4 Voltage, current, and temperature of the first 100 steps measured for battery RW9.

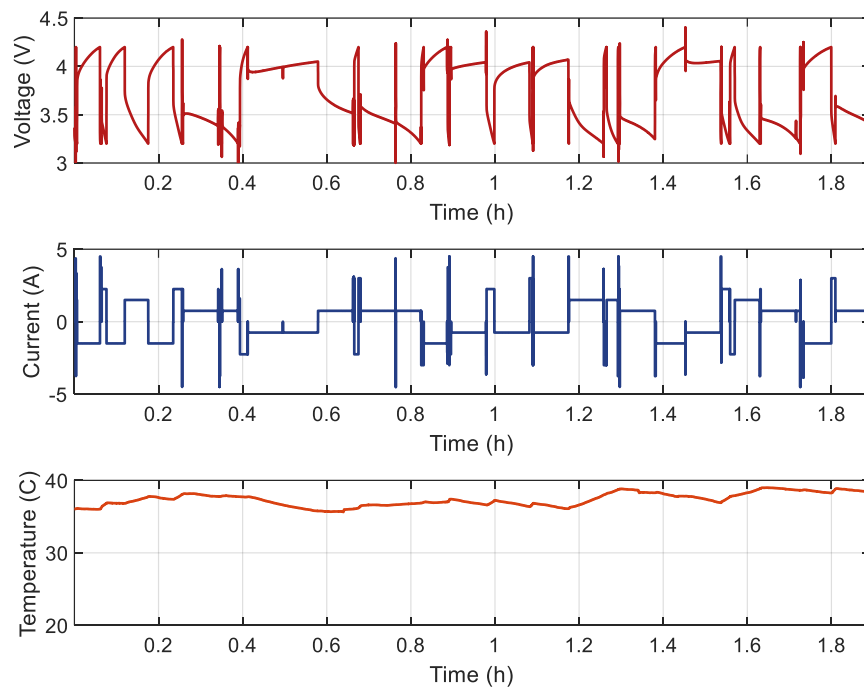


Figure 3.5 Voltage, current, and temperature of the last 100 steps measured for battery RW9.

3.2.1.2 Reference charge and discharge cycle mode.

After the start of each RW cycle, a sequence of reference charging and discharge current profiles is implemented to set a standard benchmark for the battery's SOH. Initially, by applying a 2 A constant current profile, the LIB is charged to its maximum voltage and then a 4.2 V constant voltage is sustained until its current falls to 0.01 A, then it rested for 20 minutes. Afterwards, 2 A discharge constant current profile is applied to the LIB until its voltage reduces to its minimum voltage of 3.2 V. This procedure is known as reference charging and discharging cycle mode [248]. To measure the LIB's capacity and calculate its SoH value after every RW cycle, the current cell capacity ($Q_{current}$) is calculated using the Coulomb counting method as follows:

$$Q_{current}(t) = \int_0^t I_d(t) dt \quad (3.1)$$

Where I_d is the total discharge current of the battery cell. Once the battery capacity is calculated, the SOH of the battery can be calculated, as shown in (3.2).

$$SOH = \frac{Q_{current}}{Q_{Fresh}} \cdot 100\% \quad (3.2)$$

Where $Q_{current}$ is the measured capacity after every RW cycle and Q_{Fresh} is the measured capacity of the battery at the beginning of its life. The capacities of the measured cells of the four batteries are shown in Figure 3.6.

As illustrated in Figure 3.6, the capacity fade is a non-linear and non-homogeneous process since each cell degrades in different ways, even under the same test conditions. Therefore, the main aim of this study is to investigate if the time–frequency image analysis method can capture the non-stationary behaviour of the battery during cycling.

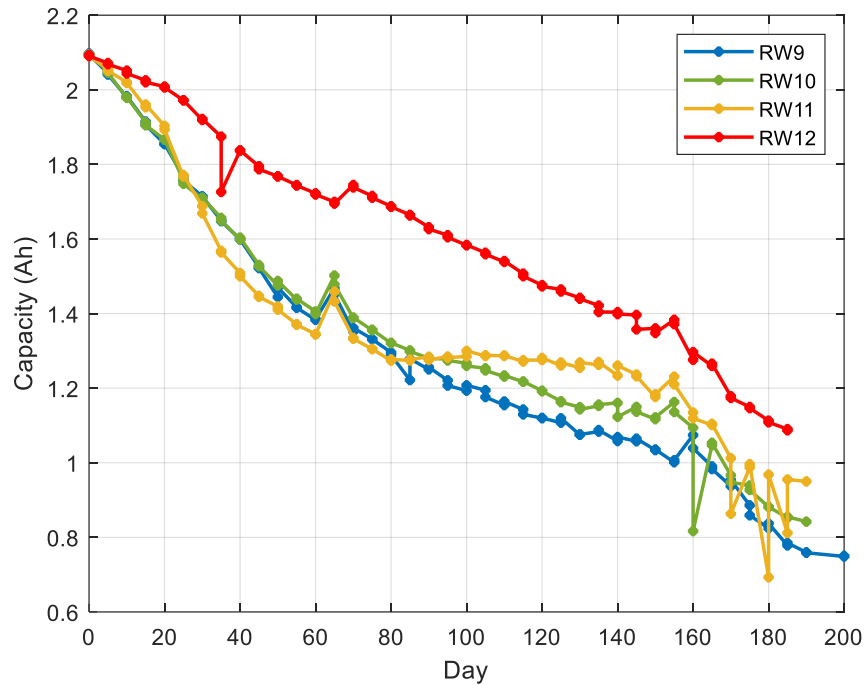


Figure 3.6 Capacities of the measured cells for four batteries, RW9, RW10, RW11, and RW12.

3.2.2 Time-Frequency Image (TFI) Analysis

3.2.2.1 Why Do We Need Time-Frequency Analysis in Lithium-ion Batteries?

The main aim of this research was the analysis and classification of the measured voltage of LIBs at different capacities using TFI analysis. As Chapter Two (Section 2.7) states, most studies have used traditional time or frequency domain methods to analyse the LIB's measured signals and extract diagnostic characteristics to describe the degradation inside the battery cell. Like most real-life signals, the measured LIB terminal voltage can exhibit non-stationary characteristics [241, 249]. Thus, analysing the LIB's measured voltage using traditional time or frequency domains is insufficient to extract comprehensive features about the degradation process inside the battery [250]. Nevertheless, time–frequency approaches can extract several domain features in order to assess the measured signal for the time and frequency domains, precisely extracting better features from the measured signal [251]. Time-frequency analysis is

used to study signals that vary in both time and frequency. This is important because many signals in nature and engineering, such as speech [252], music [253], and LIBs [254] signals, are not purely periodic and have time-varying frequency content. Time-frequency analysis allows us to study these signals in more detail by representing the signal's frequency content at each point in time. This can be useful for signal classification, compression, and denoising tasks. Therefore, the main goal of a time–frequency signal processing analysis is to extract useful information features from the measured battery terminal voltage by converting the time series signal into the time–frequency domain [255]. There are several methods for performing time-frequency analysis, including the Short-Time Fourier Transform (STFT) [256], the Wigner-Ville Distribution (WVD) [257], and the Continuous Wavelet Transform (CWT) [258]. These methods are used in various fields, such as signal processing, control systems, and fault diagnosis systems [259, 260].

3.2.2.2 Theoretical Background of Time-Frequency Analysis

Fourier spectrum analysis was historically one of the most popular methods for investigating global amplitude-frequency distributions due to its power and ease of use. However, as can be seen from the definition of Fourier analysis given in equation (3.1), where $x(t)$ is the input signal and $X(\omega)$ is the Fourier transformed signal, the Fourier analysis provides a global representation of the signal, resulting in a complete loss of time information, and is thus unsuitable for analysis of nonstationary signals. Moreover, the Fourier transform assumes that the amplitude and phase of the input signal $x(t)$ are time-invariant [261]. However, this assumption is invalid for many real-world signals [262].

$$X(\omega) = \int_{-\infty}^{\infty} x(t)e^{-i\omega t} dt \quad (3.1)$$

Studying nonstationary signals requires a class of analysis known as time-frequency analysis; that is, the frequency content of the measured signal is determined at each point in time. In order to analyse the frequency components over time, the STFT was developed by Gabor [263]. The STFT is a technique used to analyse signals in the frequency domain by

dividing the signal into small overlapping segments and then applying the Fourier transform to each segment as expressed in (3.2):

$$X(\tau, \omega) = \int_{-\infty}^{\infty} \omega(t - \tau)x(t)e^{-i\omega t} dt \quad (3.2)$$

Where $X(\tau, \omega)$ represents the coefficients of the STFT, $\omega(t - \tau)$ is the window length, and $x(t)$ is the input signal in the time domain. The result is a set of spectrograms, which are two-dimensional representations of the signal's frequency content over time. This technique allows for analysing non-stationary signals, which have time-varying frequency content. It can reveal information about the frequency content of a signal at specific points in time. The main parameters that can be modified when using STFT are the window size $\omega(t)$, which determines the length of the segments and the overlap between segments, which controls the trade-off between frequency and time resolution. Since STFT applies the traditional Fourier spectrum analysis to each window, the data must be linear and stationary inside each window (piece-wise stationarity) for the analysis to be valid [264].

This assumption of piece-wise stationarity may not always be valid for nonstationary data in the real world. Even when it can be applied, it is difficult to ensure that the window length matches with the stationary scales, as evidenced by the constant window length employed in STFT. In addition, the technique has contradictory window size requirements, resulting in a trade-off between time and frequency domain localisation [265].

To overcome the limitations of STFT, CWT analysis was introduced in [266]. The advantage of CWT is that the window length can be adjusted according to the temporal scales being observed and can thus be seen as an adjustable window Fourier transform analysis, as shown in Figure 3.7. It should be noted that the STFT has a constant time and frequency resolution for both low and high frequencies, as illustrated by Figure 3.7 (a), where the continuous wavelet transform can be seen as a variation of the STFT where the length of the window is varied as a function of frequency (Shown in Figure 3.7 (b)).

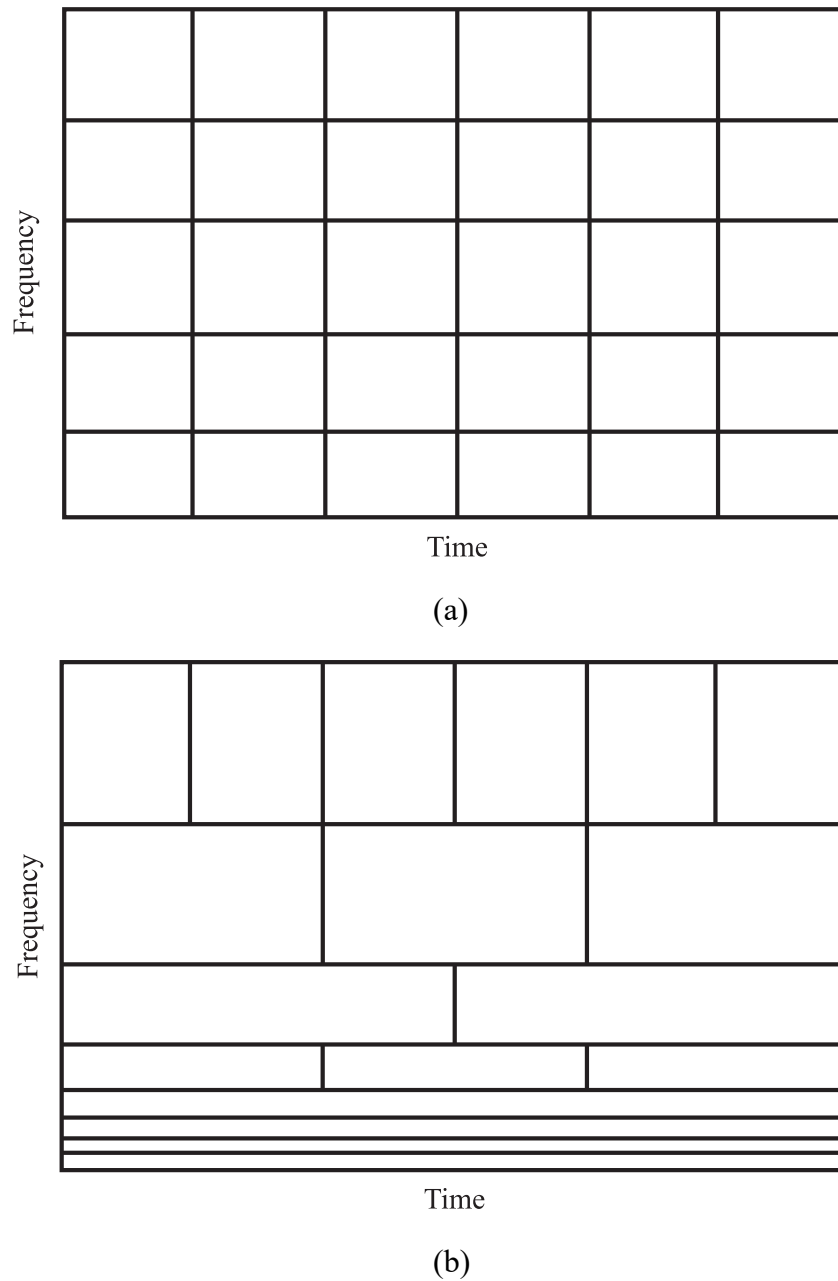
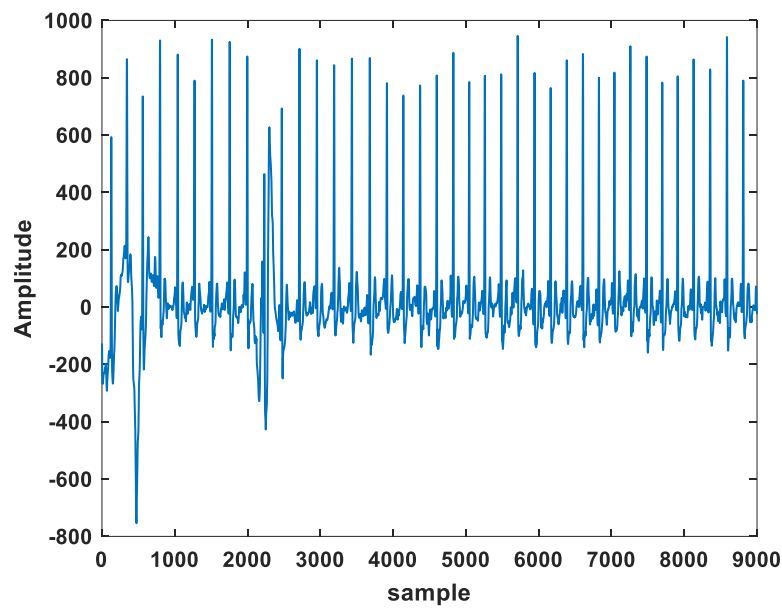


Figure 3.7 Window functions of (a) STFT and (b) CWT.

Accordingly, the CWT has high time resolution and low-frequency resolution at high frequencies, while at low frequencies, the time resolution is low, and the frequency resolution is increased. This is particularly useful for analysing transient oscillations, where localising the

oscillation along time is essential. However, unlike the STFT, which only uses sines and cosines as basic functions, CWT analysis adopts a board class of signals as its basis functions $\psi(t)$. Figure 3.8 demonstrates the spectrograms of STFT and CWT in analysing the time-domain signal in time-frequency domain. The CWT is particularly effective in analysing the time-domain signal, as shown in Figure 3.8 (b). The resolution of the resulting spectrogram reveals the variations in energy concentration within the signal and identifies the regions of significant change in time and frequency. Conversely, the STFT spectrogram does not clearly visualise the signal's energy concentration, primarily due to the specific window function employed in the STFT analysis.



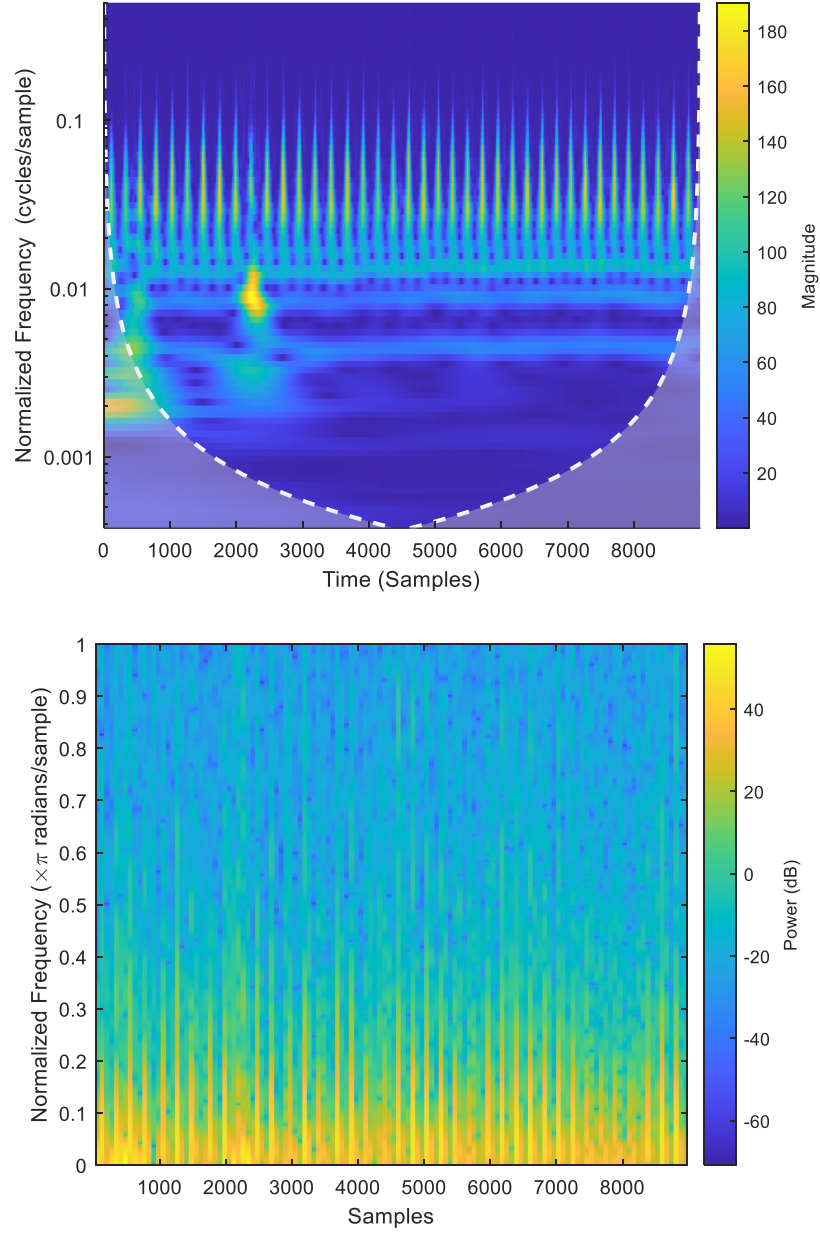


Figure 3.8 (a) Example of STFT and CWT in analysing signal in time-frequency domain. (a) The analysed signal, (b) the CWT spectrogram, and (c) the STFT spectrogram.

Mathematically, the CWT of the measured signal $x(t)$ can be expressed as shown in Eq (3.3).

$$\psi_{a,b}(t) = \frac{1}{\sqrt{a}} \psi\left(\frac{t-b}{a}\right) \quad (3.3)$$

Where, $\psi_{a,b}(t)$ is an analysis wavelet and called child wavelet, $a \in (0, +\infty)$ is the scale parameter of the wavelet transform, and $b \in (-\infty, +\infty)$ is the translation or shift parameter in time. The function $\psi(t)$ is known as the mother wavelet with finite length and fast depletion. Two limit conditions must be satisfied in the mother wavelet signal, which are $(\int_{-\infty}^{+\infty} \psi(t)dt = 0$ and $\int_{-\infty}^{+\infty} |\psi(t)|^2 dt = 1)$ [241]. For the given time series signal $x(t)$, the wavelet coefficients $wt(a, b)$ are obtained by the convolution integral of the mother wavelet $\psi(t)$ and the given signal $x(t)$, as presented in (3.4):

$$wt(a, b) = \frac{1}{\sqrt{a}} \int_{-\infty}^{\infty} x(t) \psi^* \left(\frac{t-b}{a} \right) dt \quad (3.4)$$

Where, ψ^* means the complex conjugate of function ψ . Throughout this procedure, the signal $x(t)$ is divided into a sequence of scaled and shifted wavelet coefficients, in which the wavelet set is the basis function. After this, the signal $x(t)$ was altered by CWT and sent to the 2D time–frequency domains.

CWT transforms the measured signal from the time domain to a TFI, whose energy concentrations visualise changes in frequency components over time as the battery degrades. The CWT works by projecting the measured voltage signal onto a set of wavelet coefficients $wt(a, b)$, which are generated by dilating and translating the mother wavelet function $\psi(t)$. This process provides a high-resolution analysis of both time and frequency domains. The wavelet function is compressed for high frequencies, resulting in better time resolution and less frequency resolution. On the other hand, the wavelet function is stretched for low frequencies, which offers higher frequency resolution and lower time resolution. This characteristic of CWT allows for better localisation of voltage features and improved resolution in the spectrogram. In the proposed prediction scheme, shown in Figure 3.2, a CWT was applied to the measured terminal voltage to transform it from a time-domain signal into a time–frequency domain scalogram image. This conversion process aimed to extract more helpful information about the degradation process inside the LIB in both time and frequency domains during a randomised charging/discharging current profile. Inspired by EIS analysis, the proposed technique aims to

capture the changes in the frequency components of LIB over its lifetime and develop a CNN model to capture these changes and linked them with the capacity degradation of the LIBs.

With this approach, the 1D time domain signals are transformed into TFI. Figure 3.9 shows an example schematic of the battery-measured voltage at three different capacities and the transformed time–frequency domain representation features for each capacity. It can be observed that there are clear discriminative variations of the CWT coefficients at each capacity in the TFI. Therefore, LIB degradation is well reflected by the multi-domain TFI features, which can thus be used as input for the DL-CNN to classify the battery’s capacity during the degradation.

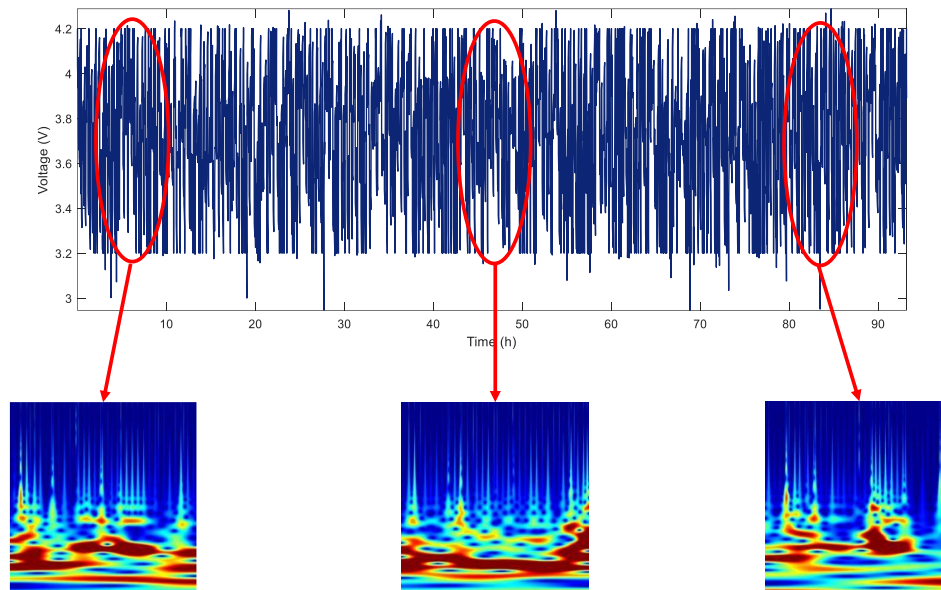


Figure 3.9 Measured LIB voltage and transformed TFI energy concentration spectrum information of the measured voltage at three different capacity values.

3.2.3 Time-Frequency Image Analysis and Classification Using Deep Learning Algorithm

The obtained TFIs from the measured battery voltage at different capacities are fed into deep learning predictive model to extract the relationship between the TFIs and the corresponding

capacity. This research adopts a data-driven method based on a transfer deep learning model to perform capacity classification in LIB.

Generally, DL-CNN builds from three types of layers, namely: (1) convolution layers, (2) pooling layers, and (3) fully connected layers [267]. The convolution and pooling layers are linked to form convolution blocks, and many of these blocks are stacked to create a deep architecture. The fully connected layer is generally used as the final layer in the classification or regression. The general architecture of DL-CNN is shown in Figure 3.10 [268].

The convolutional layer combines the input image from the initial layer with several filters, known as kernels, which are then fed to the activation function to create a feature map [269]. The output features map is the convolutional result of the input maps and can be calculated as in (3.5) [270].

$$x_j' = f \left(\sum_{i \in M_j} x_i^{l-1} * k_{ij}^l + b_j^l \right) \quad (3.5)$$

Here, $*$ is the convolutional operation, x_i is i th input map, k is a $F \times F$ convolutional filter, b_j is the additive bias, M_j is the feature map of the convolutional layer, and l is the l th layers in the neural network. Lastly, the obtained results from the convolutional layers are fed to the activation function. The commonly used activation function is the rectified linear unit (ReLU), defined as in (3.6) [270, 271].

$$ReLU(x) = \max(0, x) \quad (3.6)$$

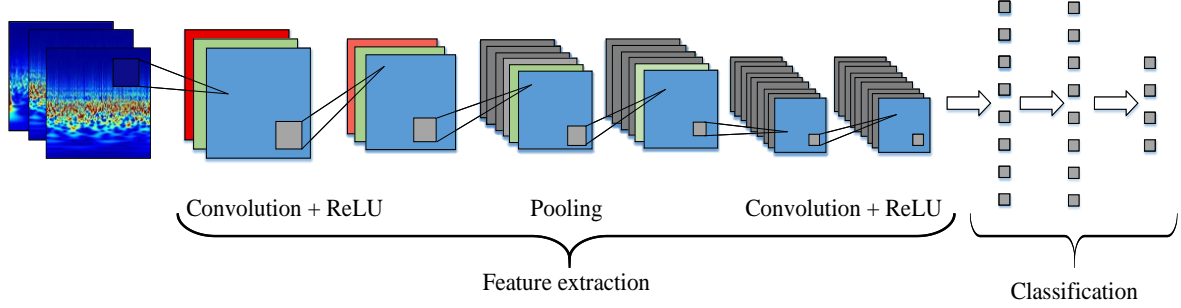


Figure 3.10 Deep learning convolutional neural network architecture.

In the Pooling layer, which follows the convolutional layer, low-resolution maps are created from the essential local information. The maximum value is derived from each region using the max-pooling layer, as shown in Figure 3.11 [270]. In other words, Pooling layer is a pooling operation that calculates the maximum value for patches of a feature map and uses it to create a down sampled (pooled) feature map. For example, considering a scenario wherein a 4×4 input matrix necessitates the application of max pooling (as shown in Figure 3.11). The process involves straightforwardly dividing the 4×4 matrix into distinct regions, and subsequently, generating a reduced output of size 2×2 . Each element within this output corresponds to the maximum value found within its respective shaded region in the input matrix.

In a fully connected layer, a 1-D vector is utilised to represent all the feature maps that are fully connected to the output layer. The output of the fully connected layer is described as given in (3.7).

$$O_i = f \left(\sum_{j=1}^d x_j^F w_{ij} + b_i \right) \quad (3.7)$$

Where O_i is the output layer, x_j^F is the j^{th} neuron in the fully connected layer, w_{ij} is the weight related to O_i and x_j^F , b_i is the bias corresponding to O_i , and f is the activation function [272].

In this study, two deep transfer learning algorithms (AlexNet and VGG-16 DL-CNN) were applied to classify the generated results from TFI. The classification results are presented in the Results and Discussion section.

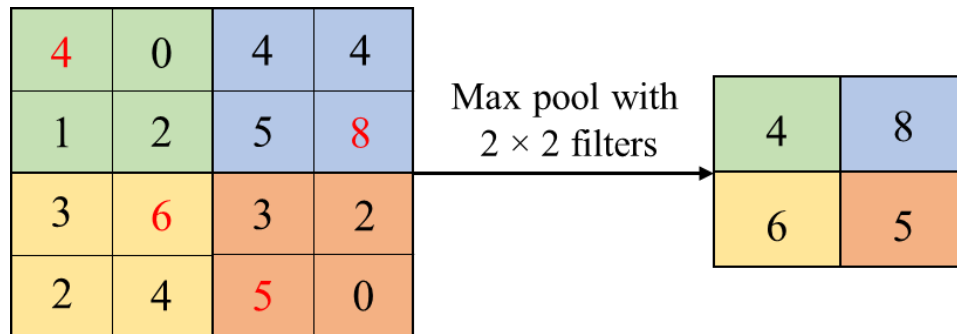


Figure 3.11 Max pooling layer. The maximum number in each region is selected.

3.3 Results and Discussions

The proposed scheme (see Figure 3.2) was implemented using the MATLAB environment. First, the results of TFI estimation using complex Morlet mother wavelet transform (CMMW) (from Time-Frequency Analysis toolbox in MALAB) will be presented in this section. Then the image analysis and classification results using deep learning algorithms will be demonstrated.

3.3.1 Time-Frequency Image Results

Figure 3.12(a) shows the measured voltage signal of the first cycle of RW9 at the beginning of the life of the LIB, indicating that no degradation had occurred at this point and the battery's capacity was full (here, $C = 2.1$ Ah). Figure 3.12(c) presents the measured voltage at the end of the LIB's life and shows that the battery degraded, and its capacity decreased to its minimum value ($C = 0.8$ Ah). From both results, it can be clearly observed that the battery had aged and that the time period of the measured voltage (31.07 h) at the end of life was less than that for

the first cycle of the battery (93.18 h). The battery has reached its threshold voltage level frequently due to increased LIB's internal resistance, which inherently reduces the LIB capacity.

To extract valuable features capable of describing the degradation phenomena inside the battery from the measured voltage, CMMW was applied using Equations (3.3) and (3.4) to the LIB terminal voltage, as illustrated in Figures 3.12(b) and 3.12(d). In the TFI, the energy concentration of the measured voltage of the LIB is shown at different capacities, with the horizontal and vertical axes representing time and frequency, respectively. The amplitude of the wavelet coefficients are represented in different colours on the TFI [269]; red indicates that the energy density level is high. In Figure 3.12(b), when the LIB is at the beginning of its life, the energy distribution is concentrated in the middle-frequency range of the image and varies from 1–2 Hz [273]. In contrast, Figure 3.12(d) shows the energy distributed in the image's middle and high-frequency bands (up to 100 Hz), meaning that the amplitude of the wavelet coefficients increased to cover the rapid changes between the upper and lower voltage range. Comparing the TFIs for the battery at the beginning and end of its life clearly shows a significant difference in the energy density distribution. Therefore, the capacity degradation of the battery is well reflected by the TFI information and multiple domain features can be calculated using TFI.

The proposed CMMW processed the datasets for the four test batteries. Figure 3.13 presents a sample of the results of the time–frequency images of the measured LIB terminal voltage at different capacities. They show the energy concentration distribution of the battery terminal voltage according to the level of degradation in the TFI. As shown in Figure 3.12, as the battery's capacity decreases, the energy distribution in the TFI changes, clearly illustrating the degradation process inside the battery cell. From the extracted wavelet coefficients using CMMW, the energy concentration for wavelet coefficients is calculated in the form of TFIs, which are then fed to the pre-trained CNN for image pattern recognition and classification.

To further validate the proposed technique, the experimental datasets of the LIBs: RW10, RW11 and RW12 at different capacity range from 2.1 Ah to 1.2 Ah have been tested. Table

3.2 demonstrates the proposed TFI method's effectiveness in predicting these cells' capacity. Ongoing research mainly attempts to apply the proposed technique to quantify which type of degradation mode most affects the battery's capacity.

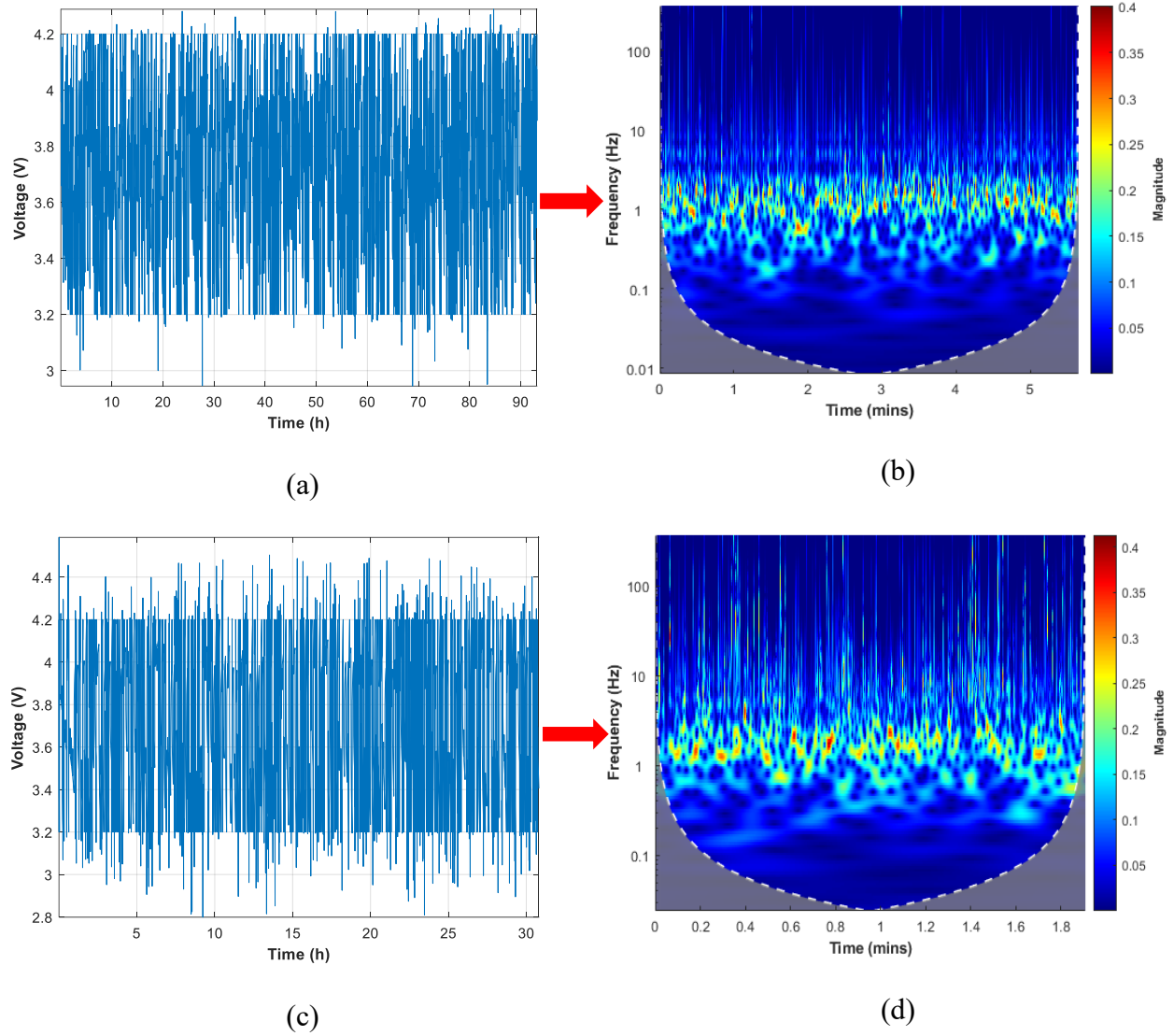


Figure 3.12 Time-domain measured voltage and plot of TFI energy concentration spectrum of battery cell (RW9): (a) measured voltage signal (beginning of life), (b) wavelet energy concentration spectrum (beginning of life), (c) measured voltage signal (end of life), and (d) wavelet energy concentration spectrum (end of life).

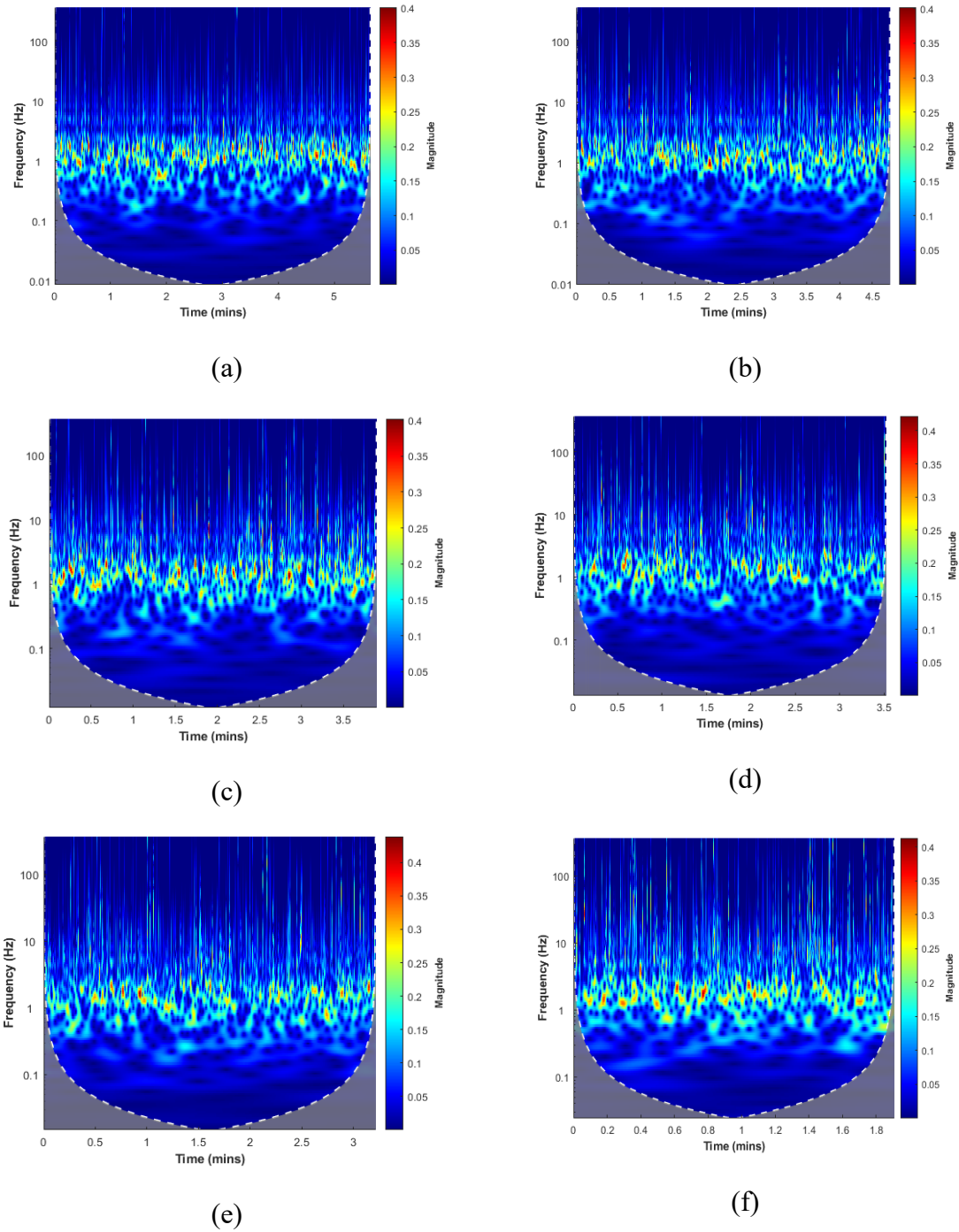
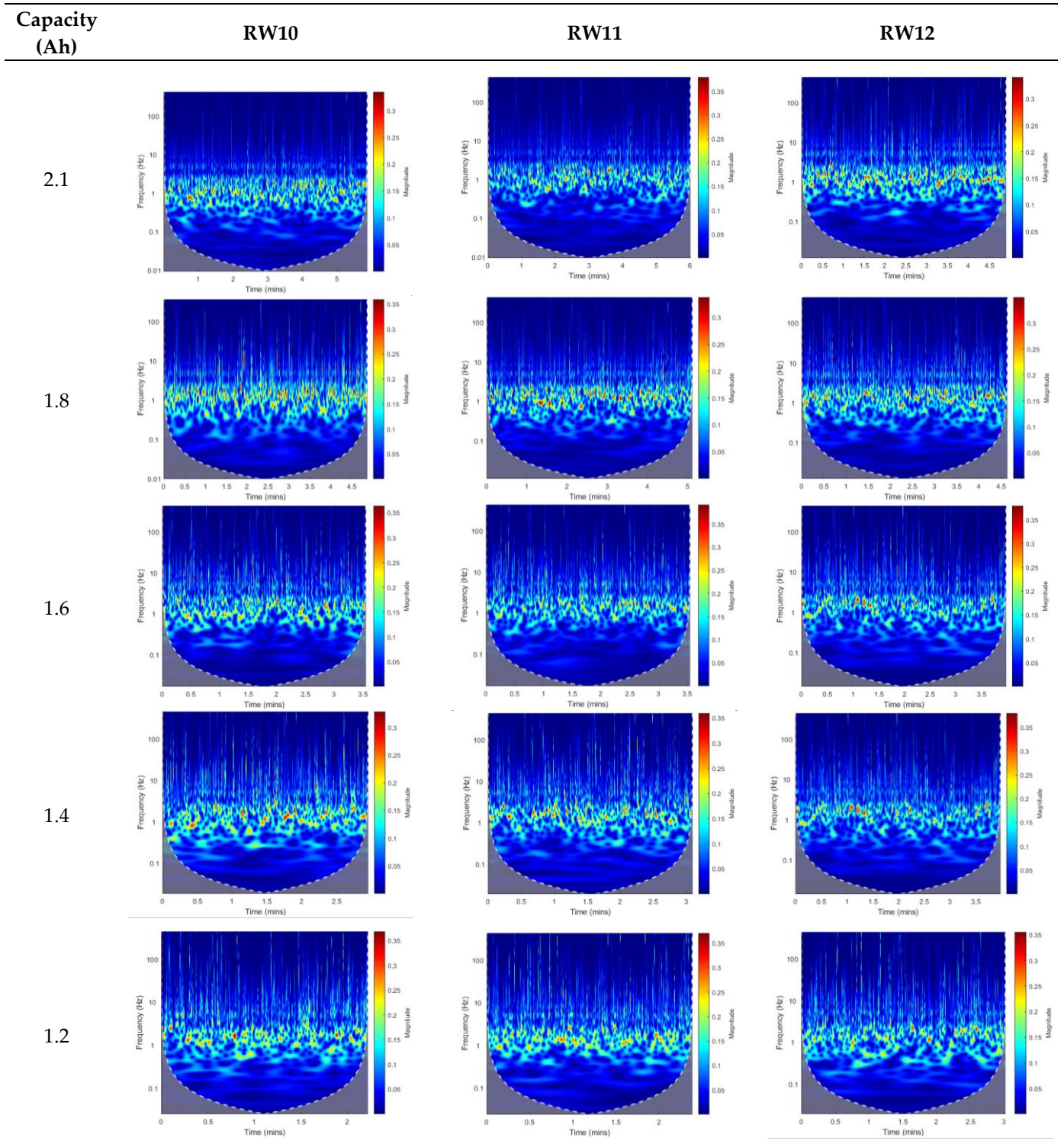


Figure 3.13 TFI energy concentration spectrum results of the battery RW9 measured voltage at different capacities: (a) 2.1 Ah, (b) 1.8 Ah, (c) 1.6 Ah, (d) 1.4 Ah, (f) 1.2 Ah, (e) 0.8 Ah.

Table 3.2 TFI energy for different LIBs at different capacity values.



3.3.2 Deep Learning Classification CNN Results

In this subsection, we demonstrate how the generated TFIs from the measured terminal voltage at different capacities through CWT were fed into AlexNet and VGG-16 DL-CNNs for capacity classification after they had been trained for TFI classification. The Stochastic gradient descent (SGDM) and adaptive moment estimation (ADAM) optimisation algorithms were used to train the generated TFIs.

3.3.2.1 AlexNet Neural Network

The AlexNet neural network was created in 2012 by Krizhevsky et al.[274], and is built from eight layers (five convolutional and three fully connected layers), as shown in Figure 3.14. In this study, we assumed that the battery's capacity had been classified into five classes from the first measured capacity value, which is 2.1 Ah, to the measured capacity value of 1.20 Ah in the experimental dataset, similar to the work presented in [275, 276]. Each battery's voltage per RW cycle was labelled to show its corresponding capacity. The datasets of LIBs RW9–12 were split into training data (70% of all TFI in the four folds) and 30% for testing data. Therefore, the LIB capacity estimation can be considered a 5-class classification. The size of the generated TFIs is $227 \times 227 \times 3$, which is suitable for the pretrained AlexNet network. The training setting for modelling the network and the AlexNet architecture are given in Tables 3.3 and 3.4. The AlexNet output layer was replaced with a new output layer with five neurons corresponding to five classes of capacity values. Since the AlexNet network is not trained to classify TFIs, only the weights of the last convolution layer and fully connected layer were trained, while the first four convolution layers were not. Training only the last layers of the AlexNet network reduced the training time of the model [267]. It should note that, the last layers should be trained again if a different dataset have used as input to the model.

During the training phase, SGDM and ADAM optimisers were utilised with an initial learning rate of 0.0001, and the batch size was set at 50. Once the training process was finished, the model's classification accuracy was evaluated using the test dataset. Classification accuracy was calculated to assess the model's accuracy, and the test dataset results are given in Table

3.5. The results show that the trained model correctly classified the test data with an accuracy rate of 95.69%. Moreover, the SDGM and ADAM optimisers performed well in updating our model weights. Thus, these classification results demonstrate that the proposed method achieved accurate predictions of battery capacity for each battery cell.

Table 3.3 Hyperparameter settings for the trained AlexNet model.

Hyperparameters	Values
Momentum	0.9
Initial learning rate	0.0001
Learning rate drop factor	0.1
Learning rate drop period	10
Number of epochs	50
Batch size	15
Optimiser	SGDM, ADAM

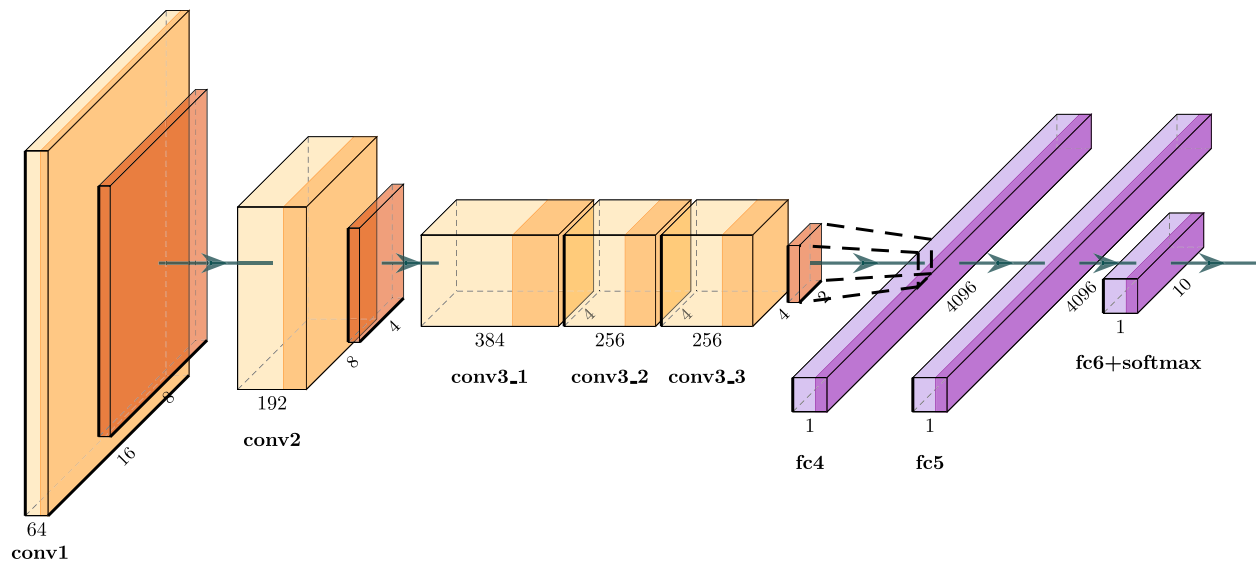


Figure 3.14 AlexNet model structure.

Table 3.4 AlexNet architecture.

Name	Type	Activations	Learnable
Data 227×227×3 images	Image input	$227 \times 227 \times 3$	—
Conv 1	Convolution	$55 \times 55 \times 96$	Weights $11 \times 11 \times 3 \times 96$ Bias $1 \times 1 \times 96$
Pool 1	Max Pooling	$27 \times 27 \times 96$	—
Conv 2	Convolution	$27 \times 27 \times 256$	Weights $5 \times 5 \times 48 \times 256$ Bias $1 \times 1 \times 256$
Pool 2	Max Pooling	$13 \times 13 \times 256$	—
Conv 3	Convolution	$13 \times 13 \times 384$	Weights $3 \times 3 \times 256 \times 384$ Bias $1 \times 1 \times 384$
Conv 4	Convolution	$13 \times 13 \times 384$	Weights $3 \times 3 \times 192 \times 384$ Bias $1 \times 1 \times 384$
Conv 5	Convolution	$13 \times 13 \times 256$	Weights $3 \times 3 \times 192 \times 256$ Bias $1 \times 1 \times 256$
Pool 5	Max Pooling	$6 \times 6 \times 256$	—
Fc6	Fully Connected	$1 \times 1 \times 4096$	Weights 4096×9216 Bias 4096×1
Fc7	Fully Connected	$1 \times 1 \times 4096$	Weights 4096×4096 Bias 4096×1
Fc8	Fully Connected	$1 \times 1 \times 1000$	Weights 1000×4096 Bias 1000×1
Prob Softmax layer	Softmax	$1 \times 1 \times 1000$	—
Output	Classification		—

Table 3.5 Capacity prediction accuracy for each battery cell using AlexNet.

Optimiser	RW9		RW10		RW11		RW12	
	SGDM	Adam	SGDM	ADAM	SGDM	ADAM	SGDM	ADAM
Accuracy	95.0673%	95.69%	91.96%	94.20%	93.39%	94.27%	90.25%	91.5%

3.3.2.2 VGG-16 Neural Network

The second pre-trained model tested in this study is a convolutional neural network from Oxford Visual Geometry Group (VGG), a 16-layer network (see Figure 3.15) [277]. VGG-16 has achieved classification accuracy on the ImageNet dataset, and Table 3.6 shows the layers structure of VGG-16. With the same hyperparameters settings, the VGG-16 model is compared with the AlexNet model, and the prediction accuracy results are presented in Table 3.7. The comparison classification results from Tables 3.5 and 3.7 for AlexNet and VGG-16 models show that the model's accuracy will increase as the DL-CNN is deeper. However, as the DL-CNN become deeper, the training time will increase, and more computational complexity will be added to the model.

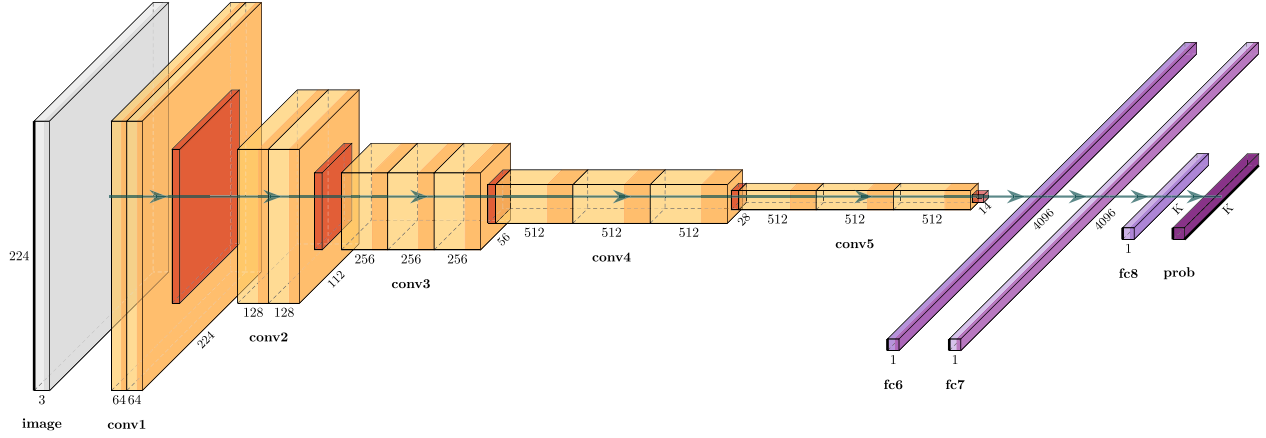


Figure 3.15 VGG-16 model structure.

Table 3.6 VGG-16 architecture.

Name	Type	Activations	Learnable
Data 224×224×3 images	Image input	224 × 224 × 3	—
Block 1- Conv 1	Convolution	224 × 224 × 64	Weights 3 × 3 × 3 × 64, Bias 1 × 1 × 64
Block 1- Conv 2	Convolution	224 × 224 × 64	Weights 3 × 3 × 3 × 64, Bias 1 × 1 × 64
Block 1- Pool	Max Pooling	112 × 112 × 64	—
Block 2- Conv 1	Convolution	112 × 112 × 128	Weights 3 × 3 × 64 × 128, Bias 1 × 1 × 128
Block 2- Conv 2	Convolution	112 × 112 × 128	Weights 3 × 3 × 128 × 128, Bias 1 × 1 × 128
Block 2- Pool	Max Pooling	56 × 56 × 128	—
Block 3- Conv 1	Convolution	56 × 56 × 256	Weights 3 × 3 × 128 × 256, Bias 1 × 1 × 256
Block 3- Conv 2	Convolution	56 × 56 × 256	Weights 3 × 3 × 128 × 256, Bias 1 × 1 × 256
Block 3- Pool	Max Pooling	28 × 28 × 256	—
Block 4- Conv 1	Convolution	28 × 28 × 512	Weights 3 × 3 × 256 × 512, Bias 1 × 1 × 512
Block 4- Conv 2	Convolution	28 × 28 × 512	Weights 3 × 3 × 256 × 512, Bias 1 × 1 × 512
Block 4- Pool	Max Pooling	14 × 14 × 512	—
Block 5- Conv 1	Convolution	14 × 14 × 512	Weights 3 × 3 × 512 × 512, Bias 1 × 1 × 512
Block 5- Conv 2	Convolution	14 × 14 × 512	Weights 3 × 3 × 512 × 512, Bias 1 × 1 × 512
Block 5- Pool	Max Pooling	7 × 7 × 512	—
Fc1	Fully Connected	1 × 1 × 4096	Weights 4096 × 4096, Bias 4096 × 1
Fc2	Fully Connected	1 × 1 × 4096	Weights 4096 × 4096, Bias 4096 × 1
Prob Softmax layer	Softmax	1 × 1 × 1000	—
Output	Classification	—	—

Table 3.7 Capacity prediction accuracy for each battery cell using VGG-16.

Optimiser	RW9		RW10		RW11		RW12	
	SGDM	ADAM	SGDM	ADAM	SGDM	ADAM	SGDM	ADAM
Accuracy	95.52%	95.52%	95.09%	95.60%	94.29%	94.92%	92.25%	95.5%

3.3.2.3 Explore Network Predictions using Deep Learning Visualisation Techniques.

Deep learning networks are frequently called "black boxes" because it is not always clear why a network makes a particular decision. You can transform network behaviour into output that a person can interpret using an interpretability technique. This interpretable output can subsequently be used to answer inquiries regarding a network's predictions. The following example focuses on visualisation approaches, which are interpretability techniques that explain network predictions by visual representations of what a network "sees." Therefore, this section will show how the AlexNet DL-CNN extracts features from the TFI's input images. Or in other words, this section answered the question of "Why should I trust the results of DL-CNN?". To answer this question and interprets the working of the DL-CNN, three deep-learning visualisation techniques are used in this section [278-281]:

- 1- Activation's function visualisation technique.
- 2- Gradient-weighted class activation mapping (Grad-CAM) visualisation technique.
- 3- Occlusion sensitivity visualisation technique.

Figure 3.16 shows an example of an input image fed into the AlexNet DL-CNN to investigate how the AlexNet DL-CNN will identify what the input figure represents.

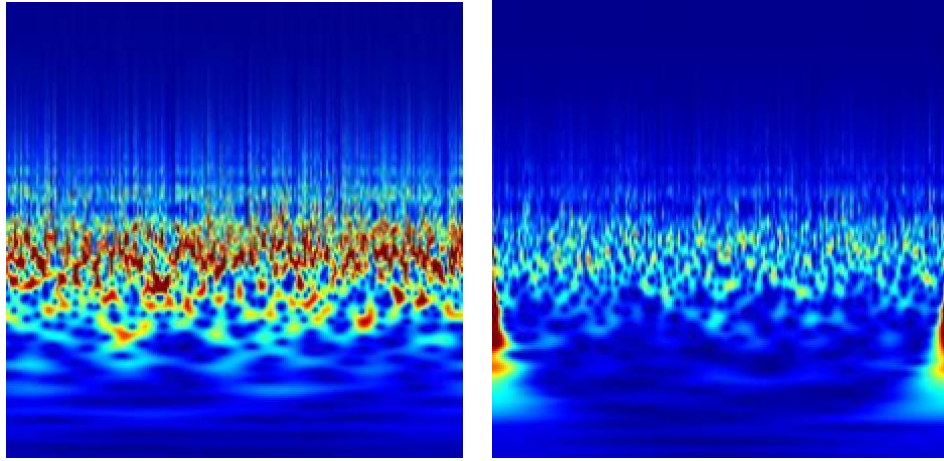


Figure 3.16 Example of the input TFIs images at BOL and EOL of RW9 LIB fed into the AlexNet DL-CNN.

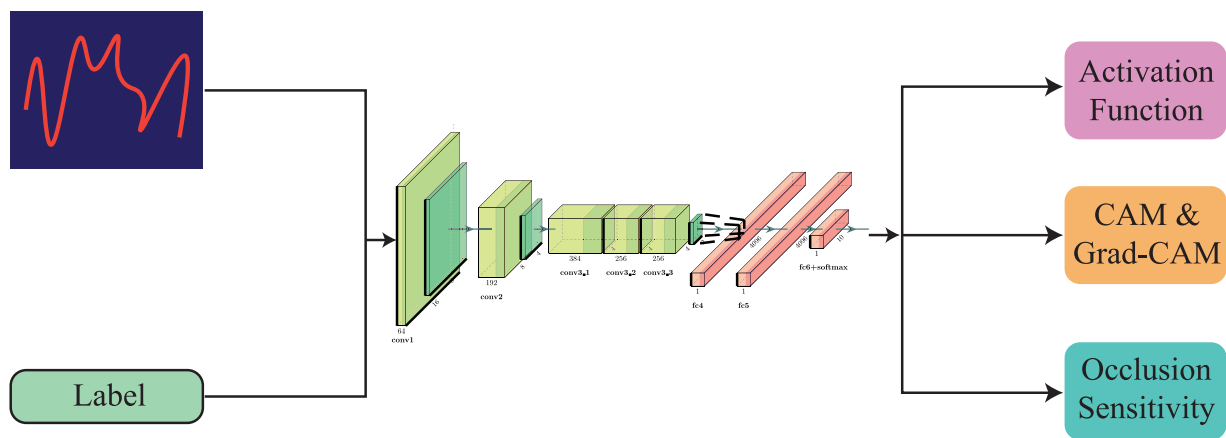


Figure 3.17 Overall flowchart of the given example.

Figure 3.17 illustrates the overall flowchart in this section. To start with this explanation, we will assume that the trained DL-CNN correctly classified the input TFI images into their corresponding class (2.1Ah for the BOL TFI image and 1.2Ah for the EOL TFI image). Then, the visualisation techniques will be applied to understand why the DL-CNN classified the input image to their corresponding values (labels).

1- Activation's function visualisation technique

Visualising the activations of each layer is one of the simplest methods of explaining network behaviour. Most neural networks learn to recognise characteristics such as colour and edges in their first convolutional layer. The network learns to recognise more complex features in deeper convolutional layers. Examining the output activations of the *norm1* layer after the network has processed the TFIs is shown in Figure 3.18 and Figure 3.19 for BOL and EOL, respectively.

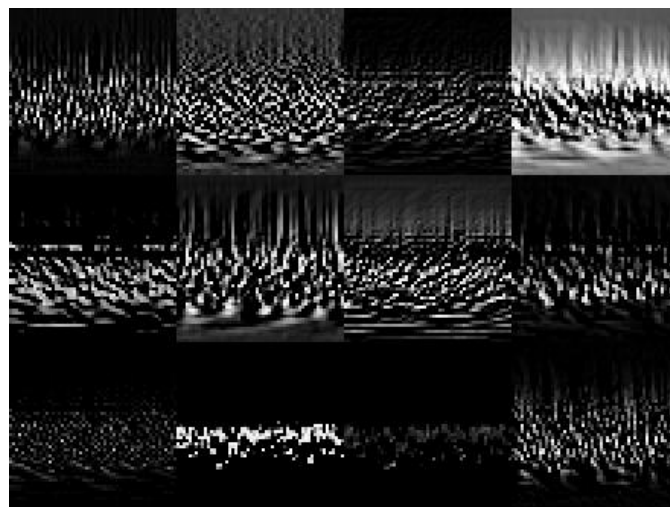


Figure 3.18 The activation functions of the *norm1* layer for TFI in the BOL state.

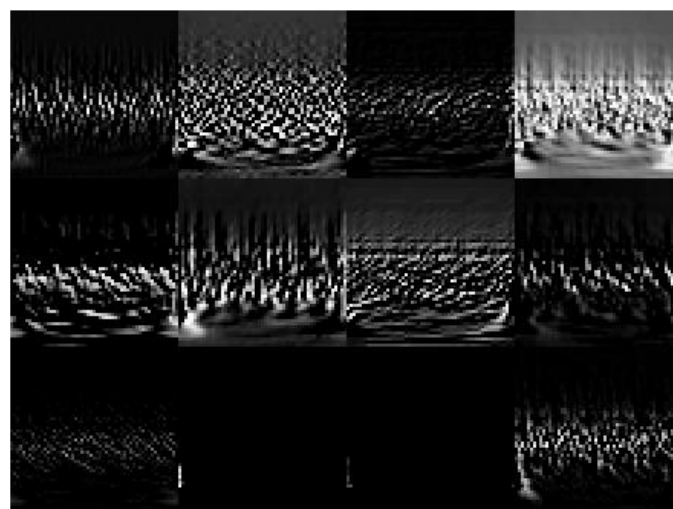


Figure 3.19 The activation functions of the *norm1* layer for TFI in the EOL state.

Strong positive activations are represented by white pixels, while strong negative activations are represented by black pixels. The network learning low-level characteristics, such as edges and textures in the first layers, can be observed. Comparing the obtained activation function results for both TFIs in Figure 3.18 and Figure 3.19 shows how AlexNet DL-CNN can correctly extract features that can be used to discriminate between different LIBs. On the other hand, Figure 3.20 and Figure 3.21 show the extracted feature in the deeper layer (*conv5*) of the AlexNet DL-CNN. Figure 3.20 and Figure 3.21 are revealed the strongest activating function focusing on the energy concentration distribution levels, indicating that this layer is extracting out more complex features such as the location and the intensity of the energy levels at a specific frequency value. Mapping the change in the energy concentration of the obtained TFI at a specific frequency value is used to estimate the capacity of the LIB. More sophisticated visualisation techniques can be used to learn more about the network's activity.

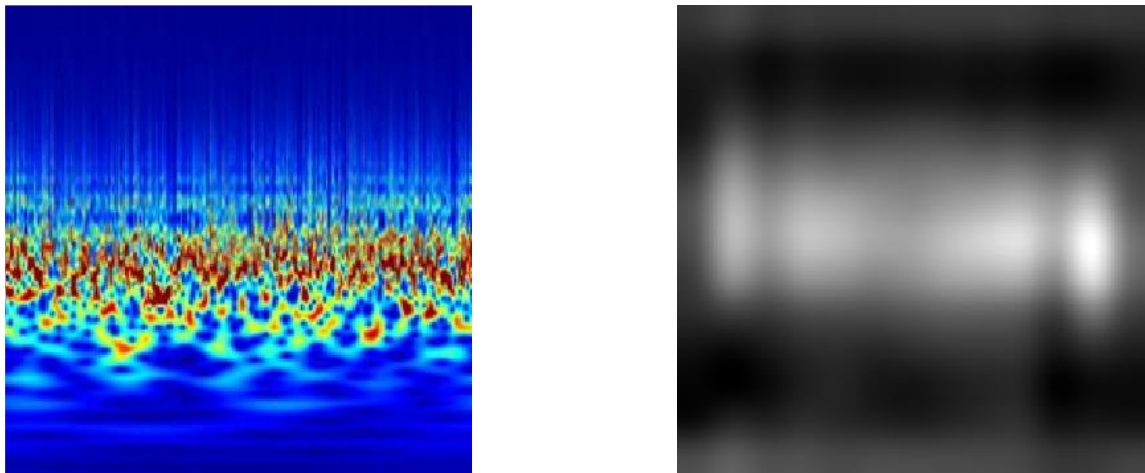


Figure 3.20 The activation functions of the deeper layer (*conv5*) in the AlexNet DL-CNN at the BOL of the LIB.

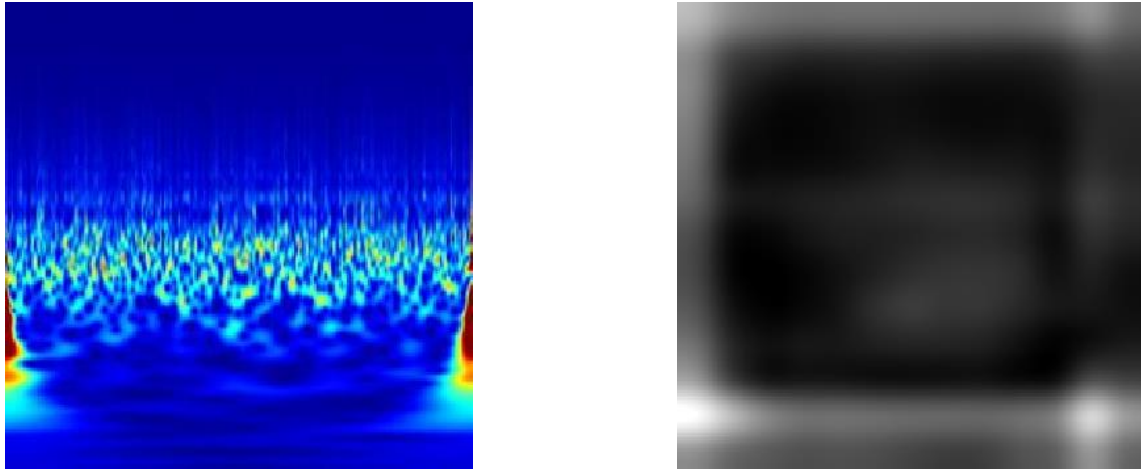


Figure 3.21 The activation functions of the deeper layer (conv5) in the AlexNet DL-CNN at the EOL of the LIB.

2- Gradient-weighted class activation mapping (Grad-CAM) visualisation technique.

Gradient-weighted Class Activation Mapping (Grad-CAM) is a technique used to visualise the regions in an image that are most important for a given classification. It works by using the gradients of the final convolutional layer of a DL-CNN to generate a heatmap that highlights the areas of the image the model uses to make its prediction. This can be useful for understanding how a model is making its decisions and can also help with debugging and improving the performance of the model [279].

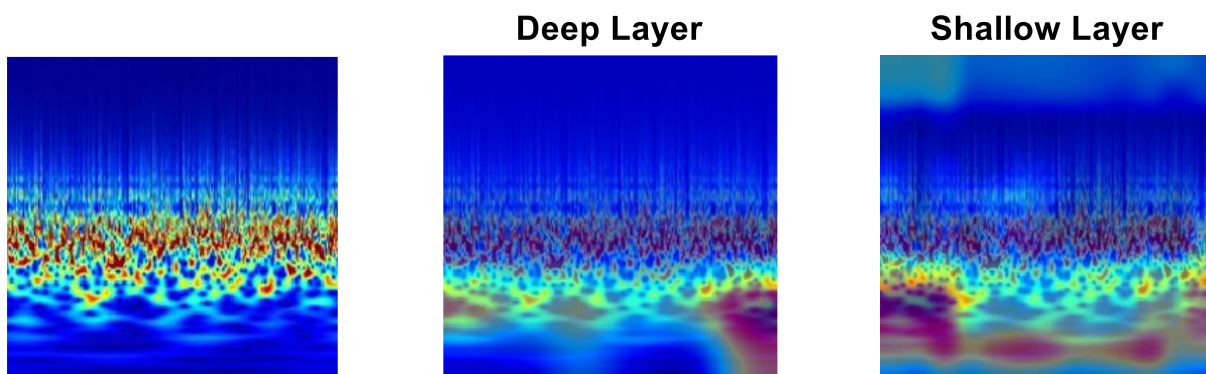


Figure 3.22 The obtained results of the Grad-CAM visualisation technique for deeper and shallow layers for TFI in the BOL of LIB.

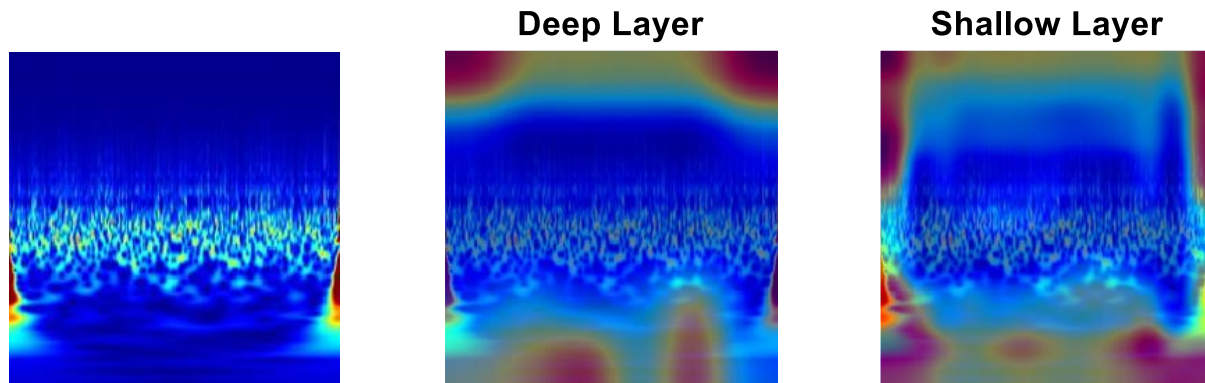


Figure 3.23 The obtained results of the Grad-CAM visualisation technique for deeper and shallow layers for TFI in the EOL of LIB.

Figure 3.22 illustrates the results of the Grad-CAM visualisation method for the more deep and shallow layers of AlexNet DL-CNN, respectively. As shown in Figure 3.22, the Grad-CAM map for the network's deeper layer emphasises the energy concentration distribution in the obtained TFI, indicating that the shape of the energy distribution is crucial for categorising this TFI as a BOL state (2.1Ah label). Similarly, Figure 3.23 shows the results of the Grad-CAM visualisation method for LIB at its EOL state. As shown in Figure 3.23, the energy concentration distribution differs from the energy distribution in Figure 3.22. This difference is seen in the deeper layer of the AlexNet DL-CNN.

3- Occlusion sensitivity visualisation technique.

Occlusion sensitivity is a technique used to visualise which parts of an image a DL-CNN uses to make a prediction. The method involves occluding parts of the image with a black square and then seeing how the forecast changes. If a certain area of the image is important for the prediction, then occluding it should result in a large change in the prediction. This can help to identify which parts of an image are important for a given task, and can also be used to understand what a DL-CNN has learned [282].

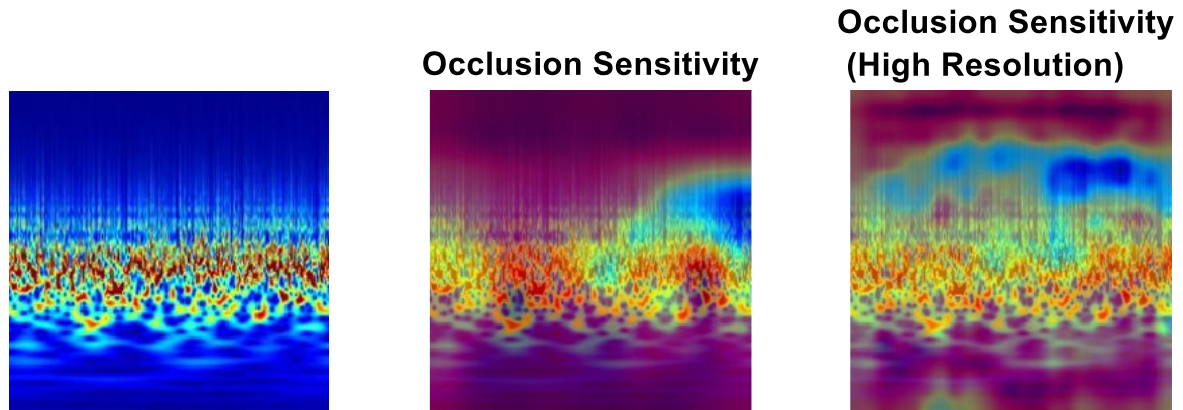


Figure 3.24 The obtained results of the occlusion sensitivity visualisation method with lower and high-resolution sensitivity of LIB at its BOL.

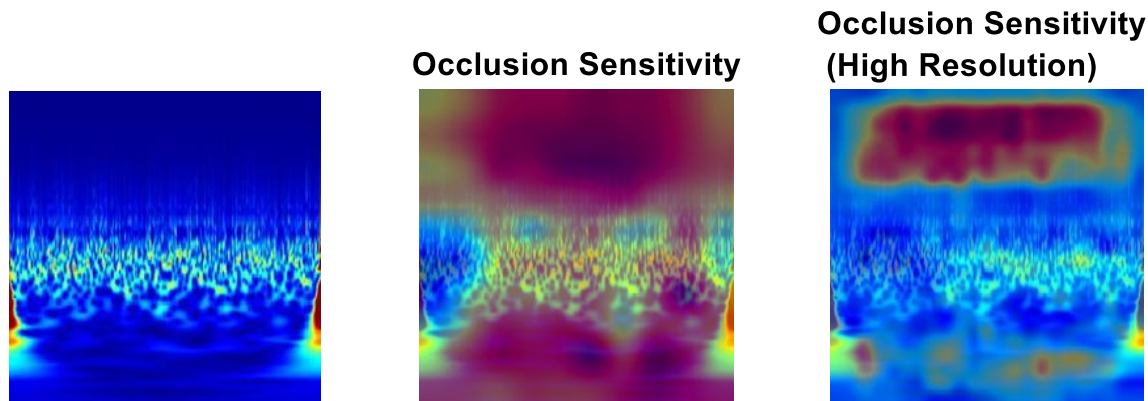


Figure 3.25 The obtained results of the occlusion sensitivity visualisation method with lower and high-resolution sensitivity of LIB at its EOL.

Figure 3.24 and Figure 3.25 show the occlusion sensitivity visualisation method results with lower and high-resolution sensitivity of LIB at its BOL and EOL, respectively. The lower-resolution map shows that the intensity of the energy concentration in the obtained TFIs is the main feature used for capacity prediction. The higher resolution map shows that the shape of the energy distribution is most important to the classification.

Based on the obtained results in this subsection, it can be thus concluded that the DL-CNN is appropriately trained to extract a promising feature that can be discriminated between the

different levels of SOH or the capacity of LIBs. It is worth mention that similar conclusion can be obtained by using all the generated TFIs at different capacity values.

3.3.3 Deep Learning Regression CNN Results

In the previous section, the capacities of the LIBs were classified into five discrete values (2.1Ah, 1.8Ah, 1.6Ah, 1.4Ah, and 1.2Ah). However, to predict the capacity of the LIBs between the specified classes, the two DL-CNNs have been modified one more time as regression DL-CNNs. To do that, the last three layers (fully connected layer, SoftMax layer, and classification layer) are replaced by two new layers: (1) a fully connected layer with one output instead of five, and (2) a regression layer, as shown in Figure 3.26. Both AlexNet and VGG-16 DL-CNN have been modified. The developed models of both DL-CNNs were trained in the same procedure as the previous section.

Root Mean Squared Error (RMSE) and Absolute Error (AE) were utilised to evaluate the accuracy of the proposed technique for estimating the capacity of LIBs. These evaluation criteria are expressed as follows:

$$RMSE = \sqrt{\frac{1}{N} \sum_{i=1}^N (\hat{C}_i - C_i)^2} \quad (3.8)$$

$$AE = |(\hat{C}_i - C_i)| \quad (3.9)$$

Where \hat{C} and C_i the estimated and actual capacity of LIBs, respectively, N is the number of data points.

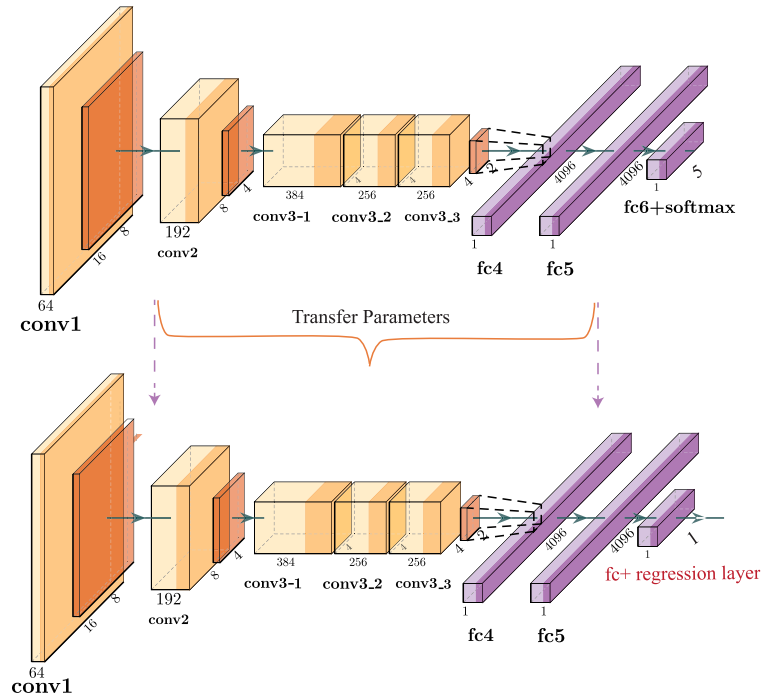
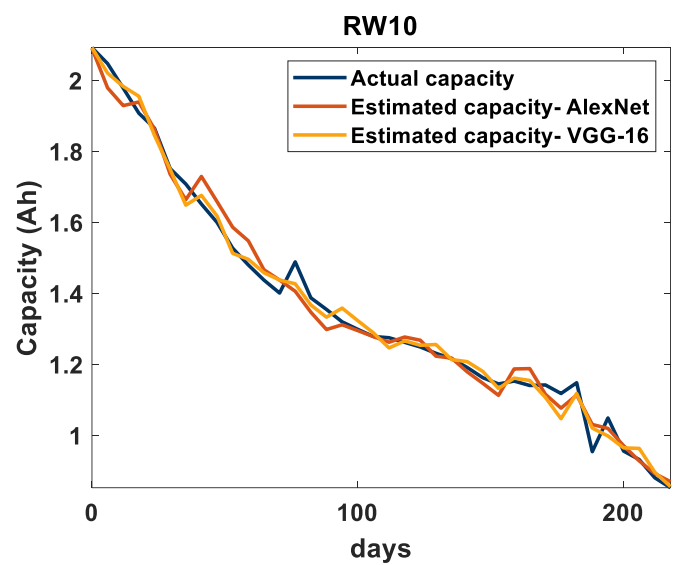
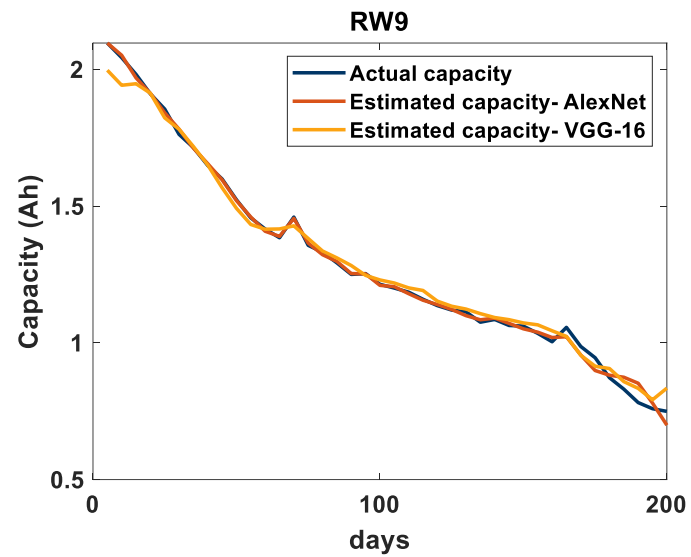


Figure 3.26 AlexNet structure transfer learning from image classification into image regression—all the parameters from conv1 to conv3-3 layers transferred without any modification.

Figure 3.27 shows the estimation results of 4 LIBs RW9, RW10, RW11, and RW12. As shown in Figure 3.27, the estimated capacity results of all tested LIBs are very close to the actual or measured capacity curves. The RMSE and AE of each tested LIBs are presented in Table 3.8 and Table 3.9 of AlexNet and VGG-16 DL-CNNs, respectively. The lowest RMSE is 2.02% and 2.74% for RW9 and RW11 LIBs for AlexNet and VGG-16 DL-CNNs. The highest estimation RMSE is 5.03% for LIB number RW11 for AlexNet DL-CNN and the highest RMSE for VGG-16 DL-CNN is 4.96%.

Moreover, the maximum absolute estimation error for AlexNet is 6.84% for RW10, as shown in Table 3.8, and 6.63% for VGG-16 DL-CNN for the same LIB, as shown in Table 3.9. The average capacity estimation errors are 3.47%, 3.58%, 5.71%, and 5.22% for RMSE and max error for AlexNet and VGG-16 DL-CNNs, respectively. Figure 3.28 shows the bar graph of the RMSE for the estimated capacity of the LIBs using AlexNet and VGG-16 DL-CNNs.

Based on the obtained results, the effectiveness of the proposed approach for capacity estimation of LIBs.



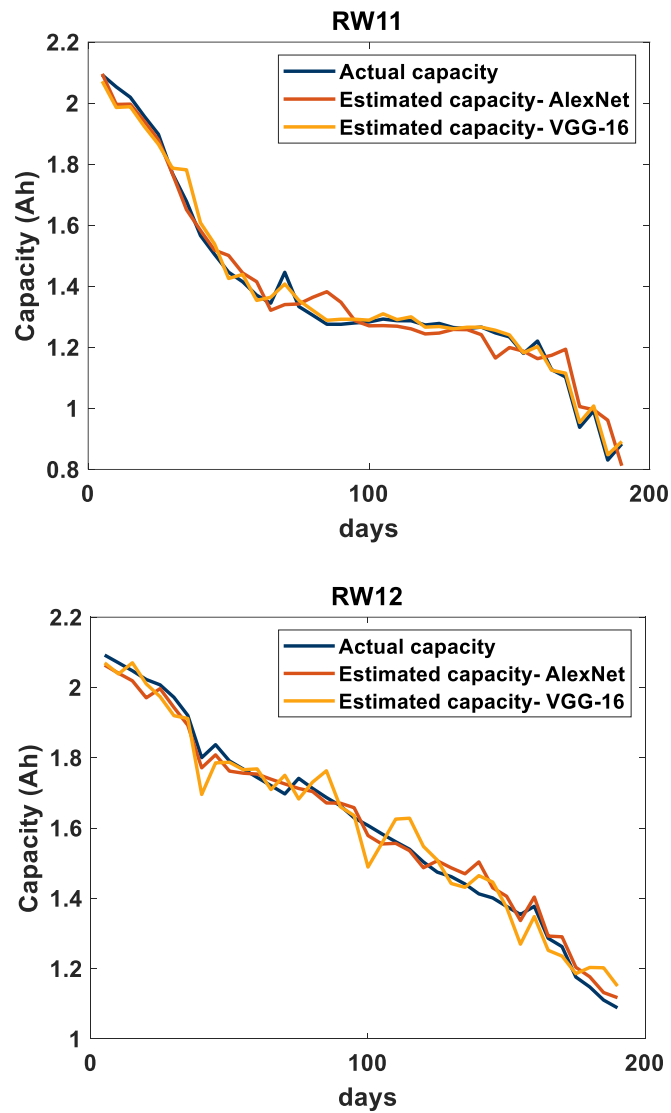


Figure 3.27 Capacity estimation results of AlexNet and VGG-16 DL-CNNs.

Table 3.8 RMSE and AE of AlexNet DL-CNN.

	RW9	RW10	RW11	RW12	Average
RMSE (%)	2.02	3.93	5.03	2.90	3.47%
AE (%)	4.35	6.84	6.92	4.72	5.71%

Table 3.9 RMSE and AE of VGG-16 DL-CNN.

	RW9	RW10	RW11	RW12	Average
--	------------	-------------	-------------	-------------	----------------

RMSE (%)	3.60	3.04	2.74	4.96	3.58%
AE (%)	4.01	6.63	3.82	6.44	5.22%

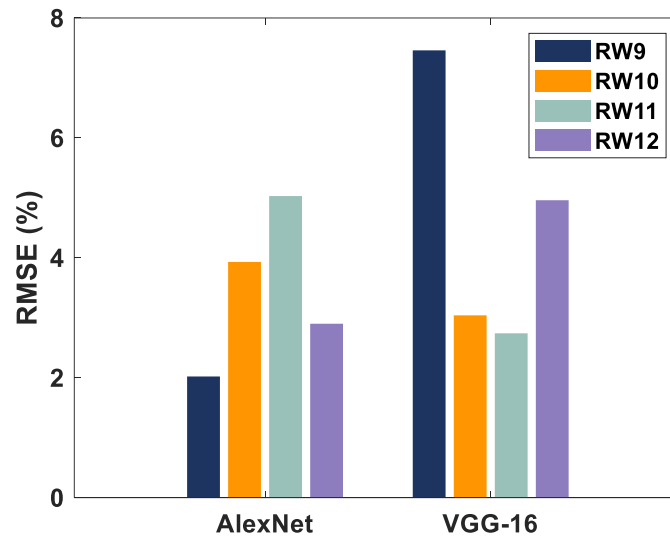


Figure 3.28 The RMSE for capacity estimation of four LIBs using AlexNet and VGG-16 DL-CNNs.

3.4 Summary

This chapter presented a novel capacity assessment approach for LIBs using multi-domain features derived from a TFI algorithm. Instead of using 1D raw terminal voltage data or extracting multiple statistical features, CWT converted the battery's terminal voltage into a 2D image feature. The proposed method employed CWT to create a 2D time-frequency representation of the battery terminal voltage, called a TFI, with multi-domain features.

To validate the effectiveness of this method, experimental data from four LIB cells provided by NASA's Prognostics Centre of Excellence (PCoE) were used. The generated time-frequency images clearly displayed the battery's degradation process through the energy concentration distribution of the measured voltage at various capacity levels.

Two pre-trained deep learning convolutional neural networks (DL-CNNs), AlexNet and VGG-16, were used to classify the created TFIs at different capacities into five classes. The

classification results achieved an accuracy of 95.69% using AlexNet and 95.52% using the VGG-16 network.

Additionally, image regression models were developed by modifying the structures of the AlexNet and VGG-16 DL-CNNs. The regression results demonstrated high-capacity estimation accuracy, with an average RMSE of 3.47% for AlexNet DL-CNN and 3.58% for VGG-16 DL-CNN.

The accuracy of this proposed method suggests that it can serve as an effective health prognostic tool for managing LIBs in various applications, such as electric vehicles and grid applications.

Chapter 4 Capacity Estimation of Lithium-ion Batteries Based on Adaptive Empirical Wavelet Transform and Long Short-term Memory Neural Network

4.1 Brief Introduction

This chapter presents a novel generalised approach for estimating the capacity of LIBs based on the adaptive empirical wavelet transform (EWT). The adaptive EWT is a potent tool for analysing the charging-discharging terminal voltage signal with non-stationary and transient phenomena in LIBs. EWT-based MRA is used to extract information related to the degradation trend in the time-frequency domain. Using the adaptive EWT in conjunction with wavelet decomposition, the ageing features of LIBs can be retrieved from the charging/discharging voltage signal over a frequency band range. The advantage of employing the EWT method over other approaches, such as continuous wavelet transform and discrete wavelet transform, is that there is no need for a mother wavelet selection procedure since EWT is an adaptive approach and the mother wavelet signal is designed based on the measured signal. Specifically, the measured voltage signals of the LIBs are decomposed into nine multi-resolution modes to display the high and low-frequency components.

Moreover, 13 statistical features are extracted to investigate the correlation between the capacity degradation and the extracted features. Afterwards, an LSTM model is developed to estimate the capacity of the LIBs. The proposed approach has been validated using two datasets: (1) NASA's randomised dataset with 24 LIBs cycled under generally varying operational conditions and (2) Stanford University's dataset with 10 LIBs cycled with electrical vehicle discharge current profile.

Moreover, the proposed approach has been compared with conventional wavelet transform methods, CWT and DWT. In addition, the developed technique has also been compared with the state-of-the-art. Figure 4.1 shows the graphical abstract of the proposed method in this chapter.

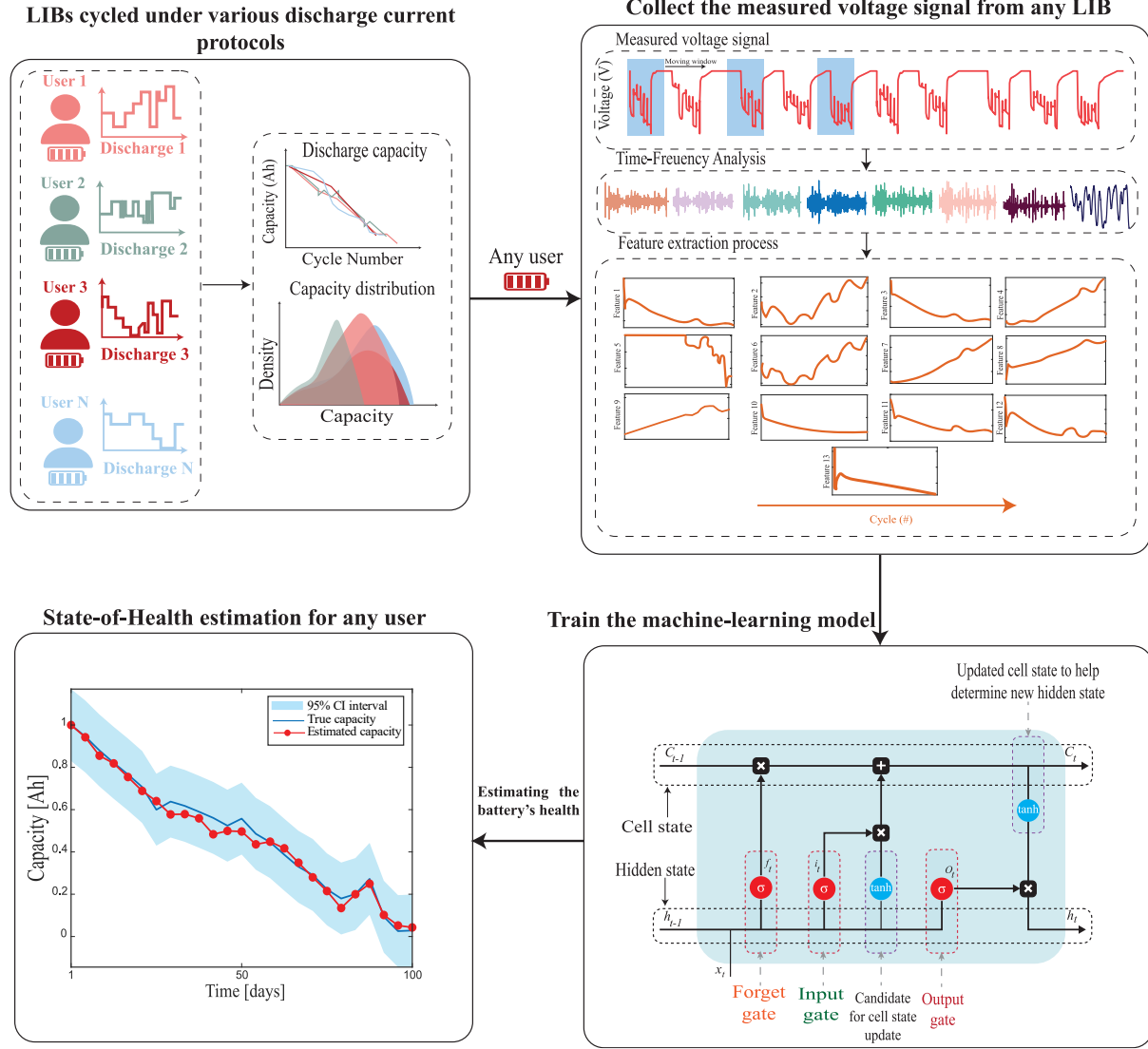


Figure 4.1 Graphical abstract of the proposed framework for the capacity estimation of LIBs.

4.2 The Proposed Framework for Capacity Estimation

The details of a proposed framework for the capacity estimation of LIBs are discussed next. As shown in Figure 4.2, the proposed framework involves four main steps. The first step is collecting and preparing the ageing datasets. Two experimental datasets published by the Prognostics Centre of Excellence (PCoE) NASA [247] and Stanford University [283] were used to validate the proposed framework. The second step is applying EWT to the

charge/discharge voltage signal to decompose it into specific numbers of multi-resolution intrinsic mode functions (IMFs). Then, the correlation between each obtained IMFs and the charge/discharge voltage is evaluated. The most correlated IMF ‘‘Fundamental mode’’ is removed from the measured charge/discharge voltage signal. The third step is to create a feature pool by extracting 13 statistical features from the filtered charge/discharge voltage signal. Then, the Pearson correlation method is applied to select the most critical features from the constructed feature pool. Finally, the selected features are fed into the LSTM model for model training and evaluation. The following subsections will detail the operating flow of the proposed estimation method.

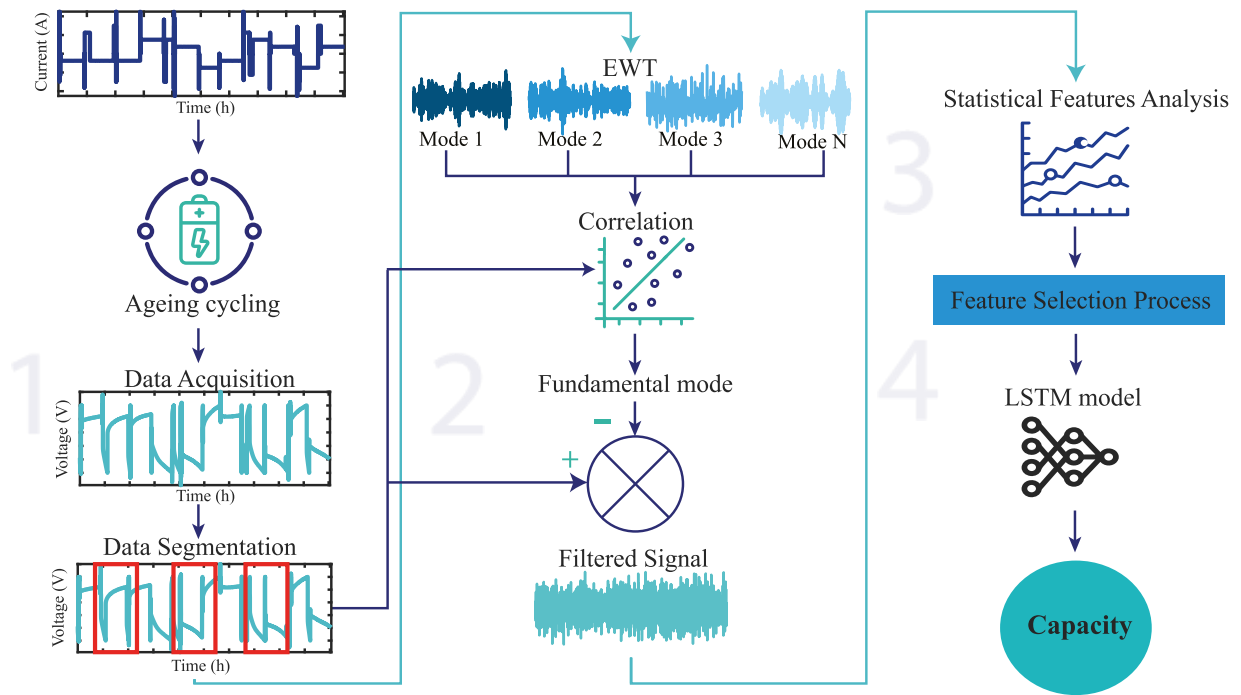


Figure 4.2 The proposed method for capacity estimation of LIBs based on EWT.

4.2.1 Experimental Datasets

The real-world operating environment of LIBs involves various dynamic stress factors, such as random current profiles and temperatures; these factors significantly influence the health and degradation characteristics of LIBs. Therefore, this work uses two public datasets for the case study acquired from NASA Ames's prognostics research centre [247] and Energy

Resources Engineering research centre at Stanford University [283] to analyse the LIB capacity deterioration in real-world operating conditions.

For the NASA dataset, 28 LIBs were used to emulate real-world battery operation. An overview of the general characteristics of the LIBs dataset is presented in Table 4.1. Moreover, Figure 4.3 shows this dataset's flowchart of the cycling procedure. These 28 LIBs were split into seven subgroups of 4 LIBs and cycled using seven different randomised charging/discharging current profiles, as presented in Table 4.2. Furthermore, as shown in Table 4.2, the cycling protocols for each group are divided into three steps: (1) constant-current (CC) charge step, (2) constant voltage (CV) charge step, and (3) random walk discharge step. LIBs in each protocol group underwent a time-varying charge/discharge profile.

Moreover, the first five subgroups were cycled at room temperature (25 °C), while the last two subgroups (6 and 7) were cycled at 40 °C. Figure 4.4 illustrates an example of the measured raw data of the voltage and current of cell 9 in group 3 at its first cycles or BOL and EOL or last cycles. It is worth noting that during the first cycles (Figure 4.4(a)), the battery voltage only reaches the upper and lower limits (3.2V and 4.2V) a few times. While at the experiment's last cycles (Figure 4.4(b)), the battery is observed to reach the upper and lower voltage limits during nearly every step requiring a current of 2A or more. This is due to the deterioration of the battery's health during the experiment, which decreases its charge storage capacity and raises its internal resistance [247]. Figure 4.5 shows the voltage and current signals for three different LIBs cycled using three diverse charging/discharging profiles.

A reference performance test (RPT) was performed regularly after each number of randomised cycles for each subgroup. A 2A constant charge/discharge current was applied between the LIBs voltage limits to calculate the LIBs capacity (Q_{dis}) by integrating the current from the 2 A charges curves as presented in (4.1).

$$Q_{dis} = \frac{1}{3600} \int I(t) dt \quad (4.1)$$

NASA's randomised dataset contained 28 LIBs cycled with seven different cycling protocols, making the capacity estimation more complex than the previously published datasets like [183], where a single protocol and constant charge-constant discharge profile were utilised.

Table 4.1 The properties of the LIBs.

LIB's properties	18650 LIBs
Manufacture	LG Chem
Chemistry	Lithium cobalt oxide vs graphite
Number of cells	28
Nominal capacity	2.10 Ah
Capacity range	2.10 Ah \rightarrow 0.80 Ah
Voltage range	4.2 – 3.2 V
Cycling protocols	7

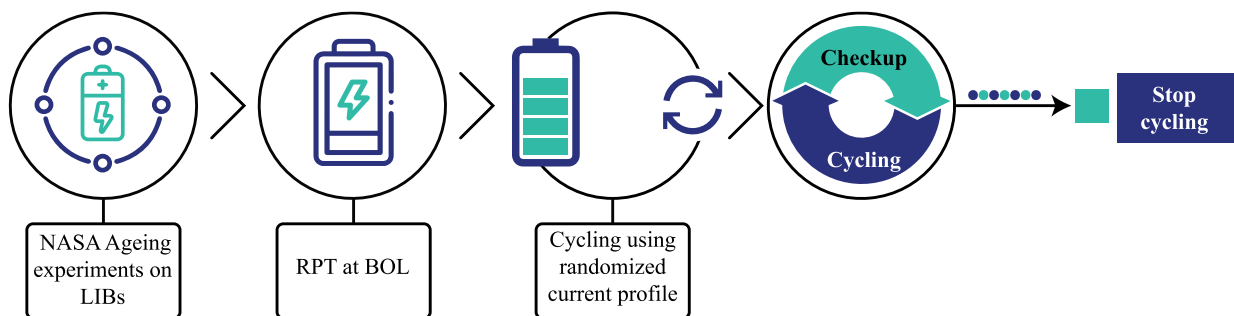
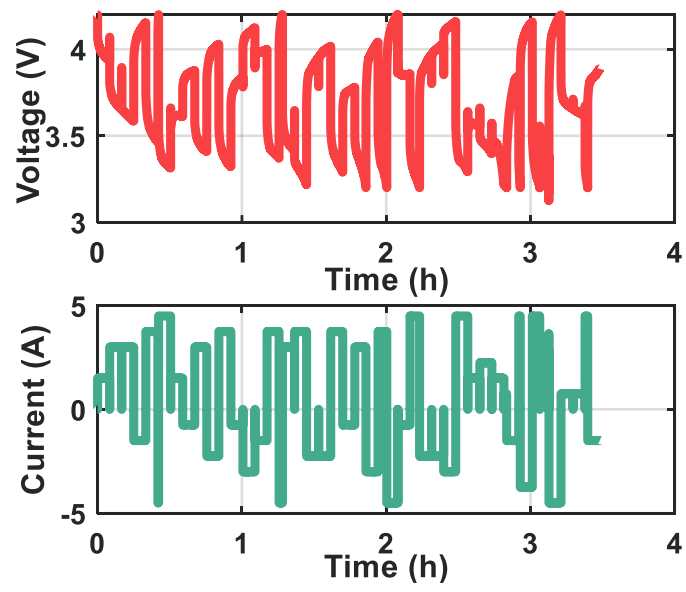


Figure 4.3 The cycle process for the NASA Randomised dataset.

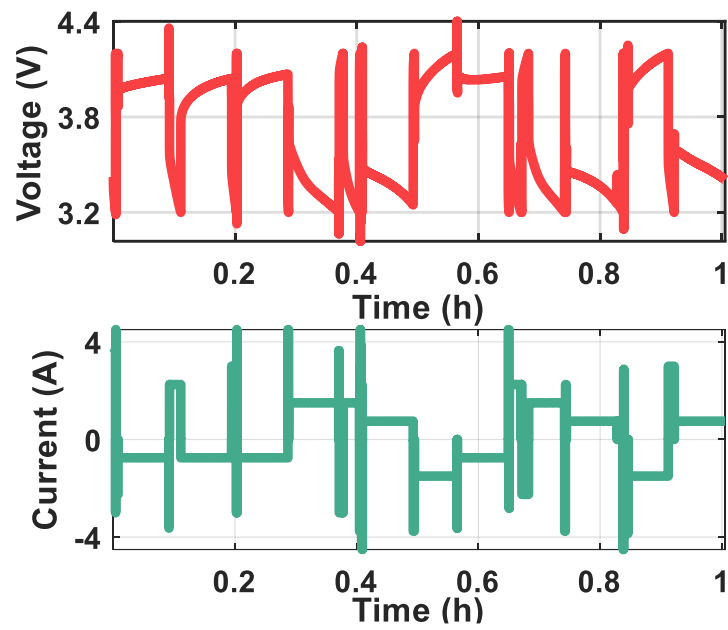
Table 4.2 Summary of the seven cycling protocols applied to NASA LIBs.

Test procedure Item	CC charge step		CV charge step	Discharge step	
	<i>Charge rate</i>	<i>Charge cut-off voltage (V)</i>	<i>Charge stop condition</i>	<i>Discharge rate</i>	<i>Discharge cut-off voltage (V)</i>
Group 1 (Cells 1, 2, 7, 8)	2A with a randomly selected duration (i.e., 0.5, 1, 1.5, 2, or 2.5h)	4.2	The current drops below a threshold, or the charging time exceeds the allotted interval.	A value was randomly selected between 0.5A and 4A every 5 minutes.	3.2
Group 2 (Cells 3-6)	2A	4.2	Same as Group 1	Same as Group 1.	3.2
Group 3 (Cell 9-12)	A value was randomly selected from a set (i.e., 0.75A, 1.5A, 2.25A, 3A, 3.75A, and 4.5A) every 5 minutes	4.2	N/A	A value was randomly selected from a set (i.e., 0.75A, 1.5A, 2.25A, 3A, 3.75A, and 4.5A) every 5 minutes.	3.2
Group 4 (Cells 13-16)	2A	4.2	Same as Group 1	Same as Group 1, except the probability distribution was designed to be skewed towards selecting lower currents.	3.2

Group 5 (Cells 17-20)	2A	4.2	Same as Group 1	Same as Group 4, except the probability distribution was designed to be skewed towards selecting higher currents.	3.2
Group 6 (Cells 21-24)	2A	4.2	Same as Group 1	Same as Group 4 except with an ambient temperature of 40 °C.	3.2
Group 7 (Cells 25-28)	2A	4.2	Same as Group 1	Same as Group 5 except with an ambient temperature of 40 °C.	3.2

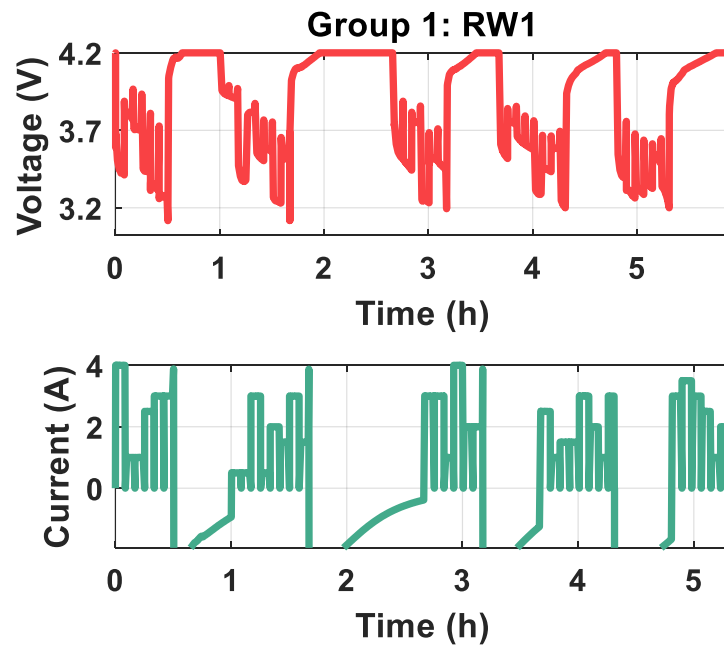


(a)

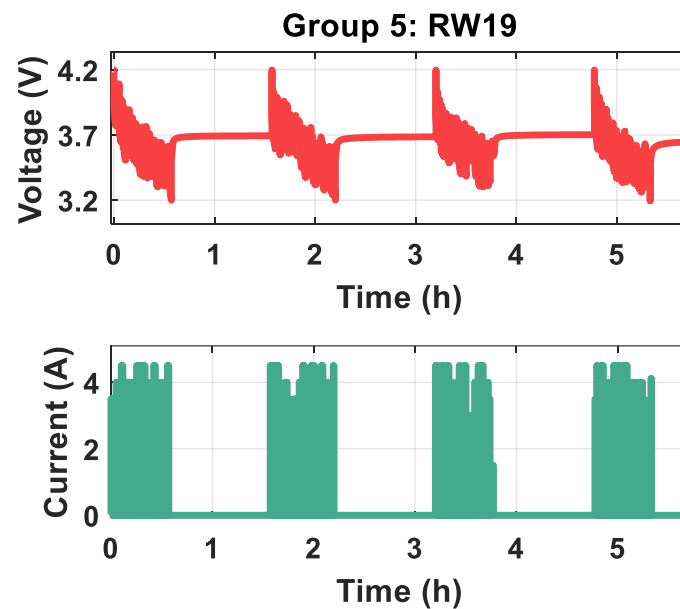


(b)

Figure 4.4 Voltage and current signals of the cell RW9 at (a) the beginning of life (BOL) and (b) the end of life (EOL).



(a)



(b)

Figure 4.5 The measured voltage and current signals for three different LIBs.

Figure 4.6 illustrates the capacity fading across all seven groups to explain this difficulty better. As shown in Figure 4.5, the time-varying charge/discharge current profile resulted in a more heterogeneous capacity fades behaviour among the LIBs in each protocol group. Different patterns of capacity fading were also seen throughout the cycling test, even within LIBs of the same cycling group, most notably in groups 3, 4, and 7.

The experimental dataset [283] developed by Stanford University comprises EV real-driving profiles and RPTs for ten INR21700-M50T NMC LIBs at 23°C collected over 23 months. This dataset aims to simulate a realistic driving scenario for EVs using the Urban Dynamometer Driving Schedule (UDDS), which gradually decreases the battery's SOC from 80% to 20%. The technical specifications of the LIBs are presented in Table 4.3.

The UDDS cycling current profile and the measured voltage for three cycles are shown in Figure 4.7. Also, Figure 4.7 depicts the six-step sequence that makes up a single cycle (listed in Table 4.4).

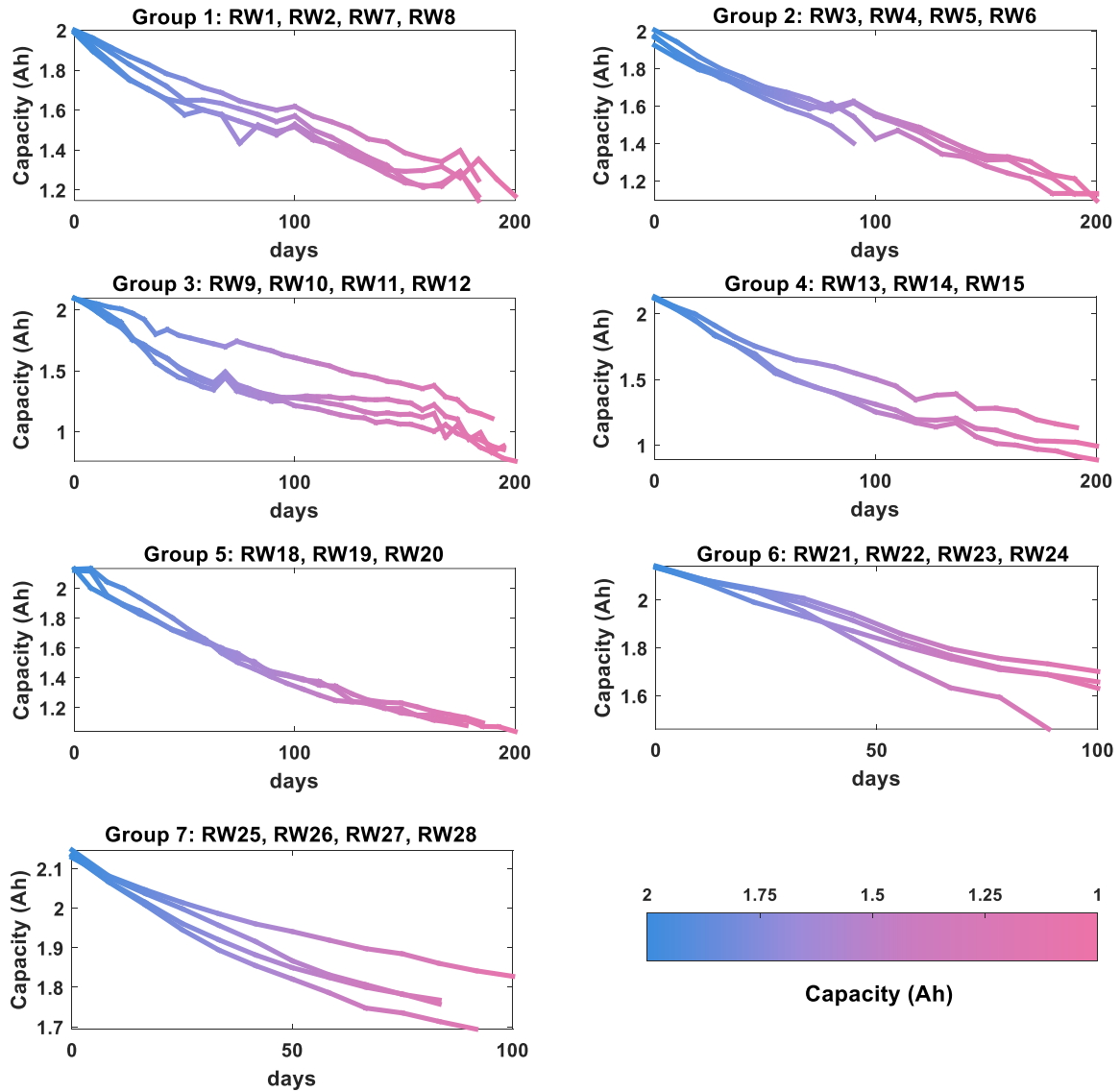


Figure 4.6 The capacity fade for all the LIBs of each group.

The cycle begins with a charge using a C-rate of $C/4$, $C/2$, $1C$, or $3C$ during a CC charge. When the LIB voltage reaches 4V, a CV phase (Step 2) begins and lasts until the current drops below 50mA. The third step (continuous charging at $C/4$) and the fourth are intended to charge the LIB to 4.2V, or 100% SOC. Step 5 uses a $C/4$ constant current to discharge the LIB from 100% SOC to 80% SOC. The LIB is discharged from 80% to 20% via a series of UDDS cycles in Step 6.

Table 4.3 The technical specifications of INR21700-M50T NMC LIB.

LIB's properties	INR21700-M50T
Manufacture	LG Chem
Positive electrode	LiNiMnCoO ₂
Negative electrode	Graphite and silicon
Number of cells	10
Nominal capacity	4.85 Ah
Capacity range	4.85 Ah → 4.45 Ah
Voltage range	4.2 – 2.5 V
Cycling protocols	1

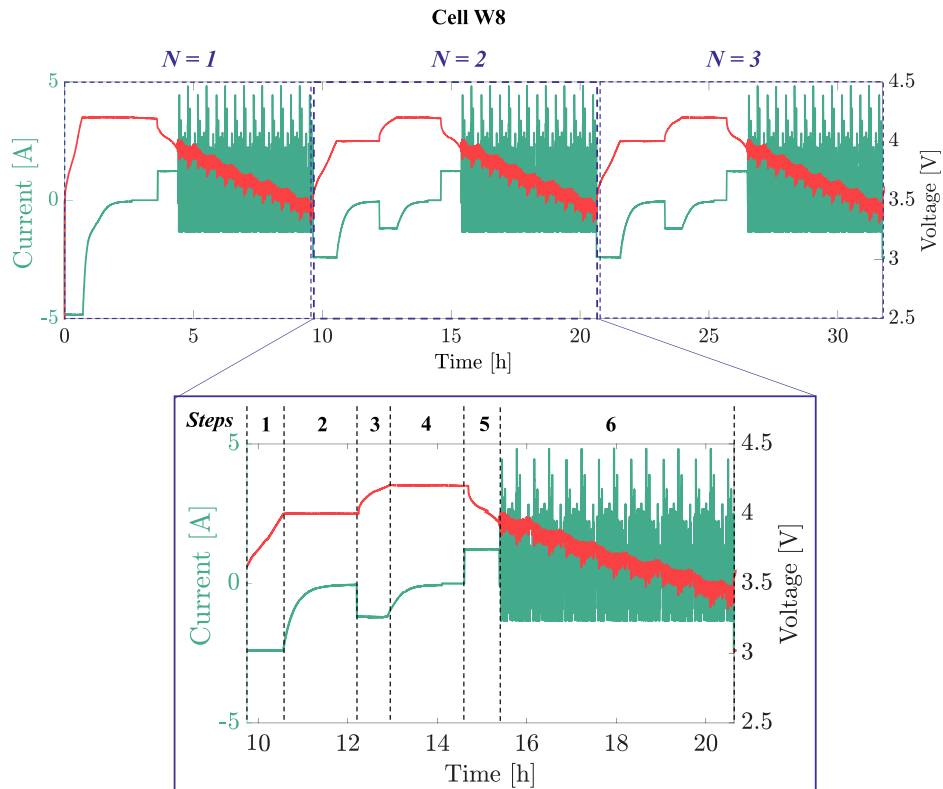


Figure 4.7 UDDS current profile and the measured voltage signals.

Following a set number of UDDS cycles, an RPT was conducted (for most LIBs, every 25 cycles). Using the voltage limits of the LIBs as a reference, a constant charge/discharge current of $C/20$ was applied, and the LIB's capacity Q_{dis} was determined by integrating the current from each of the $C/20$ A charge curves, as shown in Eq (4.1). Figure 4.8 depicts the total discharge capacity of the 10 LIBs.

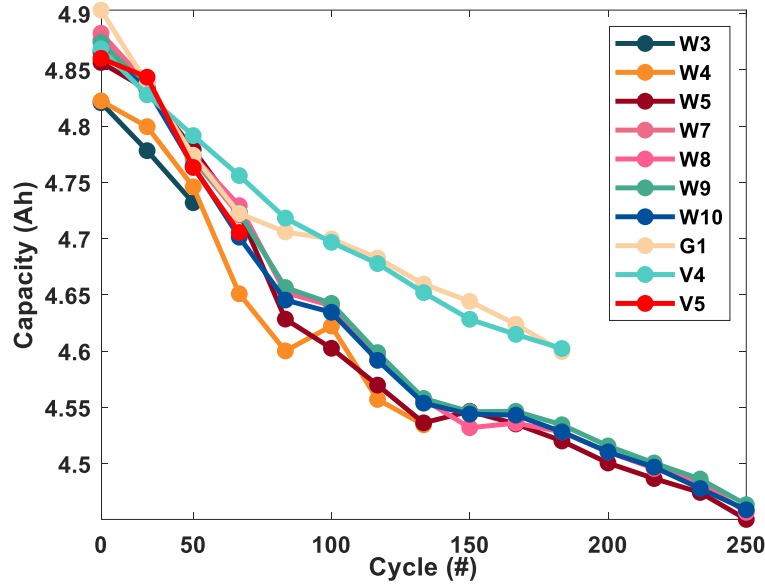


Figure 4.8 The discharge capacity of the Stanford dataset.

In this thesis, 24 LIBs selected from the NASA dataset (LIBs 2, 16, 17, and 18) were left out due to the presence of false data that caused specific cycles to have a negative duration ([284, 285]) and 8 LIBs were selected from Stanford University dataset (LIBs W3 and W7 were neglected since the cycling test was terminated for these two LIBs).

4.2.2 Empirical Wavelet Transform (EWT)

EWT is a relatively new signal decomposition method proposed by Gilles [286]. The EWT is an entirely adaptive advanced signal processing approach applied to decompose nonlinear and non-stationary signals into several multi-resolution modes by designing a suitable wavelet filter bank adapted to the processed signal (the charging/discharging voltage signal). The following steps are utilised for the execution of the EWT [286]:

1. The frequency spectrum $\hat{v}(\omega)$ of the real-time series signal $v(t)$ is obtained using the Fourier transform.
2. The Fourier spectrum is segmented to identify a predetermined number of EWT modes (N).

3. The number of EWT modes (N) is then compared with the number of local maxima (K) of the Fourier spectra: If $K > N$, then (N) a number of local maxima is taken for analysis. If $K < N$, then a smaller number of EWT modes are expected, and (N) is reset to an appropriate value.
4. To design the filters, the boundaries are computed by taking the midpoint of the sequential local maxima. The frequencies corresponding to local maxima are denoted by $\lambda = (\lambda_l)$, where l ranges from 1, 2... N .
5. The calculated boundaries are then used to create the N wavelet filter bank, which consists of one low-pass filter and ($N - 1$) bandpass filter. The empirical scaling function $\hat{\phi}_n(\omega)$ and empirical wavelet function $\hat{\psi}_n(\omega)$ corresponding to the low-pass and bandpass filters can be expressed as shown in (4.2) and (4.3), respectively.

$$\hat{\phi}_n(\omega) = \begin{cases} 1 & \text{if } |\omega| \leq \omega_n - \tau_n \\ \cos \left[\frac{\pi}{2} \beta \left(\frac{1}{2\tau_n} (|\omega| - \omega_n + \tau_n) \right) \right] & \text{if } \omega_n - \tau_n \leq |\omega| \leq \omega_n + \tau_n \\ 0 & \text{Otherwise} \end{cases} \quad (4.2)$$

$$\hat{\psi}_n(\omega) = \begin{cases} 1 & \text{if } \omega_n + \tau_n \leq |\omega| \leq \omega_{n+1} - \tau_{n+1} \\ \cos \left[\frac{\pi}{2} \beta \left(\frac{1}{2\tau_{n+1}} (|\omega| - \omega_{n+1} + \tau_{n+1}) \right) \right] & \text{if } \omega_{n+1} - \tau_{n+1} \leq |\omega| \leq \omega_{n+1} + \tau_{n+1} \\ \sin \left[\frac{\pi}{2} \beta \left(\frac{1}{2\tau_n} (|\omega| - \omega_n + \tau_n) \right) \right] & \text{if } \omega_n - \tau_n \leq |\omega| \leq \omega_n + \tau_n \\ 0 & \text{Otherwise} \end{cases} \quad (4.3)$$

β is an arbitrary $\mathbb{C}^k([0,1])$ function and ω is the instant frequency value. ω_n represents the centre frequency of N^{th} segment; likewise, ω_{n+1} denotes the centre frequency of $(N + 1)^{th}$ segment. $2\tau_n$ is the width of the transition phase interval between two sequential frequency segments with centre frequency ω_n . Now, the EWT coefficients $\mathcal{W}_f^\varepsilon(n, t)$ can be defined similarly to the traditional wavelet transform. The inner product of the signal with the scaling function calculates the approximation coefficients.

$$\mathcal{W}_f^\varepsilon(n, t) = \langle f, \psi_n \rangle = \int f(\tau) \overline{\psi_n(\tau - t)} \quad (4.4)$$

$$= \left(\hat{f}(\omega) \overline{\hat{\psi}_n(\omega)} \right)^v \quad (4.5)$$

Where $\psi_n(\omega)$ is the frequency spectrum of the scaling function $\psi_n(t)$, and $\hat{f}(\omega)$ is the Fourier transform of the signal $f(t)$. The inner products of the signal with the empirical wavelet calculate the detail coefficients of the EWT.

$$W_f^\varepsilon(n, t) = \langle f, \psi_n \rangle = \int f(\tau) \overline{\psi_n(\tau - t)} \quad (4.6)$$

$$= \left(\hat{f}(\omega) \overline{\hat{\phi}_1(\omega)} \right)^v \quad (4.7)$$

Where $\phi_l(\omega)$ is the Fourier counterpart of the wavelet function, $\phi_l(t)$.

Furthermore, since LIB defects might develop at any point in the cycling process, it's crucial to employ battery health monitoring in a partial voltage signal to track the status of the LIB in real time. With this in mind, the voltage profile collected throughout a single charge and discharge cycle was segmented into 1-hour ($\Delta t = 1h$) buffers to facilitate rapid monitoring and feature extraction. It is worth to mention that the selection of the buffer size has been done by comparing different buffer's size and it is found that 1h buffer size is suitable to extract the health features from the measured voltage signal.

4.2.3 Fundamental Mode Filtering

As illustrated in Figure 4.2, the proposed approach begins by decomposing the measured voltage. $v_n(t)$ into N modes, where at least one of the obtained modes is similar or 'closer' to the original measured voltage signals; this mode is known as the fundamental mode. Thus, the LIB measured voltage $v_n(t)$ can be expressed as:

$$v_n(t) = \sum_{i=1}^n Mode_i(t) + Mode_f(t) + res(t) \quad (4.8)$$

Where, f in $Mode_f(t)$ refers to the fundamental between n modes. Hence, the need to remove the fundamental mode that is common in healthy and aged states of the LIB. Therefore, the measured voltage signal is:

$$v_c(t) = v_n(t) - Mode_f \quad (4.9)$$

The Pearson correlation coefficient algorithm is applied to determine the fundamental mode among other modes [287]. The Pearson correlation coefficient quantifies the linear dependence between two N-dimensional random variables, x and y. The ρ -correlation coefficient varies between 1 and -1, considered positive and negative, respectively. Pearson correlation coefficient is calculated as follows:

$$\rho(x, y) = \frac{\sum(x_n - \bar{x})\sum(y_n - \bar{y})}{\sqrt{\sum(x - \bar{x})^2}\sqrt{\sum(y_n - \bar{y})^2}} \quad (4.10)$$

Where \bar{x} and \bar{y} are the mean values of x_n and y_n , respectively.

4.2.4 Feature Extraction and Selection

The purpose of the feature extraction and selection procedure is to minimise the dimensionality of the input data by generating metrics that indicate the most significant factors influencing the capacity degradation of LIBs. 13 statistical features (health indicator) were extracted from the filtered voltage signal $v_c(t)$. Table 4.4 presents the mathematical definitions of the extracted features.

Table 4.4 Extracted characteristics features.

No.	Name	Feature formula	No	Name	Feature formula
F_1	Clear ance Factor	$\frac{\max v_c(t) }{\left(\sum_{i=1}^N \sqrt{v_c(t)} / N\right)^2}$	F_2	Crest Factor	$\frac{\max v_c(t) }{\sqrt{\sum_{i=1}^N v_c(t)^2} / N}$
F_3	Impul se Factor	$\frac{\max v_c(t) }{\sum_{t=1}^N v_c(t) / N}$	F_4	Kurtosis	$\frac{\frac{1}{N} \sum_{i=1}^N (v_i - \bar{v})^4}{\left[\frac{1}{N} \sum_{i=1}^N (v_i - \bar{v})^2\right]^2}$

F_5	Mean	$\sum_{i=1}^N v_c(t)/N$	F_6	Peak value	$\max v_c(t) $
F_7	RMS	$\sqrt{\sum_{i=1}^N v_c(t)^2/N}$	F_8	SINAD	$\frac{P_{signal} + P_{noise} + P_{distortion}}{P_{noise} + P_{distortion}}$
F_9	SNR	$10\log_{10}\left(\frac{\text{signal amplitude}}{\text{noise amplitude}}\right)$	F_{10}	Shape Factor	$\frac{F_7}{\sum_{i=1}^N v_c(t) /N}$
F_{11}	Skewness	$s = \frac{\frac{1}{N} \sum_{i=1}^N (v_i - \bar{v})^3}{\left[\frac{1}{N} \sum_{i=1}^N (v_i - \bar{v})^2\right]^{3/2}}$	F_{12}	SD	$\sqrt{\frac{\sum_{i=1}^N (v_i - \bar{v})^2}{N - 1}}$
F_{13}	THD	$\frac{\sum \text{harmoinc power}}{\text{fundamental freuqncy pow}}$			

However, not all these features certainly contribute to the target output ‘‘capacity’’. Some of the extracted features are redundant and will increase the computational cost of the system. Therefore, the feature selection step is significantly essential to prioritise the characteristics that have the most significant impact on the capacity degradation of the LIB and disregard the less useful features. Principal component analysis (PCA) is one of the most applied techniques for dimensionality reduction [288]. However, in this work, PCA did not apply to the extracted features since it would construct linear combinations of inputs. For the sake of simplicity, we wanted to rank individual features directly rather than ranking combinations of features [289]. Therefore, the Pearson correlation approach is selected again to measure the similarity between the extracted features and the target output (capacity). The values of Pearson’s correlation coefficients are employed to rank the extracted features. Then, each feature F_i is given a score (a value between -1 and 1), based on their Pearson correlation coefficients with respect to the

capacity and ranked based on its score. In this study, the extracted feature is considered and selected as a hopeful feature if its absolute score is greater than 0.85.

The LIBs were cycled for M randomised current profiles during the ageing experiment, and each has been segmented into L buffers. Therefore, the number of whole buffers is $N = L \times M$. These buffers are explored to apply EWT and extract health indicators. Afterwards, $F = 13$ health indicators (presented in Table 4) are calculated for each buffer. As such, the input vector feature to the LSTM model is designed to be as follows:

$$F = \begin{bmatrix} F_{1,1} & F_{1,2} & F_{1,3} & \cdots & F_{1,13} \\ F_{2,1} & F_{2,2} & F_{2,3} & \cdots & F_{2,13} \\ \vdots & F_{3,2} & F_{3,3} & \ddots & \vdots \\ F_{N,1} & F_{N,2} & F_{N,3} & \cdots & F_{N,13} \end{bmatrix} \quad (4.11)$$

Where F denotes the extracted health feature. Each row of the extracted feature in F has a corresponding discharge capacity $[C_1 \ C_2 \ \cdots \ C_N]$ that serves as the true output of the LSTM model.

4.2.5 Long Short-Term Memory Neural Network (LSTM)

LSTM is a specialised recurrent neural network (RNN) model. Compared to classic RNN, LSTM has added a cell state C to the hidden layer, which overcomes the problem that RNN processing lengthy sequence data is susceptible to gradient disappearance or gradient explosion, consequently enhancing the estimation accuracy [290]. The LSTM structure is depicted in Figure 4.9, and each component will be detailed in depth below.

The internal state C , located in the middle of each linearly excited neuron, is the essential component of LSTM. It is possible to think of it as a carrier via which either newly added information or information that has been withdrawn is eliminated. "Gates" are the structures responsible for appropriately managing the flow of information throughout this procedure [290].

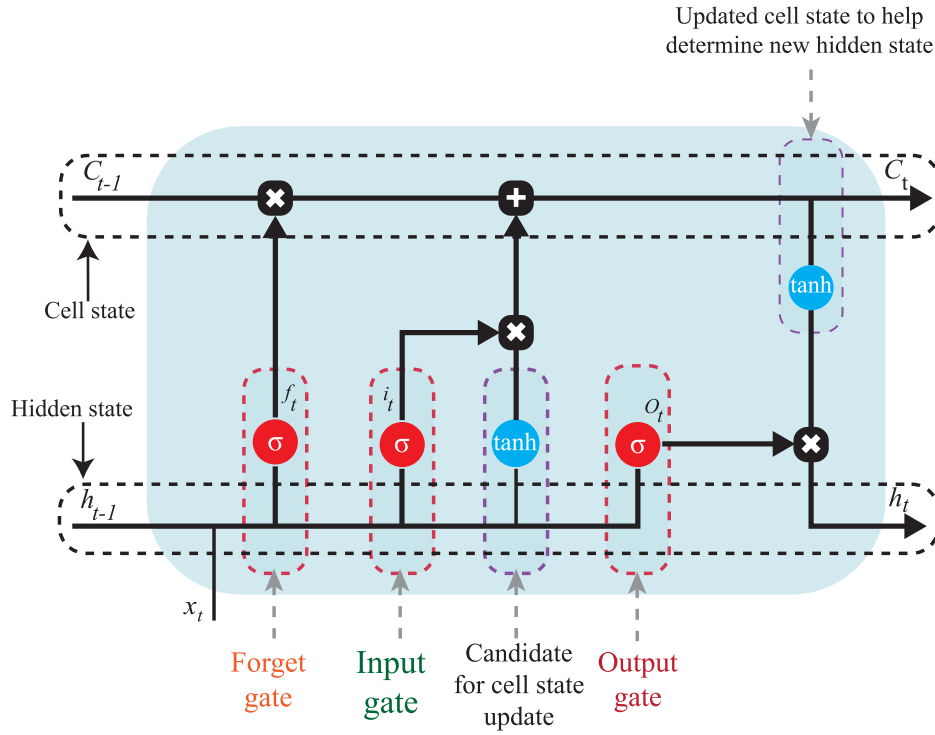


Figure 4.9 LSTM structure.

Forget gate: The initial phase of LSTM is determining which data should be discarded. In particular, the inputs of the forget gate are x_t and h_{t-1} , while the output is a number between 0 and 1. A value of 1 denotes that the state value is fully maintained, whereas a value of 0 implies that the state value is fully discarded. The mathematical definition of the forget gate can be expressed as follows [291]:

$$f_t = \sigma(W_{fx}x_t + W_{fh}h_{t-1} + b_f) \quad (4.12)$$

Where σ is the sigmoid activation function, W_f denotes the weight matrix, x_t is the input of the current timestep, h_{t-1} is the hidden output state of the LSTM at the previous timestep, and b_f represents the bias value of the forget gate.

The following phase, which belongs to the input gate, is to ascertain what new data have been added to the internal state. This stage is divided into two distinct steps. In the first step of the process, a sigmoid layer called the input gate decides which value should be updated, and in

the second step, a tanh layer decides which value should be added to the state. The output of the first step i_t and the second step \tilde{c}_t can be expressed as follows:

$$i_t = \sigma(W_{ix}x_t + W_{ih}h_{t-1} + b_i) \quad (4.13)$$

$$\tilde{c}_t = \tanh(W_c[h_{t-1}, x_t] + b_c) \quad (4.14)$$

Where σ and \tanh are the sigmoid activation function, W denotes the weight matrix, x_t is the input of the current timestep, h_{t-1} is the hidden output state of the LSTM at the previous timestep, and $b_{i,c}$ represents the bias value of the input gate.

By combining the above Eqs. (4.12-4.14), the previous internal state c_{t-1} is updated to the current state c_t as follows:

$$c_t = f_t * c_{t-1} + i_t * \tilde{c}_t \quad (4.15)$$

Where f_t represents the output value of the forget gate at time t , c_{t-1} is the long-term state of the unit at time $t - 1$, i_t is the output value of the input gate at time t \tilde{c}_t is the current unit state at time t .

As the final stage in the process, the output gate uses a sigmoid layer to decide what data to output.

$$o_t = \sigma(W_{ox} + W_{oh}h_{t-1} + b_o) \quad (4.16)$$

Where σ is the sigmoid activation function, W_o denotes the weight matrix, h_{t-1} is the hidden output state of the LSTM at the previous timestep, and b_o represents the bias value of the output gate.

$$h_t = o_t * \tanh(c_t) \quad (4.17)$$

Where o_t represents the actual value of the output gate at the time t , and c_t denotes the long-term state of the unit at time t [291].

The weights and bias parameters presented in Eqs (4.12-4.16) are tuned and updated by applying the Adam optimiser. In addition, the dropout technique is employed to avoid the

overfitting problem during the training process of the LSTM model [185]. Figure 4.10 shows the structure of the developed LSTM model used in this chapter.

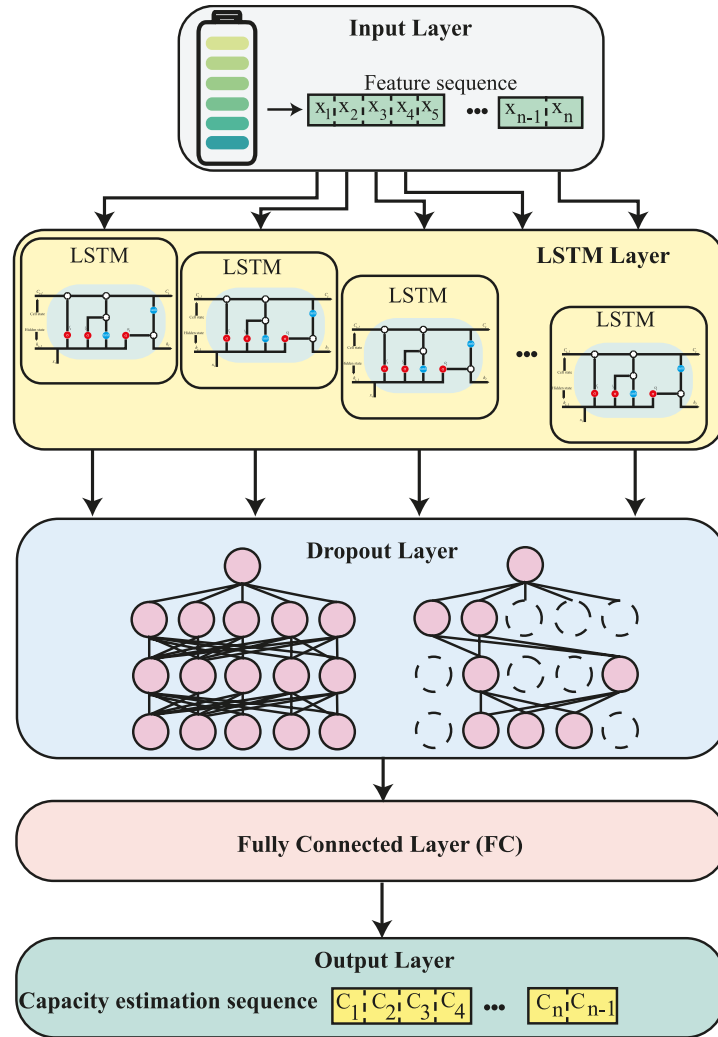


Figure 4.10 The structure of the designed LSTM model.

4.2.6 Evaluation Criteria

The cross-validation (CV) method is used to evaluate the accuracy of the developed LSTM model [292]. In cross-validation, data is randomly divided into K folds; each is repeatedly used for training and validation. The aim behind the folds is to use each portion of the dataset at least once for validation, even though they are independent subsets. In this work, the accuracy

of the developed LSTM model was evaluated using nine- folds cross-validation, as shown in Figure 4.11. Specifically, the dataset of NASA was first divided into seven mutually exclusive folds corresponding to the seven cycling groups as described in subsection 4.1.1.

Moreover, the dataset of Stanford University was divided into two folds, whereas each fold includes 4 LIBs. Figure 4.11 shows that the nine iterations were executed, each including training, validation, and testing. One LIB was set aside for testing, and the remaining LIBs were split 70:30 between a training and validation set.

Root Mean Squared Error (RMSE) and Absolute Error (AE) were utilised to evaluate the accuracy of the proposed technique for estimating the capacity of LIBs. These evaluation criteria are expressed as follows:

$$RMSE = \sqrt{\frac{1}{N} \sum_{i=1}^N (\hat{C}_i - C_i)^2} \quad (4.18)$$

$$AE = |(\hat{C}_i - C_i)| \quad (4.19)$$

Where \hat{C} and C_i denote the estimated and actual capacity of LIBs, respectively, N is the number of data points.

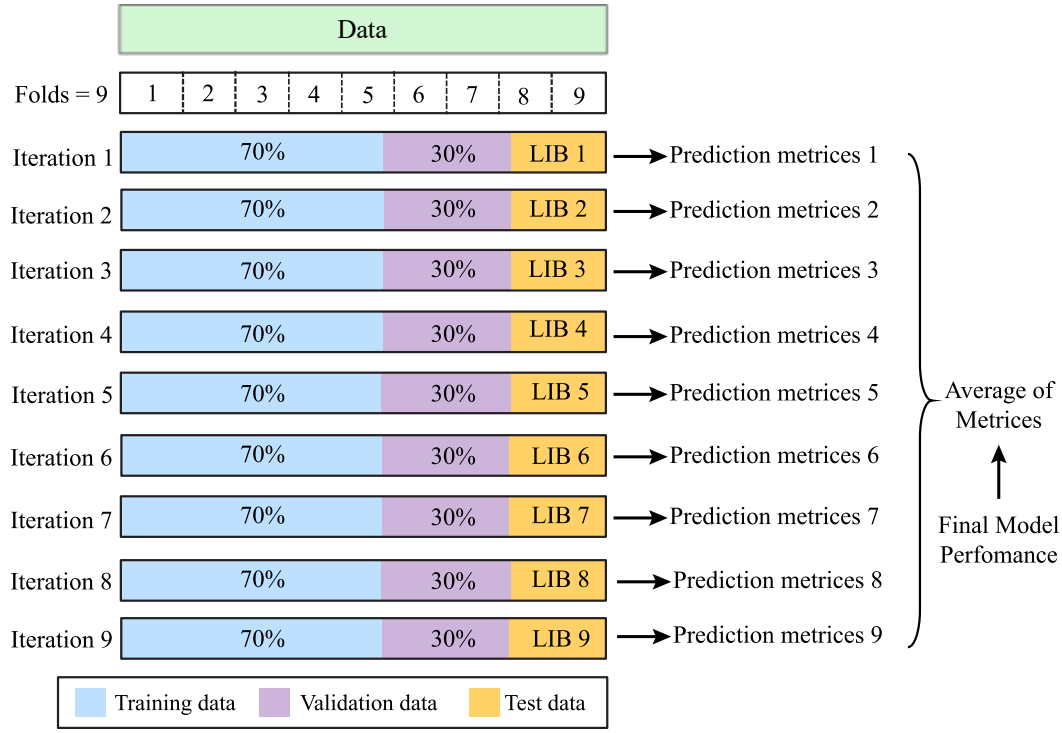


Figure 4.11 Cross-validation approach for training, validating, and testing the LSTM model. In each cross-validation iteration, one LIB was selected as the test set.

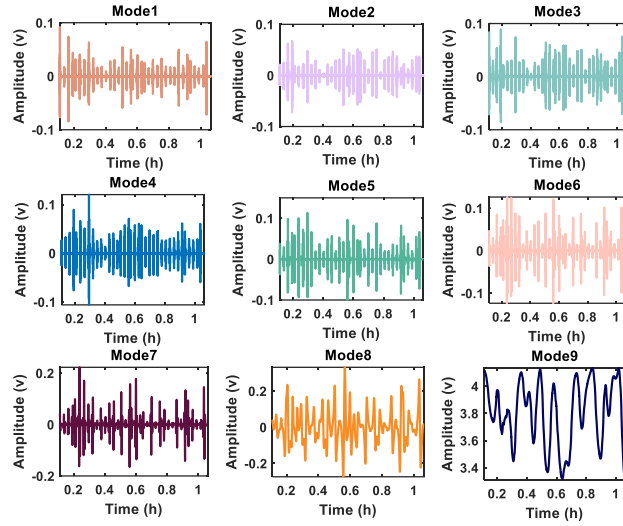
4.3 Results and Discussion

4.3.1 EWT Results

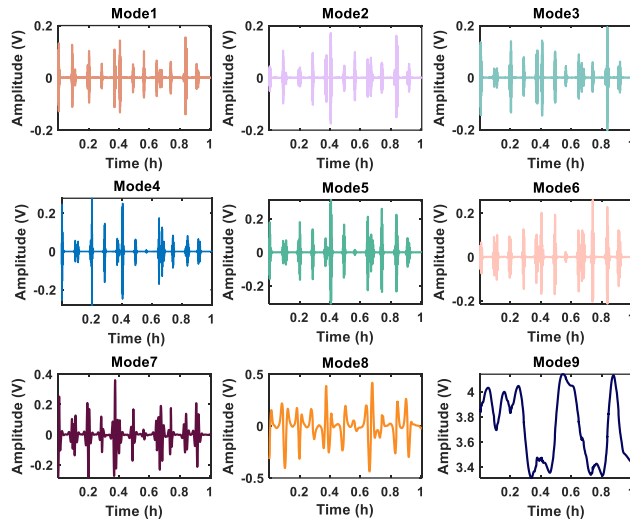
The proposed approach of the EWT-based characteristic analysis of LIBs is newly introduced. The proposed method is applied to 32 LIBs from two datasets that cycled at several current profiles and temperatures. The EWT has applied to the charge/discharge measured voltage with the time-frequency domain, allowing the individual characteristics of each measured voltage signal to be seen more clearly. The MRA decomposition process is implemented to extract information from these phenomena for analysing and evaluating the voltage signal with nonstationary and transients phenomena. Figure 4.12(a) and (b) show the corresponding EWT modes of the measured voltage for battery RW9 at its first cycle ($C=2.1$ Ah) and last cycle (0.8 Ah), respectively.

As shown in Figure 4.12(a), the EWT method has decomposed the measured voltage signal into nine modes with different resolution levels. The first four modes in Figure 4.12(a) represent the high-frequency components of the decomposed measured voltage. In contrast, the rest of the other modes (mode 5 - mode 9) show the low-frequency components of the measured voltage of the LIB. In the same way, the first four modes in Figure 4.12(b) show the high-frequency components, and the last four modes illustrate the low-frequency components of the measured voltage signal for battery RW9 at its last cycle. By comparing the obtained EWT modes of the same battery at different capacity values, it is clear that comprehensive information can be extracted from each mode. For example, the variation of the high-frequency components of the LIB can be seen in the first and last cycles (Figure 4.12(a) and Figure 4.12 (b)). Moreover, it can be seen that the high-frequency components can detect the transient in the measured voltage signal better than the low-frequency components.

The centre frequencies and bandwidth of the decomposed voltage using EWT at the first and last cycles are illustrated in Figure 4.13(a) and Figure 4.13(b), respectively. It is important to note that the first five high-frequency modes (modes 1 - 5) show a clear difference in the amplitude and the phase between the BOL and EOL decomposed signals. In contrast, the last four low-frequency modes (modes 6 - 9) do not show the difference in amplitude or phase between the BOL and EOL decomposed signals. One of the fundamental advantages of using signal decomposition is its ability to separate the components with maximum degradation characteristics. As shown in both figures, the frequency band of each mode is 5 Hz since the sampling frequency of the experimental dataset is 10 Hz. Therefore, due to the field's sample rate restrictions, the measured sensor's discharge voltage contains only low-frequency information. In contrast, high-frequency information is absent from the data, this is because the collected data from the BMS is collected using low sampling frequency rate (10Hz). Therefore, due to the low sampling frequency rate limitation, only the low frequency range can be calculated from the measured voltage signal. A recently published study by Li et al.[293] found that the reconstructed EIS from the measured field data (voltage and current) only contained low-frequency information.



(a)



(b)

Figure 4.12 EWT decomposition modes of the measured voltage for battery RW9 at its (a) first cycle and (b) last cycle.

Moreover, it is found that the information in the low-frequency part can be linked with the cause of the degradation inside the LIB, such as the diffusion-reaction and mass transfer process.

According to [235], the information in the low-frequency band range is related to the diffusion-reaction and mass transfer process inside the active particles of the LIB. The diffusion-reaction process is a critical factor that directly impacts the capacity degradation of the LIBs [294]. The above discussion highlights the ability of the proposed EWT to extract more hidden information from the measured voltage signal, and the obtained information can be linked to the cause of the ageing inside the LIBs.

Moreover, the obtained central frequencies result in Figure 4.13(a) and Figure 4.13(b) shows that not all the extracted modes by EWT can be used for the feature extraction of the capacity degradation for the LIBs. Therefore, in this context, the fundamental mode identification step uses the Pearson correlation coefficient between each decomposed mode and the original measured voltage signal $v_n(t)$.

The fundamental mode is then subtracted from $v_n(t)$ leading to the filtered voltage signal $v_c(t)$. Afterwards, the filtered voltage signal is used for feature extraction and capacity estimation. Figure 4.14 shows an example of the calculated similarity between the measured voltage and the decomposed intrinsic mode functions (IMF) for 6 LIBs from two groups of NASA in the BOL and EOL status. As shown in Figure 4.14, IMF8 and IMF4 are the most correlated IMF with the measured voltage. It can be seen that IMF8 and IMF9 are the common IMFs in the BOL and EOL status of the LIB. Therefore, removing the common IMFs between the healthy and aged status of the LIBs would enhance the quality of the extracted features from the filtered voltage signal. The extracted features related to ageing are presented in the following subsection. The relationship between the extracted IMFs and the measured voltage signal has been examined using Pearson correlation. It should be noted that utilizing other correlation methods, like Spearman correlation coefficient, might reveal a stronger connection with the eliminated IMFs.

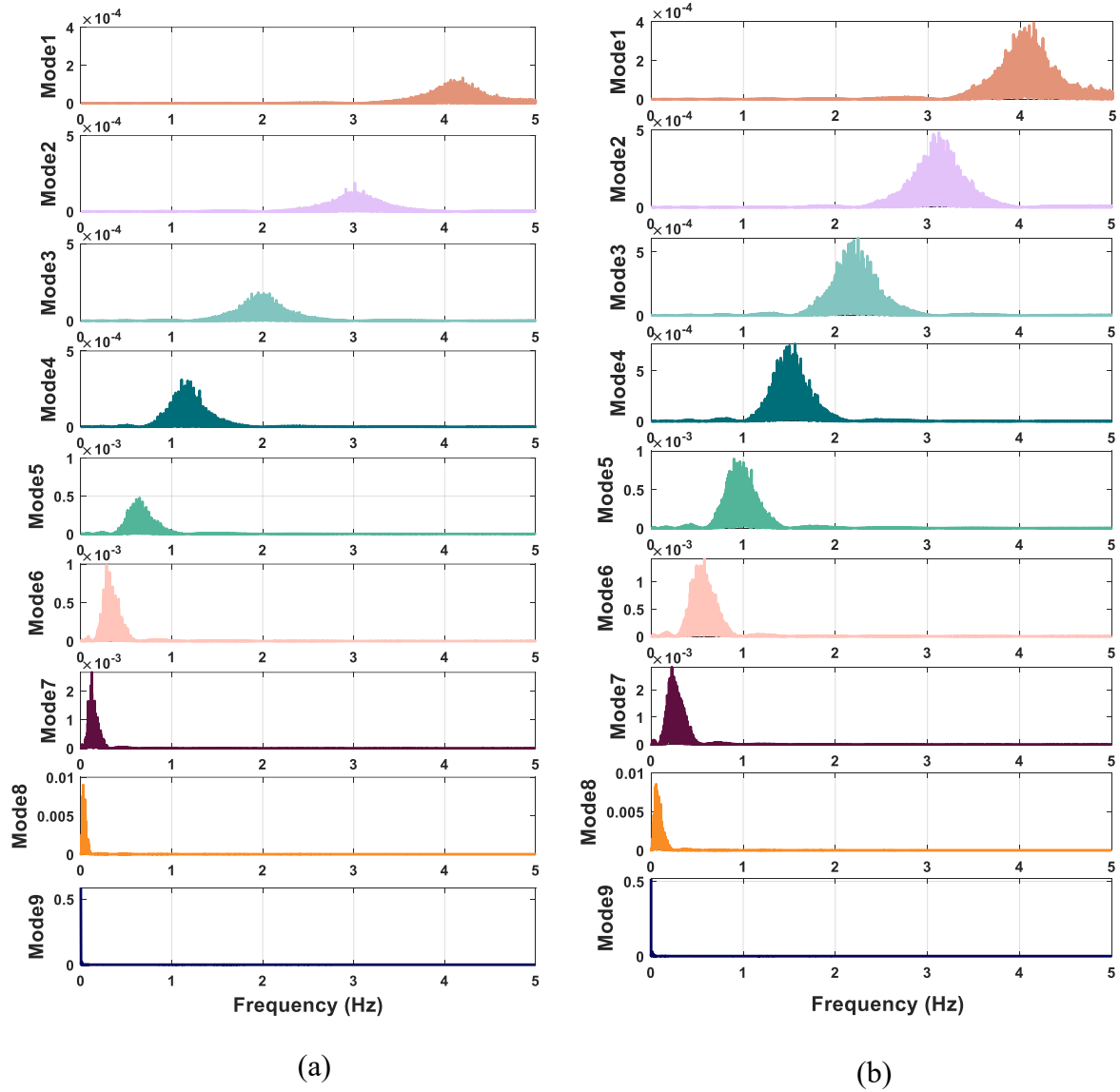


Figure 4.13 Central frequencies and bandwidth of EWT decomposition for battery RW9 at its (a) first cycle and (b) last cycle.

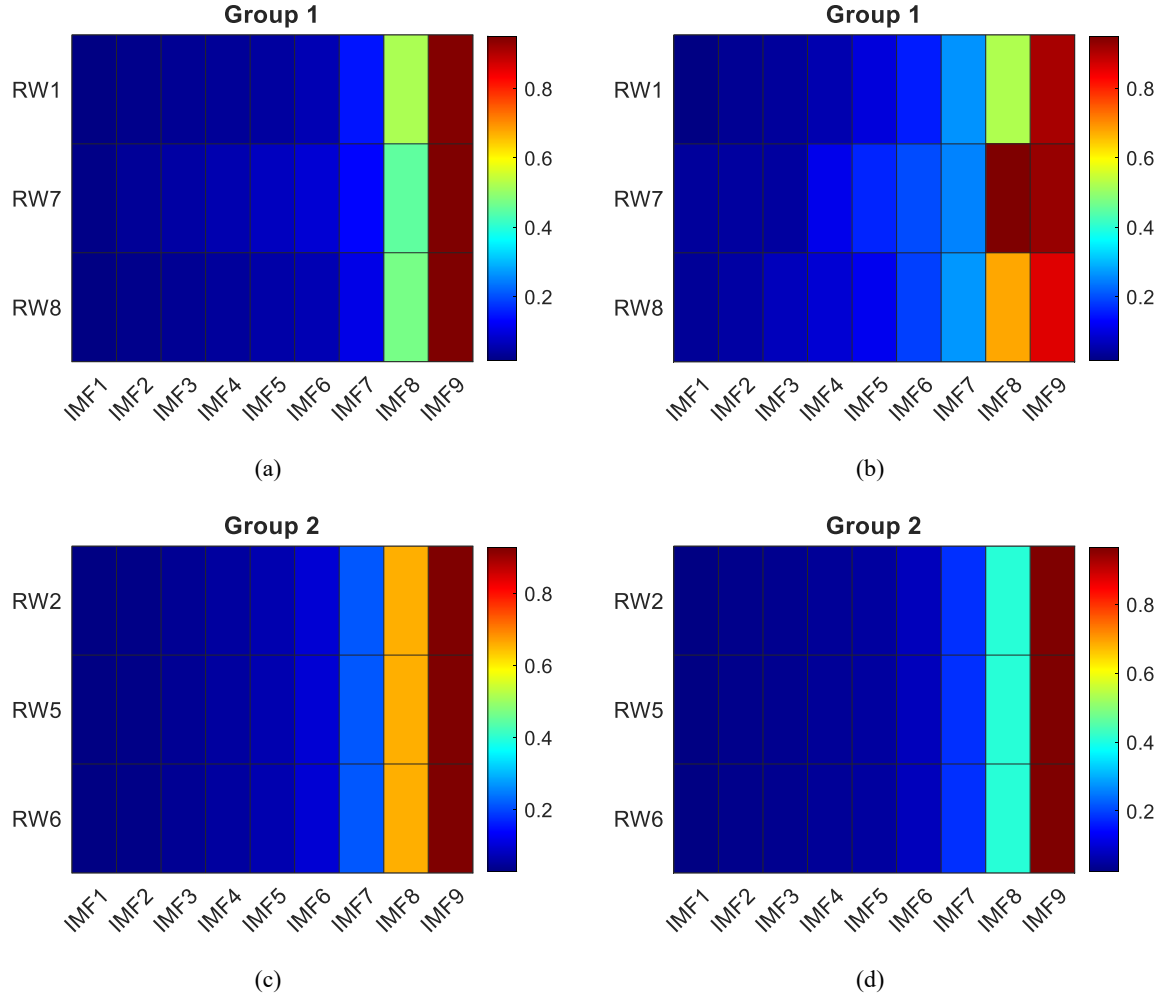


Figure 4.14 Example of the correlation between the IMFs and measured voltage. (a) and (c) the IMFs at the BOL, (b) and (d) the IMFs at the EOL of the LIBs.

4.3.2 Features Extraction Results

Once the filtered voltage signal $v_c(t)$ is obtained from the EWT approach, the filtered voltage signal can be used for the statistical features extraction step. 13 statistical features have been calculated in this work, as presented in Table 4.4. Figures 4.15 and 4.16 show an example of the trends for 13 extracted features throughout the life of LIBs cycled for LIB RW1 from the NASA dataset and LIB W8 from the Stanford University dataset. The detected obtained trajectories for the calculated features throughout the LIBs' life strongly correlate with the battery's capacity degradation, even if the battery cycled at an entirely different current profile

or operating condition. As shown in both Figures 4.15 and 4.16, some features, such as F2, show an apparent reduction in value over the LIB lifetime.

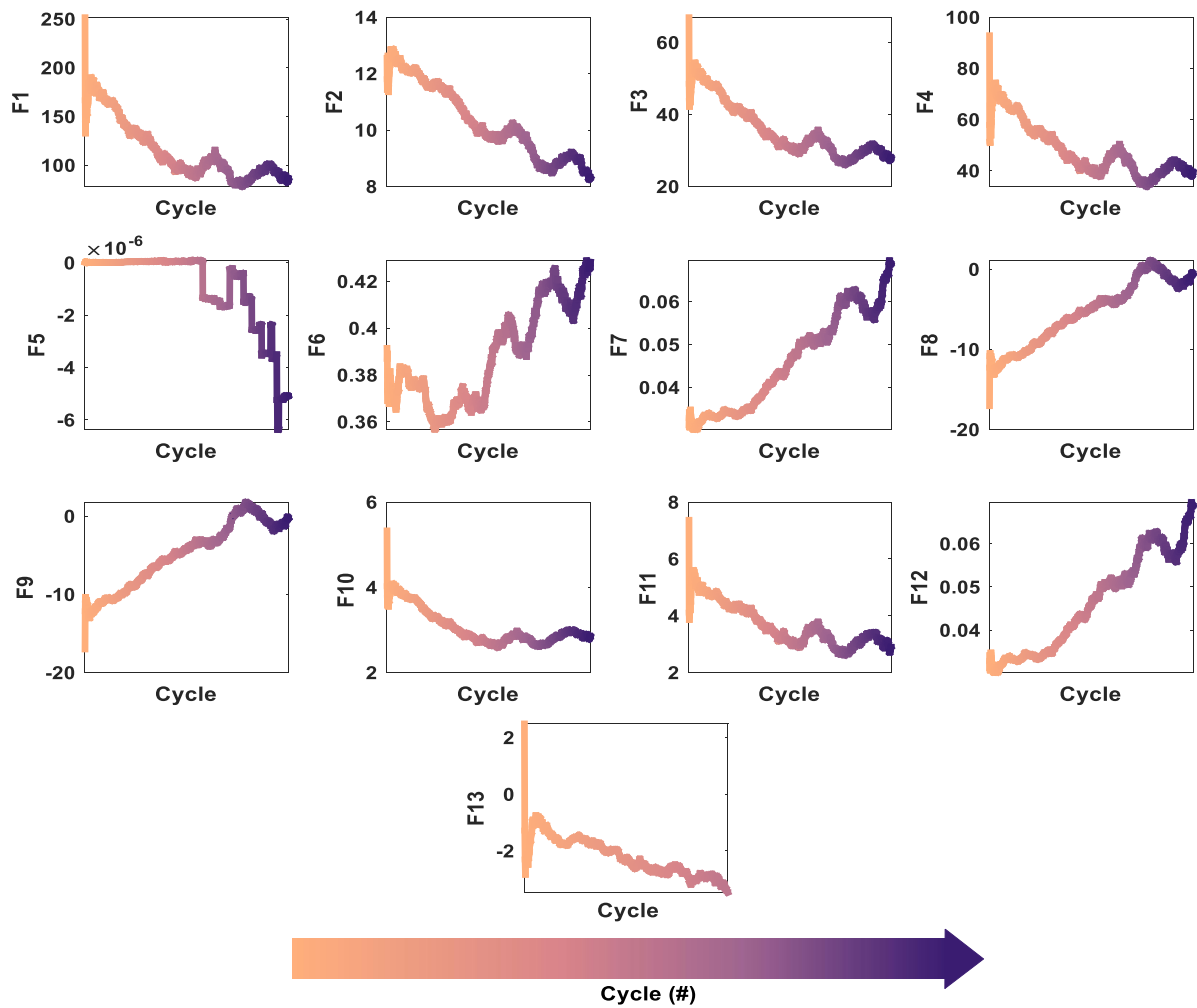


Figure 4.15 Example visualisation of the 13 extracted features for LIB RW1 in group 1 from the NASA dataset.

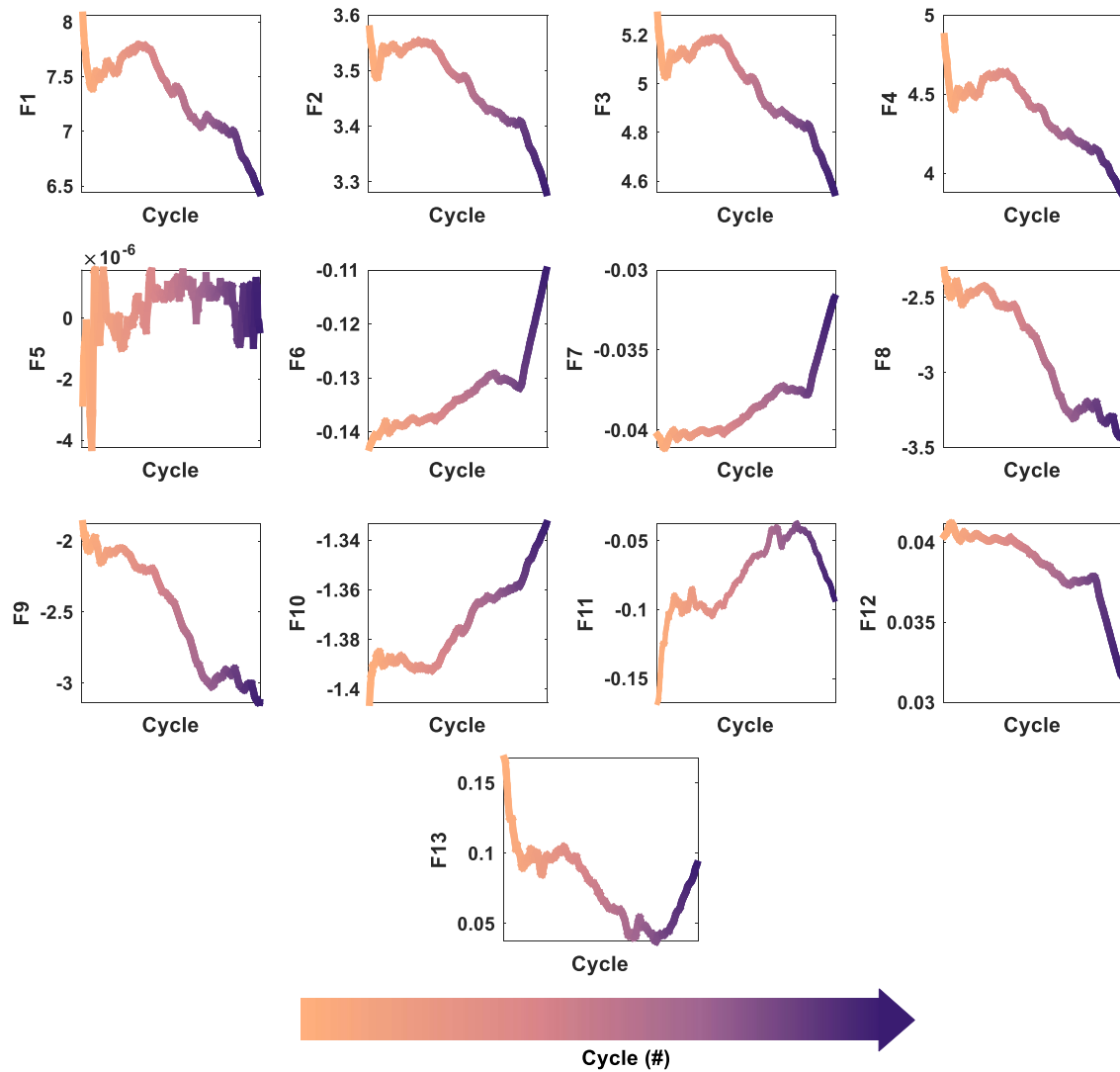


Figure 4.16 Example visualisation of the 13 extracted features for LIB W8 in Stanford University's dataset.

Moreover, physically, the LIB systems addressed by each dataset (NASA and Stanford datasets) have been subjected to distinctly varied cycle circumstances and usage patterns. Thus, as a result, they may display diverse ageing characteristics. When greater randomness is added to the cycle patterns, the LIB systems often display more ageing characteristics [285].

However, not all the extracted features are contributed to capacity degradation. For example, feature F5 in both datasets is not shown a clear relation to the capacity degradation of the LIB.

Therefore, the Pearson correlation coefficients method is applied to the extracted features pool for dimension reduction to reduce training time and improve the trained model estimation accuracy. Figure 4.17 shows the Pearson correlation coefficients of the extracted features for all the selected LIBs from the NASA and Stanford University datasets. As presented in Figure 4.17, some of the extracted features have small correlation coefficient values with respect to the capacity degradation of the LIB. Therefore, excluding these features would significantly improve the estimation accuracy of the trained model and reduce the computational complexity. As for the feature selection process, the absolute values of the Pearson correlation coefficient equal to or above 0.85 are selected for the model training and capacity estimation process [295]. In this way, the extracted features with low correlations values (less than 0.85) are removed to reduce the negative influence of unrelated information on estimation accuracy. Notably, the feature extraction process has been implemented on a parallel pool of workers on the multi-core computer to reduce the computational time of the feature extraction from all voltage signals.

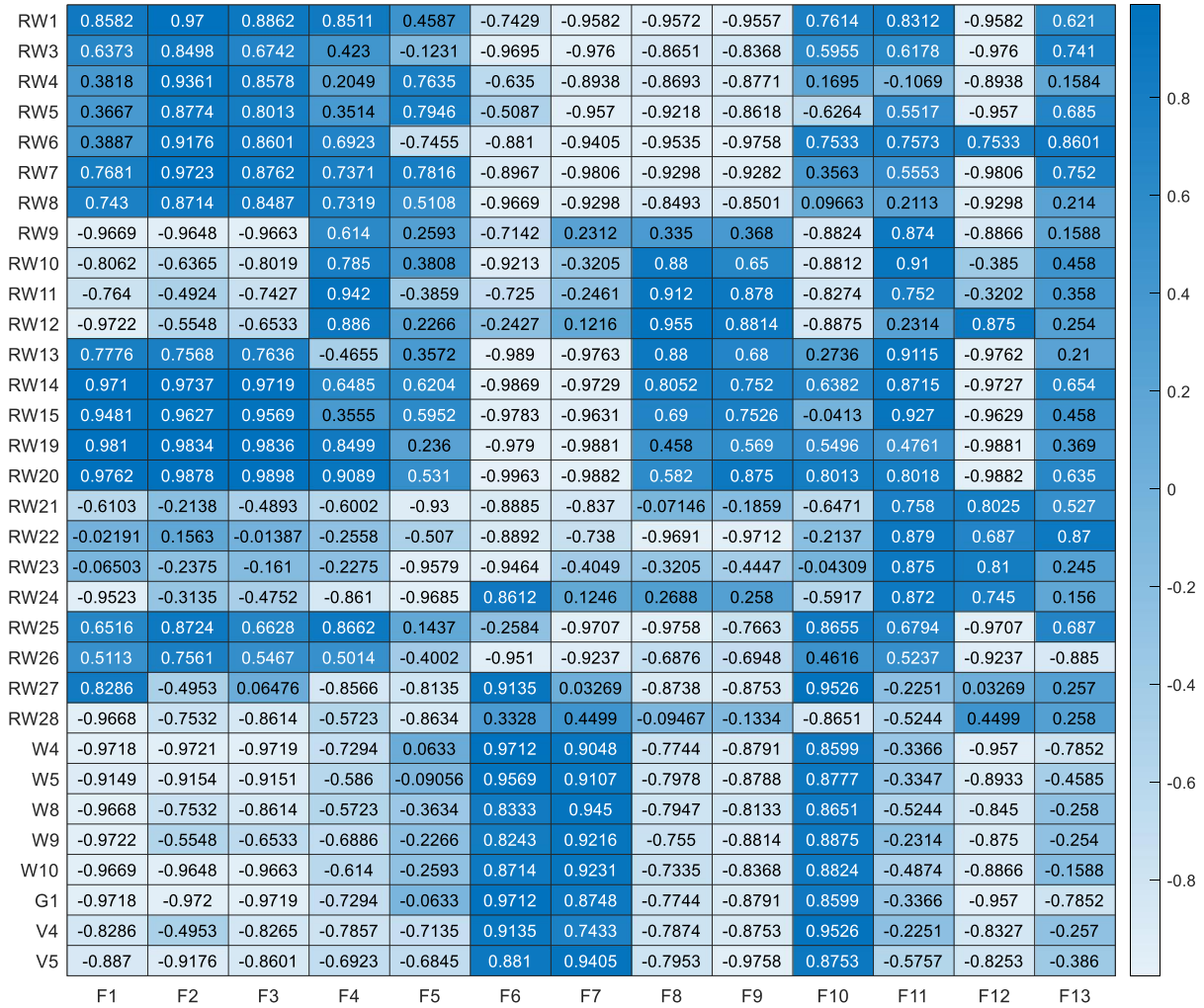


Figure 4.17 The correlation matrix of the extracted features for all the selected LIBs from the NASA and Capacity Estimation Results

4.3.3 Capacity Estimation Results

Two case studies are reported here to analyse the LSTM model's performance for the capacity estimation of LIB. One with normal input data (noise-free) and the other one with the addition of zero-mean additive white Gaussian noise (AWGN) with a mean standard deviation (σ) of 5% to the measured voltage signal. Moreover, CWT and DWT techniques have been applied in both case scenarios to demonstrate the effectiveness of the EWT technique in battery data analysis compared with other wavelet transform methods. Morlet and Daubechies (DB3)

wavelets were selected as mother wavelets to analyse the measured voltage for CWT and DWT methods, respectively.

4.3.3.1 Capacity Estimation for The First Scenario

Figure 4.18 shows the estimation results of 9 LIBs known as RW1, RW4, RW9, RW14, RW19, RW22, RW25, W5, and W9. It is worth mentioning that the first five LIBs (RW1, RW4, RW9, RW14, and RW19) have been cycled at room temperature (25 °C), the RW22 and RW28 have been cycled at (40 °C), and the last two LIBs (W5 and W9) have been cycled at (23 °C). As mentioned in Section 4.2, the aim of the proposed method is to estimate the LIB's capacity at various cycling and temperature working conditions; thus, the testing dataset is chosen to show how the trained LSTM model will behave these three different temperature values. Due to the absence of other temperature ranges in the dataset, the efficacy of the proposed method is evaluated only for the temperature ranges listed above. Therefore, further investigation is required to assess the accuracy of the proposed method at various temperature ranges.

As shown in Figure 4.18, the estimated capacity results of all tested LIBs are very close to the actual or measured capacity curves. The RMSE and AE of each tested LIBs are presented in Table 4.5. The lowest RMSE is 0.44%, and the highest estimation RMSE is 1.84% for battery number RW14. Moreover, the maximum absolute estimation error is 4.98% for RW9, as shown in Table 4.5, and the average capacity estimation errors are 1.26% and 2.74% for RMSE and max error, respectively. Figure 4.18 shows that the trained LSTM model can accurately capture the regenerated capacity of the LIBs. For example, in RW4 and RW9, it can be seen that the capacity of the LIBs is slightly increased. The physical explanation of this capacity regeneration phenomenon is still unclear; it could be an artefact of the measuring procedure, such as when reference tests are performed. However, regardless of the reasons, accurate estimation for the regenerated capacity of the LIBs is significantly important since the capacity measurement provided in a practical application may exhibit similar behaviour. Moreover, Figure 4.18 shows that the LIBs that cycled at (40 °C) have degraded faster than the LIBs that cycled at (25 °C). This observation is clearly apparent in Figure 4.18 for the LIBs RW22 and

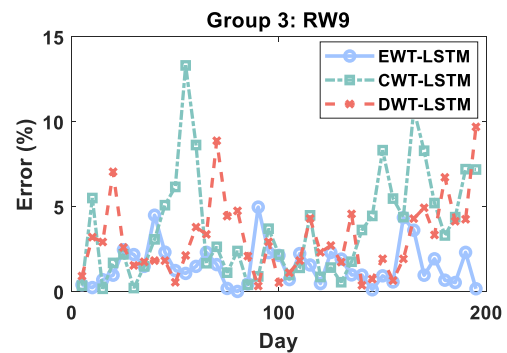
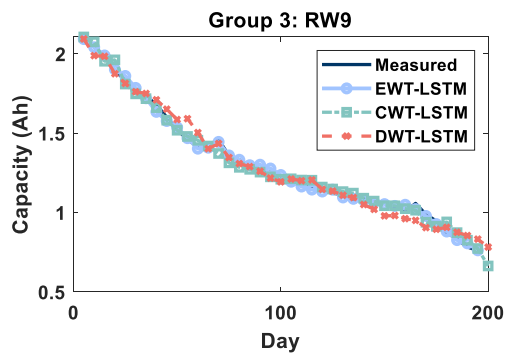
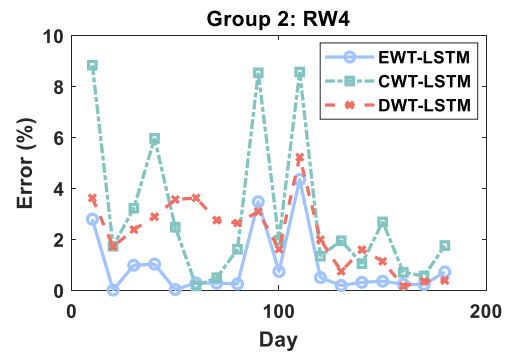
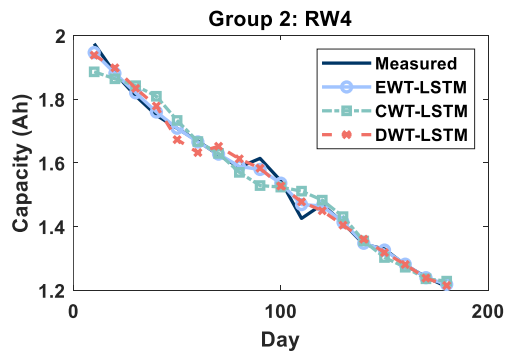
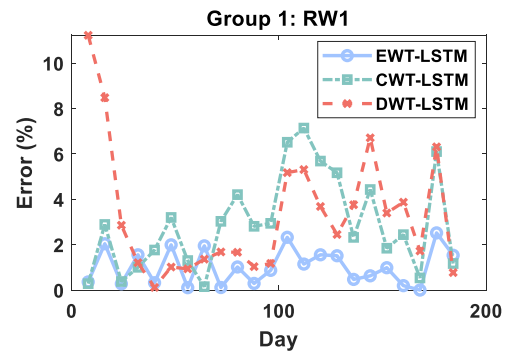
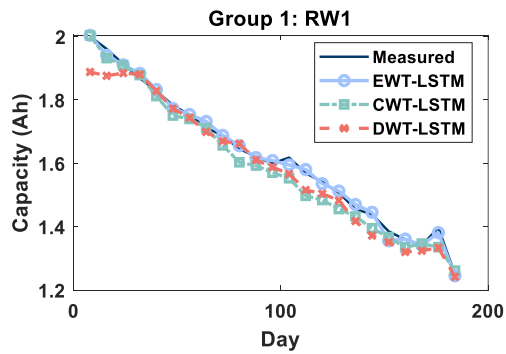
RW25. However, according to the obtained results in Table 4.5, the proposed method is robust under different operating temperatures.

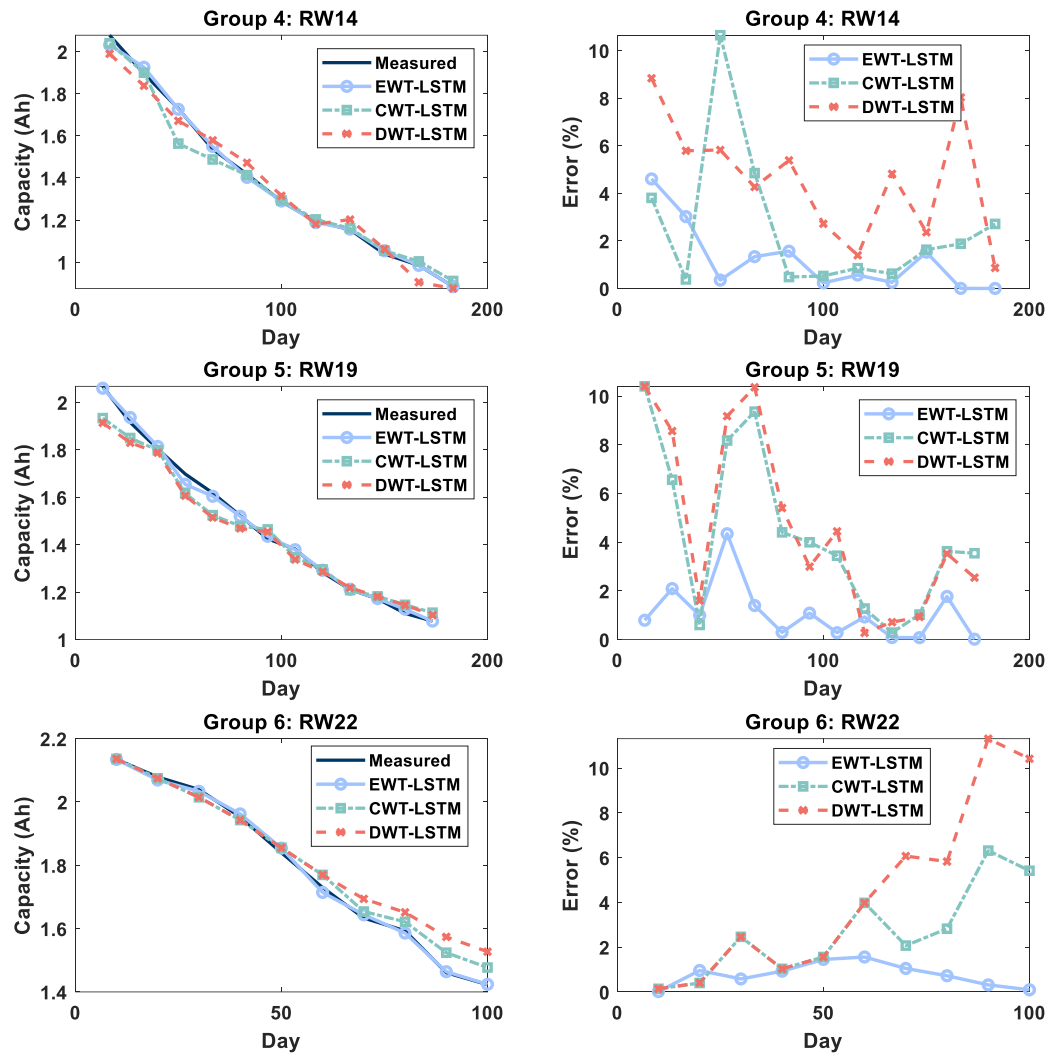
By comparing the results of the EWT-LSTM method to the other CWT-LSTM and DWT-LSTM wavelet transforms methods, it is clearly seen that the proposed EWT-LSTM method can significantly improve the capacity estimation accuracy of the LIBs. In detail, the average RMSEs of CWT-LSTM and DWT-LSTM are 4.19% and 4.61%, while the average RMSE of EWT-LSTM was 1.26%. Moreover, the proposed EWT-LSTM has shown it is superior to both CWT-LSTM and DWT-LSTM, with AE decreases of 67.22% and 68.02%, respectively. This improvement in the capacity estimation accuracy of LIB is due to the power of adaptability of the EWT technique in decomposing the voltage signal. No special requirement like the mother wavelet selection process is needed since EWT can directly construct its own basis functions based on the measured voltage signal. Thus, this adaptive basis function avoids needing a predefined mother wavelet.

Table 4.5 RMSEs and AEs of the capacity estimation results in a noise-free scenario.

Battery name	Criteria	EWT-LSTM	CWT-LSTM	DWT-LSTM
RW1	RMSE (%)	1.29	3.57	4.28
	AE (%)	2.32	7.13	11.22
RW4	RMSE (%)	1.53	4.10	2.56
	AE (%)	4.34	8.83	5.22
RW9	RMSE (%)	1.79	3.60	4.84
	AE (%)	4.98	13.32	9.70
RW14	RMSE (%)	1.84	5.47	5.18
	AE (%)	4.60	10.64	8.83
RW19	RMSE (%)	1.57	5.76	6.69
	AE (%)	2.09	10.39	10.39
RW22	RMSE (%)	0.91	3.27	5.76
	AE (%)	1.55	6.31	11.31

RW25	RMSE (%)	1.35	6.97	7.25
	AE (%)	3.02	8.15	14.52
W5	RMSE (%)	0.44	2.97	2.91
	AE (%)	0.67	5.86	4.46
W9	RMSE (%)	0.67	2.02	2.05
	AE (%)	1.10	4.69	1.56
Average	RMSE (%)	1.26	4.19	4.61
	AE (%)	2.74	8.36	8.57





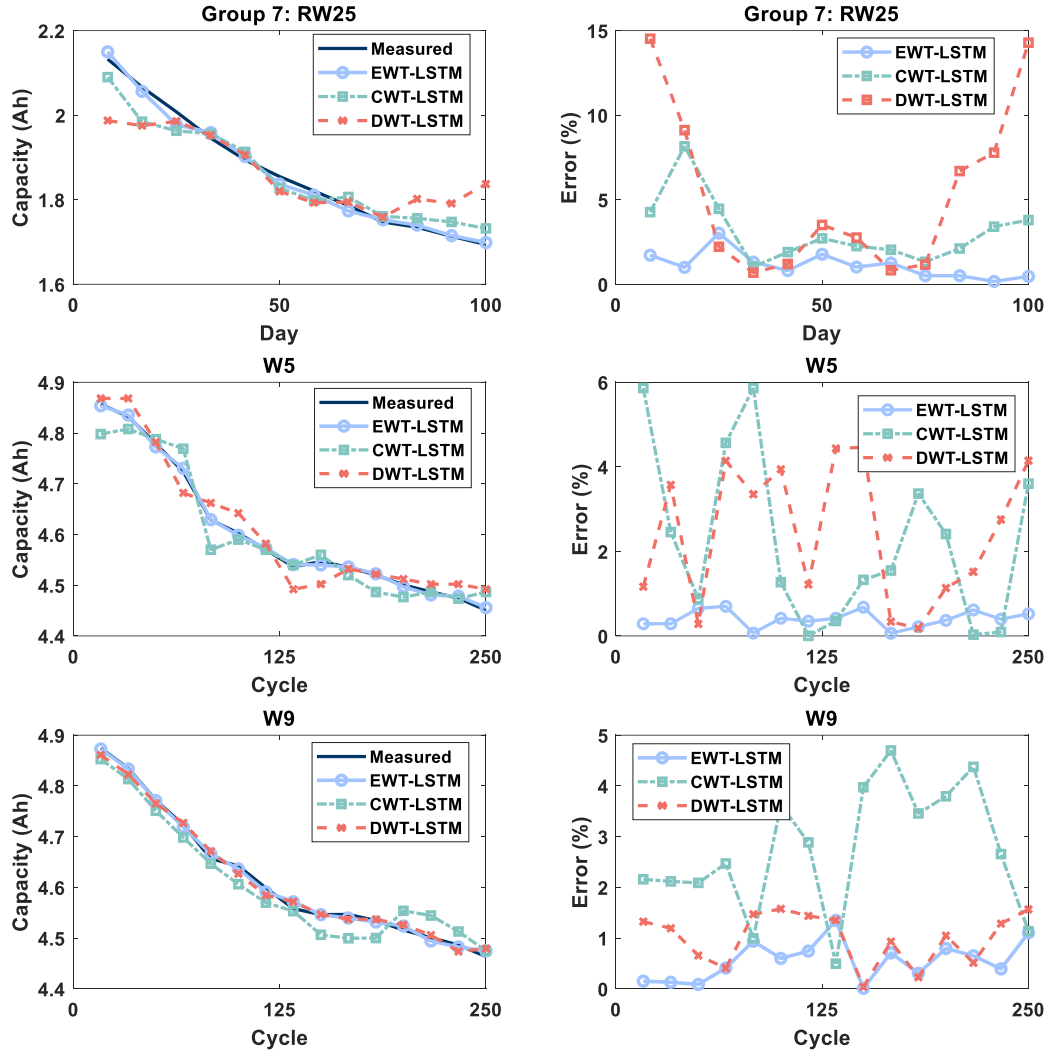


Figure 4.18 Validation results of the first scenario.

4.3.3.2 Capacity Estimation for the Second Scenario

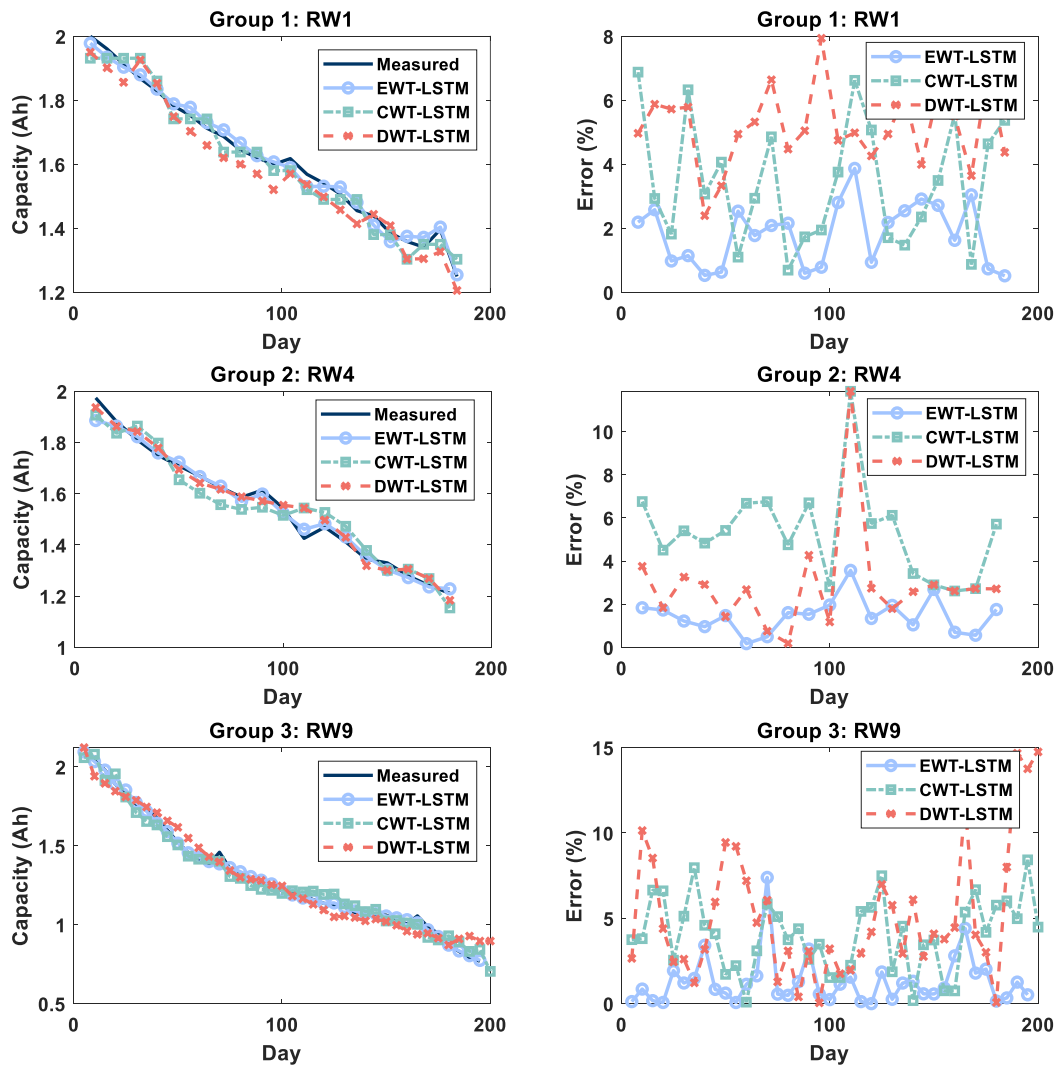
This subsection illustrates the model's robustness when coping with noisy sensor data. Before sending the measured voltage signal to the proposed framework presented in Figure 4.2, it is augmented with additive zero-mean white Gaussian noise (AWGN) having a mean, standard deviation (σ) of 5%. This noise level exceeds most sensor limits accepted in the industry. Table 4.6 displays the result metrics of the validation set of LIBs.

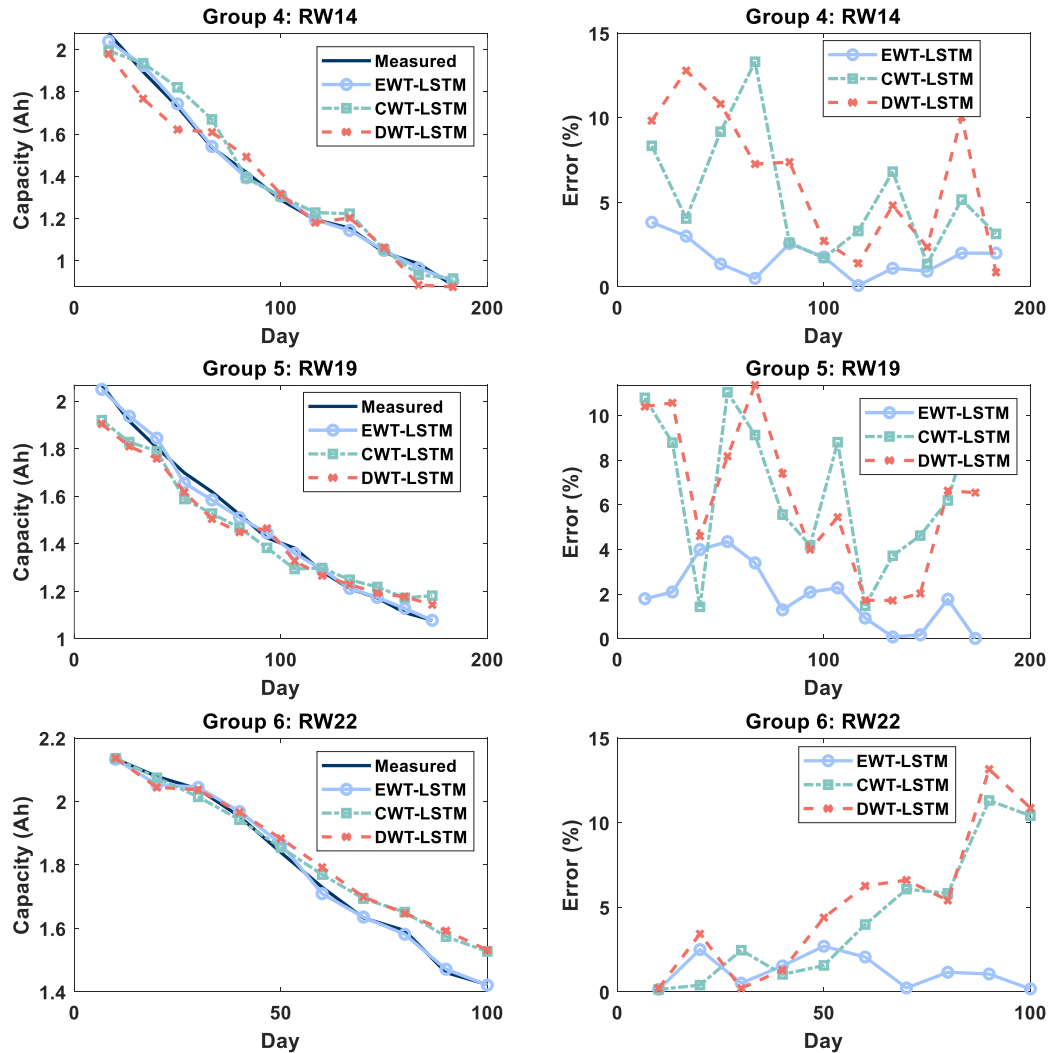
Figure 4.19 displays the capacity estimation results and errors of the EWT-LSTM, CWT-LSTM, and DWT-LSTM methods. As shown in Fig. 18, the EWT-LSTM method significantly outperforms other wavelet methods' estimation accuracy. Specifically, Table 5 shows that the average RMSE of the entire testing dataset for the EWT-LSTM method is still less than 2%, with the best-case RMSE being 0.89% and the worst-case RMSE being 2.30%. On the other hand, the average RMSE value is 5.49% and 5.97% for CWT-LSTM and DWT-LSTM methods, respectively. In addition, the proposed EWT-LSTM has demonstrated dominance over CWT-LSTM and DWT-LSTM even in noisy environments, with AE reductions of 63.93% and 67.85%, respectively. The results indicate that the EWT-LSTM method is quite robust when estimating the capacity of the LIB with a noisy measured voltage signal. The EWT technique has demonstrated its efficiency in estimating the capacity of LIBs under dynamic operating conditions such as randomised cycling current profiles and different temperature ranges. Nonetheless, this method might not yield comparable improvements when it comes to capacity estimation in static operating scenarios.

Table 4.6 RMSEs and AEs of the capacity estimation results in a noisy scenario.

Battery name	Criteria	EWT-LSTM	CWT-LSTM	DWT-LSTM
RW1	RMSE (%)	2.06	3.96	5.28
	AE (%)	3.87	6.87	7.93
RW4	RMSE (%)	1.67	5.73	3.75
	AE (%)	3.56	11.86	11.86
RW9	RMSE (%)	1.96	4.56	6.41
	AE (%)	7.39	8.42	14.74
RW14	RMSE (%)	2.036	6.41	7.53
	AE (%)	3.82	13.31	12.78
RW19	RMSE (%)	2.30	7.90	7.81
	AE (%)	4.34	11.04	11.36
RW22	RMSE (%)	1.51	5.74	6.60
	AE (%)	2.69	11.31	13.15

RW25	RMSE (%)	1.76	7.62	9.35
	AE (%)	3.72	14.61	17.68
W5	RMSE (%)	0.89	4.24	4.04
	AE (%)	1.62	7.86	6.43
W9	RMSE (%)	0.91	3.33	2.98
	AE (%)	1.50	4.84	5.19
Average	RMSE (%)	1.61	5.49	5.97
	AE (%)	3.61	10.01	11.23





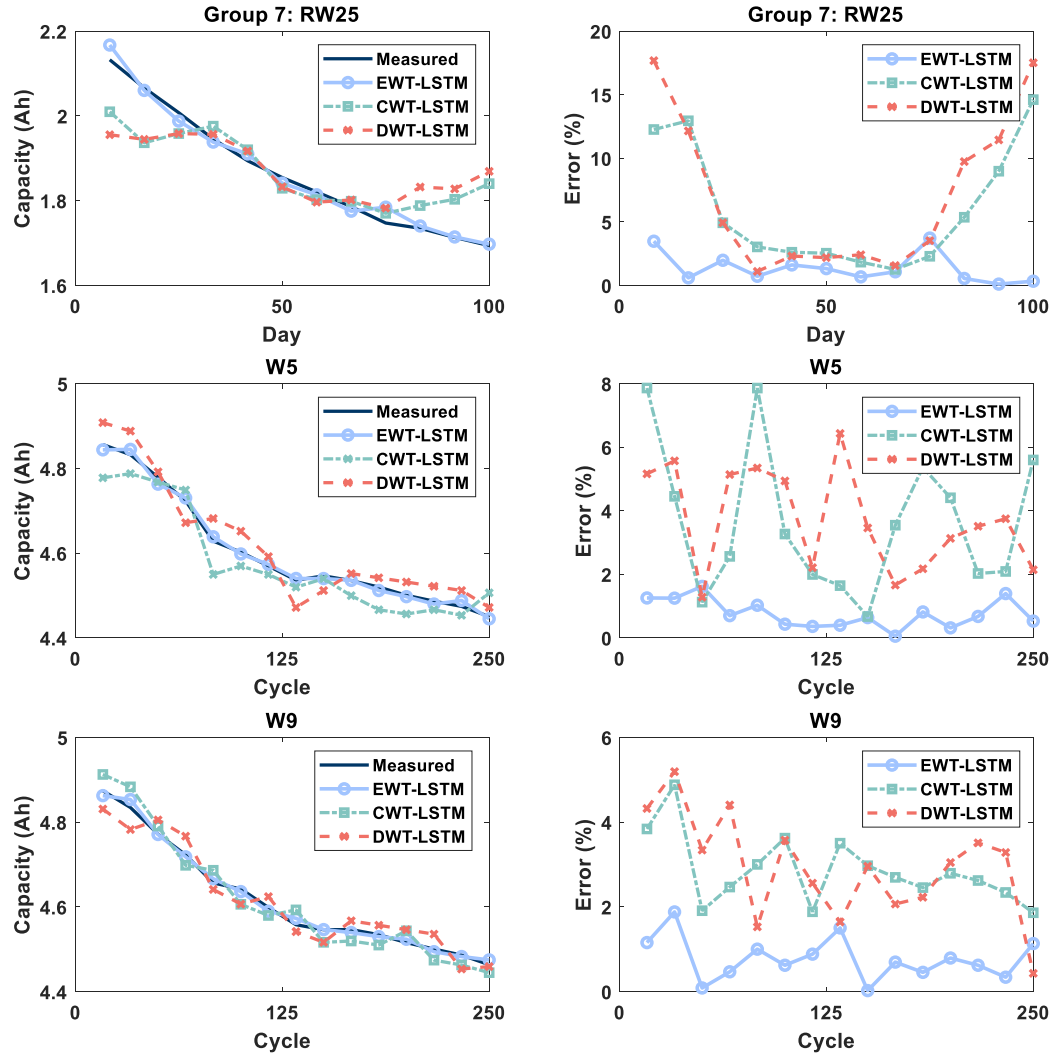


Figure 4.19 Capacity estimation results of the second scenario.

4.3.4 Comparative Analysis with The State-of-the-Art Methods

To demonstrate the superiority of the proposed method in the capacity estimation of LIBs, it is vital to compare the results of the proposed method with recently published studies. There have been reports in the literature of the NASA randomised battery dataset for capacity estimation using several methods/data-driven algorithms in the past four years. Table 4.7 compares the average RMSEs for capacity estimation of LIBs using the NASA randomised dataset in the recently published literature. For example, Richardson et al. [284] estimated the

capacity of NASA randomised data set by using the total time elapsed during the load pattern and the charge throughput as input features into the GPR model. The average RMSE value for the GPR model was 4.3%. One more time, Richardson et al. [188] developed a GPR model for capacity estimation of the NASA randomised dataset, but this time, the authors used the charging voltage as an input feature into the GPR model. The average RMSE value was 2%-to-3%.

Toughzaoui et al. [296] proposed a combined CNN-LSTM method using a *K*-means clustering algorithm for capacity estimation and RUL prediction of NASA randomised dataset. The RMSE value was 1.4%. Roman et al. [197] proposed a machine-learning pipeline for the capacity estimation of LIBs using segments of charge voltage and current curves as promising features. The authors trained several machine learning models, such as GPR, RF, and DNN, to estimate the capacity of the LIBs. The average RMSE values for these models varied between 2.7% -5.54%. Shen et al. [189] developed a deep-learning CNN to estimate the capacity of the LIBs. Specifically, the authors utilised voltage, current, and charge capacity as input features in the developed CNN. The RMSE value was 1.47%. Liu et al.[297] estimated the capacity of the LIBs by proposing a novel health feature known as voltage variance during an equal time (VVETI). The extracted VVETI is fed into an extreme learning machine model (ELM) to estimate the capacity of the LIBs. The RMSE value of the proposed approach was 1.36%.

Table 4.7 demonstrates that the proposed method in this study is generally superior to Richardson's and Roman's and marginally better than Liu and Shen's, indicating that the proposed method provides more accurate evaluations.

Table 4.7 Comparison of the RMSEs of NASA randomised data set for capacity estimation of LIBs.

Ref	Algorithm	RMSE (%)
Richardson et al. [284]	GPR	4.3
Richardson et al. [188]	GPR	2-3
Toughzaoui et al. [296]	CNN-LSTM	1.4
Roman et al. [197]	Several algorithms have been proposed (GPR, RF, and DNN)	2.7-5.54
Shen et al. [189]		
Liu et al. [297]	ELM	1.36
Proposed method	LSTM	1.26

4.3.5 Computational Complexity

All the experimental results were performed on a PC operating with Windows 10, and the detailed specification of the hardware is described in Table 4.8. MATLAB 2021b was used to implement the proposed framework for estimating the capacity of LIBs.

Table 4.9 summarises the computational time for training and testing datasets for the developed LSTM model. The computational time in Table 4.9 included the time spent extracting the 13 diagnostics features and LSTM tuning and training. It should be noted that the computational time for the training step is much higher than the computational time for testing the trained LSTM model due to the number of LIBs used in the training process. While the computational time presented in Table 4.9 is only for one LIB from the testing dataset.

Table 4.8 The PC specifications for implementing the proposed framework.

Hardware	Specifications
Operating system	Windows 10
CPU	Intel(R) Xeon(R) CPU E5-1650 v2 @ 3.50GHz 3.50 GHz
RAM	32.0 GB
ROM	512 GB

Table 4.9 The results of the computational time for training and testing datasets.

LIB group	Training (s)	Testing (s) (One LIB from each group)
Group 1	450.049	3.245
Group 2	485.655	3.563
Group 3	394.147	3.828
Group 4	461.341	3.675
Group 5	382.974	3.870
Group 6	422.678	2.954
Group 7	480.542	2.781
Stanford University's dataset	752.513	7.521

4.4 Summary

This chapter proposed a new generalised approach for the capacity estimation of LIBs. The proposed method focuses on the LIB capacity degradation assessment using an adaptive EWT technique. The EWT is a powerful adaptive tool that can extract the electrochemical characteristics of the LIBs cycled at various current profiles and temperatures from the measured voltage signals simultaneously in both time and frequency domains.

Specifically, the measured voltage signals of the LIBs are decomposed into nine multi-resolution modes to show the high and low-frequency components contained in the measured signals. The EWT techniques obtained results show that the frequency band ranges from 0.8 Hz to 5 Hz. This frequency band range is related to the diffusion-reaction process inside the LIB during its operation.

Moreover, the extracted nine multi-resolution modes demonstrate that some modes did not change as the LIB degraded; these modes are removed from the measured voltage signal since these modes are common in the health and aged states of the LIBs. The advantage of applying the EWT method over other techniques, such as continuous wavelet transform and discrete wavelet transform, is that no mother wavelet selection process is required since the EWT is an adaptive approach, and the mother wavelet signal is designed based on the measured signal. In this work, 13 statistical features were extracted from the filtered voltage signal.

However, not all the extracted features strongly correlated with the degradation of the LIBs. In this regard, the Pearson correlation coefficient is applied to the extracted features to reduce the dimension of the extracted features matrix and focus only on the essential features.

Finally, a LSTM model has been developed and trained to estimate the capacity of the LIBs.

To validate the performance of the proposed approach, 32 LIBs from two different datasets have been used in this chapter. These LIBs have been cycled at different current profiles to simulate the operation of the LIBs in a real-world application and various temperature values as well. The capacity estimation results show that the proposed estimation scheme can

accurately estimate the capacity degradation of LIBs cycled at different cycling and temperature conditions with an average RMSE of 1.26% and max error of 2.74% due to the ability of EWT to adapt to various operating conditions and extract promising features related to the capacity degradation inside the LIBs.

Chapter 5 Lithium-ion Batteries Capacity Degradation Trajectory Prediction Based on Decomposition Techniques and NARX Algorithm

5.1 Brief introduction

It is critical to accurately predict the future capacity degradation of the LIBs to guarantee safe, reliable operation with minimal maintenance costs. However, because of the complicated and nonlinear characteristics of the battery's degradation throughout its lifetime, predicting the amount of capacity that will still be available in LIBs are a complex process. In addition, the phenomena of capacity regeneration significantly impact the accuracy of the remaining capacity projection. The capacity regeneration phenomenon is caused by rest time can increase (regenerate) the battery capacity and influence the degradation tendency. For this purpose, the signal decomposition method is becoming a more attractive and promising method for overcoming the difficulty of the capacity regeneration phenomena due to its simplicity and capability to accommodate the nonlinear dynamic behaviour of the LIB. Therefore, this chapter investigates the performance of three signal decomposition techniques in analysing the capacity regeneration phenomenon: the DWT, the EMD, and the VMD techniques. The nonlinear autoregressive neural network (NARX) algorithm is developed to predict the trajectory of the future capacity of the LIBs. The proposed algorithms' performance is analysed using two datasets from NASA Ames Research centre and the centre for advanced life cycle engineering (CALCE). The comparison results demonstrate that the variational mode decomposition method combined with the nonlinear autoregressive neural network outperforms other methods with 2.385% RMSE and 1.6% MAE.

5.2 The Proposed Framework for Capacity Degradation Trajectory Prediction

The proposed prognostics framework for RUL prediction consists of four main steps as shown in Figure 5.1. The first step is to extract the capacity from the ageing datasets. The extracted capacity to the present time is then decomposed to remove the regenerated capacity in the second step. The denoised capacity is then used to train the NARX machine learning

model in the third step. The last step is to predict the future capacity trajectory using the trained model.

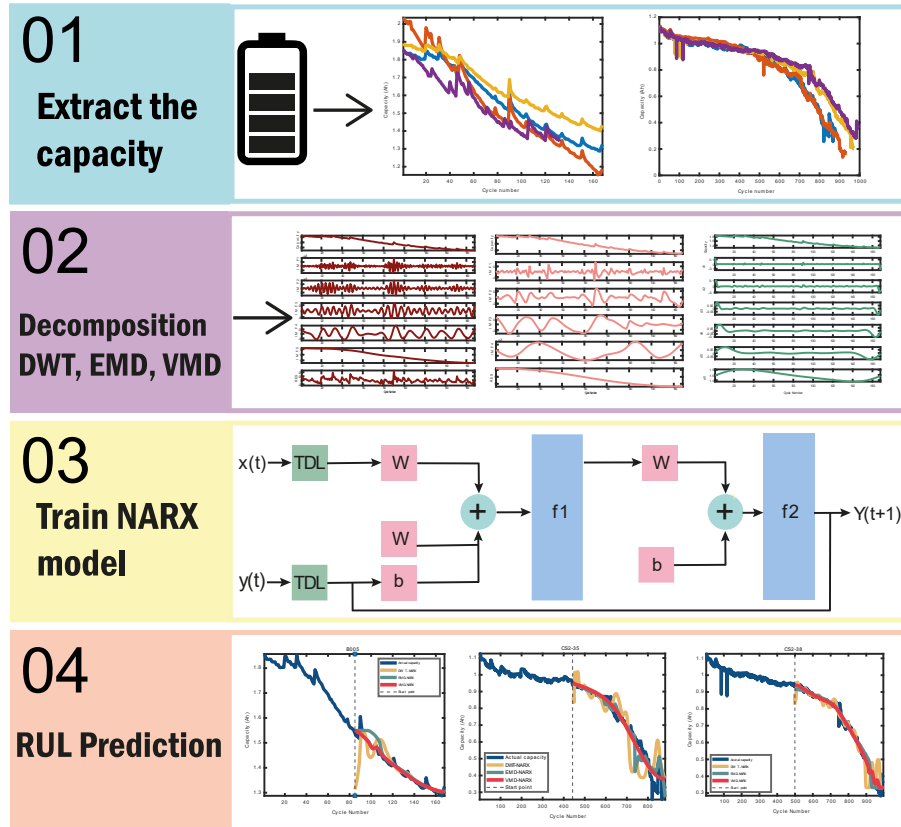


Figure 5.1 The proposed framework for capacity trajectory prediction of LIBs.

5.2.1 Lithium-ion Batteries Datasets

5.2.1.1 NASA Dataset

The first dataset is the LIBs dataset from NASA [298]. The dataset consists of four LIBs, B0005, B0006, B0007, and B018. These four LIBs have been cycled under constant-current constant voltage protocol. Table 5.1 contains the precise specifications of the LIBs chosen by NASA. Figure 5.2 depicts the capacity degradation curve as a function of the number of cycles. Several types of batteries will exhibit a rise in capacity during the discharge process, demonstrating the non-stationarity and nonlinearity of the LIBs capacity signal.

Table 5.1 The properties of the LIBs for the NASA dataset.

Battery No	Charging			Discharging		Operating conditions	
	Constant current (A)	Upper voltage limit (V)	Cut-off current (mA)	Constant current (A)	Cut-off voltage (V)	Temperature (°C)	Initial capacity (Ah)
B005	1.5	4.2	20	2	2.7	25	1.86
B006	1.5	4.2	20	2	2.7	25	2.04
B007	1.5	4.2	20	2	2.7	25	1.89
B018	1.5	4.2	20	2	2.7	25	1.86

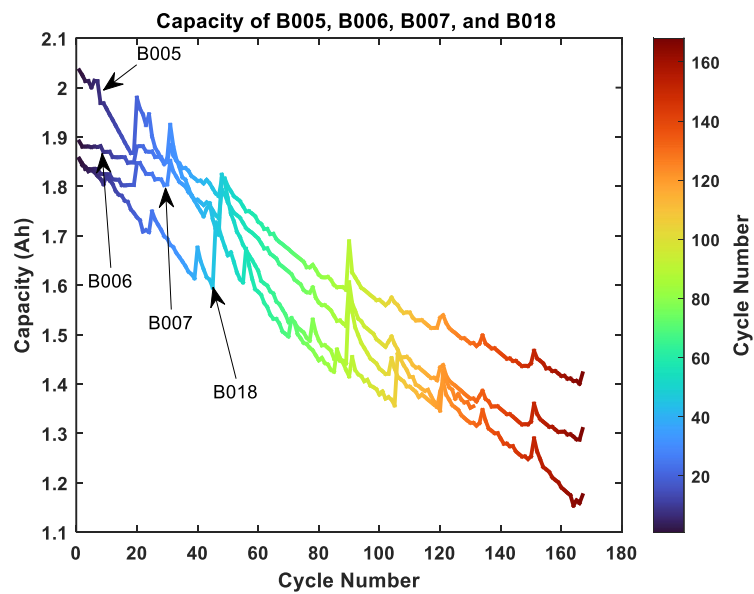


Figure 5.2 Capacity degradation of NASA dataset.

5.2.1.2 CALCE Dataset

The second dataset is supplied by the Centre for Advanced Life Cycle Engineering (CALCE) [299, 300]. This study examines four LIBs known as CS2-35, CS2-36, CS2-37, and CS2-38. Figure 5.3 depicts the capacity degradation curve as a function of the number of cycles. Table 5.2 contains the detailed specifications for the selected CALCE LIBs.

Table 5.2 The properties of the LIBs for CALCE dataset.

Battery No	Charging			Discharging		Operating conditions	
	Constant current (A)	Upper voltage limit (V)	Cut-off current (mA)	Constant current (A)	Cut-off voltage (V)	Temperature (°C)	Initial capacity (Ah)
CS2_35	1.5	4.2	20	2	2.7	25	1.1
CS2_36	1.5	4.2	20	2	2.7	25	1.1
CS2_37	1.5	4.2	20	2	2.7	25	1.1
CS2_38	1.5	4.2	20	2	2.7	25	1.1

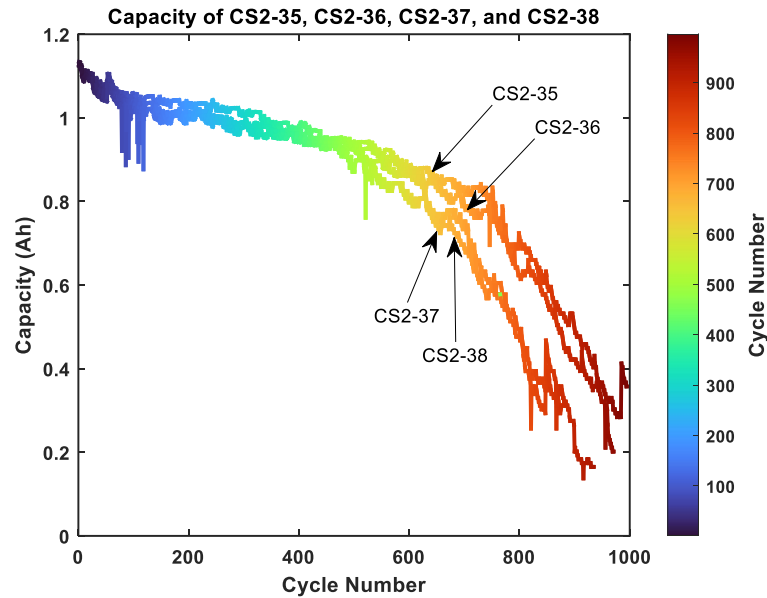


Figure 5.3 Capacity degradation of CALCE dataset.

5.2.2 Discrete Wavelet Transform (DWT)

The Discrete Wavelet Transform (DWT) is a technique used to decompose a signal into different frequency bands [301]. It is similar to the Fast Fourier Transform (FFT), but it provides more detailed frequency information by dividing the signal into multiple frequency bands (also known as sub-bands or scales) instead of a single frequency spectrum [302].

The DWT works by convolving the signal with a series of wavelet functions localised in both time and frequency [303]. This allows for a more accurate representation of the signal's frequency content, as it can capture both broad and narrow frequency bands. The output of the DWT is a set of coefficients which represent the different frequency components of the signal.

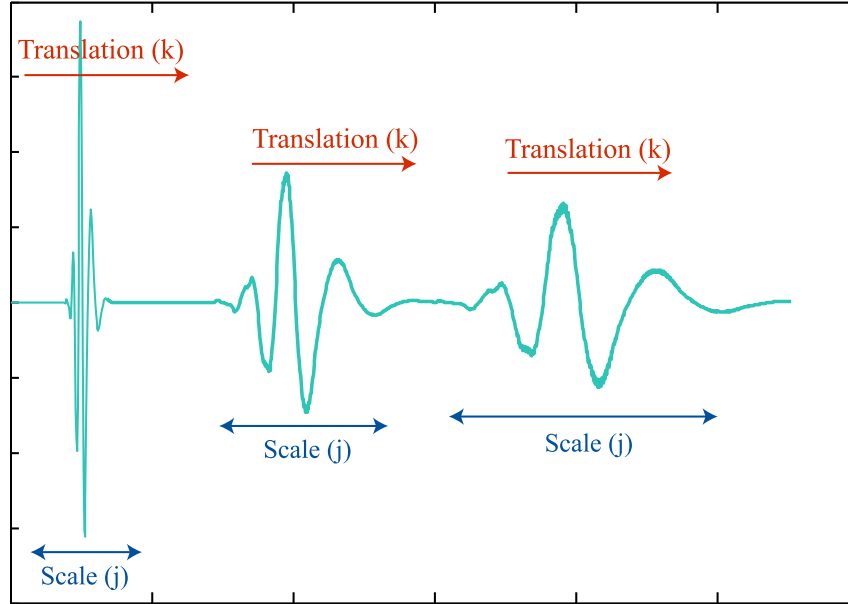


Figure 5.4 Translation and scaling functions of the DWT [303].

The DWT of a signal $x(t)$ can be described as:

$$DWT(j, k) = \frac{1}{\sqrt{2^j}} \int_{-\infty}^{\infty} x_t \psi * \left(\frac{t - k2^j}{2^j} \right) \quad (5.1)$$

Where $\psi(t)$ is the mother wavelet function, j and k are the scale (an integer indicating how the wavelet is stretched or compressed, as shown in Figure 5.4) and translation parameters of the DWT, respectively. These two parameters are utilised to provide a multi-resolution analysis of the analysed signal $x(t)$. The analysed signal $x(t)$ is decomposed into low-frequency components known as approximate components (a_n) and high-frequency components are known as detail components (d_n); the $c(t)$ can be defined as:

$$x(t) = \sum_{k=0}^{2^{N-J}-1} a_{j,k} 2^{-j/2} \phi(2^j t - k) + \sum_{j=1}^J \sum_{k=0}^{2^{N-J}-1} d_{j,k} 2^{-j/2} \psi(2^j t - k) \quad (5.2)$$

The first sum in equation (5.2) represents the low-pass filtered version of the signal, while the second sum represents the high-pass filtered version. These two filtered signals are then downsampled by a factor of two to obtain the next level of decomposition. This process can be repeated multiple times to obtain a multi-level signal decomposition.

In the DWT, the "mother wavelet" $\psi(t)$ is the basic wavelet function used to generate all other wavelet functions. The most commonly used mother wavelets in the DWT include:

- 1- Haar wavelet: The most straightforward wavelet function is a square-shaped function that is easy to compute and has a fast implementation [304]. However, it has poor frequency localisation and is unsuited for signals with fine structures [304]. Figure 5.5 shows the Haar wavelet.
- 2- Daubechies wavelets: These wavelets, named after their inventor [305], are a family of orthogonal wavelets that have been widely used in image and signal processing. They are characterised by high-frequency localisation, good time resolution and low computational complexity [306]. Common examples of Daubechies wavelets include the db4 and db8 wavelets which are shown in Figures 5.6 and 5.7, respectively.
- 3- Symlets wavelets: are also a family of orthogonal wavelets, they are similar to Daubechies wavelets, but they have a more symmetric scaling function and wavelet function, which makes them well-suited for signals with both fine and coarse structures [307, 308]. Figure 5.8 illustrates an example of one type of Symlet wavelet Sym4.

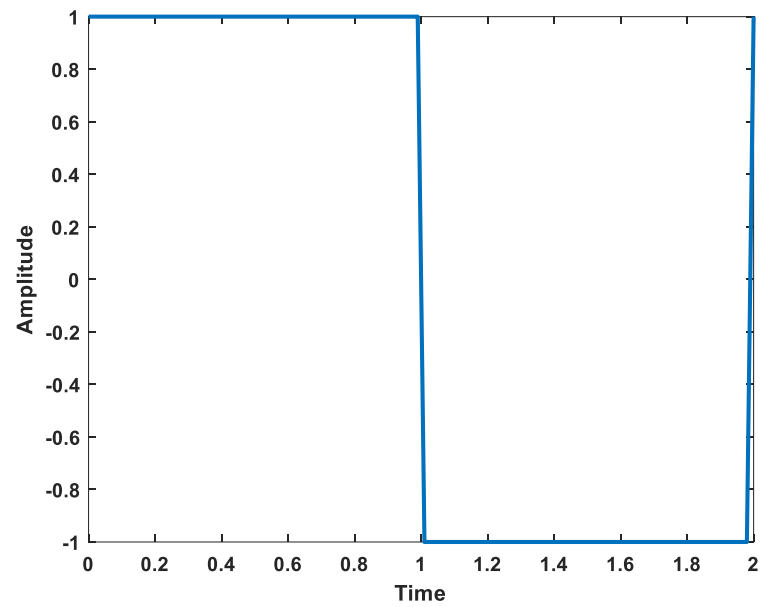


Figure 5.5 Haar mother wavelet function.

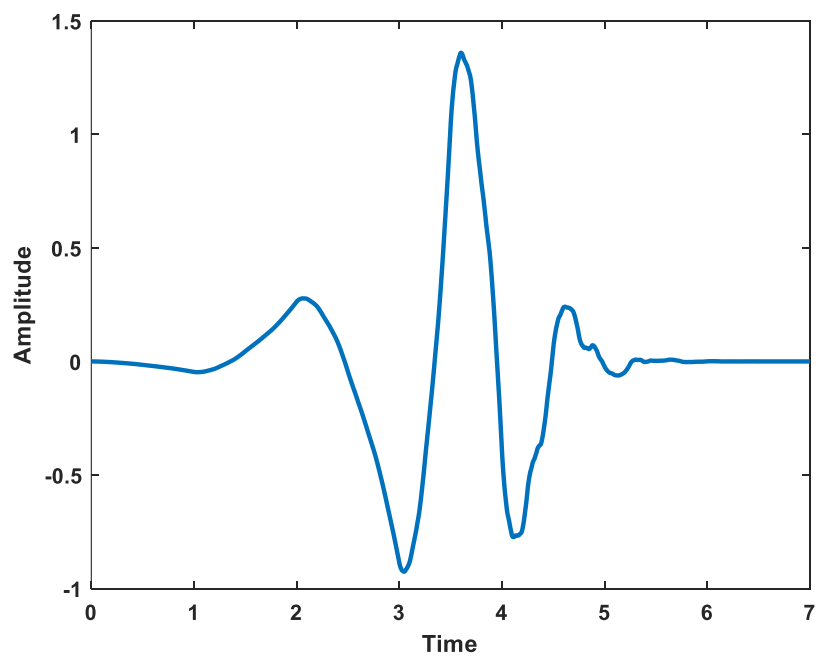


Figure 5.6 Daubechies (db4) mother wavelet function.

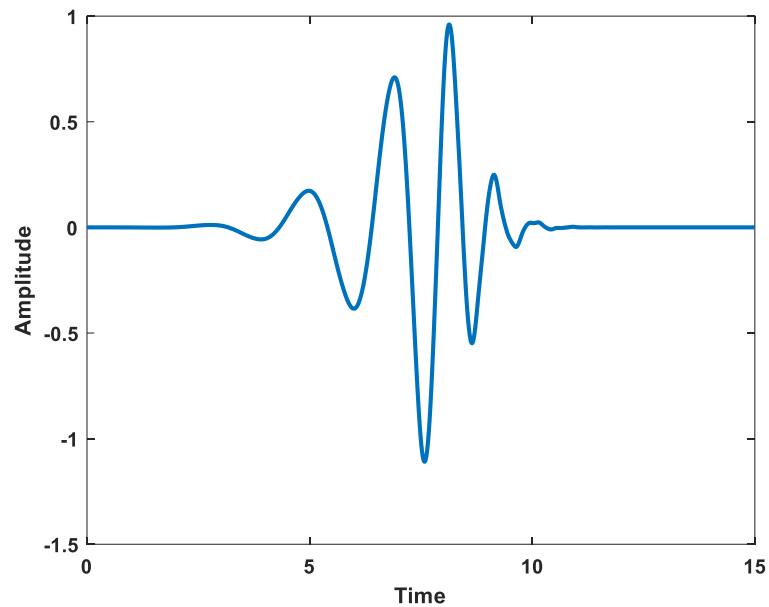


Figure 5.7 Daubechies (db8) mother wavelet function.

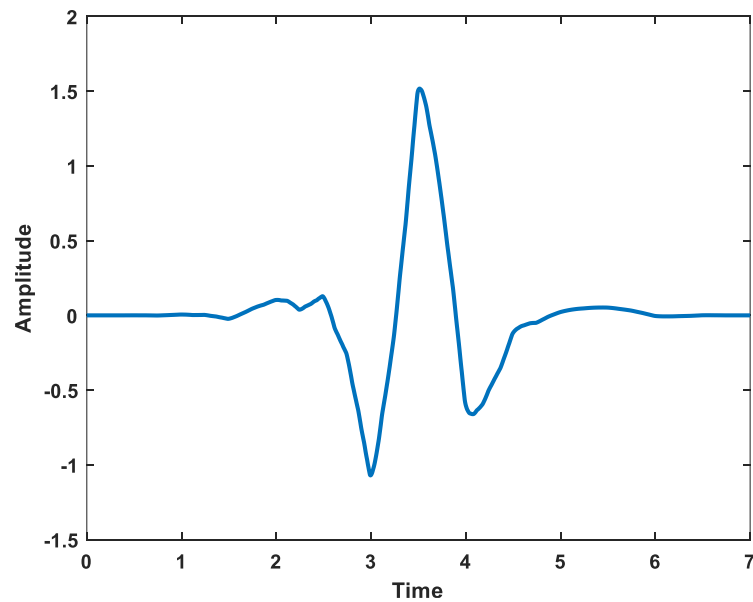


Figure 5.8 Symlets (sym4) mother wavelet function.

- 4- Coiflets are also a family of orthogonal wavelets. They are similar to Daubechies wavelets but designed to have more compact support, making them well-suited for signals with high-frequency noise [309].

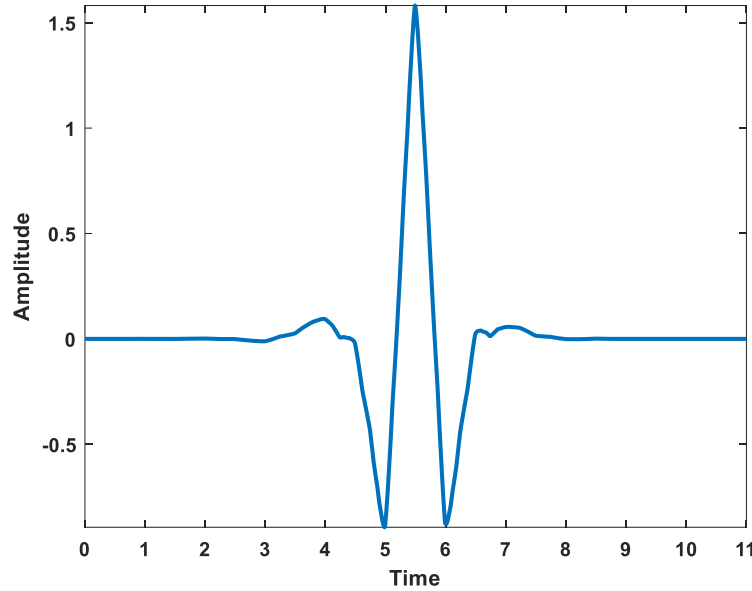


Figure 5.9 Coiflets (coif4) mother wavelet function.

The choice of mother wavelet will depend on the specific characteristics of the signal being analysed and the goals of the analysis. Different wavelets have different properties and are better suited for different types of signals and applications. In this study, the Daubechies (db4) [310] was selected as a mother wavelet function to analyse the capacity of the LIBs.

5.2.3 Empirical Mode Decomposition (EMD)

The EMD is a non-parametric technique that can be used to decompose a signal into a set of IMFs that represent the different frequency components of the signal [311]. EMD is based on the idea that a signal can be broken down into a sum of oscillatory components, each with a unique frequency and amplitude [312]. The EMD algorithm starts by identifying the local extrema of the signal and fitting a cubic spline through them. Then it calculates the mean of the upper and lower envelopes of the signal and subtracts it from the original signal. This process is repeated until a set of IMFs are obtained. The mathematical expression for the EMD is a recursive process. The EMD algorithm starts with the original signal $x(t)$, and decomposes it into a set of IMFs, which are defined as:

$$x(t) = \sum_{i=1}^n imf_i(t) + r_n(t) \quad (5.3)$$

Where $imf_i(t)$ is the extracted IMFs components and $r_n(t)$ is the residual component. The EMD analysis method is implemented using the following main steps:

- 1- Find all the local extrema of $x(t)$, design the upper $x_u(t)$ and lower $x_l(t)$ envelopes of $x(t)$ respectively using cubic spline interpolation.
- 2- From the designed upper and lower envelopes, calculate the mean envelope as presented in (5.4):

$$m(t) = \frac{[x_u(t) + x_l(t)]}{2} \quad (5.4)$$

- 3- Obtain the IMF as shown in (5.5):

$$h_1(t) = x(t) - m(t) \quad (5.5)$$

- 4- Check the properties of the obtained IMF $h_1(t)$ is satisfied with the termination criterion. If yes, output the $x(t)$ as the residue $r_n(t)$ and stop the EMD calculation. If not, replace $x(t)$ with $h_1(t)$ and repeat the steps until the $r_n(t)$ becomes monotonic functions, which means that no more IMF can be extracted.

Figure 5.10 illustrates a schematic diagram of the implementation of the EMD. One of the main advantages of EMD is that it can identify the underlying frequency components of non-linear and non-stationary signals, which is not possible with traditional frequency analysis methods such as the Fourier Transform. EMD can also handle multi-component signals, separating each component into an IMF.

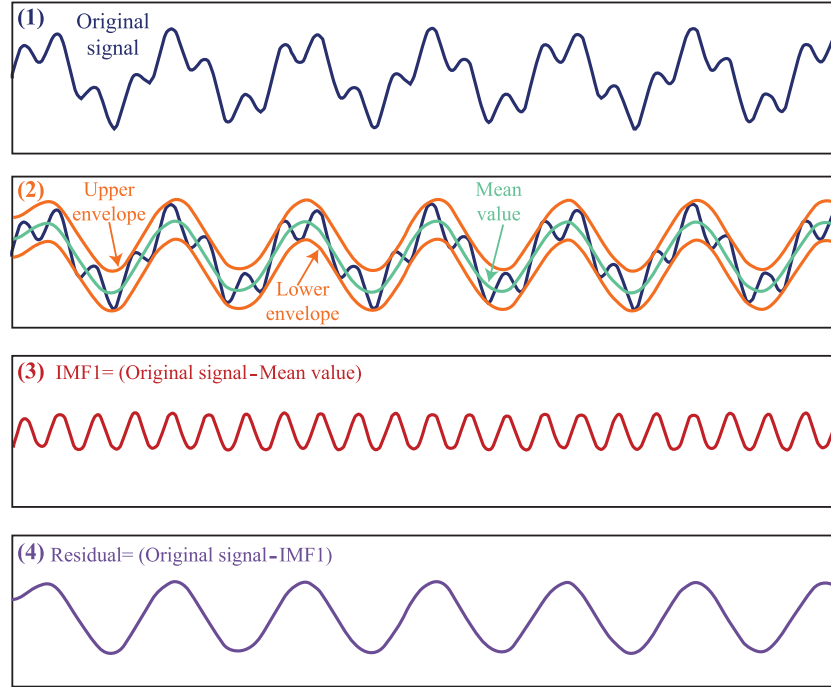


Figure 5.10 Schematic diagram of the implementation of the EMD.

5.2.4 Variational Mode Decomposition (VMD)

The VMD is a signal decomposition method that decomposes a signal into a set of IMFs similar to the EMD method. VMD is based on a variational formulation and is derived from the theory of HHT [313].

The VMD method decomposes a signal into a sum of IMFs by minimising a cost function, defined as the sum of the signal's energy and a regularisation term that promotes the smoothness of the IMFs. The cost function can be written as:

$$\min_{\{u_k\}, \{w_k\}} \left\{ \sum_k \left\| \partial_t \left[\left(\delta(t) + \frac{j}{\pi t} \right) \cdot u_k(t) \right] e^{-jw_k} \right\|_2^2 \right\} \quad (5.6)$$

Where u_k is the extracted IMF, w_k is the centre frequency of each u_k , $\delta(t)$ is the impulse function, and k is the modal component number [313]. The VMD algorithm solves this optimisation problem by iteratively updating the amplitude, frequency, and phase of the IMFs until the cost function is minimised. The algorithm starts with an initial guess for the amplitude,

frequency and phase; then iteratively updates them until the cost function is minimised. Table 5.3 presents the implementation steps of the VMD algorithm.

Table 5.3 Implementation steps of VMD algorithm.

Input: Original signal, $x(t)$

Initialise:

IMF_count = 0

Set the amplitude, frequency and phase of the IMFs.

Step 1: Update the amplitude, frequency and phase of the IMFs.

Step 2: Calculate the cost function.

Step 3: Check if the cost function has converged.

If the cost function has converged:

IMF_count = IMF_count + 1

Store the IMF in an IMF array.

Subtract the IMF from the original signal.

If the cost function has not converged:

Go back to step 1 with the updated amplitude, frequency and phase.

Repeat steps 3-7 until the residue signal is a monotonic function or until the desired number of IMFs has been extracted.

Output: IMFs, $c(t)$

5.2.5 Nonlinear Autoregressive with Exogenous Input (NARX) Data-Driven Algorithm

The NARX data-driven algorithm is a type of time series modelling algorithm that is used to predict future values of a system based on past values and any external input variables (exogenous inputs) [314]. NARX models are nonlinear dynamic system models particularly useful in modelling systems with complex, nonlinear behaviour [315].

The NARX algorithm is an extension of the Autoregressive with Exogenous Inputs (ARX) algorithm, which is a linear time series modelling algorithm. The main difference between the two is that while the ARX algorithm uses linear models to describe the relationship between the inputs and outputs, the NARX algorithm uses nonlinear models [316].

The NARX model is represented as follows [316]:

$$y(t) = f(y(t-1), y(t-2), \dots, y(t-d_y), \dots, x(t-1), x(t-2), \dots, x(t-d_x)) \quad (5.7)$$

Where $f()$ is a nonlinear function characterising the dynamics of the system, and d_u and d_y are the time delays for the input and output, respectively. Figure 5.11 shows the detailed architecture of the NARX network.

As shown in Figure 5.11, W and b define the network's weight and bias parameters, and there are two tapped-delays lines (TDL); the first TDL is linked to the input data, and the second TDL is linked to the output "target" data. The TDL is expressed as presented in (5.8):

$$TDL = \begin{bmatrix} x(t-1), x(t-2), \dots, x(t-d_x) \\ y(t-1), y(t-2), \dots, y(t-d_y) \end{bmatrix}^T \quad (5.8)$$

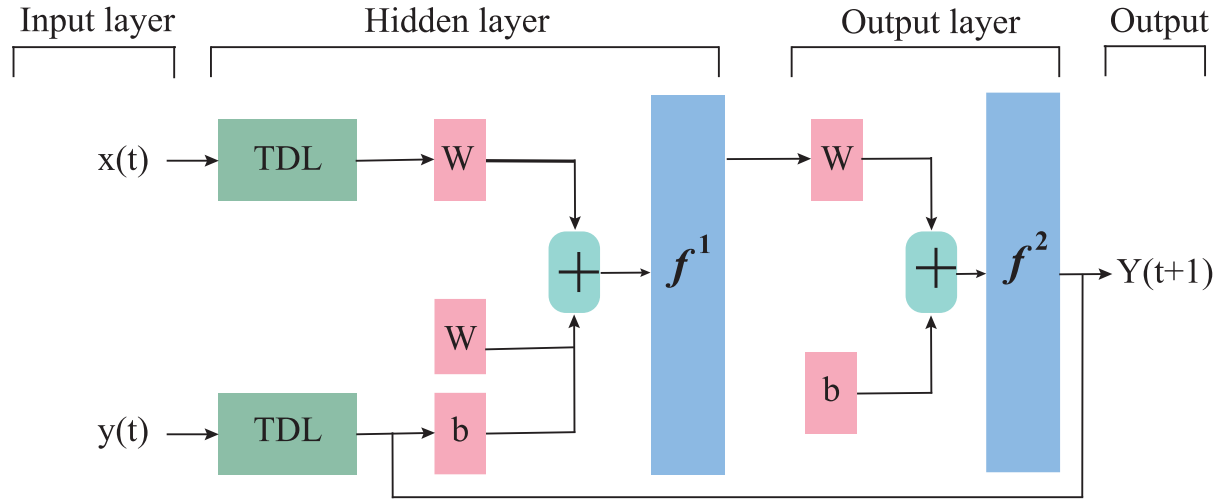
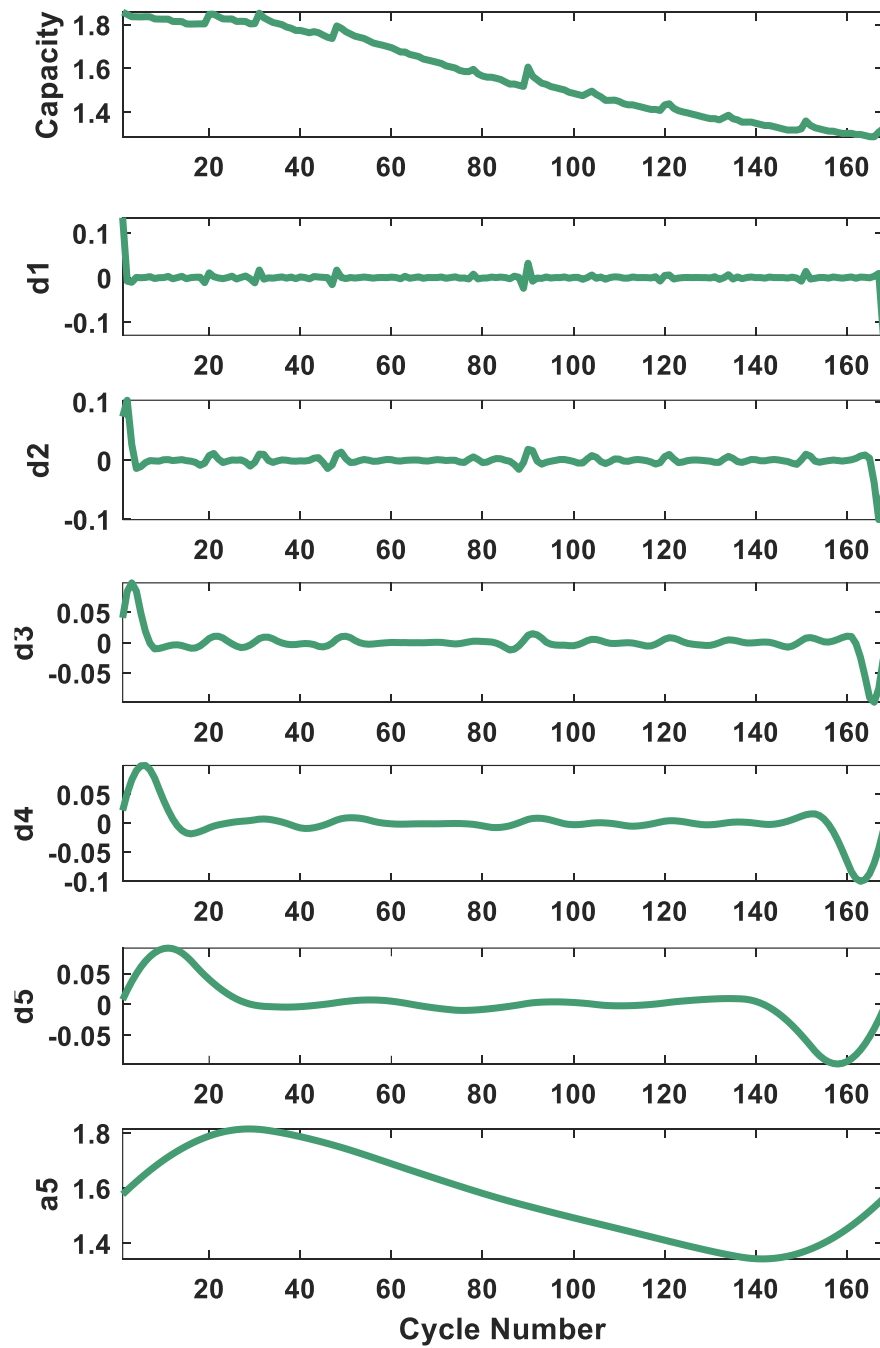


Figure 5.11 The architecture of the NARX model.

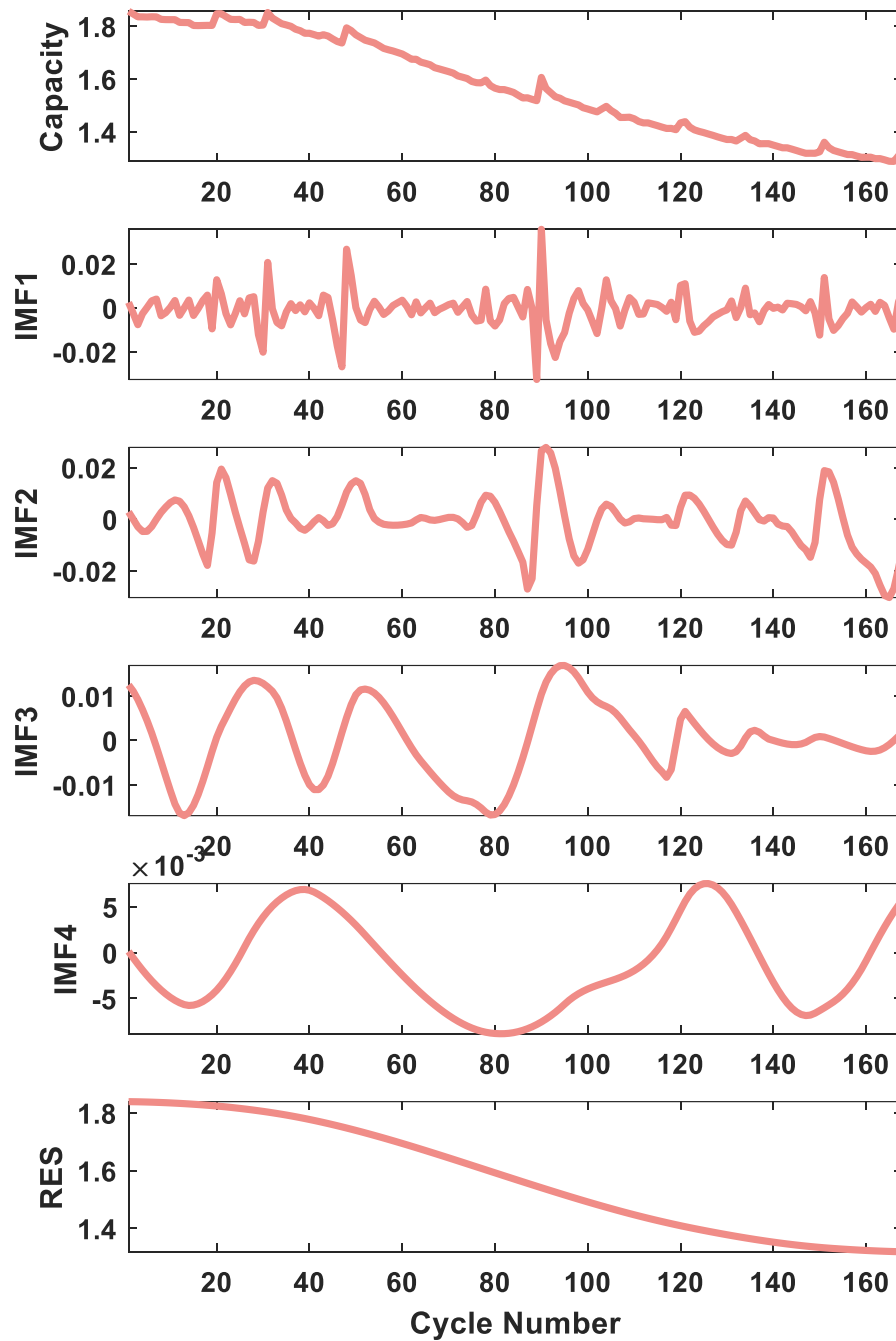
5.3 Results and Discussion

5.3.1 DWT, EMD, and VMD Results

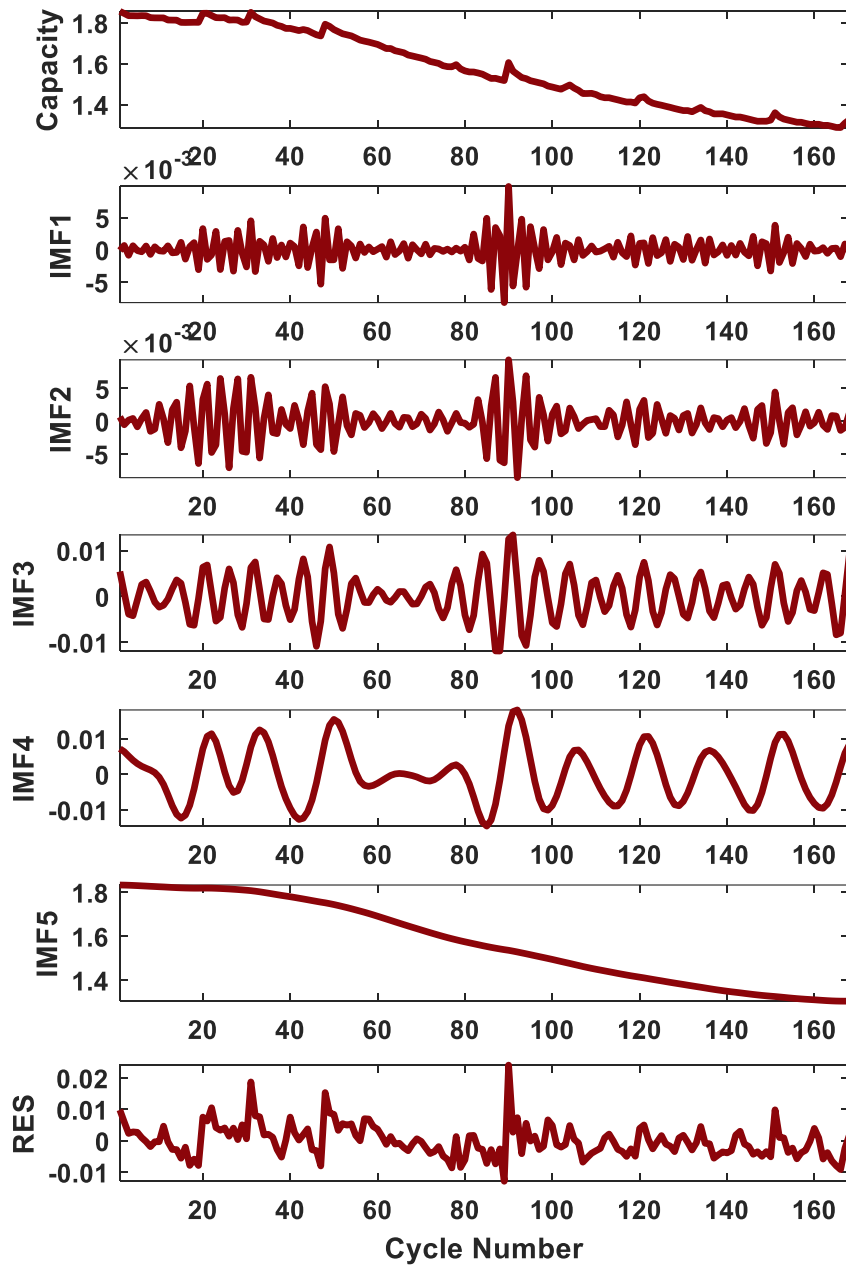
Due to the complex nonlinear ageing mechanisms, LIBs capacity regeneration phenomenon of LIBs can adversely influence the RUL prediction accuracy of the LIBs. The DWT, EMD, and VMD methods can extract the capacity sequence features effectively, making the NARX algorithm's prediction more accurate. Figure 5.12 shows the IMFs of DWT, EMD, and VMD of B005 LIB, respectively. As shown in Figure 5.12, all three decomposition methods can decompose the capacity data of the LIBs correctly and discriminate between the regenerated capacity and the actual capacity degradation. For example, Figure 5.12(a) illustrates the decomposition results of the DWT analysis method, and the DWT decomposed the capacity into five details (d1 to d5) components and one approximate component (a5). The details components represent the high-frequency capacity regeneration, and the approximate component represents the low-frequency trend of the LIB.



(a) DWT



(b) EMD



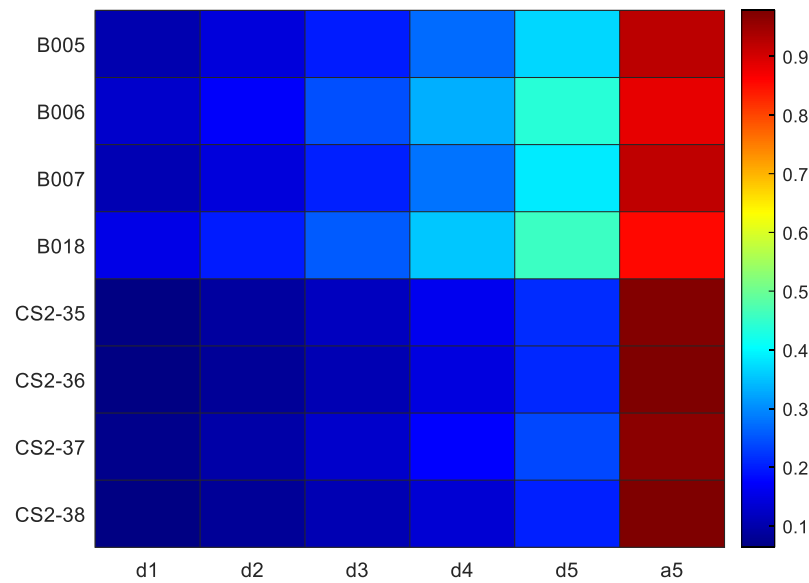
(c) VMD

Figure 5.12 The extracted IMFs and RES of (a) DWT, (b) EMD, and (c) VMD.

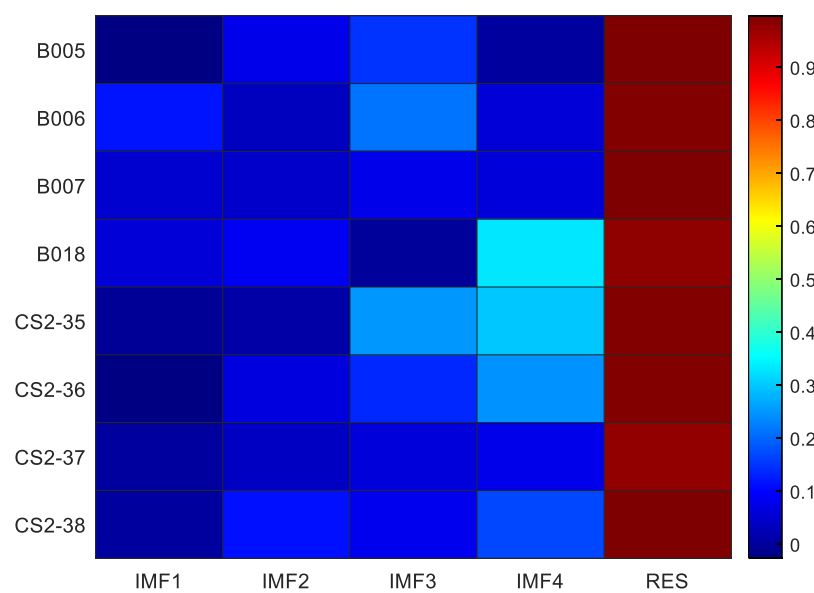
Figure 5.12(b) shows the decomposition results of the EMD method, and the EMD method decomposed the capacity into four IMFs and one RES. IMF1 and IMF2 illustrate the high-frequency capacity regeneration, while IMF3 and IMF4 show the low-frequency of regeneration capacity. The RES is the degradation decay of the capacity of the LIB. Figure 5.12(c) shows the decomposition results of VMD; as shown in Figure 5.12(c), the VMD method decomposed the capacity into five IMFs and one RES. Similarly, to the EMD method, IMF1 and IMF2 represent the high-frequency regenerated capacity, and IMF3 and IMF4 represent the low-frequency fluctuations of the capacity. IMF5 is remarkably similar to the capacity degradation curve, which represents the capacity curve trend. The Pearson correlation analysis method is applied to calculate the relationship between the extracted IMFs and the actual capacity of the LIBs.

Figure 5.13 illustrates the correlation results of the extracted results and the capacity degradation of the LIBs. As shown in Figure 5.13(a), the correlation between the approximate component (a5) and the capacity is above 0.9, indicating that the a6 and the original capacity data showed a high degree of correlation. Figure 5.13(b) shows the correlation results of the EMD method; the RES components are highly correlated with the capacity data of the LIBs. Figure 5.13(c) shows that the correlation between the capacity data and IMFs5 is high for all LIBs. However, as shown in Figure 5.13(a), (b), and (c) that the correlation between the capacity data and each IMFs (or details components for DWT) is lower than 0.2; thus, these components can be removed using only the most highly correlated components to predict the RUL of the LIBs. Moreover, Figure 5.14(a) and (b) show the capacity and denoised data of B005 and CS2-35 LIBs. Only the highly correlated components are used to create the denoised data, which are a5, RES, and IMF5 for DWT, EMD, and VMD, respectively.

The results show that the EMD and VMD analysis methods outperform the DWT method because these methods are adaptive techniques, and no mother wavelet function selection process is required.



(a) DWT



(b) EMD

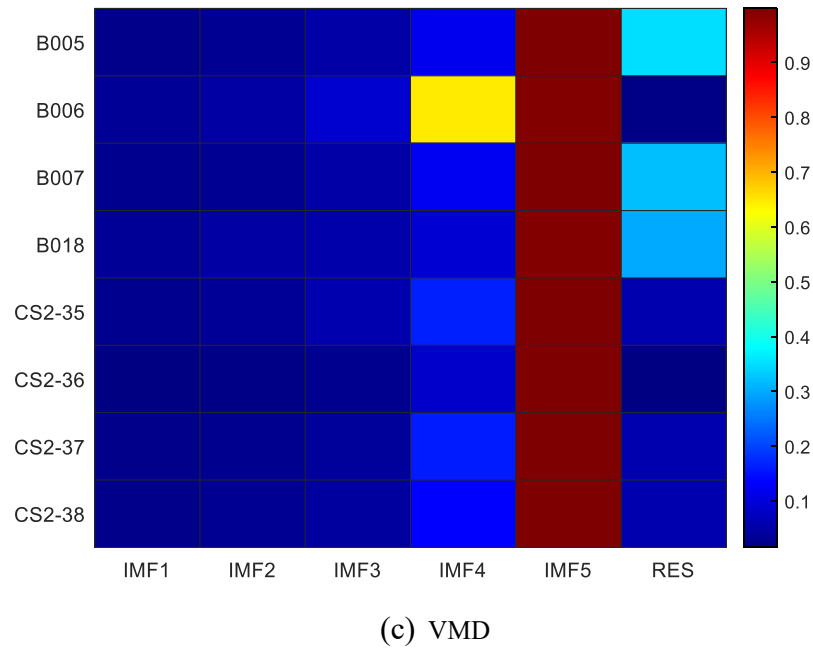
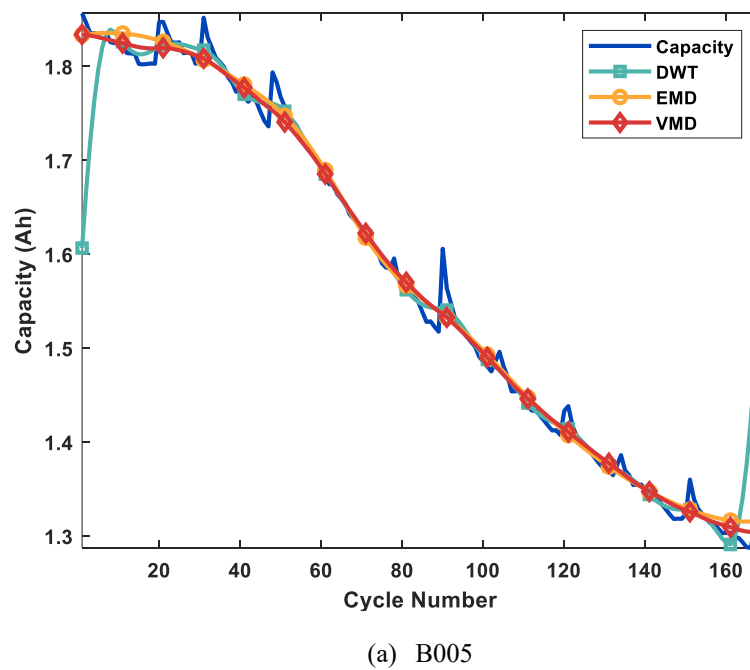
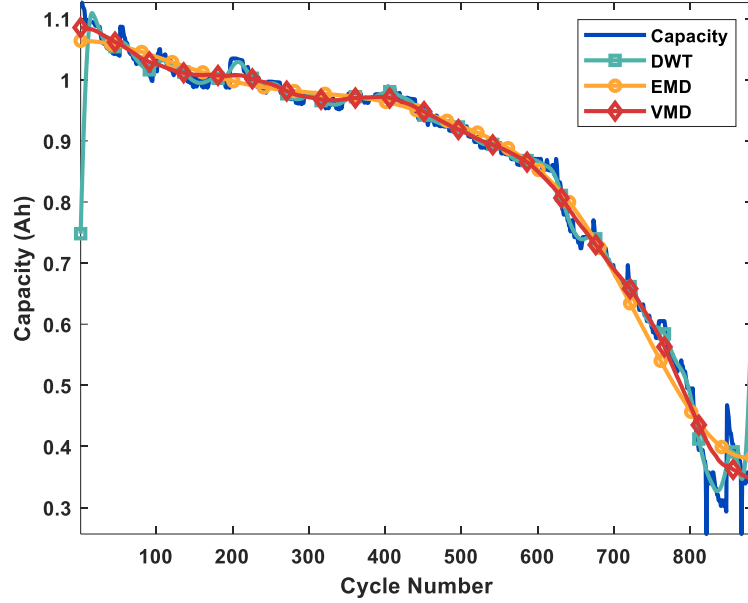


Figure 5.13 Pearson correlation results of (a) DWT, (b) EMD, and (c) VMD.





(b) CS2-35

Figure 5.14 The denoised capacity results of (a) B005 and (b) CS2-35 LIBs.

5.3.2 NARX Prediction Results

The denoised capacity curve is used to train the NARX to predict the future value of the capacity. As presented in section 2, NASA and CALCE datasets are selected to validate the performance of the proposed methods. The NARX model is trained using two different approaches to validate the capability of the proposed method to predict the trajectory of the capacity with different amount of available training datasets.

1. The first 50% of the LIBs capacity of NASA and CALCE datasets is used to train the NARX model, while the last 50% of the capacity data is kept aside as test samples.
2. The first 30% of the LIBs capacity of the NASA and CALCE dataset is used to train the NARX model, while the rest (70%) of the data is kept aside as a testing dataset.

The root mean square error (RMSE) and mean absolute error (MAE) are employed to verify the performance of the NARX model. MAE is selected over AE because MAE takes the mean of all the absolute errors, making it sensitive to the scale of the data. AE only considers the

absolute value of individual errors, and it might not provide a comprehensive picture of how the model is performing across the entire dataset.

$$RMSE = \sqrt{\frac{1}{N} \sum_{i=1}^N (\hat{C}_i - C_i)^2} \quad (5.9)$$

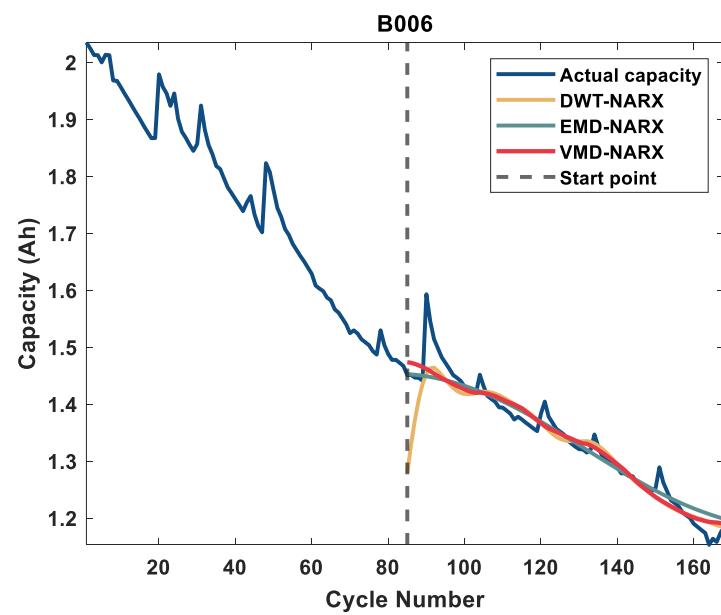
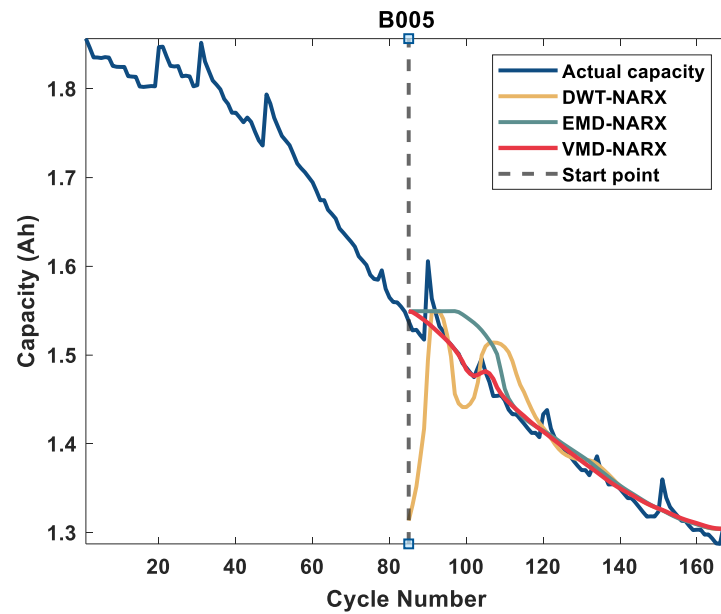
$$MAE = \frac{1}{N} \sum_{i=1}^N |(\hat{C}_i - C_i)| \quad (5.10)$$

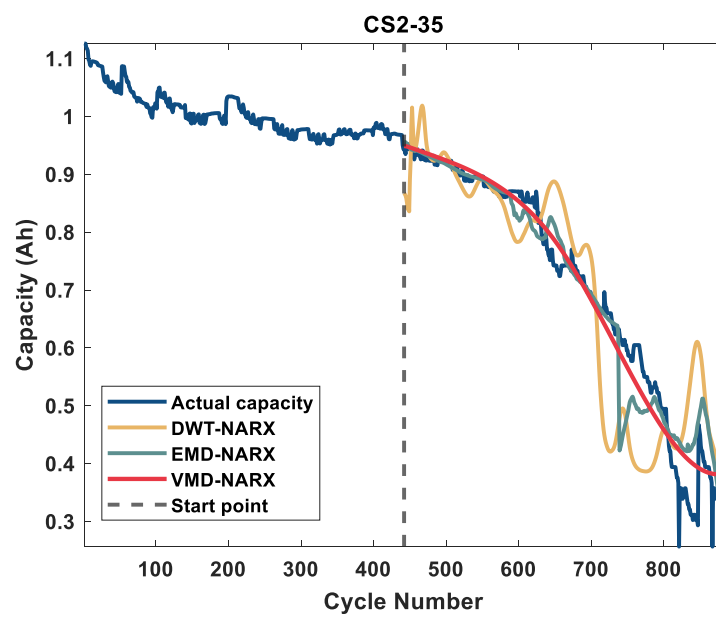
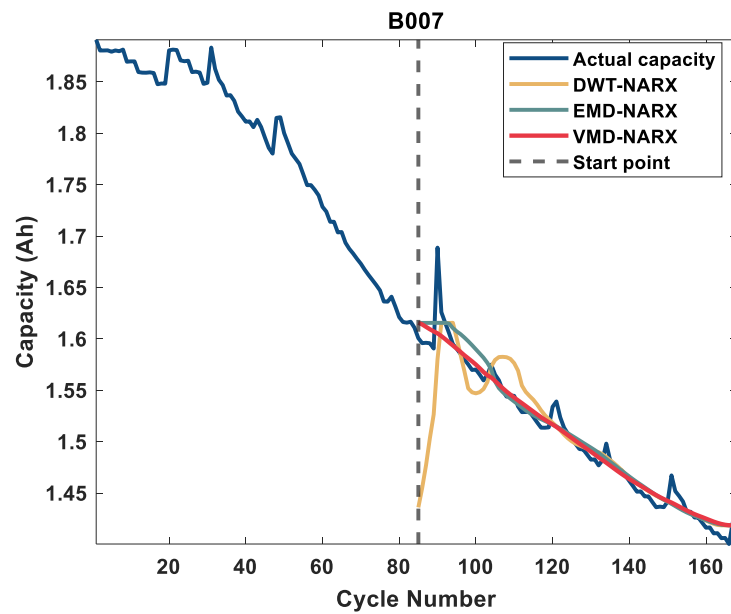
Where the C_i and \hat{C}_i are the actual and predicted capacity, respectively. N is the number of cycles.

5.3.2.1 Mid-life Capacity Trajectory Prediction

Figure 5.15 shows the future capacity degradation trajectory prediction results for NASA and CALCE datasets. It can be seen that EMD and VMD have a higher performance than DWT due to their adaptivity advantage. The mother wavelet selection for DWT can significantly affect the prediction results. The deficient performance of the DWT-NARX model can be clearly seen in B005 and CS2-35 LIBs; in B005, the DWT-NARX started the prediction from the wrong point (around 1.35Ah), and in CS2-35, the model failed to follow the correct degradation trajectory of the LIB. Moreover, as shown in Figure 5.15, the VMD analysis method has higher prediction accuracy than the EMD analysis method; this observation can be seen clearly in B006 and CS2-35 LIBs.

The RMSE and MAE results are presented in Figure 5.16 (a) and (b), respectively. The average RMSE is 0.0680, 0.02528, and 0.02385 for the DWT, EMD, and VMD decomposition methods. The average MAE is 0.0371, 0.0181, and 0.0160 for DWT, EMD, and VMD methods. From the RMSE and MAE results, it is clear that the VMD-NARX method can accurately predict the future trajectory of the capacity of LIBs.





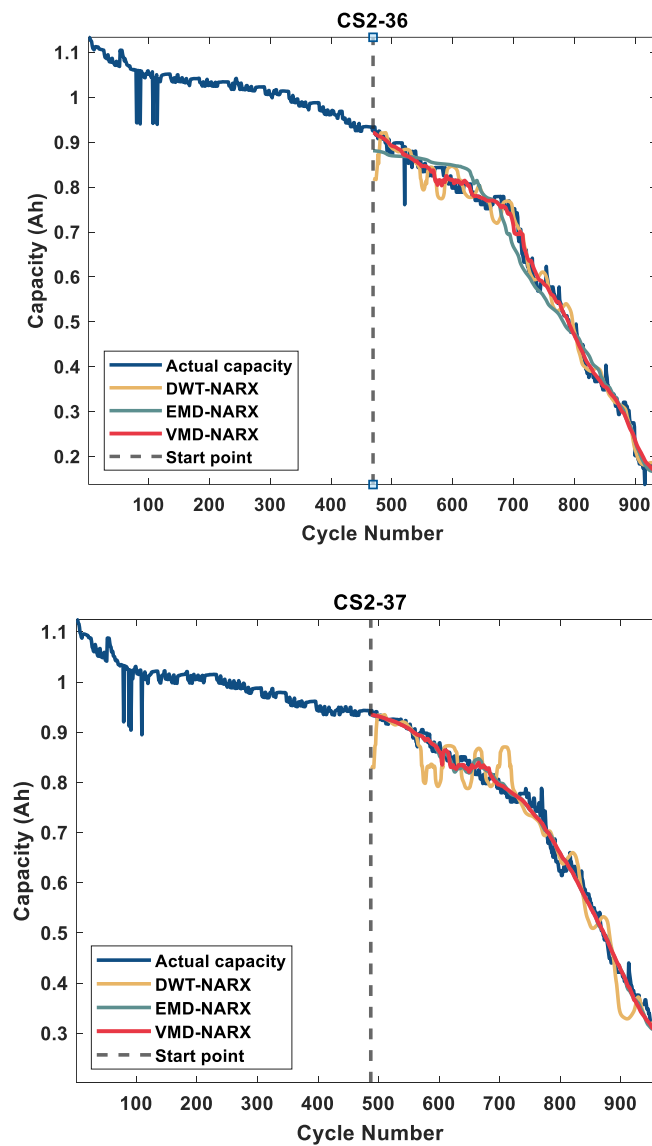
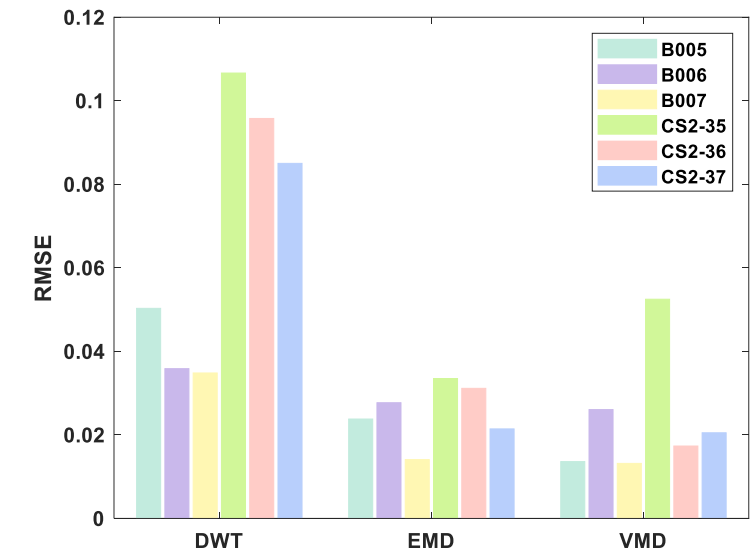


Figure 5.15 Capacity trajectory prediction results of NASA and CALCE datasets.



(a) RMSE.

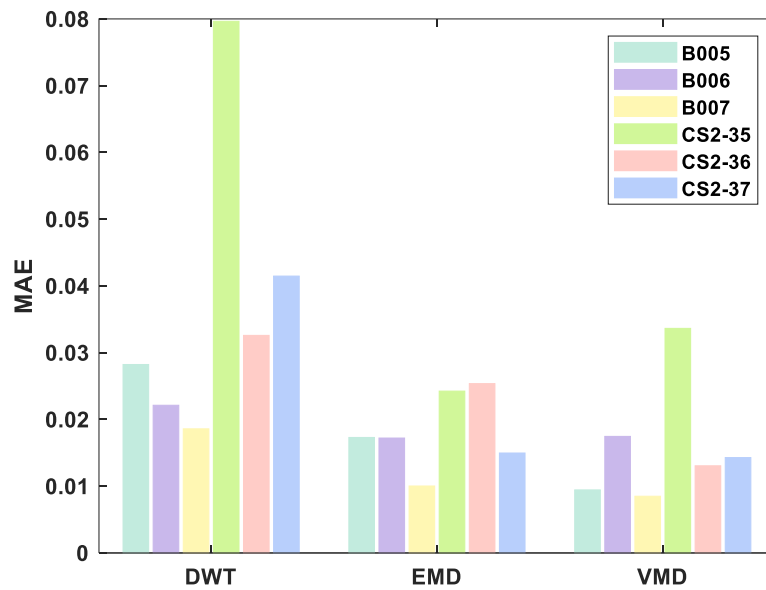


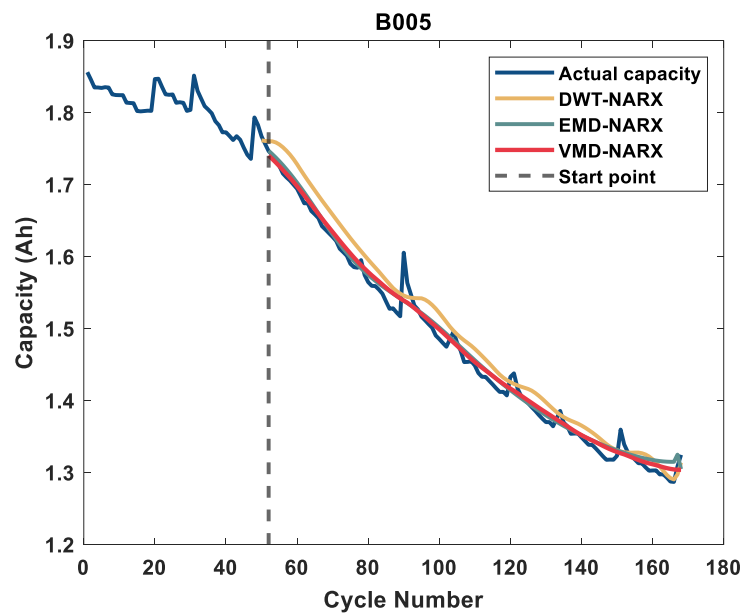
Figure 5.16 (a) RMSE and (b) MAE results for DWT, EMD, and VMD decomposition techniques.

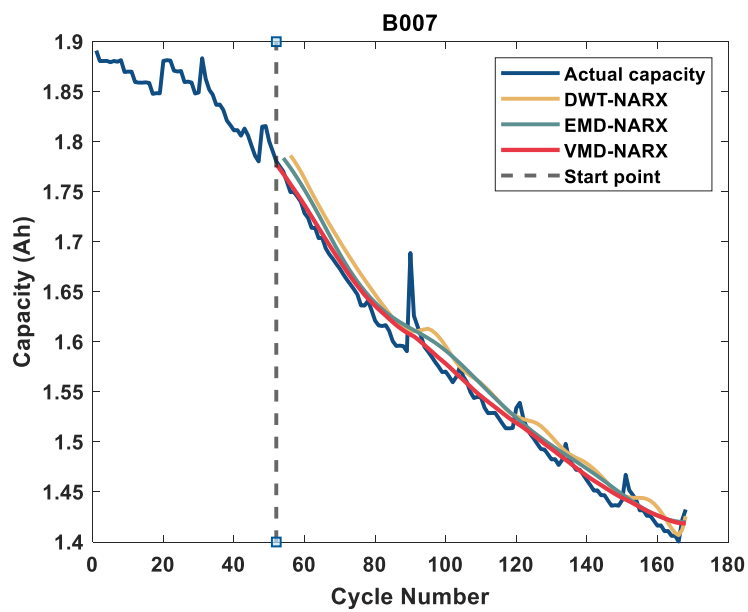
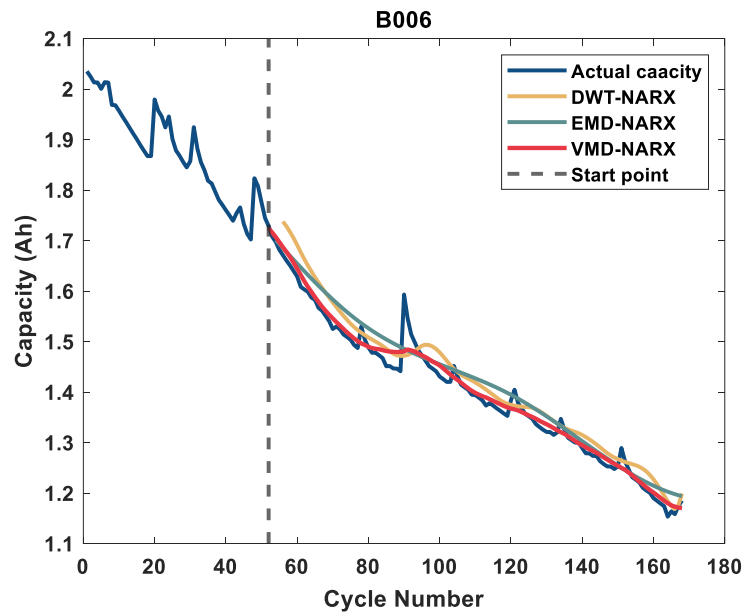
5.3.2.2 Early-Life Capacity Trajectory Prediction

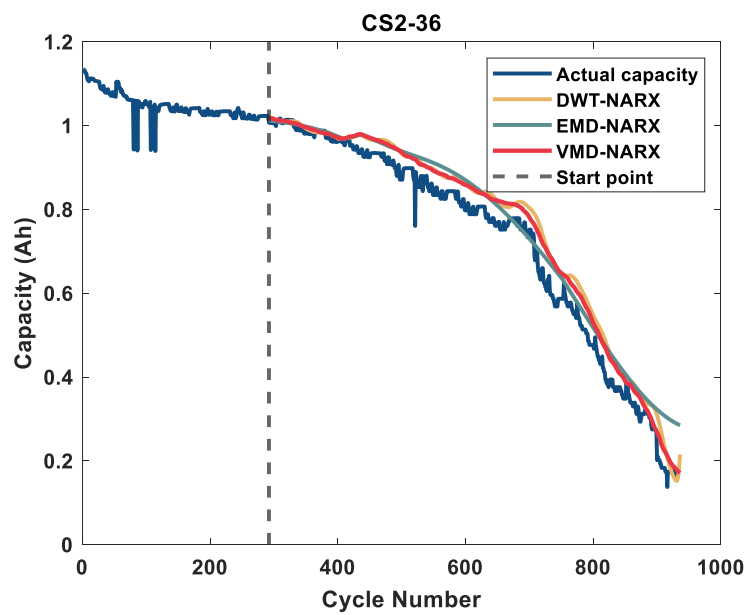
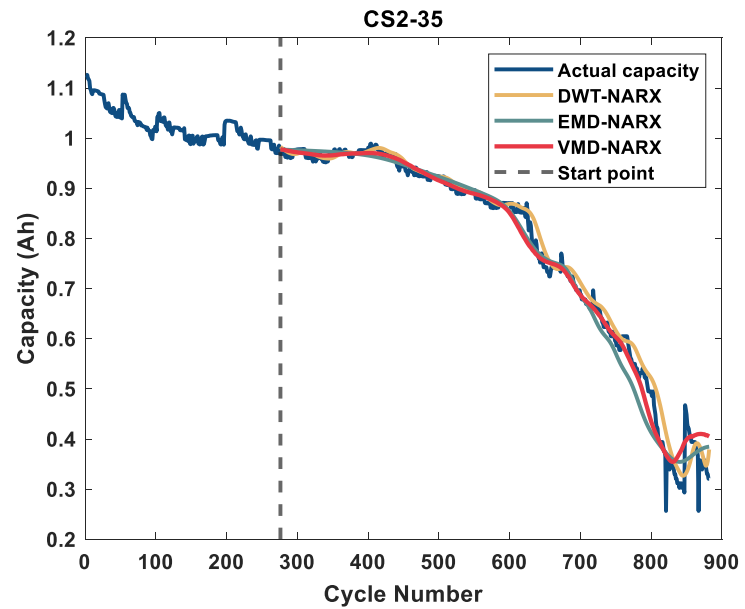
To validate the robustness of the proposed method, it is crucial to evaluate the proposed method's accuracy with minimal access to historical capacity data. Consequently, in this section, only 30% of the available datasets were used to train the NARX models of DWT, EMD, and VMD.

Figure 5.17 illustrates the capacity trajectory prediction results of NASA and CALCE datasets. Specifically, the prediction accuracy of VMD-NARX is superior to that of DWT-NARX and EMD-NARX. This is due to the ability of the VMD method to determine the centre frequency of each signal by solving the variational problem iteratively; consequently, the VMD algorithm is more robust in decomposing the measured capacity. Using VMD-NARX methodology, the RMSE for B005 is 0.0129, and the MAE is 0.035. While the same LIB RMSE value is increased to 0.0454 when DWT-NARX is used, the MAE is altered to 0.0772. Using the VMD-NARX method for capacity degradation trajectory prediction has increased prediction accuracy by 83.29% compared to the DWT-NARX method and by 60.55% compared to the EMD-NARX method.

The robustness of the VMD-NARX method is clearly observed in Figure 5.17 for LIB CS-37. The RMSE value using the VMD-NARX method is 0.0240, while the RMSE value is 0.634 and 0.0719 for DWT-NARX and EMD-NARX methods, respectively. This means the VMD-NARX method improved the prediction accuracy by 96.21% and 66.62% compared with DWT-NARX and EMD-NARX methods. The RMSE and MAE values for all the tested LIBs are shown in Figure 5.18 (a) and (b).







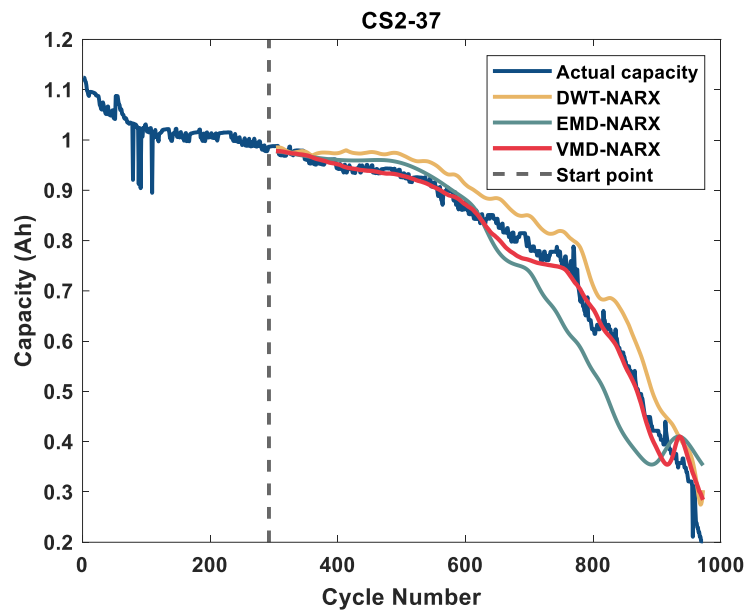
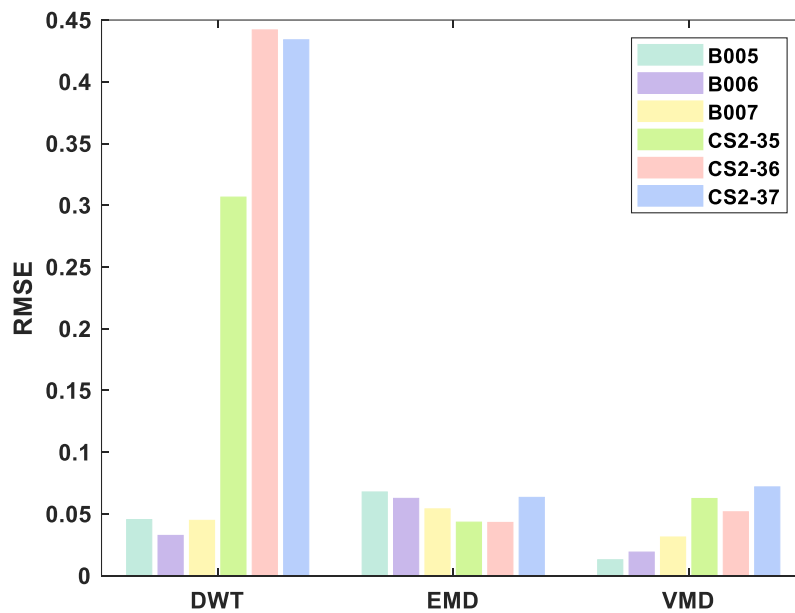


Figure 5.17 Capacity trajectory prediction results of NASA and CALCE datasets at the early-life case.



(a) RMSE

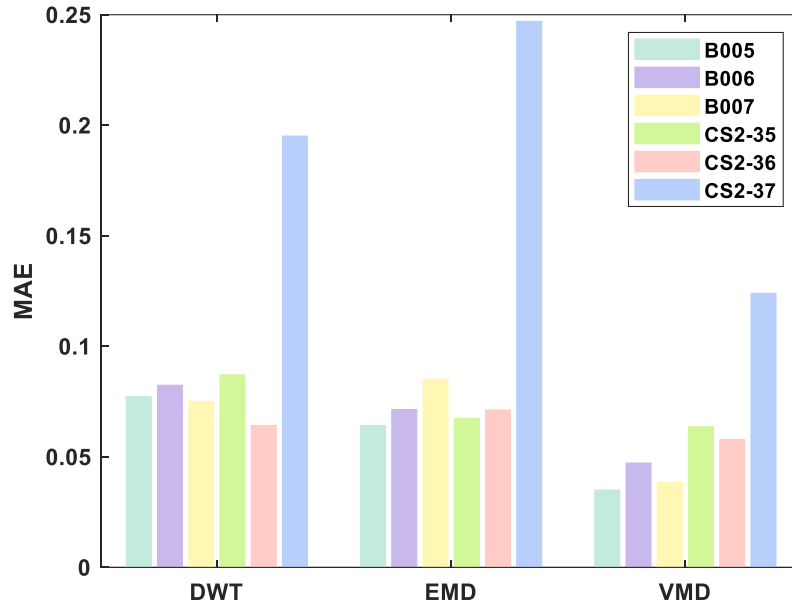


Figure 5.18 (a) RMSE and (b) MAE results for DWT, EMD, and VMD decomposition techniques.

To demonstrate the superiority of the proposed method for capacity prediction, it was compared with other existing methods. For example, Pang et al [317] developed a fusion method based on ICA and GPR algorithm to predict the RUL of LIBs. The proposed method has been validated using NASA dataset (Section 5.2.1.1). the average RMSE was 0.0748. Similarly, Zhang et al [318] proposed a deep learning LSTM based method along with variable input dimension to enlarge the training dataset and enhance the model generalization ability. The model has been validated using NASA dataset (Section 5.2.1.1) as well. The RMSE was 1.1 and the MAE was 1.0. The authors in [319] proposed a combined LSTM and BLS algorithm to predict the capacity of LIBs. The proposed method has been validated using both NASA and CALCE dataset. The average RMSE for the proposed method was 0.0423 and the MAE was 1.67.

Based on the comparison with the recent published articles, the proposed VMD-LSTM method has proven its generality and capacity to predict the capacity of the LIBs with maximum RMSE 0.08 and MAE of 0.153, which indicates the superiority of the proposed method compared to the existing state-of-the-art methods.

5.4 Summary

In this chapter, DWT, EMD, and VMD decomposition analysis methods were applied to overcome the challenge of the regeneration capacity in LIBs. The regeneration capacity can significantly impact the prediction accuracy for the trajectory of the future capacity and thus affect the utilisation of LIBs in second-life applications. The obtained results show that the VMD and EMD decomposition techniques outperform the DWT decomposition technique due to their adaptivity advantage. No mother wavelet selection process is needed in these techniques. The performance of the DWT analysis method depends on the accurate selection of the mother wavelet function. After denoise the capacity curve from the regenerated capacity, the denoised data was used to train the NARX model to predict the future trajectory of the capacity. Two datasets were used to train the NARX model. The prediction results demonstrate the ability of the VMD-NARX model to predict the future capacity trajectory with 2.385% RMSE and 1.6% MAE. Finally, the method that has been proposed can be applied to predict the capacity in the second-life applications of LIBs. Its robustness has been demonstrated by using the minimum values of capacity cycle as an input to the model.

Chapter 6 **Conclusion and Future Work**

6.1 Conclusions

6.1.1 Time-Frequency Image technique and Deep Learning CNNs for Capacity estimation of LIBs

A novel framework for capacity estimation of LIBs based on Time-frequency Image analysis was developed to provide a new path of using an imaging approach in estimating the capacity of the LIBs. The method used the energy concentration feature obtained from the Time-Frequency Image; instead of using 1D raw data or extracting multiple statistical characteristics, the battery's terminal voltage was transformed into a 2D image feature using CWT. The CWT produced a TFI, representing the battery's terminal voltage as a 2D image with time and frequency axes. Experimental data on four LIBs cells from the Prognostics Centre of excellence (PCoE) NASA were used to validate the method. The generated TFIs clearly showed the degradation process of the LIB at different capacity values. Two pre-trained DL-CNNs were used to classify the generated TFIs into five classes based on their capacity values. The classification accuracy was 95.69% using the AlexNet network and 95.52% using the VGG-16 network. These results suggest that the proposed method can effectively predict the health of LIBs used in applications such as electric vehicles and grid systems. Moreover, image regression models have been developed by modifying the structure of the AlexNet and VGG-16 DL-CNNs. The regression results showed high-capacity estimation accuracy with an average RMSE of 3.47% for AlexNet DL-CNN and 3.58% for VGG-16 DL-CNN.

6.1.2 The general framework for Capacity Estimation Based on Adaptive Empirical Wavelet Transform and LSTM.

The generalisation of the proposed TFI in Chapter 3 is limited because of the mother wavelet selection process. Therefore, chapter 4 overcomes this limitation by developing a general framework for the capacity estimation of LIBs. Specifically, the proposed method uses an adaptive EWT technique to assess the degradation of LIB capacity. The EWT technique extracts electrochemical characteristics of the LIBs from the measured voltage signals in both time and frequency domains. The measured voltage signals are decomposed into nine multi-

resolution modes to show high and low-frequency components of the signals. The extracted modes show a frequency range of 0.8 Hz to 5 Hz, related to the LIB's diffusion-reaction process. Some modes that did not change as the LIB degraded were removed since they were common in both healthy and aged states. EWT has an advantage over other techniques, as no mother wavelet selection process is required. Thirteen statistical features were extracted from the filtered voltage signal, but not all were strongly correlated with LIB degradation. The Pearson correlation coefficient was applied to reduce the dimension of the extracted features matrix to focus on essential features. Finally, a LSTM neural network model was developed and trained to estimate LIB capacity. 32 LIBs from two datasets were cycled at different current profiles to validate the approach. The capacity estimation results show that the proposed method can accurately estimate the capacity degradation of LIBs cycled under different conditions with an average RMSE of 1.26% and a max error of 2.74%. The EWT technique adapts to various operating conditions and extracts promising features related to capacity degradation inside the LIB.

6.1.3 Capacity Degradation Trajectory Prediction of LIBs

Once the capacity of the LIBs has been estimated, it is significantly vital to predict the future degradation trajectory of the capacity of the LIBs. Therefore, Chapter 5 presented a framework for the capacity degradation trajectory of LIBs based on three decomposition techniques, DWT, EMD, and VMD. The advantage of using time-frequency decomposition techniques is to overcome the challenge of the regeneration capacity in LIBs. The regeneration capacity can significantly impact the prediction accuracy of future capacity trajectory, thereby affecting the use of LIBs in second-life applications. The results showed that the EMD and VMD decomposition methods outperformed the DWT method due to their adaptivity advantage, and they do not require selecting a mother wavelet function. The DWT method's performance relies on accurately selecting the mother wavelet function. The denoised data obtained from the regenerated capacity was used to train the NARX model to predict the future capacity trajectory. Two datasets were utilised to train the NARX model. The prediction outcomes demonstrate the VMD-NARX model's ability to forecast the future capacity trajectory with an RMSE of 2.385% and an MAE of 1.6%.

6.2 Future work

This study proposed a novel algorithm for capacity and degradation trajectory prediction of LIBs running inside EVs and working under real-world operating conditions. The obtained results show a high accuracy and robustness of the proposed algorithms. Therefore, and based on the developed techniques in this thesis, several future works are summarised as follows:

- The methods presented in this study focus on the cell level of LIBs; however, in real-world applications such as EVs, LIBs are constructed from a vast number of cells arranged in series and parallel configurations. This battery pack setup introduces additional complexities when attempting to estimate the battery pack's capacity during operation. Challenges include variations between cells, temperature distribution throughout the entire pack, and differing degradation paths due to cell orientation within the pack. As a result, future research should explore the effectiveness of the developed techniques at the battery pack level rather than solely at the cell level.
- Future research should integrate the developed algorithms into the BMS for real-time, online capacity estimation and prediction. However, implementing these data-driven methods in a BMS necessitates continuously updating model parameters to ensure accurate capacity estimation results. To address this challenge, developing a cloud-based digital model that guarantees precise capacity estimation outcomes throughout the LIB's lifespan is crucial. Figure 6.1 shows a flowchart of the proposed solution for a cloud-based approach for online capacity estimation of LIBs.
- The quality of training datasets plays a vital role in determining model performance. In the context of automotive applications, battery degradation is heavily impacted by the load patterns experienced by the battery. Lab-generated data typically covers only a limited number of load profiles, which hampers the model's ability to learn realistic battery ageing behaviour. Consequently, creating a model that simulates the battery's degradation path based on diverse user behaviours is essential to understand the ageing process better. The methods presented in this thesis have undergone validation and testing using diverse online datasets, including those from NASA, Stanford

University, and Maryland University. Nevertheless, incorporating an in-house cycling dataset with varied operating conditions (such as current profile, temperature, and C-rate) could significantly enhance our understanding of the degradation processes within LIBs. Consequently, it would also lead to improved estimation accuracy for the developed methods.

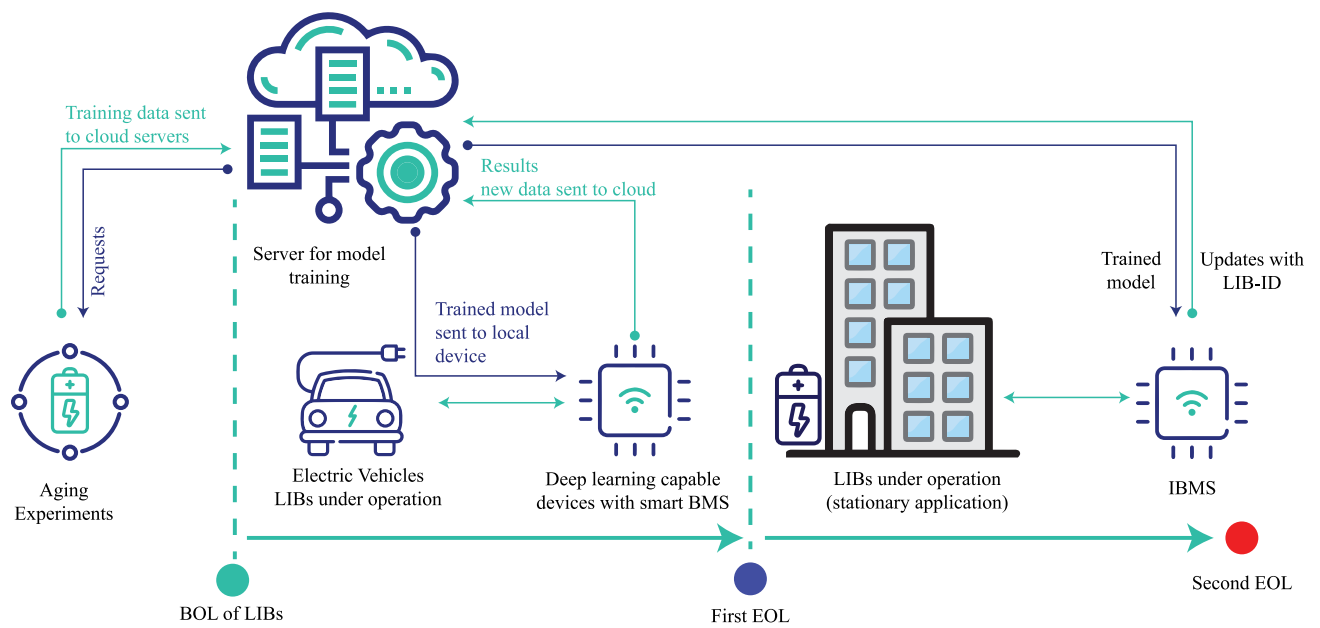


Figure 6.1 Flowchart of the cloud-based approach for online capacity estimation of LIB.

- Creating a fast classification method for retired LIBs using unsupervised machine learning algorithms, such as clustering techniques, is crucial. After reaching the end of their primary use, LIBs typically retain 70%-80% of their initial capacity and can be repurposed for secondary applications. Before utilising these batteries for secondary purposes, the main challenge is efficiently categorising the large quantities of retired batteries into distinct subgroups. Therefore, one of our future works plans is to develop an algorithm to effectively ranked the retired LIBs. Figure 6.2 presents an overview of the potential solution.

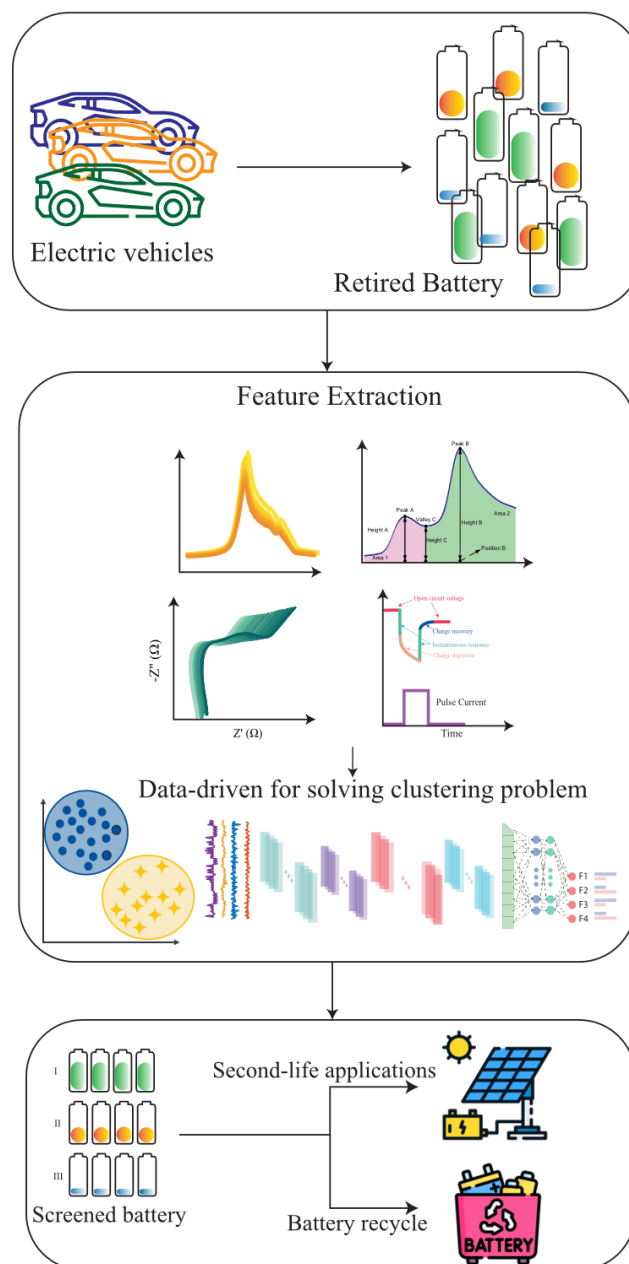


Figure 6.2 Flowchart of the proposed future work for sorting the retired LIB.

References

1. Kouridis, C. and C. Vlachokostas, *Towards decarbonizing road transport: Environmental and social benefit of vehicle fleet electrification in urban areas of Greece*. Renewable and Sustainable Energy Reviews, 2022. **153**: p. 111775.
2. Muratori, M. and T. Mai, *The shape of electrified transportation*. Environmental Research Letters, 2020. **16**(1): p. 011003.
3. Xiong, S., J. Ji, and X. Ma, *Environmental and economic evaluation of remanufacturing lithium-ion batteries from electric vehicles*. Waste Management, 2020. **102**: p. 579-586.
4. Costa, C.M., et al., *Electric vehicles: To what extent are environmentally friendly and cost effective?—Comparative study by european countries*. Renewable and Sustainable Energy Reviews, 2021. **151**: p. 111548.
5. Stampatori, D., P.P. Raimondi, and M. Noussan, *Li-ion batteries: A review of a key technology for transport decarbonization*. Energies, 2020. **13**(10): p. 2638.
6. Tian, Y., et al., *Promises and challenges of next-generation “beyond Li-ion” batteries for electric vehicles and grid decarbonization*. Chemical reviews, 2020. **121**(3): p. 1623-1669.
7. Yang, Y., et al., *On the sustainability of lithium ion battery industry—A review and perspective*. Energy Storage Materials, 2021. **36**: p. 186-212.
8. Xie, J. and Y.-C. Lu, *A retrospective on lithium-ion batteries*. Nature communications, 2020. **11**(1): p. 2499.
9. Frith, J.T., M.J. Lacey, and U. Ulissi, *A non-academic perspective on the future of lithium-based batteries*. Nature Communications, 2023. **14**(1): p. 420.
10. Bibra, E.M., et al., *Global EV outlook 2022: Securing supplies for an electric future*. 2022.
11. Muralidharan, N., et al., *Next-Generation Cobalt-Free Cathodes—A Prospective Solution to the Battery Industry's Cobalt Problem*. Transition Metal Oxides for Electrochemical Energy Storage, 2022: p. 33-53.
12. Stefan M. Knupfer, R.H., Patrick Hertzke, Patrick Schaufuss, *Electrifying insights: How automakers can drive electrified vehicle sales and profitability*. 2017.
13. Plett, G., *Battery management systems*. Vol. 1. 2015: Artech House.
14. Plett, G., *Battery Management Systems, Volume II*. 2015, Norwood: Artech House.

-
15. Williard, N., et al., *Lessons learned from the 787 dreamliner issue on lithium-ion battery reliability*. Energies, 2013. **6**(9): p. 4682-4695.
 16. ALUND, N.N., *Tesla 'spontaneously' catches fire on California highway; 6,000 gallons of water needed to put it out*, in USA TODAY NEWS. 2023.
 17. Li, W., et al., *Digital twin for battery systems: Cloud battery management system with online state-of-charge and state-of-health estimation*. Journal of Energy Storage, 2020. **30**: p. 101557.
 18. Zhang, Y., et al., *Aging characteristics-based health diagnosis and remaining useful life prognostics for lithium-ion batteries*. ETransportation, 2019. **1**: p. 100004.
 19. Broussely, M., et al., *Main aging mechanisms in Li ion batteries*. Journal of power sources, 2005. **146**(1-2): p. 90-96.
 20. Vetter, J., et al., *Ageing mechanisms in lithium-ion batteries*. Journal of power sources, 2005. **147**(1-2): p. 269-281.
 21. Wu, Y., *Lithium-Ion Batteries: Fundamentals and Applications*, ed. Y. Wu. Vol. 4. 2015, Baton Rouge: CRC Press.
 22. Andrea, D., *Lithium-Ion Batteries and Applications: A Practical and Comprehensive Guide to Lithium-Ion Batteries and Arrays, from Toys to Towns, Volume 2*. 2020, Norwood: Artech House.
 23. Jiang, J. and C. Zhang, *Fundamentals and application of lithium-ion batteries in electric drive vehicles*. 2015: Wiley-Blackwell.
 24. Kanevskii, L. and V. Dubasova, *Degradation of lithium-ion batteries and how to fight it: A review*. Russian Journal of Electrochemistry, 2005. **41**(1): p. 1-16.
 25. Birkel, C.R., et al., *Degradation diagnostics for lithium ion cells*. Journal of Power Sources, 2017. **341**: p. 373-386.
 26. Pender, J.P., et al., *Electrode degradation in lithium-ion batteries*. ACS nano, 2020. **14**(2): p. 1243-1295.
 27. Henschel, J., et al., *Lithium ion battery electrolyte degradation of field-tested electric vehicle battery cells—A comprehensive analytical study*. Journal of Power Sources, 2020. **447**: p. 227370.
 28. Rinkel, B.L., et al., *Electrolyte oxidation pathways in lithium-ion batteries*. Journal of the American Chemical Society, 2020. **142**(35): p. 15058-15074.
 29. Li, T., et al., *Degradation mechanisms and mitigation strategies of nickel-rich NMC-based lithium-ion batteries*. Electrochemical Energy Reviews, 2020. **3**(1): p. 43-80.
 30. Li, A., et al., *A review on lithium-ion battery separators towards enhanced safety performances and modelling approaches*. Molecules, 2021. **26**(2): p. 478.
 31. Yang, S.-c., et al., *A coupled electrochemical-thermal-mechanical degradation modelling approach for lifetime assessment of lithium-ion batteries*. Electrochimica Acta, 2019. **326**: p. 134928.

-
32. Schweidler, S., et al., *Investigation into mechanical degradation and fatigue of high-Ni NCM cathode material: a long-term cycling study of full cells*. ACS applied energy materials, 2019. **2**(10): p. 7375-7384.
 33. Reniers, J.M., G. Mulder, and D.A. Howey, *Review and performance comparison of mechanical-chemical degradation models for lithium-ion batteries*. Journal of The Electrochemical Society, 2019. **166**(14): p. A3189.
 34. Liu, J., et al., *Aging mechanisms and thermal stability of aged commercial 18650 lithium ion battery induced by slight overcharging cycling*. Journal of power sources, 2020. **445**: p. 227263.
 35. Barkholtz, H.M., et al., *Multi-scale thermal stability study of commercial lithium-ion batteries as a function of cathode chemistry and state-of-charge*. Journal of Power Sources, 2019. **435**: p. 226777.
 36. Feng, X., et al., *Influence of aging paths on the thermal runaway features of lithium-ion batteries in accelerating rate calorimetry tests*. Int. J. Electrochem. Sci, 2019. **14**(1): p. 44-58.
 37. Pastor-Fernández, C., et al., *Critical review of non-invasive diagnosis techniques for quantification of degradation modes in lithium-ion batteries*. Renewable and Sustainable Energy Reviews, 2019. **109**: p. 138-159.
 38. Zhu, J., et al., *Investigation of lithium-ion battery degradation mechanisms by combining differential voltage analysis and alternating current impedance*. Journal of Power Sources, 2020. **448**: p. 227575.
 39. Dienwiebel, I., M. Winter, and M. Börner, *Visualization of degradation mechanisms of negative electrodes based on silicon nanoparticles in lithium-ion batteries via quasi in situ scanning electron microscopy and energy-dispersive x-ray spectroscopy*. The Journal of Physical Chemistry C, 2022. **126**(27): p. 11016-11025.
 40. Tanim, T.R., et al., *Extreme fast charge challenges for lithium-ion battery: variability and positive electrode issues*. Journal of The Electrochemical Society, 2019. **166**(10): p. A1926.
 41. Reniers, J.M., G. Mulder, and D.A. Howey, *Review and performance comparison of mechanical-chemical degradation models for lithium-ion batteries*. Journal of The Electrochemical Society, 2019. **166**(14): p. A3189-A3200.
 42. Lin, Q., et al., *Towards a smarter battery management system: A critical review on optimal charging methods of lithium ion batteries*. Energy, 2019. **183**: p. 220-234.
 43. Meng, H. and Y.-F. Li, *A review on prognostics and health management (PHM) methods of lithium-ion batteries*. Renewable and Sustainable Energy Reviews, 2019. **116**: p. 109405.
 44. Ng, K.S., et al., *Enhanced coulomb counting method for estimating state-of-charge and state-of-health of lithium-ion batteries*. Applied Energy, 2009. **86**(9): p. 1506-1511.
 45. Goud, J.S., R. K. and B. Singh, *An Online Method of Estimating State of Health of a Li-Ion Battery*. IEEE Transactions on Energy Conversion, 2021. **36**(1): p. 111-119.

-
46. Movassagh, K., et al., *A critical look at coulomb counting approach for state of charge estimation in batteries*. Energies, 2021. **14**(14): p. 4074.
 47. Zhang, S., et al., *A rapid online calculation method for state of health of lithium-ion battery based on coulomb counting method and differential voltage analysis*. Journal of Power Sources, 2020. **479**: p. 228740.
 48. He, L. and D. Guo, *An improved coulomb counting approach based on numerical iteration for SOC estimation with real-time error correction ability*. IEEE Access, 2019. **7**: p. 74274-74282.
 49. Zou, Y., et al., *Combined state of charge and state of health estimation over lithium-ion battery cell cycle lifespan for electric vehicles*. Journal of Power Sources, 2015. **273**: p. 793-803.
 50. Weng, C., J. Sun, and H. Peng, *A unified open-circuit-voltage model of lithium-ion batteries for state-of-charge estimation and state-of-health monitoring*. Journal of Power Sources, 2014. **258**: p. 228-237.
 51. Yu, Q.-Q., et al., *A comparative study on open circuit voltage models for lithium-ion batteries*. Chinese Journal of Mechanical Engineering, 2018. **31**(1): p. 1-8.
 52. Chiang, Y.-H., W.-Y. Sean, and J.-C. Ke, *Online estimation of internal resistance and open-circuit voltage of lithium-ion batteries in electric vehicles*. Journal of Power Sources, 2011. **196**(8): p. 3921-3932.
 53. Bian, X., et al., *An open circuit voltage-based model for state-of-health estimation of lithium-ion batteries: Model development and validation*. Journal of Power Sources, 2020. **448**: p. 227401.
 54. Bian, X., et al., *State-of-health estimation of lithium-ion batteries by fusing an open circuit voltage model and incremental capacity analysis*. IEEE Transactions on Power Electronics, 2021. **37**(2): p. 2226-2236.
 55. Theuerkauf, D. and L. Swan, *Characteristics of Open Circuit Voltage Relaxation in Lithium-Ion Batteries for the Purpose of State of Charge and State of Health Analysis*. Batteries, 2022. **8**(8): p. 77.
 56. Cui, Y., et al., *State of health diagnosis model for lithium ion batteries based on real-time impedance and open circuit voltage parameters identification method*. Energy, 2018. **144**: p. 647-656.
 57. Fang, Q., et al., *A state of health estimation method for lithium-ion batteries based on voltage relaxation model*. Energies, 2019. **12**(7): p. 1349.
 58. Amifia, L.K., *Direct Comparison using Coulomb Counting and Open Circuit Voltage Method for the State of Health Li-Po Battery*. Journal of Robotics and Control (JRC), 2022. **3**(4): p. 455-463.
 59. Chen, L., et al., *A new state-of-health estimation method for lithium-ion batteries through the intrinsic relationship between ohmic internal resistance and capacity*. Measurement, 2018. **116**: p. 586-595.
 60. Ciucci, F., *Modeling electrochemical impedance spectroscopy*. Current Opinion in Electrochemistry, 2019. **13**: p. 132-139.

-
61. Wang, X., et al., *A review of modeling, acquisition, and application of lithium-ion battery impedance for onboard battery management*. eTransportation, 2021. **7**: p. 100093.
 62. Barsoukov, E. and J.R. Macdonald, *Impedance Spectroscopy Theory, Experiment, and Applications*, 2nd ed.(Hoboken, NJ: John Wiley & Sons, Inc., 2005), 2005.
 63. Westerhoff, U., et al., *Analysis of lithium-ion battery models based on electrochemical impedance spectroscopy*. Energy Technology, 2016. **4**(12): p. 1620-1630.
 64. Meddings, N., et al., *Application of electrochemical impedance spectroscopy to commercial Li-ion cells: A review*. Journal of Power Sources, 2020. **480**: p. 228742.
 65. Lohmann, N., et al., *Electrochemical impedance spectroscopy for lithium-ion cells: Test equipment and procedures for aging and fast characterization in time and frequency domain*. Journal of Power Sources, 2015. **273**: p. 613-623.
 66. Wang, L., et al., *Instantaneous estimation of internal temperature in lithium-ion battery by impedance measurement*. International Journal of Energy Research, 2020. **44**(4): p. 3082-3097.
 67. Andre, D., et al., *Characterization of high-power lithium-ion batteries by electrochemical impedance spectroscopy. I. Experimental investigation*. Journal of Power Sources, 2011. **196**(12): p. 5334-5341.
 68. Maheshwari, A., M. Heck, and M. Santarelli, *Cycle aging studies of lithium nickel manganese cobalt oxide-based batteries using electrochemical impedance spectroscopy*. Electrochimica Acta, 2018. **273**: p. 335-348.
 69. Zhou, X., et al., *Impedance characterization of lithium-ion batteries aging under high-temperature cycling: Importance of electrolyte-phase diffusion*. Journal of Power Sources, 2019. **426**: p. 216-222.
 70. Stroe, D.I., et al. *Diagnosis of lithium-ion batteries state-of-health based on electrochemical impedance spectroscopy technique*. in *2014 IEEE Energy Conversion Congress and Exposition (ECCE)*. 2014. IEEE.
 71. Messing, M., T. Shoa, and S. Habibi, *Estimating battery state of health using electrochemical impedance spectroscopy and the relaxation effect*. Journal of Energy Storage, 2021. **43**: p. 103210.
 72. Wang, X., et al. *State estimation of lithium ion battery based on electrochemical impedance spectroscopy with on-board impedance measurement system*. in *2015 IEEE Vehicle Power and Propulsion Conference (VPPC)*. 2015. IEEE.
 73. Mc Carthy, K., et al., *Electrochemical impedance correlation analysis for the estimation of Li-ion battery state of charge, state of health and internal temperature*. Journal of Energy Storage, 2022. **50**: p. 104608.
 74. Luo, F., et al., *Rapid prediction of the state of health of retired power batteries based on electrochemical impedance spectroscopy*. Journal of Energy Storage, 2021. **41**: p. 102866.

-
75. Rastegarpanah, A., J. Hathaway, and R. Stolkin, *Rapid model-free state of health estimation for end-of-first-life electric vehicle batteries using impedance spectroscopy*. *Energies*, 2021. **14**(9): p. 2597.
 76. Waag, W., S. Käbitz, and D.U. Sauer, *Experimental investigation of the lithium-ion battery impedance characteristic at various conditions and aging states and its influence on the application*. *Applied energy*, 2013. **102**: p. 885-897.
 77. Vyroubal, P. and T. Kazda, *Equivalent circuit model parameters extraction for lithium ion batteries using electrochemical impedance spectroscopy*. *Journal of Energy Storage*, 2018. **15**: p. 23-31.
 78. Andre, D., et al., *Characterization of high-power lithium-ion batteries by electrochemical impedance spectroscopy. II: Modelling*. *Journal of Power Sources*, 2011. **196**(12): p. 5349-5356.
 79. Stroe, D.I. and E. Schaltz, *Lithium-Ion Battery State-of-Health Estimation Using the Incremental Capacity Analysis Technique*. *IEEE Transactions on Industry Applications*, 2020. **56**(1): p. 678-685.
 80. Jiang, B., H. Dai, and X. Wei, *Incremental capacity analysis based adaptive capacity estimation for lithium-ion battery considering charging condition*. *Applied Energy*, 2020. **269**: p. 115074.
 81. He, J., et al., *State-of-Health Estimation of Lithium-Ion Batteries Using Incremental Capacity Analysis Based on Voltage–Capacity Model*. *IEEE Transactions on Transportation Electrification*, 2020. **6**(2): p. 417-426.
 82. Goh, T., et al., *Capacity estimation algorithm with a second-order differential voltage curve for Li-ion batteries with NMC cathodes*. *Energy*, 2017. **135**: p. 257-268.
 83. Wang, L., et al., *State of health estimation of battery modules via differential voltage analysis with local data symmetry method*. *Electrochimica acta*, 2017. **256**: p. 81-89.
 84. Wei, M., et al., *Remaining useful life prediction for 18650 sodium-ion batteries based on incremental capacity analysis*. *Energy*, 2022. **261**: p. 125151.
 85. Li, X., et al., *State of health estimation for Li-Ion battery using incremental capacity analysis and Gaussian process regression*. *Energy*, 2020. **190**: p. 116467.
 86. Pan, W., et al., *A health indicator extraction and optimization for capacity estimation of Li-ion battery using incremental capacity curves*. *Journal of Energy Storage*, 2021. **42**: p. 103072.
 87. He, J., et al., *Comparative study of curve determination methods for incremental capacity analysis and state of health estimation of lithium-ion battery*. *Journal of Energy Storage*, 2020. **29**: p. 101400.
 88. Li, X., et al., *State-of-health estimation for Li-ion batteries by combing the incremental capacity analysis method with grey relational analysis*. *Journal of Power Sources*, 2019. **410-411**: p. 106-114.
 89. Li, X., Z. Wang, and J. Yan, *Prognostic health condition for lithium battery using the partial incremental capacity and Gaussian process regression*. *Journal of Power Sources*, 2019. **421**: p. 56-67.

-
90. Li, Y., et al., *A quick on-line state of health estimation method for Li-ion battery with incremental capacity curves processed by Gaussian filter*. Journal of Power Sources, 2018. **373**: p. 40-53.
 91. Riviere, E., et al. *LiFePO₄ Battery State of Health Online Estimation Using Electric Vehicle Embedded Incremental Capacity Analysis*. in *2015 IEEE Vehicle Power and Propulsion Conference (VPPC)*. 2015.
 92. Farmann, A., W. Waag, and D.U. Sauer, *Adaptive approach for on-board impedance parameters and voltage estimation of lithium-ion batteries in electric vehicles*. Journal of Power Sources, 2015. **299**: p. 176-188.
 93. You, H.W., et al., *Analysis of equivalent circuit models in lithium-ion batteries*. AIP Advances, 2018. **8**(12): p. 125101.
 94. Madani, S.S., E. Schaltz, and S. Knudsen Kær, *An electrical equivalent circuit model of a lithium titanate oxide battery*. Batteries, 2019. **5**(1): p. 31.
 95. Zhang, J.a., et al., *Variable-order equivalent circuit modeling and state of charge estimation of lithium-ion battery based on electrochemical impedance spectroscopy*. Energies, 2021. **14**(3): p. 769.
 96. Tan, X., et al., *Online state-of-health estimation of lithium-ion battery based on dynamic parameter identification at multi timescale and support vector regression*. Journal of Power Sources, 2021. **484**: p. 229233.
 97. Pérez, G., et al., *Modelling of Li-ion batteries dynamics using impedance spectroscopy and pulse fitting: EVs application*. World Electric Vehicle Journal, 2013. **6**(3): p. 644-652.
 98. Jossen, A., *Fundamentals of battery dynamics*. Journal of power sources, 2006. **154**(2): p. 530-538.
 99. Yang, X., et al., *Battery states online estimation based on exponential decay particle swarm optimization and proportional-integral observer with a hybrid battery model*. Energy, 2020. **191**: p. 116509.
 100. Hu, X., S. Li, and H. Peng, *A comparative study of equivalent circuit models for Li-ion batteries*. Journal of Power Sources, 2012. **198**: p. 359-367.
 101. Seaman, A., T.-S. Dao, and J. McPhee, *A survey of mathematics-based equivalent-circuit and electrochemical battery models for hybrid and electric vehicle simulation*. Journal of Power Sources, 2014. **256**: p. 410-423.
 102. Naseri, F., et al., *An Enhanced Equivalent Circuit Model With Real-Time Parameter Identification for Battery State-of-Charge Estimation*. IEEE Transactions on Industrial Electronics, 2022. **69**(4): p. 3743-3751.
 103. Xia, B., et al., *A novel observer for lithium-ion battery state of charge estimation in electric vehicles based on a second-order equivalent circuit model*. Energies, 2017. **10**(8): p. 1150.
 104. Amir, S., et al., *Dynamic Equivalent Circuit Model to Estimate State-of-Health of Lithium-Ion Batteries*. IEEE Access, 2022. **10**: p. 18279-18288.

-
105. Fan, J., et al. *A novel State of Health estimation method for Lithium-ion battery in electric vehicles*. in *Journal of Physics: Conference Series*. 2019. IOP Publishing.
 106. Lin, X., et al., *State of charge estimation with the adaptive unscented Kalman filter based on an accurate equivalent circuit model*. *Journal of Energy Storage*, 2021. **41**: p. 102840.
 107. Qiu, X., W. Wu, and S. Wang, *Remaining useful life prediction of lithium-ion battery based on improved cuckoo search particle filter and a novel state of charge estimation method*. *Journal of Power Sources*, 2020. **450**: p. 227700.
 108. Zhang, C., et al., *Online estimation of battery equivalent circuit model parameters and state of charge using decoupled least squares technique*. *Energy*, 2018. **142**: p. 678-688.
 109. Lai, X., et al., *A comparative study of global optimization methods for parameter identification of different equivalent circuit models for Li-ion batteries*. *Electrochimica Acta*, 2019. **295**: p. 1057-1066.
 110. Qian, K., et al., *Modified dual extended Kalman filters for SOC estimation and online parameter identification of lithium-ion battery via modified gray wolf optimizer*. *Proceedings of the Institution of Mechanical Engineers, Part D: Journal of Automobile Engineering*, 2022. **236**(8): p. 1761-1774.
 111. Gantenbein, S., M. Weiss, and E. Ivers-Tiffée, *Impedance based time-domain modeling of lithium-ion batteries: Part I*. *Journal of Power Sources*, 2018. **379**: p. 317-327.
 112. Huang, J., *Diffusion impedance of electroactive materials, electrolytic solutions and porous electrodes: Warburg impedance and beyond*. *Electrochimica Acta*, 2018. **281**: p. 170-188.
 113. Munoz-Condes, P., et al., *On Condition Maintenance Based on the Impedance Measurement for Traction Batteries: Development and Industrial Implementation*. *IEEE Transactions on Industrial Electronics*, 2013. **60**(7): p. 2750-2759.
 114. Christensen, A. and A. Adebisoyi. *Using on-board electrochemical impedance spectroscopy in battery management systems*. in *2013 World Electric Vehicle Symposium and Exhibition (EVS27)*. 2013. IEEE.
 115. Westerhoff, U., et al., *Electrochemical impedance spectroscopy based estimation of the state of charge of lithium-ion batteries*. *Journal of Energy Storage*, 2016. **8**: p. 244-256.
 116. Deng, Z., et al., *Electrochemical impedance spectroscopy study of a lithium/sulfur battery: modeling and analysis of capacity fading*. *Journal of The Electrochemical Society*, 2013. **160**(4): p. A553.
 117. Zhang, C., et al., *Characterization of electrochemical impedance equivalent model and parameters for Li-ion batteries echelon use*. *Dianli Xitong Zidonghua(Automation of Electric Power Systems)*, 2013. **37**(1): p. 54-58.

-
118. Cho, S.Y., et al., *Battery Impedance Analysis Considering DC Component in Sinusoidal Ripple-Current Charging*. IEEE Transactions on Industrial Electronics, 2016. **63**(3): p. 1561-1573.
 119. Wang, Q.K., et al., *State of Charge-Dependent Polynomial Equivalent Circuit Modeling for Electrochemical Impedance Spectroscopy of Lithium-Ion Batteries*. IEEE Transactions on Power Electronics, 2018. **33**(10): p. 8449-8460.
 120. Wang, X., X. Wei, and H. Dai, *Estimation of state of health of lithium-ion batteries based on charge transfer resistance considering different temperature and state of charge*. Journal of Energy Storage, 2019. **21**: p. 618-631.
 121. Piret, H., et al., *Tracking of electrochemical impedance of batteries*. Journal of Power Sources, 2016. **312**: p. 60-69.
 122. Xiong, R., et al., *A systematic model-based degradation behavior recognition and health monitoring method for lithium-ion batteries*. Applied Energy, 2017. **207**: p. 372-383.
 123. Wang, L., et al., *Electrochemical impedance spectroscopy (EIS) study of $\text{LiNi}_{1/3}\text{Co}_{1/3}\text{Mn}_{1/3}\text{O}_2$ for Li-ion batteries*. Int. J. Electrochem. Sci, 2012. **7**(1): p. 345-353.
 124. Zhang, Q., et al., *Electrochemical Impedance Spectroscopy Based State-of-Health Estimation for Lithium-Ion Battery Considering Temperature and State-of-Charge Effect*. IEEE Transactions on Transportation Electrification, 2022. **8**(4): p. 4633-4645.
 125. Doyle, M., T.F. Fuller, and J. Newman, *Modeling of galvanostatic charge and discharge of the lithium/polymer/insertion cell*. Journal of the Electrochemical society, 1993. **140**(6): p. 1526.
 126. Fuller, T.F., M. Doyle, and J. Newman, *Simulation and optimization of the dual lithium ion insertion cell*. Journal of the electrochemical society, 1994. **141**(1): p. 1.
 127. Jokar, A., et al., *Review of simplified Pseudo-two-Dimensional models of lithium-ion batteries*. Journal of Power Sources, 2016. **327**: p. 44-55.
 128. Horner, J.S., et al., *A pseudo-two-dimensional (P2D) model for FeS_2 conversion cathode batteries*. Journal of Power Sources, 2022. **544**: p. 231893.
 129. Dao, T.-S., C.P. Vyasarayani, and J. McPhee, *Simplification and order reduction of lithium-ion battery model based on porous-electrode theory*. Journal of Power Sources, 2012. **198**: p. 329-337.
 130. Kim, J., et al., *Effective and practical parameters of electrochemical Li-ion battery models for degradation diagnosis*. Journal of Energy Storage, 2021. **42**: p. 103077.
 131. Bi, Y., Y. Yin, and S.-Y. Choe, *Online state of health and aging parameter estimation using a physics-based life model with a particle filter*. Journal of Power Sources, 2020. **476**: p. 228655.
 132. Han, X., et al., *Simplification of physics-based electrochemical model for lithium ion battery on electric vehicle. Part II: Pseudo-two-dimensional model simplification and state of charge estimation*. Journal of Power Sources, 2015. **278**: p. 814-825.

-
133. Zhang, D., B.N. Popov, and R.E. White, *Modeling lithium intercalation of a single spinel particle under potentiodynamic control*. Journal of the Electrochemical Society, 2000. **147**(3): p. 831.
 134. Namor, E., et al., *Parameter identification of a lithium-ion cell single-particle model through non-invasive testing*. Journal of Energy Storage, 2017. **12**: p. 138-148.
 135. Ren, L., et al., *An algorithm for state of charge estimation based on a single-particle model*. Journal of Energy Storage, 2021. **39**: p. 102644.
 136. Dey, S., B. Ayalew, and P. Pisu, *Nonlinear robust observers for state-of-charge estimation of lithium-ion cells based on a reduced electrochemical model*. IEEE Transactions on Control Systems Technology, 2015. **23**(5): p. 1935-1942.
 137. Tanim, T.R., C.D. Rahn, and C.-Y. Wang, *State of charge estimation of a lithium ion cell based on a temperature dependent and electrolyte enhanced single particle model*. Energy, 2015. **80**: p. 731-739.
 138. Li, J., et al., *A single particle model with chemical/mechanical degradation physics for lithium ion battery State of Health (SOH) estimation*. Applied energy, 2018. **212**: p. 1178-1190.
 139. Lotfi, N., et al. *Li-ion battery state of health estimation based on an improved single particle model*. in 2017 American Control Conference (ACC). 2017. IEEE.
 140. Li, J., R.G. Landers, and J. Park, *A comprehensive single-particle-degradation model for battery state-of-health prediction*. Journal of Power Sources, 2020. **456**: p. 227950.
 141. Khodadadi Sadabadi, K., X. Jin, and G. Rizzoni, *Prediction of remaining useful life for a composite electrode lithium ion battery cell using an electrochemical model to estimate the state of health*. Journal of Power Sources, 2021. **481**: p. 228861.
 142. Choi, Y. and H. Kim, *Prognostics and Health Management for Battery Remaining Useful Life Prediction Based on Electrochemistry Model: A Tutorial*. The Journal of Korean Institute of Communications and Information Sciences, 2017. **42**(4): p. 939-949.
 143. Allam, A. and S. Onori, *Online Capacity Estimation for Lithium-Ion Battery Cells via an Electrochemical Model-Based Adaptive Interconnected Observer*. IEEE Transactions on Control Systems Technology, 2021. **29**(4): p. 1636-1651.
 144. Liu, Q., et al., *The Remaining Useful Life Prediction by Using Electrochemical Model in the Particle Filter Framework for Lithium-Ion Batteries*. IEEE Access, 2020. **8**: p. 126661-126670.
 145. Ling, L. and Y. Wei, *State-of-Charge and State-of-Health Estimation for Lithium-Ion Batteries Based on Dual Fractional-Order Extended Kalman Filter and Online Parameter Identification*. IEEE Access, 2021. **9**: p. 47588-47602.
 146. Chen, C., R. Xiong, and W. Shen, *A Lithium-Ion Battery-in-the-Loop Approach to Test and Validate Multiscale Dual H Infinity Filters for State-of-Charge and Capacity Estimation*. IEEE Transactions on Power Electronics, 2018. **33**(1): p. 332-342.

-
147. Du, J., et al., *An adaptive sliding mode observer for lithium-ion battery state of charge and state of health estimation in electric vehicles*. Control Engineering Practice, 2016. **54**: p. 81-90.
 148. Moura, S.J., N.A. Chaturvedi, and M. Krstić, *Adaptive partial differential equation observer for battery state-of-charge/state-of-health estimation via an electrochemical model*. Journal of Dynamic Systems, Measurement, and Control, 2014. **136**(1).
 149. Ma, Y., et al., *State of charge and state of health estimation based on dual nonlinear adaptive observer and hysteresis model of lithium-ion battery*. Journal of Renewable and Sustainable Energy, 2021. **13**(4): p. 044702.
 150. Xu, Y., et al., *Online identification of battery model parameters and joint state of charge and state of health estimation using dual particle filter algorithms*. International Journal of Energy Research, 2022.
 151. Liu, B., X. Tang, and F. Gao, *Joint estimation of battery state-of-charge and state-of-health based on a simplified pseudo-two-dimensional model*. Electrochimica Acta, 2020. **344**: p. 136098.
 152. Shu, X., et al., *State of health prediction of lithium-ion batteries based on machine learning: Advances and perspectives*. iScience, 2021. **24**(11): p. 103265.
 153. Plett, G.L., *Extended Kalman filtering for battery management systems of LiPB-based HEV battery packs: Part 3. State and parameter estimation*. Journal of Power Sources, 2004. **134**(2): p. 277-292.
 154. Jiang, C., et al., *A state-of-charge estimation method of the power lithium-ion battery in complex conditions based on adaptive square root extended Kalman filter*. Energy, 2021. **219**: p. 119603.
 155. Wang, L., et al., *State of charge estimation for LiFePO₄ battery via dual extended kalman filter and charging voltage curve*. Electrochimica Acta, 2019. **296**: p. 1009-1017.
 156. Yang, Q., et al., *A Joint Estimation Method Based on Kalman Filter of Battery State of Charge and State of Health*. Coatings, 2022. **12**(8): p. 1047.
 157. Laurin, A., V. Heiries, and M. Montaru. *State-of-Charge and State-of-Health online estimation of Li-ion battery for the More Electrical Aircraft based on semi-empirical ageing model and Sigma-Point Kalman Filtering*. in *2021 Smart Systems Integration (SSI)*. 2021.
 158. Wassiliadis, N., et al., *Revisiting the dual extended Kalman filter for battery state-of-charge and state-of-health estimation: A use-case life cycle analysis*. Journal of Energy Storage, 2018. **19**: p. 73-87.
 159. Ma, L., et al., *Co-estimation of state of charge and state of health for lithium-ion batteries based on fractional-order model with multi-innovations unscented Kalman filter method*. Journal of Energy Storage, 2022. **52**: p. 104904.
 160. Liu, S., et al., *A method for state of charge and state of health estimation of lithium-ion battery based on adaptive unscented Kalman filter*. Energy Reports, 2022. **8**: p. 426-436.

-
161. Miguel, E., et al., *Electrochemical Model and Sigma Point Kalman Filter Based Online Oriented Battery Model*. IEEE Access, 2021. **9**: p. 98072-98090.
 162. Li, W., et al., *Electrochemical model-based state estimation for lithium-ion batteries with adaptive unscented Kalman filter*. Journal of Power Sources, 2020. **476**: p. 228534.
 163. Ding, Q., Y. Wang, and Z. Chen, *Parameter identification of reduced-order electrochemical model simplified by spectral methods and state estimation based on square-root cubature Kalman filter*. Journal of Energy Storage, 2022. **46**: p. 103828.
 164. Moura, S.J., N.A. Chaturvedi, and M. Krstic. *PDE estimation techniques for advanced battery management systems — Part I: SOC estimation*. in *2012 American Control Conference (ACC)*. 2012.
 165. Moura, S.J., N.A. Chaturvedi, and M. Krstić, *Adaptive Partial Differential Equation Observer for Battery State-of-Charge/State-of-Health Estimation Via an Electrochemical Model*. Journal of Dynamic Systems, Measurement, and Control, 2013. **136**(1).
 166. Feng, Y., et al., *Robust Estimation for State-of-Charge and State-of-Health of Lithium-Ion Batteries Using Integral-Type Terminal Sliding-Mode Observers*. IEEE Transactions on Industrial Electronics, 2020. **67**(5): p. 4013-4023.
 167. Huang, P., et al., *The state of health estimation of lithium-ion batteries based on data-driven and model fusion method*. Journal of Cleaner Production, 2022. **366**: p. 132742.
 168. Lee, G., J. Kim, and C. Lee, *State-of-health estimation of Li-ion batteries in the early phases of qualification tests: An interpretable machine learning approach*. Expert Systems with Applications, 2022. **197**: p. 116817.
 169. Li, Q., et al., *State of health estimation of lithium-ion battery based on improved ant lion optimization and support vector regression*. Journal of Energy Storage, 2022. **50**: p. 104215.
 170. Xiong, W., et al., *Early prediction of lithium-ion battery cycle life based on voltage-capacity discharge curves*. Journal of Energy Storage, 2023. **62**: p. 106790.
 171. Mawonou, K.S.R., et al., *State-of-health estimators coupled to a random forest approach for lithium-ion battery aging factor ranking*. Journal of Power Sources, 2021. **484**: p. 229154.
 172. Jayakumar, T., et al., *Machine Learning approach for Prediction of residual energy in batteries*. Energy Reports, 2022. **8**: p. 756-764.
 173. Thelen, A., et al., *Augmented model-based framework for battery remaining useful life prediction*. Applied Energy, 2022. **324**: p. 119624.
 174. Wang, Z., C. Yuan, and X. Li, *Lithium Battery State-of-Health Estimation via Differential Thermal Voltammetry With Gaussian Process Regression*. IEEE Transactions on Transportation Electrification, 2021. **7**(1): p. 16-25.
 175. Li, J., et al., *A hybrid framework for predicting the remaining useful life of battery using Gaussian process regression*. Journal of Energy Storage, 2023. **66**: p. 107513.

-
176. Wang, J., et al., *State of health estimation based on modified Gaussian process regression for lithium-ion batteries*. Journal of Energy Storage, 2022. **51**: p. 104512.
 177. Maleki, S., A. Mahmoudi, and A. Yazdani, *Knowledge transfer-oriented deep neural network framework for estimation and forecasting the state of health of the Lithium-ion batteries*. Journal of Energy Storage, 2022. **53**: p. 105183.
 178. Manoharan, A., et al., *Artificial neural networks, gradient boosting and support vector machines for electric vehicle battery state estimation: A review*. Journal of Energy Storage, 2022. **55**: p. 105384.
 179. Tang, T. and H. Yuan, *A hybrid approach based on decomposition algorithm and neural network for remaining useful life prediction of lithium-ion battery*. Reliability Engineering & System Safety, 2022. **217**: p. 108082.
 180. Rauf, H., M. Khalid, and N. Arshad, *Machine learning in state of health and remaining useful life estimation: Theoretical and technological development in battery degradation modelling*. Renewable and Sustainable Energy Reviews, 2022. **156**: p. 111903.
 181. Xia, Z. and J.A.A. Qahouq, *Lithium-Ion Battery Ageing Behavior Pattern Characterization and State-of-Health Estimation Using Data-Driven Method*. IEEE Access, 2021. **9**: p. 98287-98304.
 182. Gou, B., Y. Xu, and X. Feng, *An Ensemble Learning-Based Data-Driven Method for Online State-of-Health Estimation of Lithium-Ion Batteries*. IEEE Transactions on Transportation Electrification, 2021. **7**(2): p. 422-436.
 183. Yang, D., et al., *A novel Gaussian process regression model for state-of-health estimation of lithium-ion battery using charging curve*. Journal of Power Sources, 2018. **384**: p. 387-395.
 184. Cao, M., et al., *A deep belief network approach to remaining capacity estimation for lithium-ion batteries based on charging process features*. Journal of Energy Storage, 2022. **48**: p. 103825.
 185. Ma, Y., et al., *A novel method for state of health estimation of lithium-ion batteries based on improved LSTM and health indicators extraction*. Energy, 2022. **251**: p. 123973.
 186. Li, W., et al., *Online capacity estimation of lithium-ion batteries with deep long short-term memory networks*. Journal of Power Sources, 2021. **482**: p. 228863.
 187. Li, Y., et al., *Random forest regression for online capacity estimation of lithium-ion batteries*. Applied Energy, 2018. **232**: p. 197-210.
 188. Richardson, R.R., et al., *Gaussian Process Regression for In Situ Capacity Estimation of Lithium-Ion Batteries*. IEEE Transactions on Industrial Informatics, 2019. **15**(1): p. 127-138.
 189. Shen, S., et al., *A deep learning method for online capacity estimation of lithium-ion batteries*. Journal of Energy Storage, 2019. **25**: p. 100817.
 190. Lin, M., et al., *A multi-feature-based multi-model fusion method for state of health estimation of lithium-ion batteries*. Journal of Power Sources, 2022. **518**: p. 230774.

-
191. Wei, Z., et al., *Multistage State of Health Estimation of Lithium-Ion Battery With High Tolerance to Heavily Partial Charging*. IEEE Transactions on Power Electronics, 2022. **37**(6): p. 7432-7442.
 192. Zhu, J., et al., *Data-driven capacity estimation of commercial lithium-ion batteries from voltage relaxation*. Nature communications, 2022. **13**(1): p. 1-10.
 193. Gong, D., et al., *State of health estimation for lithium-ion battery based on energy features*. Energy, 2022. **257**: p. 124812.
 194. Cai, L., J. Lin, and X. Liao, *An estimation model for state of health of lithium-ion batteries using energy-based features*. Journal of Energy Storage, 2022. **46**: p. 103846.
 195. Park, K., et al., *LSTM-based battery remaining useful life prediction with multi-channel charging profiles*. Ieee Access, 2020. **8**: p. 20786-20798.
 196. Ren, L., et al., *Remaining useful life prediction for lithium-ion battery: A deep learning approach*. Ieee Access, 2018. **6**: p. 50587-50598.
 197. Roman, D., et al., *Machine learning pipeline for battery state-of-health estimation*. Nature Machine Intelligence, 2021. **3**(5): p. 447-456.
 198. Deng, Z., et al., *Data-Driven Battery State of Health Estimation Based on Random Partial Charging Data*. IEEE Transactions on Power Electronics, 2022. **37**(5): p. 5021-5031.
 199. Hong, J., et al., *Online accurate state of health estimation for battery systems on real-world electric vehicles with variable driving conditions considered*. Journal of Cleaner Production, 2021. **294**: p. 125814.
 200. Shi, M., et al., *A fast state-of-health estimation method using single linear feature for lithium-ion batteries*. Energy, 2022. **256**: p. 124652.
 201. Deng, Y., et al., *Feature parameter extraction and intelligent estimation of the State-of-Health of lithium-ion batteries*. Energy, 2019. **176**: p. 91-102.
 202. Chen, Z., et al., *State of health estimation for lithium-ion batteries based on temperature prediction and gated recurrent unit neural network*. Journal of Power Sources, 2022. **521**: p. 230892.
 203. Choi, Y., et al., *Machine learning-based lithium-ion battery capacity estimation exploiting multi-channel charging profiles*. Ieee Access, 2019. **7**: p. 75143-75152.
 204. Tian, J., et al., *Flexible battery state of health and state of charge estimation using partial charging data and deep learning*. Energy Storage Materials, 2022. **51**: p. 372-381.
 205. Gong, Q., P. Wang, and Z. Cheng, *An encoder-decoder model based on deep learning for state of health estimation of lithium-ion battery*. Journal of Energy Storage, 2022. **46**: p. 103804.
 206. Li, K., Y. Wang, and Z. Chen, *A comparative study of battery state-of-health estimation based on empirical mode decomposition and neural network*. Journal of Energy Storage, 2022. **54**: p. 105333.

-
207. Zhang, Y., et al., *A deep learning approach to estimate the state of health of lithium-ion batteries under varied and incomplete working conditions*. Journal of Energy Storage, 2023. **58**: p. 106323.
 208. She, C., et al., *Battery state of health estimation based on incremental capacity analysis method: Synthesizing from cell-level test to real-world application*. IEEE Journal of Emerging and Selected Topics in Power Electronics, 2021.
 209. Agudelo, B.O., W. Zamboni, and E. Monmasson, *Application domain extension of incremental capacity-based battery SoH indicators*. Energy, 2021. **234**: p. 121224.
 210. Weng, C., et al., *On-board state of health monitoring of lithium-ion batteries using incremental capacity analysis with support vector regression*. Journal of Power Sources, 2013. **235**: p. 36-44.
 211. Tang, X., et al., *A fast estimation algorithm for lithium-ion battery state of health*. Journal of Power Sources, 2018. **396**: p. 453-458.
 212. Zhang, Y., et al., *State-of-health estimation for lithium-ion batteries by combining model-based incremental capacity analysis with support vector regression*. Energy, 2022. **239**: p. 121986.
 213. Zhou, R., et al., *State of health estimation for fast-charging lithium-ion battery based on incremental capacity analysis*. Journal of Energy Storage, 2022. **51**: p. 104560.
 214. Heinrich, F. and M. Pruckner, *Virtual experiments for battery state of health estimation based on neural networks and in-vehicle data*. Journal of Energy Storage, 2022. **48**: p. 103856.
 215. Jenu, S., et al., *State of health estimation of cycle aged large format lithium-ion cells based on partial charging*. Journal of Energy Storage, 2022. **46**: p. 103855.
 216. Yang, N., et al., *Robust State of Health estimation of lithium-ion batteries using convolutional neural network and random forest*. Journal of Energy Storage, 2022. **48**: p. 103857.
 217. Wei, Z., X. Han, and J. Li, *State of health assessment for echelon utilization batteries based on deep neural network learning with error correction*. Journal of Energy Storage, 2022. **51**: p. 104428.
 218. Chang, C., et al., *Lithium-ion battery state of health estimation using the incremental capacity and wavelet neural networks with genetic algorithm*. Journal of Energy Storage, 2021. **38**: p. 102570.
 219. He, J., et al., *Partial Charging-based Health Feature Extraction and State of Health Estimation of Lithium-Ion Batteries*. IEEE Journal of Emerging and Selected Topics in Power Electronics, 2022: p. 1-1.
 220. Anseán, D., et al., *Lithium-Ion Battery Degradation Indicators Via Incremental Capacity Analysis*. IEEE Transactions on Industry Applications, 2019. **55**(3): p. 2992-3002.
 221. Dubarry, M., et al., *Identifying battery aging mechanisms in large format Li ion cells*. Journal of Power Sources, 2011. **196**(7): p. 3420-3425.

-
222. Buchicchio, E., et al., *Dataset on broadband electrochemical impedance spectroscopy of Lithium-Ion batteries for different values of the state-of-charge*. Data in Brief, 2022. **45**: p. 108589.
223. Ouyang, K., et al., *Data-Driven–Based Internal Temperature Estimation for Lithium-Ion Battery Under Variant State-of-Charge via Electrochemical Impedance Spectroscopy*. Energy Technology, 2022. **10**(3): p. 2100910.
224. Qiu, X.-Y., et al., *Electrochemical and electronic properties of LiCoO₂ cathode investigated by galvanostatic cycling and EIS*. Physical Chemistry Chemical Physics, 2012. **14**(8): p. 2617-2630.
225. Wang, X., et al., *A novel dual time scale life prediction method for lithium-ion batteries considering effects of temperature and state of charge*. International Journal of Energy Research, 2021. **45**(10): p. 14692-14709.
226. Pastor-Fernández, C., et al., *A Comparison between Electrochemical Impedance Spectroscopy and Incremental Capacity-Differential Voltage as Li-ion Diagnostic Techniques to Identify and Quantify the Effects of Degradation Modes within Battery Management Systems*. Journal of Power Sources, 2017. **360**: p. 301-318.
227. Teliz, E., C.F. Zinola, and V. Díaz, *Identification and quantification of ageing mechanisms in Li-ion batteries by Electrochemical impedance spectroscopy*. Electrochimica Acta, 2022. **426**: p. 140801.
228. Schuster, S.F., et al., *Correlation between capacity and impedance of lithium-ion cells during calendar and cycle life*. Journal of Power Sources, 2016. **305**: p. 191-199.
229. Zhang, Y., et al., *Identifying degradation patterns of lithium ion batteries from impedance spectroscopy using machine learning*. Nature Communications, 2020. **11**(1): p. 1706.
230. Faraji-Niri, M., et al., *Accelerated state of health estimation of second life lithium-ion batteries via electrochemical impedance spectroscopy tests and machine learning techniques*. Journal of Energy Storage, 2023. **58**: p. 106295.
231. Xu, T., et al., *A Hybrid Drive Method for Capacity Prediction of Lithium-Ion Batteries*. IEEE Transactions on Transportation Electrification, 2022. **8**(1): p. 1000-1012.
232. Zhang, W., et al., *Data-driven state of health estimation in retired battery based on low and medium-frequency electrochemical impedance spectroscopy*. Measurement, 2023. **211**: p. 112597.
233. Chang, C., et al., *An improvement of equivalent circuit model for state of health estimation of lithium-ion batteries based on mid-frequency and low-frequency electrochemical impedance spectroscopy*. Measurement, 2022. **202**: p. 111795.
234. Rastegarpanah, A., et al., *A rapid neural network–based state of health estimation scheme for screening of end of life electric vehicle batteries*. Proceedings of the Institution of Mechanical Engineers, Part I: Journal of Systems and Control Engineering, 2021. **235**(3): p. 330-346.

-
235. Su, X., et al., *Fast capacity estimation for lithium-ion battery based on online identification of low-frequency electrochemical impedance spectroscopy and Gaussian process regression*. Applied Energy, 2022. **322**: p. 119516.
 236. Zhou, Y., et al., *State of health estimation for lithium-ion batteries using geometric impedance spectrum features and recurrent Gaussian process regression*. Energy, 2023. **262**: p. 125514.
 237. Jiang, B., et al., *A comparative study of different features extracted from electrochemical impedance spectroscopy in state of health estimation for lithium-ion batteries*. Applied Energy, 2022. **322**: p. 119502.
 238. Lyu, C., et al. *SOH estimation of lithium-ion batteries based on fast time domain impedance spectroscopy*. in *2019 14th IEEE Conference on Industrial Electronics and Applications (ICIEA)*. 2019. IEEE.
 239. Wang, X., et al., *Lithium-ion battery temperature on-line estimation based on fast impedance calculation*. Journal of Energy Storage, 2019. **26**: p. 100952.
 240. Kim, J., *Discrete Wavelet Transform-Based Feature Extraction of Experimental Voltage Signal for Li-Ion Cell Consistency*. IEEE Transactions on Vehicular Technology, 2016. **65**(3): p. 1150-1161.
 241. Cai, Y., et al., *Online identification of lithium-ion battery state-of-health based on fast wavelet transform and cross D-Markov machine*. Energy, 2018. **147**: p. 621-635.
 242. Xu, J., et al., *A Relative State of Health Estimation Method Based on Wavelet Analysis for Lithium-Ion Battery Cells*. IEEE Transactions on Industrial Electronics, 2021. **68**(8): p. 6973-6981.
 243. Hoshi, Y., et al., *Wavelet transformation to determine impedance spectra of lithium-ion rechargeable battery*. Journal of Power Sources, 2016. **315**: p. 351-358.
 244. Cai, L., J. Lin, and X. Liao, *A data-driven method for state of health prediction of lithium-ion batteries in a unified framework*. Journal of Energy Storage, 2022. **51**: p. 104371.
 245. Cheng, G., X. Wang, and Y. He, *Remaining useful life and state of health prediction for lithium batteries based on empirical mode decomposition and a long and short memory neural network*. Energy, 2021. **232**: p. 121022.
 246. Pang, X., et al., *A lithium-ion battery RUL prediction method considering the capacity regeneration phenomenon*. Energies, 2019. **12**(12): p. 2247.
 247. Bole, B., C.S. Kulkarni, and M. Daigle. *Adaptation of an electrochemistry-based lithium battery model to account for deterioration observed under randomized use*. in *Annual Conference of the PHM Society*. 2014.
 248. Yu, J., et al., *Indirect state-of-health estimation for lithium-ion batteries under randomized use*. Energies, 2017. **10**(12): p. 2012.
 249. Kim, J., *Discrete wavelet transform-based feature extraction of experimental voltage signal for Li-ion cell consistency*. IEEE Transactions on Vehicular Technology, 2015. **65**(3): p. 1150-1161.

-
250. Feltane, A., *Time-frequency based methods for nonstationary signal analysis with application to EEG signals*. 2016: University of Rhode Island.
 251. Sejdić, E., I. Orović, and S. Stanković, *Compressive sensing meets time–frequency: An overview of recent advances in time–frequency processing of sparse signals*. Digital signal processing, 2018. **77**: p. 22-35.
 252. Li, J., et al., *Long-term variable Q transform: A novel time-frequency transform algorithm for synthetic speech detection*. Digital Signal Processing, 2022. **120**: p. 103256.
 253. Wang, Z.-K., et al., *Automatic tracking of natural frequency in the time–frequency domain for blade tip timing*. Journal of Sound and Vibration, 2022. **516**: p. 116522.
 254. Di Fonso, R., et al. *Internal Resistance Estimation of Li-ion Batteries using Wavelet Analysis*. in *2022 IEEE 13th International Symposium on Power Electronics for Distributed Generation Systems (PEDG)*. 2022. IEEE.
 255. Boashash, B. and S. Ouelha, *Automatic signal abnormality detection using time-frequency features and machine learning: A newborn EEG seizure case study*. Knowledge-Based Systems, 2016. **106**: p. 38-50.
 256. Durak, L. and O. Arikan, *Short-time Fourier transform: two fundamental properties and an optimal implementation*. IEEE Transactions on Signal Processing, 2003. **51**(5): p. 1231-1242.
 257. Pachori, R.B. and A. Nishad, *Cross-terms reduction in the Wigner–Ville distribution using tunable-Q wavelet transform*. Signal Processing, 2016. **120**: p. 288-304.
 258. Aguiar-Conraria, L. and M.J. Soares, *The continuous wavelet transform: Moving beyond uni-and bivariate analysis*. Journal of economic surveys, 2014. **28**(2): p. 344-375.
 259. Papandreou-Suppappola, A., *Applications in time-frequency signal processing*. 2018: CRC press.
 260. Feng, Z., M. Liang, and F. Chu, *Recent advances in time–frequency analysis methods for machinery fault diagnosis: A review with application examples*. Mechanical Systems and Signal Processing, 2013. **38**(1): p. 165-205.
 261. Bracewell, R.N. and R.N. Bracewell, *The Fourier transform and its applications*. Vol. 31999. 1986: McGraw-Hill New York.
 262. Li, L., et al., *Adaptive short-time Fourier transform and synchrosqueezing transform for non-stationary signal separation*. Signal Processing, 2020. **166**: p. 107231.
 263. Gabor, D., *Theory of communication. Part I: The analysis of information*. Journal of the Institution of Electrical Engineers-part III: radio and communication engineering, 1946. **93**(26): p. 429-441.
 264. Pei, S.-C. and S.-G. Huang, *STFT with adaptive window width based on the chirp rate*. IEEE Transactions on Signal Processing, 2012. **60**(8): p. 4065-4080.
 265. Rehman, N.U., *Data-driven time-frequency analysis of multivariate data*. 2011.

-
266. Bentley, P.M. and J. McDonnell, *Wavelet transforms: an introduction*. Electronics & communication engineering journal, 1994. **6**(4): p. 175-186.
 267. Shao, S., et al., *Highly accurate machine fault diagnosis using deep transfer learning*. IEEE Transactions on Industrial Informatics, 2018. **15**(4): p. 2446-2455.
 268. Nielsen, M.A., *Neural networks and deep learning*. Vol. 25. 2015: Determination press San Francisco, CA, USA.
 269. Yoo, Y. and J.-G. Baek, *A novel image feature for the remaining useful lifetime prediction of bearings based on continuous wavelet transform and convolutional neural network*. Applied Sciences, 2018. **8**(7): p. 1102.
 270. Schmidhuber, J., *Deep learning in neural networks: An overview*. Neural networks, 2015. **61**: p. 85-117.
 271. Aggarwal, C.C., *Neural networks and deep learning*. Springer, 2018. **10**: p. 978-3.
 272. Liao, Y., X. Zeng, and W. Li. *Wavelet transform based convolutional neural network for gearbox fault classification*. in *2017 Prognostics and System Health Management Conference (PHM-Harbin)*. 2017. IEEE.
 273. Zhang, Y., et al., *Identifying degradation patterns of lithium ion batteries from impedance spectroscopy using machine learning*. Nature communications, 2020. **11**(1): p. 1-6.
 274. Krizhevsky, A., I. Sutskever, and G. Hinton, *Imagenet classification with deep convolutional neural networks*. *2012 Advances in Neural Information Processing Systems (NIPS)*. Neural Information Processing Systems Foundation, La Jolla, CA, 2012.
 275. Patil, M.A., et al., *A novel multistage Support Vector Machine based approach for Li ion battery remaining useful life estimation*. Applied energy, 2015. **159**: p. 285-297.
 276. Ali, M.U., et al., *Online remaining useful life prediction for lithium-ion batteries using partial discharge data features*. Energies, 2019. **12**(22): p. 4366.
 277. Simonyan, K. and A. Zisserman, *Very deep convolutional networks for large-scale image recognition*. arXiv preprint arXiv:1409.1556, 2014.
 278. Zhou, B., et al. *Learning deep features for discriminative localization*. in *Proceedings of the IEEE conference on computer vision and pattern recognition*. 2016.
 279. Selvaraju, R.R., et al. *Grad-cam: Visual explanations from deep networks via gradient-based localization*. in *Proceedings of the IEEE international conference on computer vision*. 2017.
 280. Simonyan, K., A. Vedaldi, and A. Zisserman, *Deep inside convolutional networks: Visualising image classification models and saliency maps*. arXiv preprint arXiv:1312.6034, 2013.
 281. Ribeiro, M.T., S. Singh, and C. Guestrin. "Why should i trust you?" *Explaining the predictions of any classifier*. in *Proceedings of the 22nd ACM SIGKDD international conference on knowledge discovery and data mining*. 2016.

-
282. Zeiler, M.D. and R. Fergus. *Visualizing and understanding convolutional networks*. in *European conference on computer vision*. 2014. Springer.
 283. Pozzato, G., A. Allam, and S. Onori, *Lithium-ion battery aging dataset based on electric vehicle real-driving profiles*. Data in Brief, 2022. **41**: p. 107995.
 284. Richardson, R.R., M.A. Osborne, and D.A. Howey, *Battery health prediction under generalized conditions using a Gaussian process transition model*. Journal of Energy Storage, 2019. **23**: p. 320-328.
 285. Zhang, Y., et al., *A machine learning-based framework for online prediction of battery ageing trajectory and lifetime using histogram data*. Journal of Power Sources, 2022. **526**: p. 231110.
 286. Gilles, J., *Empirical Wavelet Transform*. IEEE Transactions on Signal Processing, 2013. **61**(16): p. 3999-4010.
 287. Schober, P., C. Boer, and L.A. Schwarte, *Correlation Coefficients: Appropriate Use and Interpretation*. Anesthesia & Analgesia, 2018. **126**(5): p. 1763-1768.
 288. Song, F., Z. Guo, and D. Mei. *Feature Selection Using Principal Component Analysis*. in *2010 International Conference on System Science, Engineering Design and Manufacturing Informatization*. 2010.
 289. Greenbank, S. and D. Howey, *Automated Feature Extraction and Selection for Data-Driven Models of Rapid Battery Capacity Fade and End of Life*. IEEE Transactions on Industrial Informatics, 2022. **18**(5): p. 2965-2973.
 290. Hochreiter, S. and J. Schmidhuber, *Long Short-Term Memory*. Neural Computation, 1997. **9**(8): p. 1735-1780.
 291. Gong, Y., et al., *State-of-health estimation of lithium-ion batteries based on improved long short-term memory algorithm*. Journal of Energy Storage, 2022. **53**: p. 105046.
 292. Browne, M.W., *Cross-Validation Methods*. Journal of Mathematical Psychology, 2000. **44**(1): p. 108-132.
 293. Li, W., et al., *Battery degradation diagnosis with field data, impedance-based modeling and artificial intelligence*. Energy Storage Materials, 2022. **53**: p. 391-403.
 294. Liao, Q., et al., *Performance assessment and classification of retired lithium ion battery from electric vehicles for energy storage*. International Journal of Hydrogen Energy, 2017. **42**(30): p. 18817-18823.
 295. Khaleghi, S., et al., *Developing a real-time data-driven battery health diagnosis method, using time and frequency domain condition indicators*. Applied Energy, 2019. **255**: p. 113813.
 296. Toughzaoui, Y., et al., *State of health estimation and remaining useful life assessment of lithium-ion batteries: A comparative study*. Journal of Energy Storage, 2022. **51**: p. 104520.
 297. Liu, W., Y. Xu, and X. Feng, *A hierarchical and flexible data-driven method for online state-of-health estimation of Li-ion battery*. IEEE Transactions on Vehicular Technology, 2020. **69**(12): p. 14739-14748.

-
298. Goebel, K., et al., *Prognostics in Battery Health Management*. IEEE Instrumentation & Measurement Magazine, 2008. **11**(4): p. 33-40.
 299. Miao, Q., et al., *Remaining useful life prediction of lithium-ion battery with unscented particle filter technique*. Microelectronics Reliability, 2013. **53**(6): p. 805-810.
 300. He, W., et al., *Prognostics of lithium-ion batteries based on Dempster–Shafer theory and the Bayesian Monte Carlo method*. Journal of Power Sources, 2011. **196**(23): p. 10314-10321.
 301. Shensa, M.J., *The discrete wavelet transform: wedding the a trous and Mallat algorithms*. IEEE Transactions on Signal Processing, 1992. **40**(10): p. 2464-2482.
 302. Wang, Y., et al., *Remaining useful life prediction of lithium-ion battery based on discrete wavelet transform*. Energy Procedia, 2017. **105**: p. 2053-2058.
 303. Ibrahim, M., et al., *Wavelet-based approach for online fuel cell remaining useful lifetime prediction*. IEEE Transactions on Industrial Electronics, 2016. **63**(8): p. 5057-5068.
 304. Stanković, R.S. and B.J. Falkowski, *The Haar wavelet transform: its status and achievements*. Computers & Electrical Engineering, 2003. **29**(1): p. 25-44.
 305. Daubechies, I., *Orthonormal bases of compactly supported wavelets*. Communications on pure and applied mathematics, 1988. **41**(7): p. 909-996.
 306. Genovese, L., et al., *Daubechies wavelets as a basis set for density functional pseudopotential calculations*. The Journal of chemical physics, 2008. **129**(1): p. 014109.
 307. Chavan, M.S., et al. *Implementation of SYMLET wavelets to removal of Gaussian additive noise from speech signal*. in *Proceedings of Recent Researches in Communications, Automation, Signal Processing, Nanotechnology, Astronomy and Nuclear Physics: 10th WSEAS International Conference on Electronics, Hardware, Wireless and Optical Communications (EHAC'11), Cambridge*. 2011.
 308. Głowacz, A., *Diagnostics of direct current machine based on analysis of acoustic signals with the use of symlet wavelet transform and modified classifier based on words*. Eksploatacja i Niezawodność, 2014. **16**(4): p. 554-558.
 309. Shyh-Jier, H. and H. Cheng-Tao, *Coiflet wavelet transform applied to inspect power system disturbance-generated signals*. IEEE Transactions on Aerospace and Electronic Systems, 2002. **38**(1): p. 204-210.
 310. Rowe, A.C. and P.C. Abbott, *Daubechies wavelets and mathematica*. Computers in Physics, 1995. **9**(6): p. 635-648.
 311. Huang, N.E., et al., *The empirical mode decomposition and the Hilbert spectrum for nonlinear and non-stationary time series analysis*. Proceedings of the Royal Society of London. Series A: mathematical, physical and engineering sciences, 1998. **454**(1971): p. 903-995.
 312. Zeiler, A., et al. *Empirical mode decomposition-an introduction*. in *The 2010 international joint conference on neural networks (IJCNN)*. 2010. IEEE.

-
313. Dragomiretskiy, K. and D. Zosso, *Variational mode decomposition*. IEEE transactions on signal processing, 2013. **62**(3): p. 531-544.
 314. Ibrahim, M., et al., *Nonlinear autoregressive neural network in an energy management strategy for battery/ultra-capacitor hybrid electrical vehicles*. Electric Power Systems Research, 2016. **136**: p. 262-269.
 315. Benrhmach, G., et al., *Nonlinear autoregressive neural network and extended Kalman filters for prediction of financial time series*. Journal of Applied Mathematics, 2020. **2020**: p. 1-6.
 316. Khaleghi, S., et al., *Online health diagnosis of lithium-ion batteries based on nonlinear autoregressive neural network*. Applied Energy, 2021. **282**: p. 116159.
 317. Pang, X., et al., *A lithium-ion battery remaining useful life prediction method based on the incremental capacity analysis and Gaussian process regression*. Microelectronics Reliability, 2021. **127**: p. 114405.
 318. Zhang, W., X. Li, and X. Li, *Deep learning-based prognostic approach for lithium-ion batteries with adaptive time-series prediction and on-line validation*. Measurement, 2020. **164**: p. 108052.
 319. Zhao, S., C. Zhang, and Y. Wang, *Lithium-ion battery capacity and remaining useful life prediction using board learning system and long short-term memory neural network*. Journal of Energy Storage, 2022. **52**: p. 104901.

Appendix A TFI Code

```
%%
%%
%% *Steps*:
% # *Time-Frequency (Continuous Wavelet Transform)*
% # *Speeding-Up Wavelet Time-Frequency Generation*
% # *Customize and Train a Pre-Trained Network (AlexNet)*
% # *Evaluate the trained model*
%
%
%% *Explore the Signals*
%%1_ Load Signals
%%
addpath(genpath(pwd))

load SINGLE1.mat;
size(Signals_Struct.Data)
unique(Signals_Struct.Labels)

%% 2_ Time Frequency Analysis using Wavelet Transform
%% Eample of how transform the measrued signals to images
figure;
Fs = 1000;
cwt(Signals_Struct.Data(1000:3600),Fs,'VoicesPerOctave',48); %title('Cycle
1');
colormap(jet);set(gca,'yscale','log');
%%
% * save these representations as images (.jpg) and train a preconfigured
% Convolutional Neural Network*
%% 3_*Speeding-Up Wavelet Time-Frequency Generation*
%% Create a Filter Bank
%
% filter bank can greatly speed up the process
sig =Signals_Struct.Data(1,:);
signalLength = length(sig);
Fs = 50;
fb = cwtfilterbank('SignalLength',signalLength,'SamplingFrequency',Fs)

%
%% Compute the Wavelet Transform
```

```
fb =
cwtfilterbank('SignalLength',signalLength,'SamplingFrequency',Fs,'VoicesPerOct
ave',32)
[wt,f] = fb.wt(sig);
%%
% *Generating Time-Frequency Images for all Signals
[r,c] = size(Signals_Struct.Data);
labels = Signals_Struct.Labels;

    ret = exist('RW','dir');
    if ret ==0
        mkdir('RW');
    end

    for ii = 1:r
        [wt,~] = fb.wt(Signals_Struct.Data(ii,:));
        saveTimeFrequencyRep(abs(wt),ii,labels);

    end

type('saveTimeFrequencyRep.m')
%implay('tf.mp4');
%%
%
%% Split the Time-Frequency Representation Images into Training and Test Sets
%%
rootFolder = pwd;
folderName = 'Data';

rng('default');
allImages = imageDatastore(strcat(rootFolder,filesep,folderName),
'IncludeSubfolders', true,...
    'LabelSource', 'foldernames');

[trainingImages, testImages] = splitEachLabel(allImages, 0.9, 'randomize');

%% *Train a Pre-Trained Network (AlexNet)*
% *You can download AlexNet support package from the Add-Ons menu. *
%% *Initialize the Network *
%%
load alexnet;
layers = alex.Layers
```

```
%%
layers(23) = fullyConnectedLayer(4); % change this based on # of classes
layers(25) = classificationLayer;
%% *Train the network*
%%
ilr = 0.0001;
mxEpochs = 50;
mbSize = 20;
opts = trainingOptions('sgdm', 'InitialLearnRate', ilr, ...
    'MaxEpochs',mxEpochs , 'MiniBatchSize',mbSize, ...
    'Plots', 'training-progress');

trainingImages.ReadFcn = @readFunctionTrain;

[myNet,info] = trainNetwork(trainingImages, layers, opts); %myNet is already
configured with the changes mentioned in the cell above and is fully trained,
%load TrainedNetwork.mat;
%
%% *Evaluate the Trained Model*
%%
testImages.ReadFcn = @readFunctionTrain;
[predictedLabels,scores] = classify(myNet, testImages);
accuracy = mean(predictedLabels == testImages.Labels)
[confmat, order] = confusionmat(testImages.Labels,predictedLabels);
figure
heatmap(order,order,confmat);
title('Confusion Matrix')
%%%
```

Appendix B EWT-LSTM Code

```
%clear;

%load data.mat

FtRW9=RW9.step(32).relativeTime/60;
FreshRW9_v= RW9.step(32).voltage;
FreshRW9_I= RW9.step(32).current;
FreshRW9_T=RW9.step(32).temperature;

AtRW9= RW9.step(end-50).relativeTime/60;
AgedRW9_v=RW9.step(end-50).voltage;
AgedRW9_I= RW9.step(end-50).current;
AgedRW9_T=RW9.step(end-50).temperature;

figure(1)
subplot(311)
plot(FtRW9,FreshRW9_v,'LineWidth',2), hold on
plot(AtRW9,AgedRW9_v,'r--','LineWidth',2), hold off
subplot(312)
plot(FtRW9,FreshRW9_I,'LineWidth',2), hold on
plot(AtRW9,AgedRW9_I,'r--','LineWidth',2), hold off
subplot(313)
plot(FtRW9,FreshRW9_T,'LineWidth',2), hold on
plot(AtRW9,AgedRW9_T,'r--','LineWidth',2), hold off
```

```
[cap28, date28]= extract_dischargeRW(RW28); % This function extract the
capacity.
```

```

[cap10, date10]=extract_dischargeRW(RW10);
[cap11, date11]=extract_dischargeRW(RW11);
[cap12, date12]=extract_dischargeRW(RW12);

cap14= reshape(cap14,[2,12]);% In the dataset the capacity measured twice at
each characterstic test

cap14=mean(cap14);

date13= reshape(date13,[2,11]);

date13=mean(date13);

cap10= reshape(cap10,[2,38]);% In the dataset the capacity measured twice at
each characterstic test

cap10=mean(cap10);

date10= reshape(date10,[2,40]);

date10=mean(date10);

figure

plot(date9,cap9), hold on, plot(date10,cap10),
plot(date11,cap11),plot(date12,cap12)

datetick('x','mmm') %mmmyyyy

%plot(0:180, 1.4*ones(1, 181),'k--','LineWidth', 2)

hold off, grid on

xlabel Date, ylabel Capacity(Ah)

legend('Battery RW21', 'Battery RW22', 'Battery RW23', 'Battery RW24')

title('Capacity Degradations in Cycle')

InitC9 = 2.0962;

InitC10 = 2.0937;

InitC11 = 2.0924;

InitC12 = 2.0921;

%xB9= normalize(yv,'range');

%xB10=normalize(charInput10,'range');

%xB11=normalize(charInput11,'range');

```

```

%xB12=normalize(charInput12,'range');
%yB9= normalize(cap9,'range');
%yB10= normalize(cap10,'range');
%yB11=normalize(cap11,'range');
%yB12=normalize(cap12,'range');

charInput9=extract_charge_preprocessingRW(RW9);%% see
'extract_full_cycles'' to extract V,I,T data.

charInput10=extract_charge_preprocessingRW(RW10);
charInput11=extract_charge_preprocessingRW(RW11);
charInput12=extract_charge_preprocessingRW(RW12);
for i=1:size(VRW1n) % Normalize the measured data
    for j= 1:size(VRW1n[271])
        vrw1n{i,:}=normalize(VRW1n{i,1},'range');
    end
end

for i=1:size(trw9N) % applying segmentation fo the measured data
    for j= 1:size(trw9N{i, 1})
        [yt9{i}, zt9{i}] =buffer(trw9N{i,1},4000);
    end

    TRW9v=cell2mat(yt9)'; % ewt and vmd expected the input to be in vector
format

end

for i=1:size(vw82) % Downsampling the buffered signals DO NOT APPLY THIS
    for j= 1:size(vw82(i,:))
        le2=mod(length(vw82(i,:)),20000);
        v1=vw82(i,1:end-le2);
        v11=reshape(v1,length(v1)/20000,[]);
        v12=mean(v11);
        w8s(i,:)= [v12];
    end
end

```

```

        end

    end

    %OPTIONAL
    for i=1:size(VRW9s2) % applying filter to smooth the data DO NOT APPLY THIS
ONE
        for j= 1:size(VRW9s2(i,:))
            VRW9smooth4{i} =smooth(VRW9s2(i,:),25); %VRW9smooth3(i,:)
        end
    end

    end

tic

    for i = 1:size(CM) % REad the file from    its location

        %imf1=vmd(VRW9smooth(i,:));

        [imf_w4{i}, resid_w4{i}] = vmd(CM{i, 1},"NumIMFs",9); %i, 1} imf_w8{i},
resid_w8{i}

        %[cA1{i},cD1{i}] = wavedec(VRW9s2(i,:),5,'db4');

        %imf_ewt1{i}= ewt(VRW9smooth(i, :));

        %helperMRAPlot(VB,imf,TT,'vmd','Empirical Wavelet transform ')

    end

toc

R_v1={};

    for i= 1:size(CM)

        for j= 1:9%size(imf_Vewt{1, i}(:,j))

            R_v1{i,j}=corrcoef(imf_w4{1,i}(:,j),CM{i, 1});

        end

    end

    %R_rw1=();

    for i= 1:size(HI28)

        R_28{i,:}=corrcoef(cap28(:,1),(HI28(:,i)));

    end

```

```

for i=1:size(CM) % do add them to each other, signal reconstrcution
    full_v4{i}=CM{i, 1}-imf_w4{:,i}(:,end); %VRW9smooth1(:,i)- TempRW9{i, 1}-
end
full_v4=full_v4';
FullFilteredCyclesv4=table(full_v4);
tic
[featureTable,outputTable] = diagnosticFeatures(inputData);
toc
featureTableSmoothw43= varfun(@(x) movmean(x, [3 0]), R5reducedDI1);

%inputSignal = voltage.Data;
    %ClearanceFactor =
max(abs(inputSignal))/(mean(sqrt(abs(inputSignal)))^2);

    %CrestFactor = peak2rms(inputSignal);

    %ImpulseFactor = max(abs(inputSignal))/mean(abs(inputSignal));

    %Kurtosis = kurtosis(inputSignal);

    %Mean = mean(inputSignal,'omitnan');

    %PeakValue = max(abs(inputSignal));

    %RMS = rms(inputSignal,'omitnan');

    % SINAD = sinad(inputSignal);

    % SNR = snr(inputSignal);

    % ShapeFactor =
rms(inputSignal,'omitnan')/mean(abs(inputSignal),'omitnan');

    % Skewness = skewness(inputSignal);

    % Std = std(inputSignal,'omitnan');

    % THD = thd(inputSignal);

%featureValues =
[ClearanceFactor,CrestFactor,ImpulseFactor,Kurtosis,Mean,PeakValue,RMS,SINAD,S
NR,ShapeFactor,Skewness,Std,THD];

```

```
%featureNames =
["ClearanceFactor","CrestFactor","ImpulseFactor","Kurtosis","Mean","PeakValue",
,"RMS","SINAD","SNR","ShapeFactor","Skewness","Std","THD"];

%    voltage_sigstats =
array2table(featureValues,'VariableNames',featureNames);

%catch

% Package computed features into a table.

% featureValues = NaN(1,13);

%    featureNames =
["ClearanceFactor","CrestFactor","ImpulseFactor","Kurtosis","Mean","PeakValue",
,"RMS","SINAD","SNR","ShapeFactor","Skewness","Std","THD"];

%    voltage_sigstats =
array2table(featureValues,'VariableNames',featureNames);

% end
```